Modélisation tridimensionnelle fortement couplée par la méthode des éléments finis étendus (XFEM) de la fracturation hydraulique avec un accent sur les barrages en béton

par

Simon-Nicolas ROTH

THÈSE PAR ARTICLES PRÉSENTÉE À L'ÉCOLE DE TECHNOLOGIE SUPÉRIEURE
COMME EXIGENCE PARTIELLE À L'OBTENTION
DU DOCTORAT EN GÉNIE
Ph.D.

MONTRÉAL, LE 10 JUILLET 2020

ÉCOLE DE TECHNOLOGIE SUPÉRIEURE
UNIVERSITÉ DU QUÉBEC

PRÉSENTATION DU JURY

CETTE THÈSE A ÉTÉ ÉVALUÉE

PAR UN JURY COMPOSÉ DE:

M. Azzeddine Soulaïmani, Directeur de Thèse
Département de génie mécanique, École de technologie supérieure

M. Pierre Léger, Co-directeur
Département des génies civil, géologique et des mines, École Polytechnique de Montréal

Mme. Marie-José Nollet, Présidente du Jury
Département de génie de la construction, École de technologie supérieure

M. Hakim Bouzid, membre du jury
Département de génie mécanique, École de technologie supérieure

M. Faouzi Ghrib, Examinateur Externe
Civil and Environmental Engineering, University of Windsor

ELLE A FAIT L'OBJET D'UNE SOUTENANCE DEVANT JURY ET PUBLIC

LE 10 JUIN 2020

À L'ÉCOLE DE TECHNOLOGIE SUPÉRIEURE

REMERCIEMENTS

J’ai réalisé cette thèse dans un contexte bien particulier. Étant marié à une conjointe plus que patiente, père de trois enfants en jeune âge, travailleur à temps plein pour Hydro-Québec, je pense que l’achèvement de ce projet relève de la folie plutôt que de la raison. Or, il semble que la folie l’a emportée sur la raison, car j’ai bel et bien réussi à terminer la thèse. Habituellement, la section remerciements dans les thèses commence par reconnaître le directeur, co-directeur et membres du jury. Dans mon cas, je dois d’abord remercier ma conjointe qui franchement a su me supporter malgré que notre vie a trop souvent été lamentablement perturbée par toutes les soirées et nuits que j’ai passées à travailler sur ma thèse. Je réalise à quel point ton amour est inconditionnel ! Je n’ai pas de mots pour te dire combien j’apprécie tout ce que tu as fait pour moi et pour m’avoir enduré et supporté durant ma thèse.

Ensuite, je dois remercier mes enfants (Alexandre, Heidi et Frédéric) qui, je l’espère, n’ont pas été perturbés par le fait que j’ai réalisé cette thèse. J’ai tout fait pour travailler sur celle-ci durant leurs heures de sommeil. J’imagine qu’avec mon sommeil réduit, ma patience envers vous a diminué ce qui vous a sûrement affecté, car une des grandes qualités des parents est justement la patience. Cependant, je crois que cet exercice vous montre que rien n’est impossible. De plus, je pense que de faire une thèse parallèlement à un travail à temps plein permet d’éviter de se spécialiser dans un secteur qui pourrait éventuellement n’avoir aucun lien avec votre carrière. Ensuite, ceci peut vous permettre de faire un pont essentiel entre la pratique et la recherche. Sans vous recommander de faire comme votre père un peu cinglé, vous m’en parlerez si un jour vous désirez vous lancer dans un tel projet.

Je tiens à exprimer mes remerciements les plus vifs et les plus sincères à mon directeur de recherche, le professeur Azzeddine Soulaïmani. Le professeur Soulaïmani m’a permis de profiter de son expérience, de ses directives, de sa patience et de son soutien aussi bien scientifique que moral. Depuis notre rencontre, il y a près de vingt ans, bien des choses ont évolué, mais mon amitié et ma gratitude envers le professeur Soulaïmani resteront présentes pour les années à venir. Ma première rencontre avec lui m’a démontré, qu’alors que d’autres professeurs doutaient de mes ambitions à réaliser certains projets, la preuve qu’avec de la confiance, de la persévérance, un travail acharné, de la patience et une amélioration de nos connaissances nous pouvons, en équipe, démontrer que *«le ciel n'est pas la limite»*.

De plus, je tiens à remercier Pierre Léger, mon co-directeur de recherche, pour la qualité de son encadrement, sa disponibilité et surtout pour la confiance qu'il a su m'accorder tout au long de ces années. Je tiens aussi à lui exprimer mon admiration et ma reconnaissance pour ses grandes qualités humaines. Elles ont été une source de motivation pendant le déroulement de cette thèse et ont fait de nos rencontres des moments fort agréables. J'ai eu la chance de rencontrer le professeur Léger sur le dossier de la modélisation du comportement atypique du barrage Daniel-Johnson. Durant toutes les années que nous avons passé sur ce dossier, il a su relever la barre à un tel niveau que nous avons réussi à dépasser les conventions normalement utilisées dans la modélisation en contexte industriel. Monsieur Léger a la capacité de relier les derniers développements scientifiques avec la pratique, tout en restant pragmatique étant donné les responsabilités liées à l'application de ces développements dans un contexte réel. C'est une grande qualité que la communauté scientifique devrait développer davantage étant donné qu'une grande partie de la recherche ne pourra probablement jamais être liée au contexte industriel. Malheureusement, bien des chercheurs ne semblent pas s'intéresser au réalisme et à l'applicabilité des méthodes développées.

Finalement, je veux exprimer ma gratitude envers mes collègues de travail. Vous avez sûrement pu observer mon état de fatigue lorsque j'arrivais au bureau après avoir dormis que quelques heures !

Modélisation tridimensionnelle fortement couplée par la méthode des éléments finis étendus (XFEM) de la fracturation hydraulique avec un accent sur les barrages en béton

Simon-Nicolas ROTH

RÉSUMÉ

Dans cette thèse, nous nous interessons à la modélisation de la fissuration dans les structures hydrauliques tridimensionnelles en béton de grandes dimensions. Dans ce contexte, le développement d'une nouvelle méthode numérique pour représenter la fissuration en intégrant la mécanique non linéaire de la rupture à l'aide d'un modèle de fissuration diffuse dans la zone d'élaboration de la fissure avec un modèle utilisant la méthode des éléments finis étendus (XFEM) dans la zone où il y a coalescence des microfissures a été réalisé. Ce nouveau modèle couple donc les avantages de l'approche de la mécanique continue de l'endommagement avec celle de la méthode des éléments finis étendus. Avant que la transition se produise entre les deux modèles, la mécanique continue de l'endommagement est utilisée comme prédicteur afin de déterminer la trajectoire de fissure. Lors de la transition, la conservation d'énergie est appliquée en assurant que la dissipation d'énergie en mode I est conservée. Ce modèle a démontré une grande capacité à reproduire les trajectoires de fissures ainsi que les courbes de résultats expérimentaux pour de nombreux cas de simulation. De plus, il a été démontré que ces résultats sont indépendants du maillage utilisé, confirmant l'objectivité du modèle.

Le modèle de fissuration développé initialement en deux dimensions a été étendu pour un contexte tridimensionnel. Un ingrédient clé pour que la méthode fonctionne dans ce contexte est l'algorithme de suivi des discontinuités. La méthode dite globale est utilisée pour suivre les discontinuités. Cette méthode a été appliquée par d'autres auteurs, mais dans cette thèse elle a été étendue à des problèmes de taille importante avec des géométries de fissures complexes. Une contribution importante a été réalisée afin de calculer l'ouverture de fissure dans le contexte de la mécanique continue de l'endommagement. Il est commun de définir une sorte de longueur caractéristique afin de relier la déformation dans la direction principale avec une ouverture de fissure. Or, il a été démontré que dans le cas où un maillage irrégulier est utilisé, l'ouverture de fissure présente des oscillations non réalistes le long de la fissure et donne des résultats très approximatifs. La méthode proposée, basée sur une formulation XFEM locale et sur l'équilibre des forces, vient régler cette problématique. Cet algorithme a notamment été utilisé dans un cas de fissuration hydromécanique où la perméabilité, liée à l'ouverture de fissure, est augmentée lors de la progression de l'endommagement. Finalement, une contribution a été réalisée en utilisant la XFEM pour la première fois avec succès dans un problème d'envergure industrielle dans le secteur du génie civil, malgré que la méthode a été publiée il y a une vingtaine d'années.

Une autre contribution a été réalisée en proposant une méthode hydromécanique 3D fortement couplée pour le calcul de problèmes de fracturation hydraulique complexes et non planaires. Un ingrédient clé est l'utilisation d'un sous-problème dans lequel un maillage hydraulique est utilisé afin de calculer l'écoulement dans les discontinuités. La complexité de l'écoule-

ment, lié aux non-linéarités causées par les différents régimes d'écoulement et à la présence de drainage, peut être calculée par la méthode proposée. La pression calculée à l'aide de ce sous-problème peut être transférée au problème hydromécanique fortement couplé. Un aspect important à considérer concerne le transfert des ouvertures de fissures de la structure vers le maillage hydraulique et, à l'inverse, le transfert des pressions hydrauliques vers le problème hydromécanique en respectant l'équilibre des charges appliquées. L'utilisation de la XFEM permet le calcul de l'ouverture de fissure ainsi que l'application de la pression sur les surfaces de la fissure pour la simulation de l'amorçage et de la propagation d'une fracture hydraulique. Les conditions de saturation partielles sont ajoutées en couplant un modèle de diffusion non linéaire prenant en compte l'effet de la saturation par une équation non linéaire variant en temps et en espace.

Mots-clés: Fissuration du béton, technique de suivi des fissures, mécanique de la rupture non linéaire, méthode des éléments finis étendus (XFEM), approche de la mécanique continue de l'endommagement, couplage hydromécanique, hydrofracturation, drainage, barrage

Strongly coupled three-dimensional modeling by the extended finite element method (XFEM) of hydraulic fracturing with emphasis on concrete dams

Simon-Nicolas ROTH

ABSTRACT

In this thesis, we are interested in the modeling of cracks in large three-dimensional hydraulic structures. In this context, the development of a new numerical method to represent cracking by integrating the nonlinear fracture mechanics approach coupling a diffuse crack model in the fracture process zone with the extended finite element method (XFEM) in the area where there is coalescence of microcracks was achieved. This new model couples the benefits of the continuous damage approach with that of the extended finite elements method. Before the transition between the two models occurs, the continuous damage approach is used as predictor to determine the crack path. During the transition, energy conservation is applied while ensuring that the mode I energy dissipation is preserved. The model demonstrated a great capacity to reproduce the crack paths as well as the experimental results for many test cases. In addition, it has been shown that these results are independent of the mesh, confirming the objectivity of the model.

The model initially developed in two dimensions has been extended for a three-dimensional context. A key ingredient for the method to work in 3D is the crack tracking algorithm. The so-called global method is used to follow discontinuities. This method has been applied by other authors, but in this thesis it has been extended to large problems with complex crack geometries. An important contribution was achieved to compute the crack opening in the context of the continuous damage mechanics approach. It is common to define a kind of characteristic length to link the strain in the principal direction with the crack opening. However, it was shown that in the case where an irregular mesh is used, the crack opening presents unrealistic oscillations along the crack and gives very approximate results. The proposed method, based on a local XFEM formulation and on the balance of loads, solves this problem. This algorithm was notably used in a hydrofracturation case where the permeability, linked to the crack opening, is increased during the progression of damage. Finally, a contribution was made by using the XFEM with success for the first time in an industrial-scale problem in the civil engineering sector, despite the fact that the method was published about twenty years ago.

Another contribution was the proposal of a strongly coupled 3D hydromechanical method for the computation of complex and non-planar hydraulic fracturing problems. A key ingredient is the use of a sub-problem in which a hydraulic mesh is used to compute the flow in the discontinuities. The complexity of the flow, linked to the non-linearities caused by the different flow regimes and the presence of drainage, can be computed by the proposed method. The pressure computed using this sub-problem can be transferred to the strongly coupled hydromechanical problem. An important aspect to consider concerns the transfer of crack openings from the structure to the hydraulic mesh and, conversely, the transfer of hydraulic pressures to the structural problem while respecting the balance of loads. The use of XFEM allows the computation of crack openings as well as the application of pressure on the crack surfaces for the simulation of the initiation and the propagation of hydraulic fracturing. The partial saturation conditions are added by coupling a non-linear diffusion model taking into account the effect of saturation by a non-linear equation varying in time and space.

Keywords: Concrete cracking, crack tracking technique, nonlinear fracture mechanics, extended finite element method (XFEM), continuous damage mechanics approach, hydromechanical coupling, hydrofracturing, drainage, dam

TABLE DES MATIÈRES

Page

LISTE DES TABLEAUX

LISTE DES FIGURES

LISTE DES ALGORITHMES

LISTE DES ABRÉVIATIONS, SIGLES ET ACRONYMES

FPZ	zone d'élaboration de fissure (*Fracture Process Zone*)
LEFM	mécanique linéaire élastique de rupture (*Linear Fracture Mechanics*)
NLFM	mécanique non linéaire de rupture (*Non-Linear Fracture Mechanics*)
CDM	Méthode de la mécanique continue de l'endommagement (*Continuous Damage Method*)
FEM	méthode des éléments finis (*Finite Element Method*)
XFEM	Éléments finis étendus (*eXtended Finite Element Method*)
PUM	Méthode de la partition de l'unité (*Partition of Unity Method*)
GFEM	Méthode des éléments finis généralisés (*Generalized Finite Element Method*)
PUFEM	Méthode des éléments finis avec une partition de l'unité (*Partition of Unity Finite Element Method*)
DM	Méthode discrète (*Discrete Method*)
PFM	Méthode du champ de phase (*Phase-Field Method*)
EFG	méthode de Galerkin sans éléments (*Element Free Galerkin*)
MLSA	Approximation des moindres carrés (*Moving Least Squares Approach*)
SDA	Approche des discontinuités fortes (*Strong Discontinuity Approach*)
SKON	Approche statique et cinématique optimale non symétrique (*Statically and Kinematically Optimal Nonsymmetric*)
KOS	Approche cinématique symétrique optimale (*Kinematically Optimal Symmetric*)
SOS	Approche statique symétrique optimale (*Statically Optimal Symmetric*)
JRC	Coefficient de rugosité de joint (*Joint Roughness Coefficient*)
CMSD	Déplacement de l'amorce de fissure (*Crack Mouth Sliding Displacement*)
CMOD	Ouverture de l'amorce de fissure (*Crack Mouth Opening Displacement*)

LISTE DES SYMBOLES ET UNITÉS DE MESURE

Indices :

$\langle\rangle_l$	phase eau-liquide
$\langle\rangle_g$	phase gazeuse
$\langle\rangle_v$	phase de vapeur d'eau
$\langle\rangle_a$	phase air sec

Operateurs :

∇x	gradient de x
$\nabla \cdot x$	divergence de x
$\|\|x\|\|$	norme du vecteur x
$\|x\|$	valeur absolue de x
$\langle \ldots \rangle$	parenthèse de Macaulay
$\odot$	produit scalaire
$\otimes$	produit tensoriel

Lettres grecques :

δ_D	distribution de Dirac
ε_i	déformation principale i
κ_i	variable interne caractérisant la valeur maximale de la déformation principale i
ϕ	angle de frottement du béton non fissuré
ϕ_α	fraction occupée par le constituant $\alpha = \{$liquide, vapeur, air$\}$
ϕ_ξ	fonction de level-set évaluée à la coordonnée naturelle ξ
ξ	coordonnées naturelles
σ	tenseur des contraintes de Cauchy
$\tilde{\sigma}$	tenseur des contraintes effectives

$\mathscr{H}$	fonction Heaviside
Γ_u	frontière ayant des déplacements imposés
Γ_p	frontière ayant des pressions imposées
Γ_t	frontière ayant des tractions imposées
Γ_d	frontière d'une discontinuité
Ω	sous-ensemble de l'ouvert R^n
Ω_c	espace des canaux causé par les discontinuités

Constantes minuscules :

μ_α	viscosité du constituant α
ν	viscosité cinématique du fluide
ρ_α	densité du constituant α
ϕ	porosité totale
b_0	coefficient de Biot initial
c_f	longueur effective de la FPZ
d_a	taille de l'agrégat maximal
f_t'	résistance à la traction
f_c	résistance à la compression
g	accélération due à la gravité
h_a	hauteur moyenne des aspérités dans la discontinuité
k	perméabilité intrinsèque
k_d	coefficient de conductivité du drain
l_c	propriété matérielle qui régit la largeur minimale possible d'une zone d'endommagement dans un continuum non local
l_d	longueur du drain
l_{rve}	élément de volume représentatif

p_{atm}	pression atmosphérique

Constantes majuscules :

A_d	aire du drain
E_0	module élastique initial
E_l	module d'élasticité isostatique de l'eau
E_s	module d'élasticité isostatique du squelette solide
G_f	énergie de rupture correspondant à l'aire sous la tangente initiale de la courbe contrainte-déformation
G_F	énergie de rupture correspondant à l'aire complète sous la courbe contrainte-déformation
R	constante des gaz parfaits
R_a	rayon d'interaction
T_0	température de référence

Variables minuscules :

$\{l_i, m_i, n_i\}$	cosinus directeurs du vecteur propre i
b	coefficient de Biot
$\mathbf{b}$	vecteur des charges corporelles
d	indice scalaire de l'endommagement
f_i	fonction de chargement
$f_{\bar{u}}^{ext}$	charges externes associées aux variables inconnues non enrichies
$f_{\hat{u}}^{ext}$	charges externes associées aux variables inconnues enrichies
$f_{\bar{u}}^{body}$	charges corporelles associées aux variables inconnues non enrichies
$f_{\hat{u}}^{body}$	charges corporelles associées aux variables inconnues enrichies
k_{cr}	coefficient de conductivité hydraulique dans la discontinuité
$\mathbf{m}_{\Gamma_d}$	direction tangente à la discontinuité

$\mathbf{n}_{\Gamma_d}$	direction normale à la discontinuité
p	degré de liberté de pression
p_c	pression capillaire
p_v	pression de vapeur
p_{vs}	pression de vapeur de saturation
p^h	forme faible de l'approximation de pression
p_α	pression du constituant α
$\mathbf{t}_d$	force cohésive
$\mathbf{u}$	degrés de liberté de déplacements (élément standard)
$\mathbf{u}^h$	forme faible de l'approximation des déplacements
$\bar{\mathbf{u}}$	degrés de libertés de déplacements standard (élément enrichi)
$\hat{\mathbf{u}}$	degrés de liberté liés à l'enrichissement (élément enrichi)
$[\![\mathbf{u}]\!]$	saut dans le champ de déplacement
u_n	ouverture normale de la surface de discontinuité
u_t	glissement tangentiel de la surface de discontinuité
$\mathbf{v}$	vecteur de vitesse du fluide
$\mathbf{v}_{cr}$	vecteur de vitesse du fluide dans la discontinuité
w_{cr}	ouverture de la discontinuité
$w_{cr}^{(m)}$	ouverture mécanique de la discontinuité
$w_{cr}^{(h)}$	ouverture hydraulique de la discontinuité
$\bar{\mathbf{x}}_i$	coordonnées globales

Variables majuscules :

$\mathbf{C_0}$	tenseur de relation constitutive contrainte-déformation non endommagée
$\mathbf{C_d}$	tenseur de relation constitutive contrainte-déformation endommagée
D_h	diamètre hydraulique

D_{va}	coefficient de diffusion de la vapeur d'eau dans l'air humide
$\mathbf{D}$	tenseur de l'endommagement anisotrope
E	module élastique
H	hauteur d'eau totale
$\mathbf{K}$	matrice des coefficients de perméabilité
K_n	raideur normale de la discontinuité
$\mathbf{N}$	fonctions de forme
$\mathscr{P}$	espace des fonctions tests liées au degré de liberté de pression
$\delta\mathscr{P}$	pondération de l'espace fonctionnel lié à la pression
R_e	nombre de Reynolds
$\mathbf{S}$	premier vecteur propre orthogonal au vecteur propre associé à la plus grande valeur propre de déformation
S_H	ensemble des noeuds enrichis
S_l	degré de saturation
S_s	stockage spécifique
T	température absolue
$\mathbf{T}$	second vecteur propre orthogonal au vecteur propre associé à la plus grande valeur propre de déformation
T_n	force normale à la discontinuité par unité de surface
T_t	force tangentielle à la discontinuité par unité de surface
$\mathscr{U}$	espace des fonctions tests liées au degré de liberté des déplacements
$\delta\mathscr{U}$	pondération de l'espace fonctionnel lié aux déplacements
$W^1 = H^1(\Omega\backslash\Gamma_d)$	fonctions Sobolev de premier ordre

INTRODUCTION

0.1 Généralités

L'analyse de l'effet des fissures sur le comportement structural d'un barrage en béton est un problème d'intérêt industriel qui est grandement stimulé par le vieillissement de ceux-ci. En effet, la présence de fissures dans un barrage peut être une source d'incertitude puisque la durabilité, l'usage fonctionnel et la stabilité de l'ouvrage peuvent être remis en cause. Un ouvrage ayant un état de fissuration important et présentant des signes de faiblesses peut dans un cas de chargement exceptionnel tels un séisme ou une crue créer une catastrophe majeure. Lorsque la fissuration se produit ou est susceptible de se produire, des travaux souvent importants deviennent essentiels. Or, le coût exorbitant de la réhabilitation d'un barrage est souvent disproportionné par rapport aux méthodes d'analyses simplistes couramment utilisées pour évaluer la pertinence des travaux ainsi que leur efficacité. Par conséquent, il est évident qu'un investissement dans une évaluation rigoureuse de la sécurité structurale et dans la confirmation de la nécessité de réaliser des travaux coûteux pourrait très bien conduire à des économies de grandes échelles pour des barrages présentant des comportements atypiques. De plus, advenant le cas où des travaux sont requis, la simulation numérique de la fissuration et des sous-pressions dans l'ouvrage est importante, car elle dicte la nature des travaux à effectuer sur l'ouvrage afin de ne pas aggraver la situation.

0.2 Problématique de recherche

Afin de statuer si un barrage fissuré a besoin de réhabilitation, il est important d'évaluer de façon efficace si les fissures posent un enjeu réel sur sa stabilité et si celles-ci peuvent se propager. La représentation des fissures dans les modèles numériques peut être réalisée par plusieurs méthodes. Cependant, peu de ces méthodes sont suffisamment robustes pour être applicable sur des structures de grandes dimensions et en mesure de tenir compte des particularités que les fissures dans les ouvrages hydrauliques possèdent, en l'occurrence, les sous-pressions. Le calcul de l'écoulement à l'intérieur des fissures amène une complication supplémentaire si celles-ci sont drainées. Dans ce cas, la distribution des pressions dans les discontinuités est la plupart du temps obtenue par les méthodes définies dans les guides. Ces guides proposent des méthodes pour estimer celles-ci dans les barrages en béton (Federal Energy Regulatory Commission (FERC), 2016; U.S. Army Corps of Engineers (USACE), 2000; Amadei *et al.*, 1989). Or, ces méthodes sont établies pour des cas simples qui sont difficilement applicables dans le cas où les fissures possèdent une géométrie complexe, des ouvertures non constantes et un drainage qui n'est pas une répétition périodique de drains équidistants. En l'absence d'une méthode appropriée pour calculer les pressions à l'intérieur des fissures, celles-ci sont souvent surestimées et cette surcharge peut occasionner une propagation de fissure non réaliste et amène à des conclusions conservatrices sur la stabilité de l'ouvrage. Une autre hypothèse souvent considérée dans les ouvrages hydrauliques concerne la prise en compte des pressions interstitielles lors du calcul de la contrainte effective. Celles-ci sont généralement calculées sur la base que le béton est saturé, donc pour un ouvrage poids, celles-ci sont appliquées selon une distribution triangulaire à l'intérieur de l'ouvrage (100% à l'amont et 0% à l'aval). Ces modèles sont conservateurs, car il a été démontré (Bažant, 1975; International Commission on Large Dams (ICOLD), 2004) que par le phénomène de séchage et de dessiccation, le béton n'est pas saturé sur une très grande partie de l'ouvrage. Les résultats d'analyses où la condition de saturation partielle a été prise en compte (Pellegrini, 1996) démontrent la forte inertie hydraulique du corps du barrage, c'est-à-dire une résistance élevée à l'écoulement d'eau. Ceci est dû à la faible perméabilité d'un béton sain et à sa forte réduction en fonction du degré de saturation. Les conditions de saturation partielle dans le corps du barrage correspondent donc à une perméabilité extrêmement faible. Des vides localisés, tels que les galeries où les drains induisent également la présence d'une zone non saturée, avec les effets susmentionnés sur la perméabilité. L'introduction de la condition de saturation partielle dans les analyses couplées rend l'analyse numérique très complexe et difficile à résoudre étant donné les fortes non-linéarités du modèle de diffusion. Cependant, ces modèles peuvent fournir des informations utiles sur l'influence des aspects non représentés par les approches plus simples.

0.3 Objectifs de la thèse

Il est proposé dans cette thèse de développer une méthode pour réaliser l'analyse de fissuration applicable aux structures hydrauliques. Dans ce contexte, l'objectif principal est de développer une méthode efficace pour modéliser un problème couplé de fissuration hydromécanique et applicable à des problèmes tridimensionnels de grandes dimensions. Il existe une grande quantité de méthodes pouvant modéliser la fissuration dans les matériaux cimentaires, par contre, ceux-ci ne sont pas tous applicables afin de répondre à l'objectif principal de la thèse. Un objectif spécifique est d'utiliser la méthode des éléments finis étendus (XFEM) afin de modéliser la fissuration. Bien que la XFEM a fait l'objet de plusieurs travaux de recherche, cette méthode a très peu été utilisée pour des problèmes tridimensionnels de grandes tailles, la recherche étant majoritairement appliquée sur des problèmes bidimensionnels. Un développement important est donc requis afin d'utiliser la méthode pour des problèmes de fissuration hydromécaniques couplés. Ce développement inclut les objectifs spécifiques suivants :

1. effectuer une revue critique de la littérature sur les modèles de fissuration et sur l'interaction hydromécanique ;
2. développer une méthode 3D pour représenter une fissure dans le contexte de la mécanique non linéaire de la rupture en intégrant un modèle de fissuration diffuse dans la zone d'élaboration de la fissure et un modèle XFEM dans la zone où il y a eu coalescence des microfissures ;
3. concevoir une méthode de propagation de fissure basée sur l'analogie avec un calcul en transfert de chaleur et trouver les points d'intersection entre le maillage et la fissure de façon à enrichir les éléments traversés par la surface de fissuration ;

4. élaborer un modèle fortement couplé hydromécanique pour trouver les pressions induites par les fissures en contact avec le réservoir dans le contexte où la fissure est drainée ;
5. calculer les pressions interstitielles avec un modèle de diffusion non linéaire de façon à considérer que l'ouvrage est partiellement saturé ;
6. montrer la validité des méthodes proposées avec des exemples et avec des démonstrations rigoureuses ;
7. commenter de manière critique les résultats obtenus et exprimer des recommandations quant aux choix et à la mise en oeuvre des méthodes de calcul.

0.4 Plan de la thèse

La présente thèse s'articule autour de trois chapitres qui ont fait l'objet de deux publications parues (chapitres 2 et 3) et d'une soumise (chapitre 4). Trois problématiques sont abordées dans ces chapitres à savoir :

1. la résolution du calcul tridimensionnel de la propagation de fissures en proposant un modèle de fissure qui couple les avantages de l'approche de la mécanique continue de l'endommagement avec ceux de la méthode des éléments finis étendus ;
2. le calcul de la fissuration hydromécanique fortement couplée dans des structures tridimensionnelles de grandes dimensions en utilisant la XFEM ;
3. la prise en compte d'un écoulement complexe et de la présence de drainage dans les discontinuités dans un modèle hydromécanique couplé ainsi que les conditions de saturation partielles.

Le chapitre 1 présente une revue de littérature portant sur les aspects importants liés à la problématique de recherche. Ainsi, une revue critique des modèles de fissuration est d'abord réalisée. La revue des lois constitutives régissant l'écoulement en milieu poreux et la revue des modèles constitutifs de l'écoulement dans les discontinuités sont ensuite présentées.

Le deuxième chapitre vise la modélisation de la propagation de fissure pour des problèmes bidimensionnels. L'objectif de ce chapitre est de développer la méthode combinant l'approche de la mécanique continue de l'endommagement avec la méthode des éléments finis étendus. Une formulation XFEM cohésive est utilisée afin de transférer la dissipation d'énergie de l'approche de la mécanique continue de l'endommagement (CDM) vers l'approche XFEM tout en assurant la conservation d'énergie lors de la transition entre les deux approches. Finalement, une technique de suivi des fissures est développée pour propager la trajectoire de fissure le long d'une seule rangée d'éléments finis en assurant que celle-ci soit indépendante du maillage.

Le troisième chapitre présente un modèle tridimensionnel de fissuration du béton robuste et applicable à l'étude de grandes structures hydrauliques tridimensionnelles, telles que des barrages béton. Le modèle de transition CDM-XFEM présenté dans le chapitre 2 est étendu en 3D. En plus, afin de permettre la simulation de la fissuration hydraulique, le modèle mécanique est fortement couplé à un modèle de poro-endommagement où la perméabilité est augmentée lors de la progression de l'endommagement. Le calcul de la perméabilité est fonction de l'ouverture de fissure qui, dans le contexte de la mécanique continue de l'endommagement, n'est pas triviale à définir. Pour arriver à cette fin, une méthode basée sur une formulation XFEM locale est proposée. Finalement, le calcul de la trajectoire de fissure en 3D, basé sur une analogie au problème de conduction thermique pour tracer l'enveloppe du champ vectoriel tangent aux discontinuités, est détaillé.

Le quatrième chapitre présente le développement, la mise en oeuvre et l'application d'un nouveau modèle hydromécanique non linéaire et fortement couplé pour une application de fissuration hydraulique tridimensionnelle et non planaire où un écoulement complexe peut se produire. La formulation de la méthode des éléments finis étendus est utilisée, car elle permet le calcul de l'ouverture de la fissure ainsi que l'application de la pression de l'eau sur les surfaces de la fissure pour la simulation de l'amorçage et de la propagation d'une fracture hydraulique.

Pour prendre en compte les effets du drainage dans la modélisation, deux modèles d'éléments finis couplés (multi physiques) sont utilisés ; (1) un modèle pour le calcul des pressions dans les discontinuités avec un maillage hydraulique avec raffinement autour des drains (2) un modèle pour la réponse mécanique fortement couplée avec l'écoulement en milieu poreux non saturé. Les deux sous-problèmes sont résolus à l'aide d'une procédure partitionnée, car ils ont des exigences de résolution différentes. Enfin, le maillage mécanique et le maillage hydraulique ont des interfaces discrètes non appariées qui doivent être couplées en respectant l'équilibre des charges appliquées.

Les présents développements ont été réalisés dans un code autonome écrit en C++ (le code contient approximativement 50000 lignes sans inclure les librairies). La validation de chacune des étapes est réalisée de façon systématique et rigoureuse avec des cas expérimentaux ou numériques communément utilisés dans la littérature. Un grand nombre de cas bidimensionnels et tridimensionnels sont utilisés afin de valider la démarche proposée pour réaliser les objectifs de la présente thèse.

Nous terminons cette thèse par une conclusion générale et des recommandations futures.

0.5 Contributions originales

La thèse présente plusieurs originalités et contributions :

1. le développement complet de la XFEM pour des problèmes tridimensionnels complexes de grandes dimensions qui est applicable dans un contexte industriel ;
2. le couplage entre l'écoulement dans les discontinuités et le calcul de la pression capillaire avec prise en compte des conditions de saturation partielles ;
3. une nouvelle méthode afin d'approximer l'ouverture de fissure dans le contexte de la mécanique continue de l'endommagement sans utilisation d'une longueur caractéristique ;

4. un nouveau modèle de fissuration 2D et 3D qui possède à la fois les avantages de la représentation continue et de l'approche discrète ;
5. la prise en compte d'un écoulement complexe présentant des non-linéarités dans les discontinuités ;
6. la possibilité de vérifier l'influence de la présence de drains dans un ouvrage et son effet dans les discontinuités.

0.6 Liste des publications

Cette thèse de doctorat contient trois articles de revue présentées dans les chapitres 2 à 4. De plus, plusieurs publications et présentations scientifiques, qui sont pertinentes au sujet de cette thèse, ont été rédigées et/ou présentées. Ces publications sont présentées à l'annexe I.

CHAPITRE 1

REVUE DE LA LITTÉRATURE ET POSITION DU PROBLÈME

1.1 Mécanique de la rupture

La mécanique de la rupture est globalement acceptée comme étant la méthode pour analyser la défaillance de structures. En 1913, Inglis (Inglis, 1913) a été le premier qui, grâce au calcul des contraintes en un point situé aux frontières d'une fissure de forme ellipsoïde dans un solide infini, a pu observer que si l'ellipsoïde rétrécit et tend vers une fissure de forme rectiligne, les contraintes en ce point tendent vers l'infini. Lorsque ces résultats furent portés à l'attention de Griffith (Griffith, 1921, 1924), il conclut qu'en présence d'une fissure, les contraintes ne pouvaient pas être utilisées comme critère de rupture, car peu importe la charge appliquée sur un milieu élastique continu contenant une fissure, les contraintes en pointe de fissure sont infinies. Ceci a conduit Griffith à proposer un critère de propagation basé sur une approche énergétique et a servi à créer les fondements de la mécanique linéaire élastique de rupture (LEFM). Ainsi, selon ce critère, une fissure se propagera si l'énergie disponible par unité de surface est égale à l'énergie nécessaire pour la propagation. Cette énergie est communément appelée *taux de restitution d'énergie*. Une autre étape a été franchie lorsque Rice en 1968 (Rice, 1968) a proposé l'intégrale J. Cette intégrale a donné un lien entre le taux de restitution d'énergie et le champ de contraintes et de déformations près de la pointe de la fissure pour tout matériau élastique. En 1957, en introduisant le concept de facteur d'intensité de contrainte, Irwin (Irwin, 1957) a apporté une seconde évolution majeure au domaine de la mécanique linéaire élastique de rupture. Le facteur d'intensité de contrainte est un paramètre qui relie directement l'intensité des contraintes près de la pointe d'une fissure au taux de restitution d'énergie.

Cependant, rapidement après l'introduction des concepts précédents, il est apparu que la LEFM prédisait de bons résultats lorsque la fracture était très fragile. Pour des matériaux ductiles ou encore des matériaux quasi-fragiles, les résultats pouvaient, dans certains cas, s'avérer inexacts.

Pour des matériaux quasi-fragiles ou ductiles, une certaine zone d'élaboration de fissure (FPZ) existe en pointe de fissure et une seconde branche de la mécanique de la rupture doit alors être utilisée pour calculer la propagation, soit la mécanique non linéaire de rupture (NLFM). Un modèle linéaire élastique de la rupture suppose que la dissipation d'énergie est uniquement causée par la progression de la fissure et qu'elle se produit dans une zone infinitésimale à la pointe de la fissure, où le champ de contrainte est censé être singulier. La dissipation volumique dans la FPZ demeure confinée de telle sorte qu'elle puisse être négligée par rapport aux dimensions de la structure. À l'inverse, un modèle non linéaire de la rupture considère qu'il y a un comportement adoucissant dans la zone d'élaboration de la fissure et donc aucune présence de singularité. Ceci est illustré à la figure 1.1. Le modèle non linéaire de rupture est représenté à gauche. Sur la figure 1.1a, la fissure de longueur totale a présente une section de longueur a_0 qui est une fissure ouverte, suivie d'une zone d'élaboration de longueur l_p. Dans la zone, représentée à la figure 1.1b, située après la pointe de fissure, l'énergie de fissuration n'est pas suffisante pour propager la fissure macroscopique. À la figure 1.1c, les contraintes de tractions sont représentées de façon à démontrer qu'immédiatement en pointe de fissure l'endommagement est très élevé, donc la contrainte est de très faible amplitude. À une certaine distance de la pointe de fissure, la contrainte maximale apparaît, car il n'y a pas d'endommagement à ce point. La zone entre ces deux points présente un endommagement graduel résultant de microfissurations. À droite de cette figure, la méthode LEFM est présentée. La zone d'élaboration est représentée par un point (singularité). La contrainte en ce point est censée être singulière et ceci est représenté à la figure 1.1c.

Le succès de la LEFM repose sur la taille de la FPZ. En fait, seule, la longueur d'élaboration ne suffit pas pour statuer sur l'applicabilité de la méthode. Hillerborg et coll. (Hillerborg *et al.*, 1976; Hillerborg, 1983) ont montré que le ratio de la taille de la structure d par rapport à la longueur caractéristique du béton l_{ch} est un paramètre important afin de déterminé le type de modèle de rupture à considérer. Dans les références (Brühwiler & Roelfstra, 1989; Brühwiler *et al.*, 1991), il a été démontré que la mécanique linéaire de rupture est applicable seulement si $d/l_{ch} < 25$. À $d/l_{ch} = 25$, une différence de 5% de la charge maximale atteinte entre le modèle

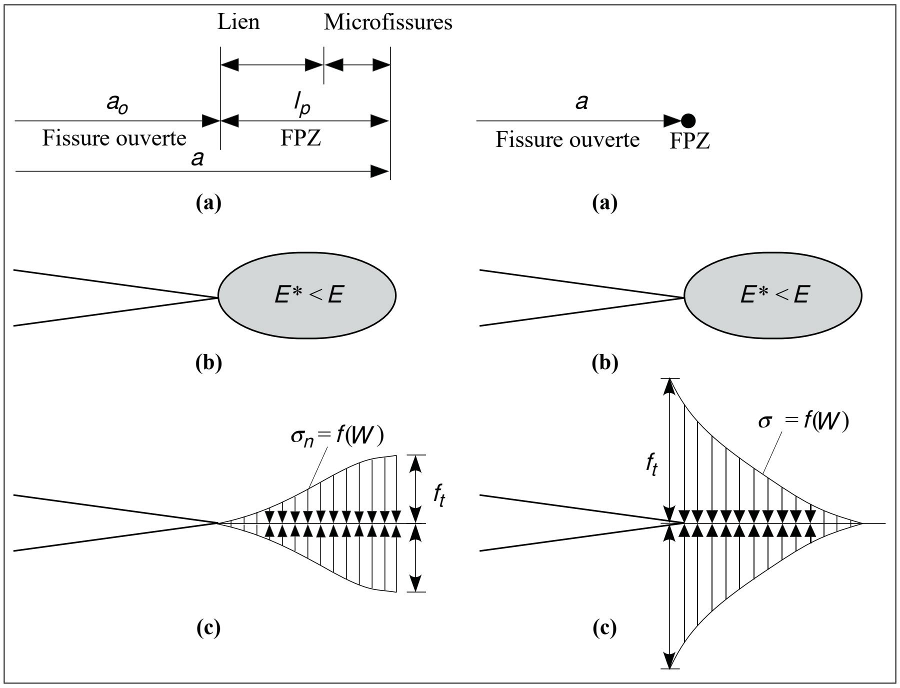

Figure 1.1 Modèle de fissuration NLFM à gauche et LEFM à droite

utilisé par les auteurs (Fictious Crack Model) et un modèle LEFM a été constatée. Il a été conclu que dans le cas d'un barrage, une épaisseur minimale de 25 mètres de béton est requise pour que la LEFM soit applicable.

Basé sur des critères objectifs, Saouma (Saouma, 2007) a résumé trois conditions pour choisir la bonne représentation :

- *Taille de la fissure* : Pour une fissure de dimension importante, l'effet de la zone d'élaboration est plus faible que pour une fissure de faible dimension. Ainsi, la LEFM est plus applicable pour les fissures de taille importantes ;
- *Type de chargement* : Si une structure est soumise à une charge plutôt qu'à des déplacements imposés où seule une réponse pré-pic est importante, les effets non linéaires peuvent être négligeables ;
- *Stabilité locale* : Dans une structure instable soumise à une charge imposée plutôt qu'à des déplacements imposés, les effets non linéaires ne sont pas aussi négligeables que pour une structure stable.

Ces conditions ainsi que le modèle à utiliser sont résumés au tableau 1.1.

Tableau 1.1 Applicabilité d'un modèle linéaire élastique de la rupture

Chargement	Fissure de petite dimension	Fissure de grande dimension
Force, instable	LEFM	LEFM
Force, stable	NLFM	LEFM
Déplacement	NLFM	LEFM

Cependant, Saouma conclut que dans tous les cas, une analyse non linéaire devrait idéalement être utilisée. Toutefois, dans de nombreux cas (mais pas tous) la complexité et les délais associés à une telle analyse donnent souvent des résultats très proches de ceux obtenus à partir d'un modèle linéaire. Ainsi, le type d'analyse à entreprendre repose sur des considérations techniques et économiques.

1.1.1 Synthèse et positionnement

La mécanique linéaire élastique de rupture vise à prévoir les conditions donnant lieu à une propagation rapide des fissures dans les matériaux fragiles considérés comme étant élastiques, homogènes et isotropes au début de la rupture. Le principal succès de cette théorie repose sur la linéarité, ce qui permet de combiner très simplement les analyses théoriques, numériques et expérimentales de la rupture. Cependant, pour un matériau cimentaire soumis à un chargement externe, il se forme une zone de tension près de la pointe de la fissure où de nombreux mécanismes de micro-défaillances inélastiques apparaissent. Ce processus comprend des micro-fissurations, des ramifications, de la coalescence des micro-fissures, des décollements d'agrégats dans la matrice du matériau, etc. Dans le béton, la zone inélastique à la pointe de la fissure est largement développée et, par conséquent, une représentation en mécanique linéaire élastique de la rupture n'est pas nécessairement appropriée pour étudier sa rupture. Donc, afin de généraliser le type de problème pouvant être analysé par les développements réalisés dans la présente thèse, la mécanique non linéaire de rupture sera considérée.

Dans cette thèse, le mécanisme de propagation de fissure sera idéalisé dans la région de la FPZ où, lors du processus de détérioration d'un solide soumis à un processus de chargement avec une fissure se propageant, le matériau passera d'un état sain à un matériau ayant une fissure microscopique pour finalement devenir macroscopique. Passant d'un état sain, à un étant où la fissure progresse, il sera considéré que dans la FPZ du solide considéré, la formation et la croissance de microfissures densément distribuées induiront une réponse non linéaire du matériau avec une dissipation d'énergie importante. Dans cette première phase, le matériau sera stable macroscopiquement même lorsque les déformations augmenteront dans une région restreinte. De plus, il sera considéré qu'aucune localisation de déformations n'aura lieu à ce stade du processus de rupture. Dans la deuxième étape, la réponse du matériau, à l'échelle macroscopique, deviendra instable. À la suite de la coalescence des microfissures, les déformations augmenteront et se localiseront dans une bande de largeur définie, formant une discontinuité faible où les déformations subiront un saut. Par la suite, la largeur de cette bande sur laquelle des forces cohésives seront maintenues, tendra vers zéro. Finalement, ces forces de cohésion disparaîtront et une zone de discontinuité forte sans contrainte apparaîtra.

1.2 Modèles de fissuration

Avec l'avènement des ordinateurs dans les années 1940 et le développement de la méthode des éléments finis (FEM) dans les années 1950 (Turner *et al.*, 1956; Clough, 1960), il n'a pas fallu attendre longtemps avant que les ingénieurs analysent des structures en béton à l'aide de la FEM (Clough, 1962; Ngo & Scordelis, 1967; Rashid, 1968; Nilson, 1967). Déjà dans ces années les deux principales approches pour modéliser des fissures sont développées :

- l'approche de fissuration discrète (Ngo & Scordelis, 1967) ;
- l'approche de fissuration diffuse (Rashid, 1968).

Ces deux approches peuvent aussi être classifiées selon ce qui a été proposé par Ingraffea (Ingraffea, 2004). Cette classification sépare les modèles de fissuration en deux branches principales qui sont elles-mêmes divisées en deux. Dans la première branche, les fissures sont représentées de façon géométrique. Deux options peuvent être considérées, soit :

- une représentation où les fissures sont incorporées dans le modèle et la discrétisation des fissures ainsi que l'extension possible de celles-ci sont fixées a priori ;
- une représentation où la géométrie du modèle ainsi que sa discrétisation sont continuellement mises à jour en fonction de la propagation des fissures.

À l'inverse, dans la deuxième branche, ni la géométrie ni sa discrétisation ne contiennent de données sur les fissures. Dans ce cas, les fissures sont représentées en modifiant la loi constitutive du matériau ou en incorporant une description cinématique spéciale dans le modèle. La figure 1.2 donne les méthodes numériques utilisées pour représenter les fissures, catégorisées selon le système de classification d'Ingraffea. Certaines de ces méthodes seront présentées dans les sections suivantes. Cependant, avant de présenter celles-ci, une difficulté commune aux différents modèles de fissuration, soit l'objectivité du modèle, est mise en évidence dans la prochaine section.

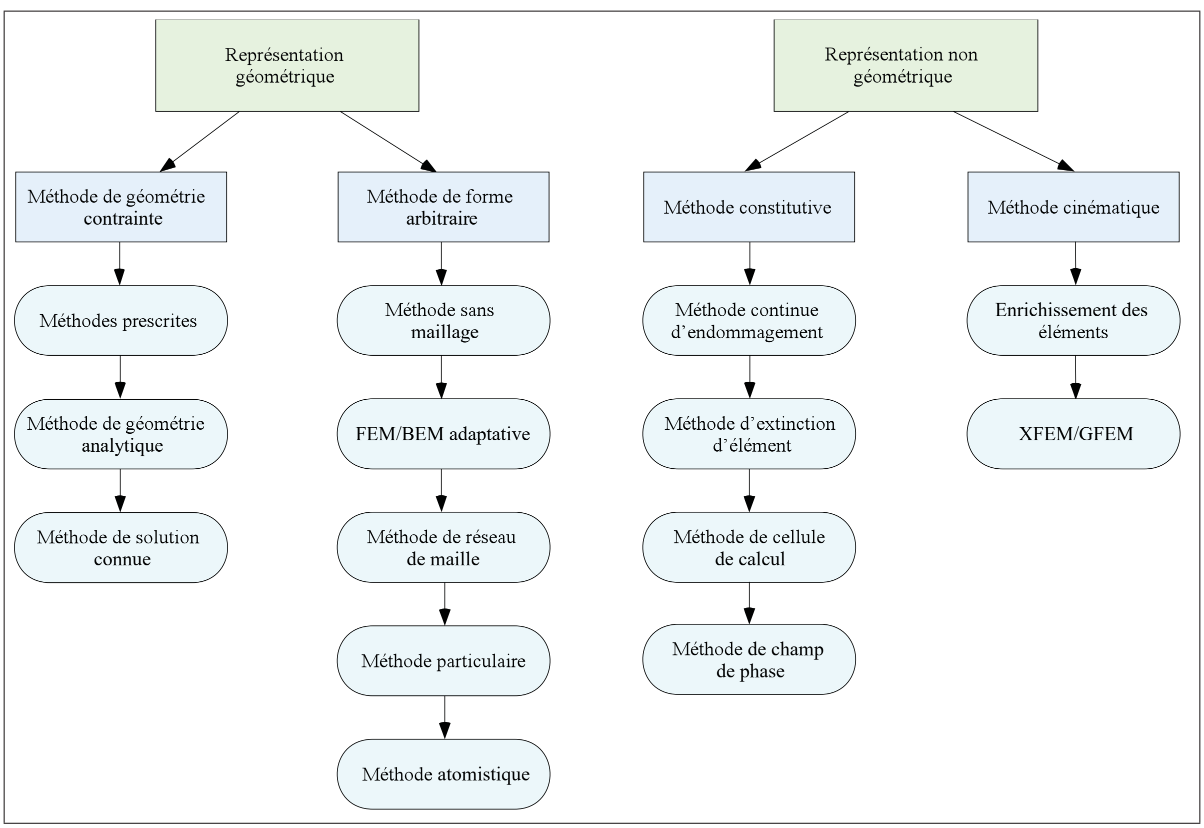

Figure 1.2 Modèle de représentation de la fissuration (adaptée de Ingraffea (2004))

1.2.1 Objectivité du modèle

Un modèle théorique doit être en mesure de donner des résultats objectifs. Si un modèle ne donne pas de résultats objectifs selon le raffinement du maillage ou de certains paramètres numériques, alors il est impossible de se baser sur ses résultats. Griffith a rapidement constaté que les contraintes en pointe de fissures tendaient vers l'infini en faisant tendre la taille de la fissure discrète d'un ellipsoïde vers une fissure de forme rectiligne. Or, il est connu que dans un matériau quasi-fragile comme le béton, cette contrainte infinie n'existe pas. Ceci peut-être expliqué par le fait que durant le processus de rupture d'un matériau considérant la NLFM, la contrainte dans la FPZ, plus particulièrement en pointe de fissure, demeure finie. Si la description mathématique de la FPZ est telle que lorsque la discrétisation du modèle numérique est raffinée à l'infini, de sorte qu'un élément en pointe de fissure tende vers un élément infinitésimal, alors il est évident que les contraintes calculées dans cet élément tendront vers l'infini. Le modèle n'est alors pas objectif puisque les résultats varient en fonction du raffinement de maillage. Du point de vue mathématique, cette dépendance au maillage est liée à la perte d'ellipticité de l'équation différentielle. Le problème aux limites est mal posé, c'est-à-dire qu'il n'a pas de solution unique continue en fonction des données d'entrée.

La problématique d'objectivité survient, peu importe le modèle de représentation de fissure utilisé dans le modèle numérique. En effet, les modèles représentent le béton endommagé ainsi que d'autres matériaux quasi fragiles en les considérants comme des matériaux ayant de l'adoucissement sous déformations. Ceci n'a pas été immédiatement accepté par la communauté scientifique, car les premiers résultats obtenus avec cette représentation n'étaient pas objectifs. En effet, la formulation d'un matériau continu ayant de l'adoucissement sous déformations conduit à une solution qui, lorsque le maillage est raffiné à l'infini, présente les caractéristiques suivantes (Jirásek, 2011) :

- la région de l'adoucissement est infiniment petite ;
- la courbe de déplacement en fonction de la charge présente toujours une instabilité (snap-back), indépendamment de la taille de la structure et de la ductilité du matériau ;

- la quantité totale d'énergie dissipée au cours du processus de rupture devient nulle.

Il est possible de constater que tous les modèles de comportement décrivant la fissuration présentent des propriétés d'adoucissement post-pic qui peuvent ne pas respecter le postulat de Drucker (Drucker, 1959). En effet, selon ce postulat, une force extérieure superposée aux forces qui existent dans l'état d'équilibre actuel doit, pour que l'équilibre soit stable, effectuer un travail non négatif durant son application ainsi que dans un cycle complet d'application et d'enlèvement de cette force. En plus des propriétés d'adoucissement, qui sont inévitables dans la relation constitutive qui doit décrire la fissuration, la modélisation d'autres phénomènes telles la friction et la perte de cohésion entraîne les difficultés mathématiques déjà énoncées et elle cause des instabilités de localisation parasites et une sensibilité à la direction du maillage.

Pour la modélisation par l'approche géométrique et la branche des modèles non géométriques utilisant les méthodes cinématiques, seul le critère de propagation de fissure doit posséder une objectivité du maillage (ceci inclut la direction de propagation). En effet, si l'ouverture de la fissure est modélisée comme une discontinuité de déplacement, il est possible de formuler une loi d'adoucissement objective reliant la traction transmise par une fissure partiellement formée à un saut de déplacement (ouverture de fissure). Dans ce cas, les résultats numériques ne présentent pas de sensibilité au maillage puisque la description physique du processus de rupture est déterminée par une grandeur bien définie, soit l'ouverture de fissure. Dans le cas où une méthode constitutive est utilisée (représentation non géométrique), il est possible d'éviter ces difficultés en combinant les relations constitutives avec une sorte de limiteur de localisation. Il est commun d'appeler ceci la régularisation de la solution d'un problème de localisation. Plusieurs techniques pouvant être regroupées en deux familles ont été adoptées pour limiter cette localisation :

- Relations cinématiques généralisées :

  théorie de l'élasticité non locale ;

  théorie de Cosserat (de Borst, 1991).

- Équations constitutives généralisées :

  concept d'énergie de rupture équivalente (Willam *et al.*, 1986) ;

modèle de gradient supérieur (Aifantis, 1984) ;

modèle non local (Eringen, 1981, 1983).

1.2.2 Approche de représentation géométrique

1.2.2.1 Méthode prescrite

Cette méthode aussi appelée fractionnement de noeud ou découplage de noeud considère qu'a priori la position de la fissure est connue. Le maillage est conçu de telle façon à inclure à l'avance la fissure et le chemin de propagation possible. Clough (Clough, 1962) a été le premier à utiliser cette méthode pour faire l'analyse de l'influence d'une fissure dans un barrage-poids. Lorsque la fissure se propage, les noeuds sont découplés afin de simuler la trajectoire de fissure. La trajectoire de fissure est donc dépendante du maillage initial puisqu'il n'y a aucun remaillage lors d'une analyse. Cette méthode est généralement appréciée pour sa simplicité et sa facilité d'implantation. La méthode prescrite a largement évolué et elle est maintenant utilisée pour modéliser l'interface entre deux matériaux, un joint de construction, la délamination dans les matériaux composites, etc. Dans ces cas, un élément d'interface (Xu & Needleman, 1994) est généralement ajouté entre les éléments (voir figure 1.3). Une loi de traction-séparation est incluse dans la formulation des éléments d'interface afin de représenter l'adoucissement.

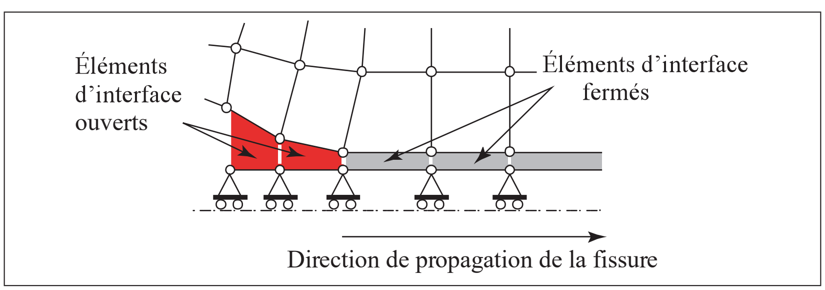

Figure 1.3 Méthode prescrite avec éléments d'interface (adaptée de (Ingraffea, 2004))

1.2.2.2 Méthode de géométrie analytique et méthode de solution connue

Ces méthodes sont utilisées pour des cas où la solution analytique est connue (Nishioka & Atluri, 1983). Pour ces modèles, plusieurs solutions analytiques pour des géométries de fissures précises ont été développées. Il est donc possible d'inclure dans un modèle discrétisé en éléments finis standards les intensités de contraintes données par les solutions analytiques. Un modèle sans fissure est utilisé pour calculer les contraintes causées par les charges sur le modèle. Dans la région fissurée, il n'y a pas de traction entre les faces des fissures ; donc les forces de traction calculées préalablement sont inversées afin de modéliser la portion de fissure macroscopique sans transfert de contrainte. Selon la géométrie de fissure, la solution analytique est ajoutée à la solution du modèle sans fissure dans la zone où se situe la pointe de fissure. Cette procédure est itérée jusqu'à ce que l'état d'équilibre soit respecté. Ces méthodes sont naturellement limitées en termes de géométrie de fissure et aussi par la géométrie du modèle analysé. En effet, les solutions analytiques développées pour un type de forme de fissure sont différentes selon la géométrie du modèle.

1.2.2.3 Méthode sans maillage

Afin d'éviter la problématique liée au maillage et remaillage des fissures, des méthodes sans maillage telle que la méthode de Galerkin sans éléments (EFG) (Lu *et al.*, 1994) ont été développées. En raison de l'absence de connectivité des éléments, des noeuds peuvent être ajoutés facilement à la partie du domaine où la solution présente un fort gradient (voir figure 1.4). Ceci rend la méthode EFG plus souple que la méthode des éléments finis. La méthode est appropriée pour les calculs en mécanique de la rupture, puisque des noeuds peuvent être ajoutés autour des pointes de fissures afin d'obtenir des données précises de facteurs d'intensité de contrainte. La méthode est basée sur une approximation des moindres carrés (MLSA) où un ensemble de noeuds, un ensemble de fonctions de base et un ensemble de fonctions de poids doivent être choisis. L'absence de connectivité n'est pas tout à fait exacte puisque pour des fins d'intégration, une structure de cellules pour le domaine doit être choisie. Cette méthode est donc coûteuse, puisque pour chaque noeud du domaine, un système linéaire doit être résolu. Afin de rendre la méthode plus efficace, des méthodes hybrides ont donc été proposées (Hegen, 1996). Dans ces méthodes, seule la partie du domaine nécessitant une meilleure approximation de la solution utilise la méthode EFG alors que le reste du domaine est approximé par la méthode des éléments finis.

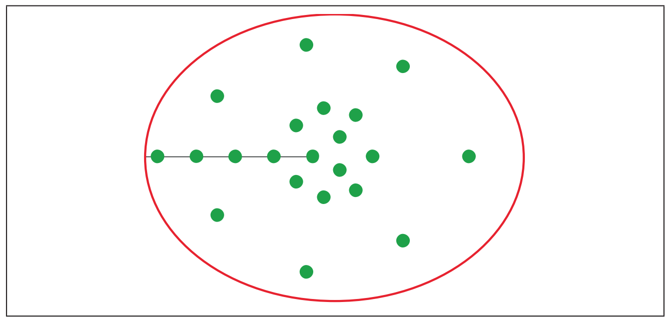

Figure 1.4   Méthode sans maillage EFG

1.2.2.4   Modèle FEM/BEM adaptatif

Le modèle de fissure discrète dans sa forme où la géométrie est contrainte présente plusieurs inconvénients. Les fissures sont forcées de se propager le long des frontières inter-éléments. Un remaillage permet d'éliminer cette dépendance et c'est pourquoi le modèle FEM/BEM fut créé (Wawrzynek & Ingraffea, 1987). Le développement de cette méthode a été rendu possible grâce aux bases de données d'éléments topologiques pouvant représenter géométriquement les surfaces de fissures. La géométrie est continuellement mise à jour durant la simulation, et ce indépendamment de la discrétisation du modèle (voir figure 1.5). Un modèle B-Rep (Boundary Representation) est généralement utilisé pour la géométrie. La B-Rep est une technique de modélisation 3D géométrique qui consiste à représenter la peau des objets par des surfaces ayant des frontières canoniques (B-splines, NURBS, ...). Le remaillage local est ensuite effectué sur la base de nouvelles surfaces. La formulation par éléments finis demeure donc standard, sans ajout de cinématique complexe pour représenter les fissures, mais au prix de devoir utiliser un algorithme de remaillage. Des difficultés liées au changement continuel de topologie et un coût de calcul important rendent cette méthode moins viable pour des problèmes tridimensionnels de grandes tailles.

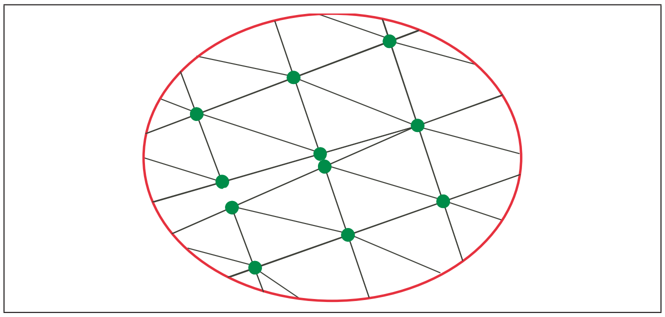

Figure 1.5 Modélisation d'une fissure par une méthode discrète

1.2.2.5 Méthode des éléments discrets

Les méthodes discrètes incluent la représentation par des réseaux de mailles (lattice), la représentation particulaire ou la représentation atomistique. La représentation par des réseaux de maille (Chiaia *et al.*, 1997) (figure 1.6) est réalisée par un ensemble de poutres ou de colonnes pouvant décrire le comportement élastique d'un matériau continu. Le réseau de maille peut se briser pour représenter des fissures. Au lieu d'utiliser des éléments de poutres, la représentation particulaire (Charmet *et al.*, 1989) utilise des formes de base tels des sphères, disques et polyèdres. La loi constitutive est incluse dans ces formes de base et en plus les liens entre celles-ci possèdent des propriétés de décohésion, ce qui permet de représenter des fissures. La représentation atomistique considère que les éléments discrets sont des atomes. Il est évident que la taille des problèmes analysés par cette méthode est de l'ordre de quelques ångström (1 Å $= 10^{-10}$ mètre). L'avantage de cette méthode est que la loi constitutive n'utilise plus de simplification phénoménologique. Elle peut donc être utilisée pour aider à comprendre le comportement d'un matériau et développer des lois constitutives. Finalement, l'approche des éléments discrets permet de représenter la fissuration à l'échelle micro ou nano. Il est donc possible de considérer un matériau hétérogène comme un ensemble de composantes dont la morphologie, la répartition et la taille influencent le comportement global.

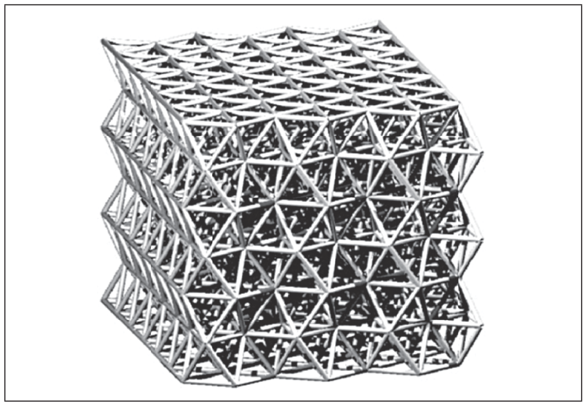

Figure 1.6 Méthode des réseaux de maille (lattice) (Chiaia *et al.*, 1997)

1.2.3 Approche de représentation non géométrique

1.2.3.1 Méthode constitutive

Dans une approche de fissuration diffuse, la coalescence d'une ou plusieurs fissures dans le volume qui est attribuée à un point d'intégration se traduit par une détérioration de la rigidité et de la force à ce point d'intégration. En règle générale, lorsque la combinaison des contraintes répond à un certain critère, par exemple, la contrainte principale atteint le critère de résistance : le processus de rupture est initié. Cela implique qu'au point d'intégration la relation contrainte-déformation isotrope est remplacée par une relation orthotrope ou anisotrope ayant pour axe de référence un système aligné avec la direction des déformations principales. Ainsi, seule la relation constitutive est mise à jour lors de la propagation des fissures et le maillage est maintenu inchangé. Dans le cas où le système d'axe d'orthotropie ayant initié la fissuration est conservé, le modèle est considéré comme fixe. Ceci a pour conséquence d'induire des contraintes en cisaillement dans une fissure ouverte qui se manifestent lorsqu'il y a une rotation des axes de déformations principales après l'initiation de la fissure. Un modèle de fissuration diffuse ro-

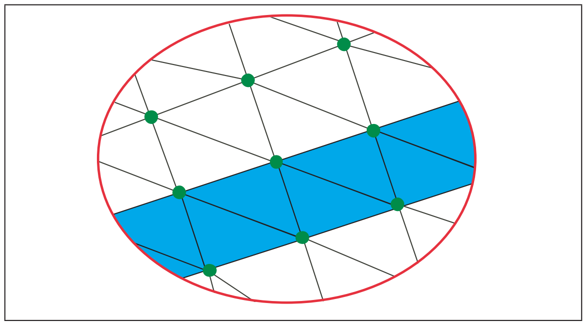

Figure 1.7 Modélisation d'une fissure par la méthode diffuse

tative (Cope *et al.*, 1980) a été créé dans le but d'éliminer ces contraintes en cisaillement. Ce modèle modifie constamment l'axe d'orthotropie de sorte qu'il soit toujours aligné avec la direction des déformations principales éliminant ainsi la contrainte tangentielle dans une fissure ouverte. Les modèles traditionnels de fissuration diffuse transfèrent des contraintes parasites à travers une fissure largement ouverte (Rots, 1988). Ceci est principalement dû aux contraintes de cisaillement générées dans les modèles de fissuration fixe. Cependant, ceci est aussi observé pour des modèles de fissuration rotative. La source de ce phénomène a été analysée dans la référence (Jirásek & Zimmermann, 1998). Il a été démontré que les contraintes parasites sont causées par une représentation inadéquate de la cinématique de la discontinuité du déplacement autour d'une fissure macroscopique. À moins que la direction de la fissure macroscopique soit parallèle aux côtés des éléments finis, les directions des déformations principales déterminées par une interpolation par éléments finis à tous les points de Gauss s'écartent de la normale de la fissure à l'échelle macroscopique. La contrainte principale a une projection non nulle sur un vecteur normal à la fissure, ce qui génère une force de cohésion agissant à travers la fissure, même à un stade très avancé du processus de fissuration lorsque celle-ci doit être complètement ouverte.

Récemment, une nouvelle approche pour la description de la propagation des fissures a été développée. À partir des travaux pionniers de Francfort et Marigo (Francfort & Marigo, 1998), les difficultés rencontrées dans le cadre de la fracture classique peuvent être surmontées par un cadre de minimisation énergétique variationnel pour la fissuration. Un ingrédient important de la méthode repose sur une description régularisée des discontinuités liées au front de fissure. L'approximation régularise ensuite une topologie de surface de fissure dans le solide au moyen d'une variable scalaire auxiliaire, interprétée comme un champ de phase (*phase field*) décrivant les parties discontinues et continues du solide. Une telle méthode a la qualité de ne nécessiter aucune prescription de la géométrie de la discontinuité et de permettre la nucléation et la ramification de fissures, fournissant un cadre très robuste pour la simulation de propagation de fissure. L'approche peut intrinsèquement s'occuper de la fusion et de la ramification de fissures multiples sans ajout d'effort ou d'heuristique. Cette approche peut être généralisée sans effort en trois dimensions, et sa mise en oeuvre est simple dans toutes les dimensions. Par contre, le coût de calcul est élevé puisqu'un maillage suffisamment raffiné dans la zone endommagée est nécessaire pour résoudre le terme de gradient.

1.2.4 Méthode cinématique

Les modèles d'éléments finis avec des discontinuités fortes (SDA) (Simo & Oliver, 1994; Simo *et al.*, 1993a) ou des zones de localisations (Droz, 1987; Belytschko *et al.*, 1988) ont donc été développés afin de pallier aux problèmes liés aux méthodes constitutives. Ces méthodes peuvent être trouvées dans la littérature sous divers noms, mais elles partagent certaines caractéristiques communes. Dans la référence (Jirasek, 2000), ces méthodes ont été classées en trois approches : (1) approche statique symétrique optimale (SOS), (2) approche cinématique symétrique optimale (KOS) et (3) approche statique et cinématique optimale non symétrique (SKON). Les deux premières approches font appel aux méthodes de Bubnov-Galerkin ou les fonctions de formes sont égales aux fonctions de tests alors que la troisième approche est similaire aux méthodes de Petrov-Galerkin où ces fonctions sont différentes. Cette dernière est celle donnant des gradients de déformations localisés à l'intérieur de la bande de fissuration avec la plus grande précision et est la seule pouvant bien représenter une séparation complète au stade avancé du processus de fracturation sans aucune contrainte parasite, mais au détriment d'avoir une matrice de rigidité non symétrique.

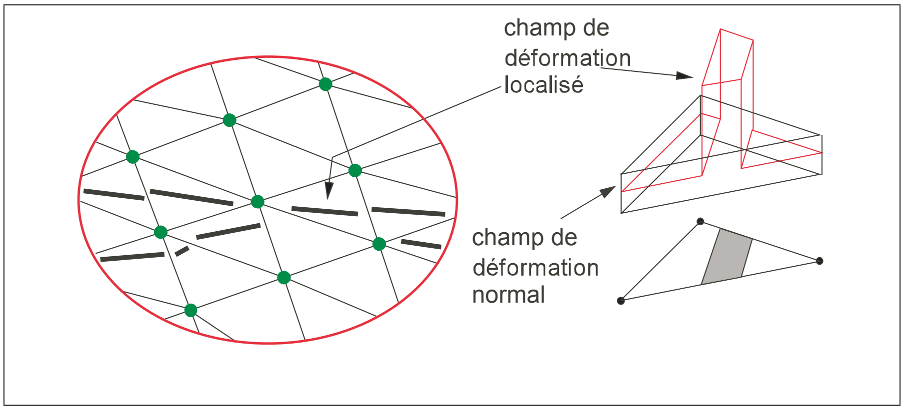

Figure 1.8 Modélisation d'une fissure par une méthode de discontinuité forte

Une autre méthode proposée pour faciliter la propagation de fissures de façon discrète sans remaillage a été suggérée par Belytschko et ses collaborateurs (Belytschko & Black, 1999; Moës *et al.*, 1999). Cette méthode appelée éléments finis étendus (XFEM) exploite la propriété de la partition de l'unité (PUM) (Babuška & Melenk, 1997). Des fonctions supplémentaires respectant la partition de l'unité peuvent être ajoutées aux fonctions de formes standards afin de représenter une discontinuité faible ou une discontinuité forte. De plus, un enrichissement particulier peut-être ajouté pour représenter le champ asymptotique d'une pointe de fissure. Bon nombre des techniques utilisées dans la XFEM sont directement liées à des techniques déjà développées dans les méthodes EFG. La XFEM peut être considérée comme une variante spéciale de la méthode des éléments finis généralisés (GFEM), introduite pour la première fois dans (Strouboulis *et al.*, 2000b,a), qui combine la méthode des éléments finis standards et la méthode de partition d'unité. L'enrichissement PUM est introduit afin d'améliorer les propriétés d'approximation sur l'ensemble du domaine. Une autre variante appelée méthode des noeuds fantômes (Hansbo & Hansbo, 2004) a été développée parallèlement à la XFEM, où un domaine matériel avec une discontinuité interne potentielle peut être modélisé par un élément avec deux paires de noeuds, à savoir les noeuds réels et les noeuds fantômes. Lors de la modélisation d'une discontinuité forte, la méthode des noeuds fantômes s'est avérée équivalente à la XFEM lorsqu'uniquement une fonction d'enrichissement Heaviside est utilisée (Areias & Belytschko, 2006).

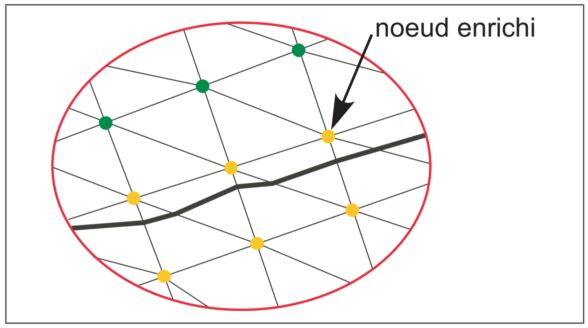

Figure 1.9 Modélisation d'une fissure par la méthode des éléments finis étendus

1.2.5 Synthèse et positionnement

L'approche discrète permet de modéliser les fissures complètement ouvertes de façon adéquate. Cependant cette approche est généralement coûteuse étant donné les opérations de remaillage ou l'addition de degrés de liberté au système matriciel. À l'inverse, les méthodes utilisant l'approche de fissuration diffuse ne sont pas efficaces lorsque la fissure est complètement ouverte. Cependant, lorsque la fissure est en cours d'initiation ou encore que le matériau est peu endommagé, ces approches sont appropriées. Les méthodes de discontinuités fortes SKON peuvent bien représenter la cinématique d'une fissure ouverte, mais au coût d'une matrice de rigidité non symétrique. De plus, pour les méthodes de discontinuités fortes la continuité de la surface de fissuration n'est pas assurée, ce qui peut causer un blocage et un transfert de contraintes parasites, à moins de forcer cette continuité par une méthode de propagation de fissure appropriée. Bien que la méthode de champ de phase semble prometteuse, il y a un aspect non négligeable de raffinement du maillage qui rend son application difficile pour le moment dans un contexte industriel.

Il est donc évident que la combinaison d'une approche diffuse dans la zone d'élaboration des fissures avec une transition vers une méthode discrète telle la XFEM semble être une approche prometteuse. Ceci fait suite à la proposition de la section précédente d'idéaliser le mécanisme de développement d'une fissure en une étape ou il y a micro-fissurations sans localisation des déformations suivie d'une étape où il y a coalescence des micro-fissures, formant une discontinuité faible où les déformations subissent un saut pour éventuellement devenir une discontinuité forte sans forces cohésives. Dans cette thèse cette combinaison de représentation de fissure sera développée.

1.3 Méthode de propagation

Dans un cadre bidimensionnel, le suivi de la propagation des fissures en utilisant une méthode dite *locale* est assez simple. Ici la terminologie qualifiant la méthode de *locale* ne signifie pas l'hypothèse classique de localité au sens d'admettre que l'état à un point donné dépend uniquement des variables d'états à ce point, mais sur le fait que la propagation de fissure est basée sur un algorithme qui évalue la trajectoire de fissure sans tenir compte de l'ensemble du modèle analysé.

Dans sa plus simple version, le modèle local considère qu'une fois qu'un élément est identifié comme étant endommagé, la discontinuité à l'intérieur de celui-ci s'étend à partir d'un point localisé sur une de ses frontières en prenant une direction tel que la direction normale à la contrainte principale maximale. Bien que ce critère de propagation de fissure garantit une discontinuité unique et continue en C_0 dans les analyses bidimensionnelles, il peut donner une discontinuité non continue et non unique dans un cadre tridimensionnel. Malgré que dans le cadre bidimensionnel il est plutôt trivial de définir une technique de propagation de fissure qui assure sa continuité, il n'est pas évident que selon le critère choisi afin de définir la direction de propagation, la trajectoire de fissure soit lisse. Par exemple, si cette direction est basée, comme suggérée plus haut, sur la normale à la contrainte principale et que celle-ci est évaluée localement, il se peut, étant donné que la pointe d'une discontinuité n'est pas située à un point où les contraintes sont connues avec précision (comme aux points de Gauss), que le vecteur normal soit incohérent avec celui calculé aux éléments voisins. Il est cependant possible d'améliorer la régularité de la discontinuité en considérant que cette direction soit calculée par une méthode non locale (Eringen, 1981, 1983; Bažant & Jirásek, 2002). Le modèle non local consiste à remplacer une variable par son homologue non local obtenu en faisant la moyenne pondérée dans un voisinage spatial autour de chaque point considéré.

Ce concept a été utilisé (Gasser & Holzapfel, 2005, 2006) en faisant la moyenne du plan de fissure normal sur un certain voisinage afin d'assurer que la surface de rupture générée est lisse en moyenne. Bien que théoriquement élégant, il est plutôt lourd d'utiliser la méthode non locale dans les codes d'éléments finis, car elle affecte la structure globale du code, elle n'est pas adaptée à la nature modulaire de la méthode des éléments finis et finalement elle augmente la quantité de communications dans un calcul parallèle.

L'idée d'utiliser la méthode non locale afin de définir la direction de propagation améliore grandement la consistance de la trajectoire de fissure, cependant elle ne résout pas les problèmes liés à l'unicité de la trajectoire de fissure pour les cas tridimensionnels. Pour une surface de fissuration en 3D, plusieurs méthodes *locales* ont été proposées afin de pallier à cette problématique. La référence (Areias & Belytschko, 2005) suggère d'ajuster la normale du plan de fissure en fonction des points d'intersection des fissures des éléments voisins. La discontinuité est discrétisée à travers une surface C_0 formée par l'union des triangles et des quadrilatères qui séparent chaque élément dans le voisinage de l'élément concerné. Au cours de l'évolution de la surface, le point de passage et le vecteur normal de la surface de discontinuité ne sont pas arbitraires et dépendent de ce qui se produit dans le voisinage de chaque élément. Cependant, dans le cas d'un trop grand nombre de points voisins, le système est surdéterminé et la fissure ne s'écarte guère d'une surface plane.

Une approche similaire est utilisée (Fries & Baydoun, 2011) afin de définir l'extension des fissures. Selon les auteurs, l'approche combine une description implicite, c'est-à-dire la méthode du level-set, avec une approche explicite pour déterminer l'incrément de fissure et pour mettre à jour la représentation de celle-ci. Il est important de préciser que bien que l'article décrive la méthode des *level-set* comme étant implicite, il n'est pas tout à fait exact dans ce cas de la classifier ainsi, car seules les propriétés de description de la fissure par des fonctions de *level-set* sont exploitées, aucune équation particulière n'est résolue afin de définir celles-ci.

La méthode des *level-set* a été appliquée efficacement à de nombreux problèmes de fronts mobiles (Osher & Sethian, 1988; Sethian, 1999). Cette méthode a été utilisée (Stolarska *et al.*, 2001; Gravouil *et al.*, 2002; Sukumar *et al.*, 2003) sous différentes formes. Par exemple, une équation de Hamilton-Jacobi peut être utilisée afin de mettre à jour les *level-set* durant le calcul de propagation de fissure. Un champ de vitesse est alors développé afin de générer la surface de fissure. Dans un tel cas, il est raisonnable de classer cette méthode comme étant implicite.

Une autre méthode est proposée dans la référence (Gürses & Miehe, 2009) où la direction de propagation est définie en fonction des forces nodales. L'expression constitutive de l'évolution des discontinuités est déterminée de façon ponctuelle par les forces aux noeuds situés au front de la fissure. Une détermination unique de l'évolution de la surface de fissure n'est pas possible uniquement grâce au vecteur de force dans le cadre tridimensionnel. Il est proposé d'utiliser les segments au front de fissure conjointement avec les forces afin de déterminer la nouvelle surface de fissure de manière unique. Les segments de front de fissure fournissent une contrainte géométrique pour la propagation et leur utilisation se traduit par des surfaces de fissure uniques et plus lisses.

Une autre stratégie élégante de suivi de fissure est appelée *méthode globale* (Oliver *et al.*, 2002, 2004). Cette méthode introduit une inconnue supplémentaire à valeur scalaire qui définit une ou plusieurs surfaces de fissure comme étant des isosurfaces de ce champ supplémentaire d'inconnues. Des surfaces de discontinuités lisses, planes ou courbes continues peuvent ainsi être décrites d'une manière robuste et stable, au prix d'avoir à résoudre un système global d'équations supplémentaire. Ce scalaire peut être défini par la résolution d'un problème thermique ou la conduction est anisotrope ou par un problème de convection-diffusion (Riccardi *et al.*, 2017).

1.3.1 Synthèse et positionnement

Les méthodes de suivi de fissure présentées peuvent être classées en deux grandes catégories, soit les méthodes locales et les méthodes globales. Les méthodes locales sont relativement peu coûteuses en temps de calcul et sont facilement applicables pour des analyses bidimensionnelles. Cependant, puisque le critère de direction de fissure est évalué localement, il se peut que la trajectoire de fissure soit non régulière. Ceci peut être amélioré en considérant une direction basée sur une approche non locale. Dans tous les cas, l'application d'une méthode locale dans un cadre tridimensionnel nécessite un algorithme afin de moyenner le front de fissure pour qu'il soit consistant entre les éléments voisins en pointe de fissure. Afin d'éviter de construire une surface de fissuration sur des critères géométriques, les approches globales ont été développées. Celles-ci ajoutent une équation à résoudre afin de définir la position de la fissure. L'analogie thermique ou la méthode des *level-set* sont très efficaces pour arriver à cette fin, cependant la résolution d'un système d'équations linéaires supplémentaire est requise.

Afin de réduire les temps de calcul, la méthode locale sera considérée pour les calculs bidimensionnels, avec la possibilité de calculer la direction de la fissure par une approche non locale. Puisque l'un des objectifs de la thèse est de modéliser les fissures dans un contexte où celles-ci ont des géométries complexes, l'analogie thermique sera évaluée. Bien qu'il a été démontré que la méthode est applicable sur des problèmes tridimensionnels, elle n'a pas été appliquée jusqu'à présent dans des problèmes de grandes tailles avec des géométries de fissuration complexes.

1.4 Interaction hydromécanique

Puisque l'écoulement dans les fissures n'est pas régi par les mêmes lois constitutives que l'écoulement dans un milieu poreux, la revue des modèles constitutifs sera présentée dans deux sections distinctes.

1.4.1 Écoulement dans le milieu continu

Le problème d'écoulement dans les milieux poreux soumis à une déformation est un sujet de recherche depuis longtemps. L'intérêt pour le rôle des mécanismes couplés de diffusion-déformation a d'abord été motivé par le problème de la consolidation. La théorie de Terzaghi sur la consolidation unidimensionnelle peut être considérée comme la première étude dans des milieux poreux déformables, qui a conduit à une théorie de consolidation unidimensionnelle sur la base du concept de contrainte effective (Terzaghi, 1923). La théorie de Terzaghi a été étendue aux cas tridimensionnels par Biot (Biot, 1935, 1941), qui a formulé la théorie linéaire de base de la poroélasticité, et elle a depuis été reformulée plusieurs fois (Biot, 1955, 1956; Verruijt, 1969; Rice & Cleary, 1976). La théorie de Biot a été à son tour étendue aux conditions triphasiques avec de l'air interstitiel comme troisième phase (Fredlund & Morgenstern, 1977; Chang & Duncan, 1983). Cet écoulement multiphasique est particulièrement important lors du calcul de la diminution de la teneur en eau liquide pendant le processus de séchage dans le béton. Ce processus de séchage est associé à des effets capillaires qui peuvent induire un retrait (Bažant & Najjar, 1972; Wittmann, 1973). Un séchage non uniforme induit des contraintes de traction qui peuvent être beaucoup plus importantes que la résistance à la traction du béton et éventuellement provoquer des fissures (Bisschop & van Mier, 2002). C'est pourquoi la plupart des travaux de recherches se concentrent sur le séchage du béton plutôt que sur l'hydratation. Les deux phénomènes sont régis par des modèles constitutifs similaires, cependant les courbes de sorption et de désorption du béton ne sont pas les mêmes (Baroghel-Bouny *et al.*, 1999). Le séchage provient du choc hydrique que subit le béton au décoffrage, lorsqu'il est soumis à l'humidité ambiante qui présente en général un degré d'humidité de l'ordre de 60 à 80 % HR (humidité relative). Au moment de la prise, le béton démarre comme parfaitement saturé, avec 100% HR. Lorsque la surface de la structure en béton est exposée à l'environnement (sauf si la partie en béton est immergée dans l'eau), celle-ci est alors en déséquilibre thermodynamique avec l'atmosphère et le séchage lui permet de retrouver un équilibre hydrique avec le milieu ambiant. Ce processus de séchage entraîne une diminution de l'humidité relative des pores, ce qui provoque une partie du retrait. Ce séchage, caractéristique au comportement du béton en jeune âge, a un effet important sur la microfissuration initiale d'une structure. Ce comportement en jeune âge concerne approximativement les 100 premiers jours de la vie du béton où les mécanismes de retrait endogène ou retrait d'hydratation, et le retrait thermique sont les principaux phénomènes causant la microfissuration initiale. La modélisation de ces phénomènes est généralement négligée lors de l'évaluation d'une structure hydraulique ayant subi des dommages causée par un chargement thermomécanique, par la réaction alcali-granulat ou par un cas de chargement séismique ou hydrostatique exceptionnel. Pour plus d'information sur le retrait, le lecteur est référé aux références (Granger, 1995; Acker & Ulm, 2001; Bažant & Jirásek, 2018), car celui-ci sera négligé dans cette thèse.

L'état des fluides interstitiels dans le béton peut être caractérisé par la température, T, la pression de l'eau liquide, p_l, la pression des gaz interstitiels, p_g, et la pression partielle de vapeur d'eau, p_v. Ainsi, en général, trois inconnues doivent être calculées, celles-ci varient dans l'espace et dans le temps, et leur évolution doit être déterminée à partir d'équations qui prennent en compte le transport de chaleur et de masse.

Il est possible de modéliser le séchage à l'échelle macroscopique comme un phénomène de diffusion non linéaire, avec une diffusion de la phase liquide de type Darcéenne et avec une diffusion de la phase gazeuse de type transport Fickéen. En faisant l'hypothèse consistant à supposer que la phase gazeuse est connexe depuis l'extérieur du solide, la pression gazeuse est pratiquement constante et l'équation faisant état de la diffusion de la phase gazeuse peut être négligée. En combinant la loi de Fick pour le transport de la phase de vapeur avec la diffusion de type Darcéenne pour la phase liquide tout en utilisant la loi de Kelvin, qui décrit la coexistence des deux phases liquide et gazeuse par l'écriture de l'égalité des enthalpies libres massiques, il est possible de réduire les trois inconnues du mouvement des fluides interstitiels dans le béton par une équation portant sur le transfert de teneur en eau. Ceci a notamment été utilisé dans les travaux de Bazant (Bažant, 1970; Bažant & Najjar, 1972) et dans (Mensi *et al.*, 1988) pour un transfert adiabatique. Afin de prendre en compte un coefficient de diffusion qui dépend de la température, une loi d'Arrhenius peut être considérée. Ceci est utilisé par (Granger, 1995), qui propose de modifier l'expression du coefficient de diffusion donné dans la référence (Mensi *et al.*, 1988) en fonction de la température en utilisant la relation (Bažant & Najjar, 1972) :

$$D(T) = D(T_0)\left(\frac{T}{T_0}\right) e^{\frac{-Q_s}{R}\left(\frac{1}{T}-\frac{1}{T_0}\right)} \tag{1.1}$$

avec $Q_s/R = 4700K^{-1}$ et T la température en Kelvin.

L'hypothèse considérée dans les modèles précédents supposant que la pression de gaz dans le matériau reste constamment égale à la pression atmosphérique de l'atmosphère environnante a été confrontée à des résultats expérimentaux et théoriques qui révèlent que cette hypothèse est inadéquate pour rendre compte la perte de masse observée pendant le séchage de matériaux à base cimentaire faiblement perméables (Mainguy *et al.*, 1999). Un modèle macroscopique d'un système multiphasique impliquant deux constituants gazeux (l'air sec et la vapeur d'eau) et une phase liquide est développé dans cette référence. Finalement, une grande variété de modèles de transport d'humidité dans les milieux poreux ont été proposés dans la littérature (Richards, 1931; Whitaker, 1977; Schrefler, 1995). Le lecteur est référé aux références (Coussy, 2010; Bear, 2018) pour une discussion détaillée de ces modèles.

Bien que l'effet de la présence d'un liquide dans les pores interstitiels a grandement été étudié, l'inverse, c'est-à-dire l'effet de la déformation du solide sur l'écoulement a été moins étudié et le couplage bidirectionnel des deux phénomènes encore moins. La présence d'un état de déformation triaxial amène une anisotropie dans la perméabilité du solide (Picandet *et al.*, 2001; Burlion *et al.*, 2003). Cependant, il manque de caractérisations expérimentales afin de définir ce changement de perméabilité. La recherche se concentre principalement à trouver des relations entre l'endommagement et le changement de perméabilité. Par contre puisque la formulation de l'endommagement entre les méthodes numériques n'est pas exprimée par les mêmes relations (modèle de fissuration, formulation de l'adoucissement, type de régularisation, etc.) il n'est pas évident de généraliser la relation perméabilité-endommagement (Bouhjiti *et al.*, 2018). De plus, tous ces travaux de recherches supposent un écoulement Darcéen dans un milieu saturé. Le couplage entre les modèles d'écoulement non saturés présentés précédemment et les relations perméabilité-endommagement proposées dans les références (Bary, 1996; Gérard, 1996; Gawin *et al.*, 2002; Choinska *et al.*, 2007; Picandet *et al.*, 2009) n'est donc pas trivial. Finalement, il existe un questionnement quant au moment où l'écoulement dans le béton endommagé passe d'un écoulement en milieu poreux à travers des microfissures non connectées (écoulement Darcéen) vers un écoulement dans une macrofissure lorsqu'il y a coalescence des microfissures (écoulement de Poiseuille) (Choińska *et al.*, 2007; Pijaudier-Cabot *et al.*, 2009; Grassl & Bolander, 2016; Bouhjiti *et al.*, 2018).

1.4.2 Écoulement dans les discontinuités

L'écoulement dans des milieux poreux endommagés a reçu beaucoup d'attention depuis que le gaz naturel joue un rôle clé dans la satisfaction des demandes énergétiques mondiales. La production de gaz naturel à partir de formations schisteuses riches en hydrocarbures, connues sous le nom de «gaz de schiste», se développe rapidement dans l'exploration et la production de pétrole et de gaz. La production de gaz naturel a considérablement augmenté ces dernières années grâce aux progrès de la technique de fracturation hydraulique des réservoirs de gaz de schiste. Cependant, la présence de dommages, de fissures, de joints ou de défauts peut modifier sensiblement le comportement physique du milieu poreux. L'écoulement dans les discontinuités avec une perméabilité plus élevée est de nature différente de l'écoulement dans le milieu interstitiel déformé. Ceci a soulevé des préoccupations concernant l'impact environnemental et le potentiel de contamination des eaux souterraines causée par la fracturation hydraulique lors de l'extraction du gaz de schiste.

Plusieurs approches ont été proposées dans la littérature afin de réaliser la simulation de la fracturation hydraulique dans les matériaux poroélastiques. La combinaison de la méthode des éléments finis avec la méthode des différences finies est proposée dans (Boone & Ingraffea, 1990). L'utilisation de l'approche des discontinuités fortes dans des milieux poreux entièrement saturés avec l'incorporation au niveau local des effets des discontinuités dans le champ de déplacement est présentée dans (Armero & Callari, 1999). Le cadre proposé implique la solution couplée de l'équation de conservation de la masse du fluide et de l'infiltration à travers le solide poreux via la loi de Darcy, en tenant compte d'un champ de pression continu avec des gradients discontinus, et conduisant à des vecteurs de flux de fluide discontinus à travers les discontinuités. Des hypothèses similaires sont utilisées dans le cadre de la méthode des éléments finis étendus dans (Jox *et al.*, 2006), et en utilisant la méthode de partition de l'unité (PUFEM) (Réthoré *et al.*, 2007). Le champ de pression dans la discontinuité peut également être modélisé en enrichissant la pression pour prendre en compte sa discontinuité dans les domaines (Abellan *et al.*, 2005) et ainsi considérer l'effet de membrane. Des schémas de couplage pour la modélisation de la propagation des fractures hydrauliques à l'aide de la XFEM pour le modèle bidimensionnel de Khristianovic-Geertsma-de Klerk (KGD) sont proposés dans (Gordeliy & Peirce, 2013). Une méthode hydromécanique numérique entièrement couplée avec une adaptation partielle et modifiée de la XFEM pour inclure des fractures intersectées, mais préexistantes est proposée dans (Watanabe *et al.*, 2012). La XFEM est également appliquée pour les milieux poreux partiellement saturés, y compris les fissures cohésives (Mohammadnejad & Khoei, 2013). Enfin, la méthode du champ de phase a été appliquée (Wheeler *et al.*, 2014; Yoshioka & Bourdin, 2016; Wilson & Landis, 2016) pour un problème de fracture couplé à la diffusion de fluides.

Pour mieux comprendre la fracturation hydraulique dans des réservoirs complexes, stratifiés et naturellement fracturés, des modèles entièrement 3D doivent être développés. Un premier travail en trois dimensions, dans lequel un forage incliné est simulé au cours des premières étapes du processus de fracturation hydraulique, a été appliqué dans l'industrie pétrolière (Morales *et al.*, 1993). Plus récemment, un modèle numérique tridimensionnel basé sur le XFEM pour la simulation de fissures cohésives dans des matériaux cimentaires, tels que le béton, dans un cadre hydromécanique a été présenté dans (Becker *et al.*, 2010). Des simulations de propagation de fractures non-planaires utilisant une méthode adaptative des éléments finis généralisés sont données dans (Gupta & Duarte, 2014). Dans la référence (Rungamornrat *et al.*, 2005) une technique de calcul est développée afin de simuler l'évolution non planaire des fractures hydrauliques dans des milieux élastiques 3D en utilisant une méthode d'élément de frontière de Galerkin symétrique pour traiter le problème d'élasticité associé à une fracture dans un domaine infini. Une formulation GFEM tridimensionnelle est proposée (Meschke & Leonhart, 2015), où des fonctions d'enrichissement motivées par la physique sont utilisées afin d'approximer la pression du liquide près des discontinuités.

Dans les références proposées, l'écoulement est du type Poiseuille qui est caractérisé par un écoulement laminaire entre deux plaques planes. Cependant, pour des écoulements plus complexes (fluide non newtonien, écoulement non parallèle, écoulement turbulent, etc.) il existe des tests expérimentaux liants la perméabilité au type d'écoulement (Louis, 1969; Barton *et al.*, 1985; Hakami, 1995; Barton & de Quadros, 1997; Aldea *et al.*, 2000; Oshita & aki Tanabe, 2000). Cependant, à notre connaissance, la littérature ne contient pas de référence qui présente un modèle numérique pour résoudre ce type de problème.

1.4.3 Synthèse et positionnement

Afin de prendre en compte les pressions interstitielles dans le béton, deux approches peuvent être considérées, soit en prenant le matériau comme étant saturé, soit en prenant celui-ci comme étant partiellement saturé. Dans le premier cas, l'équation de Darcy linéaire peut être utilisée alors que dans le second cas, une équation non linéaire variant en temps et en espace doit être utilisée. Plusieurs modèles de transport en milieu non saturé ont été présentés rajoutant d'une à trois inconnues supplémentaires au problème. Bien que l'aspect thermique soit important dans le problème de diffusion d'un milieu partiellement saturé, celui-ci sera négligé dans la thèse afin de simplifier légèrement le problème à résoudre.

L'écoulement dans les discontinuités a été représenté par plusieurs stratégies et inclus dans pratiquement toutes les approches présentées dans la section 1.2 afin de modéliser la fissuration. Par contre, peu ont été appliquées dans un contexte tridimensionnel de fracturation hydraulique et finalement, seul l'écoulement linéaire de Poiseuille est utilisé afin de modéliser le transport de fluide dans les discontinuités.

Dans cette thèse, un milieu saturé conjugué avec un écoulement de Poiseuille dans les discontinuités sera utilisé dans un premier temps. Finalement afin d'ajouter une physique plus réaliste pour modéliser la fracturation hydraulique, un milieu partiellement saturé et un écoulement complexe (turbulent et non-planaire) seront considérés. Ceci représente une contribution importante de la présente thèse.

CHAPITRE 2

A COMBINED XFEM - DAMAGE MECHANICS APPROACH FOR CONCRETE CRACK PROPAGATION

Simon-Nicolas Roth[1], Pierre Léger[2], Azzeddine Soulaïmani[3]

[1] Hydro-Québec, 75 boul. René-Lévesque Ouest, Montréal, Québec, Canada, H2Z 1A4
[2] École Polytechnique de Montréal, Department of Civil, Geological and Mining Engineering, C.P. 6079, succ. Centre-Ville, Montréal Québec, Canada, H3C 3A7
[3]École de Technologie Supérieure, Department of Mechanical Engineering, 1100, rue Notre-Dame Ouest, Montréal, Québec, Canada, H3C 1K3

Article publié dans la revue « Computer Methods in Applied Mechanics and Engineering » en janvier 2015.

2.1 Abstract

This paper presents a crack model that couples the benefits of the damage mechanics approach and the extended finite element method (XFEM). A crack-tracking technique is developed to propagate the crack path along a single row of finite elements as a function of the stress-based nonlocal method. The level sets are computed to predict the crack path, and the path is corrected with the use of continuum damage mechanics. Once a certain level of damage is reached inside an element, the previously-computed level sets are used to apply the XFEM formulation. A cohesive XFEM formulation is used to transfer energy dissipation from the damage mechanics approach to the XFEM model. Using numerous test cases, it is shown that the model is mesh independent and that it removes the spurious stress transfer exhibited by continuum damage models. Various transition damage criteria are compared, and the optimal one is determined.

Keywords : Plain Concrete Cracking, Crack Tracking Technique, Non Linear Fracture Mechanics, Extended Finite Element Method, Continuum Damage

2.2 Introduction

Based on the concept of energy dissipation in a body made of quasi-brittle material undergoing fracturing, crack propagation models can be classified into two categories ; linear elastic fracture mechanics (LEFM) and nonlinear fracture mechanics (NLFM). LEFM assumes that the energy dissipation is only caused by crack growth and that it occurs in an infinitesimal area at the tip of the crack, where the stress field is assumed to be singular. The energy dissipation is confined in the region called the fracture process zone (FPZ), located in front of the tip of the macroscopic stress-free crack, so that it can be neglected compared to the dimensions of the structure. In contrast, NLFM considers that there is a softening behavior in the FPZ and therefore no presence of singularity. Although large concrete structures like dams are often cited as possible candidates for the application of LEFM models, there are severe limitations to this approach because of the extent of the FPZ in relation to the size of the structure (Brühwiler & Wittmann, 1990).

Based on the NLFM, the mechanism of the crack propagation of quasi-brittle materials can be idealized in the following steps (Huespe & Oliver, 2011). During the first phase of the loading process on a body undergoing fracturing, when the tensile stress is close to the tensile strength, the formation and growth in the FPZ of densely distributed microcracks induces a non-linear response in the material. At this stage of the fracture process the microcracks are not localized ; the material remains stable and the load-deformation response no longer has a linear slope. When the load increases, the response of the material at the macroscopic scale becomes unstable due to the coalescence and ramification of the microscopic cracks, as well as the debonding of aggregates in the material matrix. Deformation and localization occur in a band of defined width, forming a weak discontinuity in the strain field. At this stage, the load-deformation response is in the softening branch. Thereafter, the width of the band, where cohesive forces are maintained, tends to zero. In the last stage, the cohesive forces vanish and an area of strong discontinuity with a stress-free macrocrack appears.

Numerous models exist to describe this phenomenon, and they can be classified into two basic methods : the continuum damage method (CDM) and the discrete method (DM). They may also be classified into geometrical or non geometrical models (Ingraffea, 2004). According to this classification, the CDM approach falls into a subcategory of the non-geometrical model called the constitutive method. In the CDM approach introduced by Rashid (Rashid, 1968), the coalescence of one or more cracks in a volume will result in a deterioration of the stiffness and strength of this volume. Generally, when a certain criterion is met, for example when the equivalent stress reaches the resistance criterion, the fracture process is initiated. This implies that in the damaged volume, the stress-strain relation is replaced by an effective stress-strain relation. Hence, as proposed by Kachanov (Kachanov, 1999), the behavior of a damaged material results in the constitutive relation of an undamaged material in which the usual stress is replaced by the effective stress by invoking the principle of strain equivalence. Thus, the CDM approach only updates the constitutive relationship during the propagation of cracks ; the mesh remains unchanged.

The non-geometrical model has a second subcategory, the kinematic method. In this subcategory, the crack is either embedded in the local finite element where enrichment is added at the element level and then condensed out (the strong discontinuity approach (SDA) (Simo *et al.*, 1993a)), or the enrichment is done by enriching the nodes with additional degrees of freedom as in the generalized finite element method (GFEM) (Melenk., 1995), the extended finite element method (XFEM) (Belytschko & Black, 1999), the partition of unity finite element method (PUFEM) (Babuška & Melenk, 1997) and the phantom node method (Hansbo & Hansbo, 2002).

With the non-geometrical approaches, one can conclude that the continuum approach can provide a relatively good model to describe the first stage of the idealized FPZ. However, in the final stage of failure, when damage localizes into a macroscopic crack, the continuum models are known to exhibit stress locking (spurious stress transfer), lack of objectivity (mesh-induced directional bias), and possible instab1 :ility (appearance of spurious kinematic modes) (Jirásek & Zimmermann, 1998). In contrast, the kinematic approach based on a cohesive crack model, does not describe the first phase of densely distributed microcracks very well. However, the macroscopic crack can be well-described with this approach. Consequently, combining the constitutive approach with the kinematic approach in one single approach seems an appealing technique to best describe the failure process of quasi-brittle materials.

This technique has been studied in the past and without being exhaustive, some contributions are worth mentioning. The combination of a smeared crack with an embedded crack model and cohesive laws was presented in (Jirásek & Zimmermann, 2001). The behavior of the combined model remedies certain pathologies exhibited by continuum models, such as mesh-induced directional bias. The energy transferred to the embedded crack model is accomplished by computing the difference between the fracture energy of the element and the energy dissipated by the smeared crack model. In (Simone *et al.*, 2003) the transition from a gradient damage model to a traction-free discontinuity is carried out when the damage is close to unity, without special energy treatment during the transition. Incorrect energy dissipation related to the high residual stress at the moment of the enhancement of the displacement field can develop even if the transition is done when damage is close to unity. Reference (Comi *et al.*, 2007) presents the transition from a nonlocal isotropic damage approach to a cohesive XFEM approach. The transition occurs when the damage exceeds a critical value related to the element size, and on the minimum number of elements considered necessary to resolve the localization band. Similar to (Jirásek & Zimmermann, 2001), the energy dissipated by the cohesive model corresponds to the energy not yet dissipated by the nonlocal model within the band. Recently, Cuvilliez and al. (Cuvilliez *et al.*, 2012) proposed a coupled approach involving a gradient damage model and a cohesive zone model. The approach is constructed so that the energetic equivalence between the two models is assured, whatever the damage level reached at the center of the band when switching from the damage model to the cohesive model.

A strategy based on a transition from a continuum approach to a kinematic approach for cohesive crack propagation is proposed. This process allows the benefits of the continuum damage approach to be combined with the benefits of the cohesive extended finite element method. The regularized local anisotropic continuum damage approach is used to describe the first stage of the FPZ formation. When the damage has reached a critical value, a switch to the cohesive XFEM model is achieved by ensuring that the energy that remains to be dissipated by the CDM model is transferred to the XFEM model. Because anisotropic models are less sensitive to the directional bias of a finite element mesh (Jirásek & Grassl, 2008), only the crack tracking algorithm is formulated using a stress based nonlocal theory (Giry *et al.*, 2011). This reduces the dependency of the model on the characteristic length which is a difficult parameter to determine for an engineering problem. The proposed model has the benefit of not adding any additional parameters during the energy transfer between the CDM and the cohesive XFEM models. After defining the problem formulation, the paper presents the rotating anisotropic damage model first, followed by the XFEM model, along with the cohesive law. The method used to transfer the energy not dissipated by the CDM model to the cohesive XFEM is then described in detail. The crack tracking strategy using a stress-based nonlocal theory is presented in section six. Finally, numerous validation examples are presented, including mode I and mixed mode cracking.

2.3 Problem formulation

Consider a body undergoing cracking with tractions applied on Γ_t and subjected to prescribed displacements on Γ_u and body loads $\mathbf{b}$ according to figure 2.1a. In this figure, the material is undamaged, thus the scalar damage index d as sketched in figure 2.1a is equal to zero and the material is characterized by the stress, strain and elasticity tensors $(\tilde{\sigma}, \tilde{\varepsilon}, E)$. In figure 2.1b the material characterized by the triplet $\left(\sigma, \varepsilon, \tilde{E}\right)$ has a certain amount of distributed damage caused by densely distributed microcracks. Once the damage has exceeded a certain threshold d_{crit}, it localizes into a macroscopic crack and the body Ω is divided into two parts, Ω^+ and Ω^-. The displacement discontinuity Γ_d between these two bodies is divided into two sides, denoted by Γ_d^+ and Γ_d^- and shown in figure 2.1c. The jump in the displacement field between Γ_d^+ and Γ_d^- is given by $[\![\mathbf{u}]\!]$.

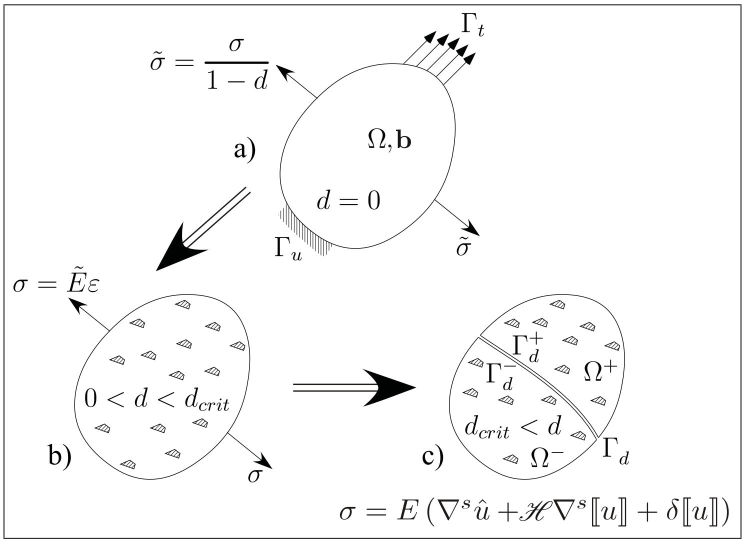

Figure 2.1 Notation for body undergoing cracking

Under the hypothesis of small displacements, the elastostatic problem is governed by the following equilibrium equations and boundary conditions :

$$
\begin{aligned}
\nabla \cdot \boldsymbol{\sigma} + \mathbf{b} &= 0 && \text{in } \Omega, \Omega^+ \cup \Omega^- \\
\mathbf{u} &= \bar{\mathbf{u}} && \text{on } \Gamma_u \\
\boldsymbol{\sigma} \cdot \mathbf{n}_t &= \bar{\mathbf{t}} && \text{on } \Gamma_t \\
\boldsymbol{\sigma} \cdot \mathbf{n}_d &= \mathbf{t}([\![\mathbf{u}]\!]) && \text{on } \Gamma_d
\end{aligned}
\tag{2.1}
$$

where $\bar{\mathbf{u}}$ is the prescribed displacement on the Dirichlet boundary and $\bar{\mathbf{t}}$ is the prescribed traction on the Neumann boundary with normal $\mathbf{n}_t$. The Cauchy stress tensor is denoted by $\boldsymbol{\sigma}$. In configuration 2.1c, cohesive tractions $\mathbf{t}$ are calculated with a constitutive law and depend on the jump in the displacement field $[\![\mathbf{u}]\!]$ and acts along the discontinuity Γ_d. This is solved for any of the configuration 2.1a, 2.1b or 2.1c. The constitutive law governing the damage of configurations 2.1b and 2.1c is detailed in the next section.

2.4 Continuum damage model

The main advantage of the continuum damage approach is that it offers the possibility to model areas where damage causes a multitude of micro-cracks that are not necessarily localized. A good example of this phenomenon is the damage caused by thermal gradients on the surface of a structure. The damage is present, but often there is no dominant crack. Another benefit of the continuum damage model is its ability to efficiently predict and continuously adjust crack directions during their evolution.

A rotating anisotropic damage model is considered in this work. To preserve symmetry of the damaged moduli tensor, the anisotropic formulation is based on the principle of energy equivalence (Sidoroff & Cordebois, 1979). This principle states that *the elastic energy in the damaged material is the same as the energy in the undamaged material as long as the applied stress is replaced by the effective stress*. The effective stress $\tilde{\sigma}$ is defined as :

$$\tilde{\sigma} = \frac{\sigma}{(1-d)} \tag{2.2}$$

where d is the scalar damage index that is equal to zero when the material is undamaged, and equal to one when it is completely damaged. In the case of an anisotropic formulation, the damage index is given by a tensor $\mathbf{M}$ and can be written in the following form :

$$\tilde{\sigma} = \mathbf{M}^{-1}\sigma \tag{2.3}$$

The elastic energy for an equivalent undamaged material (figure 2.2b) is given by :

$$\Psi_0^e = \frac{1}{2}\tilde{\sigma}\mathbf{C_0}^{-1}\tilde{\sigma} \tag{2.4}$$

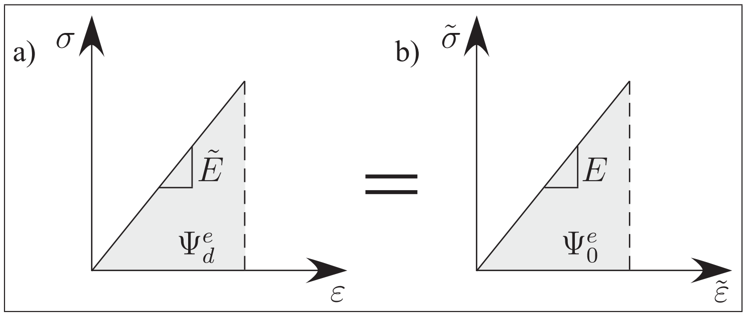

Figure 2.2 Principle of energy equivalence :
a) damaged material, b) equivalent undamaged material

with $\mathbf{C_0}$ the usual linear-elastic constitutive tensor. The energy for the damaged material (figure 2.2a) is :

$$\Psi_d^e = \frac{1}{2}\sigma \mathbf{C_d}^{-1}\sigma \tag{2.5}$$

with $\mathbf{C_d}$ the damaged constitutive tensor. Replacing the stress terms in equation 2.4 by the effective stress and by using the concept of energy equivalence, the energy from 2.4 is equal to that of 2.5. This leads to :

$$\mathbf{C_d} = \mathbf{M}^{-1}\mathbf{C_0}\left(\mathbf{M}^{-1}\right)^T \tag{2.6}$$

Replacing the anisotropic damage tensor $\mathbf{M}$ by an isotropic damage formulation $(d_1 = d_2 = d)$, the damaged and undamaged constitutive tensors by their respective modulus yields the relation :

$$\tilde{E} = E\,(1-d)^2 \tag{2.7}$$

One can notice the square term that results from the assumption of energy equivalence.

Introducing κ_i as a scalar measure of the largest principal strain ε_i reached in the material's history, a loading function f_i can be defined as :

$$f_i\,(\varepsilon_i, \kappa_i) = \varepsilon_i - \kappa_i \tag{2.8}$$

Loading is indicated by $f_i \geq 0$ and unloading by $f_i < 0$. The unloading behavior can be simulated using the secant stiffness. Damage is initiated when a tensor norm is greater than the initial threshold r_0. The tensor norm must take the behavior of concrete under tension and compression into consideration. One suitable norm that considers the effect of compressive strains and is defined as the equivalent strain $\bar{\varepsilon}$, as proposed by Ghrib (Ghrib, 1994) (graphically represented in figure 2.3), can be written in 2D as follows :

$$\bar{\varepsilon} = \sqrt{\sum_{i=1}^{2} \left(\langle \varepsilon_i^{av} \rangle^2 + m \langle -.\varepsilon_i^{av} \rangle^2 \right)} \tag{2.9}$$

where $\langle \ldots \rangle$ are the Macaulay brackets : $\langle \varepsilon_i^{av} \rangle = \varepsilon_i^{av}$ if $\varepsilon_i^{av} > 0$, $\langle \varepsilon_i^{av} \rangle = 0$ if $\varepsilon_i^{av} < 0$ and m is introduced to consider that the effect of compressive strains is smaller than that of tensile strains, defined by :

$$m = \left(\frac{f_t'}{f_c'} \right)^2 \tag{2.10}$$

with f_t', the tensile strength and f_c' the compressive strength. In figure 2.3 the influence of m on the damage surface is demonstrated for $m = 1,\ 0.5,\ 0.1$ and 0 corresponding to the norm often cited as the *Mazars norm* (Mazars, 1984).

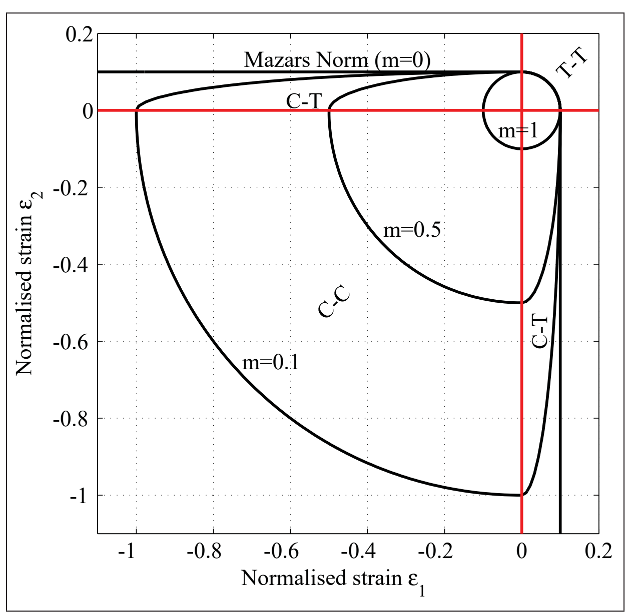

Figure 2.3 Graphical representation of the tensor norm

The damage evolution function as proposed in reference (Gunn, 1998) is given by :

$$d = 1 - \sqrt{\frac{r_0}{\bar{\varepsilon}} \exp\left(-R\left(\bar{\varepsilon} - r_0\right)\right)} \tag{2.11}$$

where r_0 is the initial threshold defined in terms of the tensile strength and the undamaged elastic modulus E_0 :

$$r_0 = \frac{f_t'}{E_0} \tag{2.12}$$

Mesh objectivity requirements are satisfied adequately by introducing a regularization based on the energy equivalence. The stress-strain diagram is adjusted such that the fracture energy is conserved regardless of the size of the element considered. Therefore, the mesh size does not have to respect a maximum size corresponding to the characteristic length of concrete. This is of great importance when analyzing a large structure such as a dam where this dimension is small compared to the size of the dam. Thus, the derivation of R in equation 2.11 is done in a way that satisfies the mesh objectivity requirements. The material fracture energy is equal to the fracture energy of the representative volume element :

$$\int_{r_0}^{\infty} \sigma \, \mathrm{d}\bar{\varepsilon} + \frac{f_t' r_0}{2} = \int_{r_0}^{\infty} E_0 \left(1 - d\right)^2 \bar{\varepsilon} \, \mathrm{d}\bar{\varepsilon} + \frac{f_t' r_0}{2} = \frac{G_F}{l_{rve}} \tag{2.13}$$

Thus,

$$R = \frac{2E_0 f_t' l_{rve}}{2E_0 G_F - {f_t'}^2 \, l_{rve}} \geq 0 \tag{2.14}$$

where G_F is the fracture energy and corresponds to the area under the complete stress-strain curve (not to be confused with G_f which corresponds to the area under the initial tangent of the stress-strain curve, $G_F \approx 2.5 G_f$), and l_{rve} is the representative volume element characteristic length. To satisfy the requirements that $R \geq 0$, l_{rve} must be smaller than :

$$l_{\mathrm{rve}} \leq \frac{2E_0 G_F}{{f_t'}^2} \tag{2.15}$$

For a typical concrete with $E_0 = 30$ GPa, $f_t' = 3$ MPa and $G_F = 100$ N/m, this corresponds to 0.67 m which is not restrictive for meshing.

The damage evolution is based on the principal strains exceeding the damage threshold r_0 :

$$\begin{aligned} &\bullet \text{ if } \kappa_1 > r_0 \text{ then } d_1 = d \\ &\bullet \text{ if } \kappa_2 > r_0 \text{ then } d_2 = d \end{aligned} \tag{2.16}$$

The anisotropic damage tensor can now be defined by :

$$\mathbf{M} = \begin{bmatrix} \frac{1}{1-d_1} & 0 & 0 \\ 0 & \frac{1}{1-d_2} & 0 \\ 0 & 0 & \beta \end{bmatrix} \tag{2.17}$$

with $\beta = \sqrt{\frac{1}{2}\left(\frac{1}{(1-d_1)^2} + \frac{1}{(1-d_2)^2}\right)}$. Damage in either of the principal directions leads to a reduction of shear resistance by the coefficient β similar to that found in smeared crack models. The damage tensor is valid in the local reference frame (aligned with the principal strains directions). Hence, in the global reference frame, this tensor must be rotated by the transformation matrix given by :

$$\mathbf{T} = \begin{bmatrix} l_1^2 & m_1^2 & l_1 m_1 \\ l_2^2 & m_2^2 & l_2 m_2 \\ 2 l_1 l_2 & 2 m_1 m_2 & l_1 m_2 + l_2 m_1 \end{bmatrix} \tag{2.18}$$

with the direction cosine $\varepsilon_1 = \{l_1, m_1\}$, $\varepsilon_2 = \{l_2, m_2\}$. The transformation from the local to the global reference frame of the damaged constitutive tensor is given by :

$$\mathbf{C}_d^{(g)} = \mathbf{T}^{\mathrm{T}} \mathbf{C}_d^{(l)} \mathbf{T} \tag{2.19}$$

Finally, the damage is considered to be distributed on a representative volume element l_{rve}. Therefore, in 2D this measure is given by the relation :

$$l_{\text{rve}} = \sqrt{V_e} = \sqrt{\sum_{i=1}^{n_{int}} w_i \det{}_i} \tag{2.20}$$

with V_e the element volume, n_{int} the number of integration points, w the weight and det the determinant associated with the Gauss point. Similarly, the strains ε are averaged over the volume and given by :

$$\varepsilon^{av} = \frac{\sum_{i=1}^{n_{int}} \varepsilon_i w_i \det{}_i}{\sum_{i=1}^{n_{int}} w_i \det{}_i} \tag{2.21}$$

These averaged strains are used to evaluate the loading/unloading function 2.8.

Algorithm 2.1 is given to compute the internal forces for a damaged element.

Algorithm 2.1 Update of internal forces for a damaged element

Evaluate the element strain tensor at step $k+1$:
$\varepsilon^{k+1} = \mathbf{Bu}$
Evaluate the element average strain tensor at step $k+1$:
$\varepsilon^{av\,k+1} = \dfrac{\sum_{j=1}^{N_{int}} \varepsilon_j^{k+1} w_j \det{}_j}{\sum_{j=1}^{N_{int}} w_j \det{}_j}$
Evaluate the element principal average strains $\varepsilon^{av\,k+1}_{i=1,2}$
Compute the equivalent strain
$\bar{\varepsilon}^{k+1} = \sqrt{\sum_{i=1}^{2} \left(\langle \varepsilon^{av\,k+1}_i \rangle^2 + m \langle - \varepsilon^{av\,k+1}_i \rangle^2 \right)}$
Evaluate the damage loading function :
$f_i \left(\varepsilon^{av\,k+1}_i, \kappa_i^{k+1} \right) = \varepsilon^{av\,k+1}_i - \kappa_i^k$
if $f_i \geq 0$ **then**
    $\kappa_i^{k+1} = \varepsilon^{av\,k+1}_i$
else
    $\kappa_i^{k+1} = \kappa_i^k$
end if
    Update the damage variable :
$d = 1 - \sqrt{\dfrac{r_0}{\bar{\varepsilon}^{k+1}} \exp\left(-R\left(\bar{\varepsilon}^{k+1} - r_0\right)\right)}$
    if $\kappa_i^{k+1} > r_0$ **then**
        $d_i = d$
    end if
    Update the damaged constitutive tensor $\mathbf{C}_d^{(g)}$
    Save $\mathbf{C}_d^{(g)}$
    Update the internal forces $\mathbf{r} = \int_\Omega \mathbf{B}^{\mathrm{T}} \mathbf{C}_d^{(g)} \mathbf{B} \, \mathrm{d}\Omega \, \mathbf{u}$

2.5 XFEM representation of the discontinuity

In contrast to the continuum damage model where the damage is distributed over a representative element volume, the XFEM allows a discontinuous displacement field to be represented across a localized crack. Thus, when a coalescence of micro-cracks occurs, a true open discrete crack can be well represented with the XFEM. The basis of this method is related to the concept of partitions of unity (Babuška & Melenk, 1997) to enrich the finite element method. A partition of unity in a domain Ω is a set of functions $\varphi_I(x)$ such that :

$$\sum_{\forall I} \varphi_I(x) = 1, \; \forall x \in \Omega \tag{2.22}$$

The property of a partition of unity is that any function $\psi(x)$ can be reproduced by a product of the partition of unity function with $\psi(x)$. Thus, the standard finite element approximation can be enhanced by introducing additional unknown $\hat{a}_I$ to the problem :

$$u^h(x) = \underbrace{\sum_{\forall I} N_I(x)\bar{a}_I}_{u^{std}} + \underbrace{\sum_{\forall I} N_I(x)\psi(x)\hat{a}_I}_{u^{enr}} \tag{2.23}$$

with N_i the standard shape functions of the finite element method and $\bar{a}_I$ the standard degrees of freedom of the problem. The first part of the right hand side of equation (2.23) represents the approximation of the standard finite element method, while the second part is the enrichment. The nodal values $\hat{a}_I$ are the additional degrees of freedom that adjust the enrichment so that they approximate the function $\psi(x)$. In the partition of unity finite element method (PUFEM) (Babuška & Melenk, 1997) the enhancement is global while the XFEM (Belytschko & Black, 1999) uses a local partition of unity ; enrichment is added only if required.

To represent a strong discontinuity such as a crack, the Heaviside function can be used for $\psi(x)$:

$$\mathscr{H}(z) = \begin{cases} 1, & z > 0 \\ 0, & \text{else} \end{cases} \tag{2.24}$$

The displacement approximation is given by :

$$u^h(x) = \sum_{\forall I} N_I(x)\bar{a}_I + \sum_{J \in S_H} N_J(x)\left[\mathscr{H}(f(x)) - \mathscr{H}(f(x_J))\right]\hat{a}_J \tag{2.25}$$

where S_H represents the set of nodes that are enriched because the discontinuity passes through the element they are attached to and x_J is the position of node J.

For elements cut by a crack, the jump in the displacement field across the crack Γ_d is thus given by the equation :

$$[\![u]\!]_{\Gamma_d} = \sum_{J \in S_H} N_J(x)\hat{a}_j,\ x \in \Gamma_d \tag{2.26}$$

In equation 2.25 the enrichment function is shifted so that the product of the shape function N_I and the enrichment function cancels out at each node, as proposed in (Belytschko *et al.*, 2001). Therefore, only those elements that are crossed by the discontinuity should be treated differently.

2.5.1 Weak form and discretization

The displacement field u can be decomposed into a continuous and a discontinuous part :

$$u = \bar{u} + \mathscr{H}\hat{u} \tag{2.27}$$

where $\bar{u}$ and $\hat{u}$ are continuous functions on Ω and $\mathscr{H}$ separating the Ω^+ domain from the Ω^- domain. Assuming test functions for displacements

$$w = \bar{w} + \mathscr{H}\hat{w} \tag{2.28}$$

and then substituing into equation 2.1 and integrating over the domain Ω leads to the weak form :

$$\int_\Omega (\bar{w} + \mathscr{H}\hat{w}) \cdot (\nabla \cdot \boldsymbol{\sigma} + \mathbf{b})\, \mathrm{d}\Omega = 0 \tag{2.29}$$

All strains are assumed to be infinitely small, such that the gradient is implicitly symmetrical. Considering that the gradient of the Heaviside function is $\nabla\mathscr{H} = \mathbf{n}_d\delta$ and applying the divergence theorem yields :

$$\begin{aligned}\int_\Omega \nabla\bar{w}\sigma \mathrm{d}\Omega + \int_\Omega \delta\left(\hat{w}\otimes\mathbf{n}_d\right)\sigma\mathrm{d}\Omega + \int_\Omega \left(\mathscr{H}\nabla\hat{w}\right)\sigma\mathrm{d}\Omega \\ + \int_\Omega \left(\bar{w}+\mathscr{H}\hat{w}\right)\mathbf{b}\mathrm{d}\Omega = \int_\Gamma \left(\bar{w}+\mathscr{H}\hat{w}\right)\sigma\mathbf{n}_t\mathrm{d}\Gamma\end{aligned} \tag{2.30}$$

Transforming the volume integral into a surface integral to eliminate the Dirac function yields :

$$\begin{aligned}\int_\Omega \nabla\bar{w}\sigma \mathrm{d}\Omega + \int_\Omega \left(\mathscr{H}\nabla\hat{w}\right)\sigma\mathrm{d}\Omega + \int_{\Omega_d} \left(\bar{w}+\mathscr{H}\hat{w}\right)\mathbf{b}\mathrm{d}\Omega \\ + \int_{\Gamma_d} \hat{w}\mathbf{t}\left(\llbracket\mathbf{u}\rrbracket\right)\mathrm{d}\Gamma_d = \int_\Gamma \left(\bar{w}+\mathscr{H}\hat{w}\right)\bar{\mathbf{t}}\mathrm{d}\Gamma\end{aligned} \tag{2.31}$$

Using the Bubnov-Galerkin method, the trial functions u and the test functions w are discretized in the same space :

$$\begin{aligned}u &= \mathbf{N}(\bar{a}+\mathscr{H}\hat{a}) \\ w &= \mathbf{N}(\bar{b}+\mathscr{H}\hat{b})\end{aligned} \tag{2.32}$$

where $\bar{a}$ and $\hat{a}$ are the nodal degrees of freedom and $\bar{b}$ and $\hat{b}$ contain the discrete values related to the test functions. Variations of $\bar{w}$ and $\hat{w}$ in terms of variations of nodal displacements are written as

$$\begin{aligned}\bar{w} &= \mathbf{N}\bar{b} \\ \hat{w} &= \mathbf{N}\hat{b}\end{aligned} \tag{2.33}$$

The gradient of the variations $\bar{w}$ and $\hat{w}$ can be written in a discretized form as :

$$\begin{aligned}\nabla\bar{w} &= \mathbf{B}\bar{b} \\ \nabla\hat{w} &= \mathbf{B}\hat{b}\end{aligned} \tag{2.34}$$

Inserting 2.32 in 2.31 using 2.33 and 2.34 the weak form yields for $\bar{w}$ and $\hat{w}$ respectively :

$$\begin{aligned}
&\int_{\Omega} \mathbf{B}^{\mathrm{T}} \sigma \mathrm{d}\Omega + \int_{\Omega} \mathbf{N}^{\mathrm{T}} \mathbf{b} \mathrm{d}\Omega = \int_{\Gamma} \mathbf{N}^{\mathrm{T}} \bar{\mathbf{t}} \mathrm{d}\Gamma \\
&\int_{\Omega^\star} \mathscr{H} \mathbf{B}^{\mathrm{T}} \sigma \mathrm{d}\Omega^\star + \int_{\Omega^\star} \mathscr{H} \mathbf{N}^{\mathrm{T}} \mathbf{b} \mathrm{d}\Omega^\star \\
&+ \int_{\Gamma_d} \mathbf{M}^{\mathrm{T}} \mathbf{t} \left([\![\mathbf{u}]\!] \right) \mathrm{d}\Gamma_d = \int_{\Gamma} \mathscr{H} \mathbf{N}^{\mathrm{T}} \bar{\mathbf{t}} \mathrm{d}\Gamma
\end{aligned} \tag{2.35}$$

in which $\Omega^\star$ has been introduced, so that the integration is performed only on the body parts where $\hat{w}$ is non-zero due to the Heaviside function and $\mathbf{M}$ comprises the shape function $\mathbf{N}$ evaluated on Γ_d. Substitution of the stress relation in the previous equation leads to the formulation of the matrix system of one enriched element :

$$\begin{bmatrix}
\int_{\Omega} \mathbf{B}^{\mathrm{T}} \mathbf{C}_d^{(g)} \mathbf{B} \mathrm{d}\Omega & \int_{\Omega^\star} \mathscr{H} \mathbf{B}^{\mathrm{T}} \mathbf{C}_d^{(g)} \mathbf{B} \mathrm{d}\Omega^\star \\
\int_{\Omega^\star} \mathscr{H} \mathbf{B}^{\mathrm{T}} \mathbf{C}_d^{(g)} \mathbf{B} \mathrm{d}\Omega^\star & \int_{\Omega^\star} \mathscr{H} \mathbf{B}^{\mathrm{T}} \mathbf{C}_d^{(g)} \mathbf{B} \mathrm{d}\Omega^\star + \int_{\Gamma_d} \mathbf{M}^{\mathrm{T}} \mathbf{T} \mathbf{M} \mathrm{d}\Gamma_d
\end{bmatrix}
\begin{Bmatrix} \bar{a} \\ \hat{a} \end{Bmatrix} = \begin{Bmatrix} f_{\bar{a}}^{ext} + f_{\bar{a}}^{body} \\ f_{\hat{a}}^{ext} + f_{\hat{a}}^{body} \end{Bmatrix} \tag{2.36}$$

where $f_{\bar{a}}^{ext}$ and $f_{\hat{a}}^{ext}$ contain the external loads and $f_{\bar{a}}^{body}$ and $f_{\hat{a}}^{body}$ contain the body loads. $\mathbf{T}$ contains the cohesive force which is detailed next. Algorithm 2.2 is given to compute the internal forces for a cohesive XFEM element.

2.5.2 Cohesive law

Similar to section 2.4, a loading/unloading function must be defined. Using the normal separation $[\![\mathbf{u}]\!]_n$ this function can be defined as :

$$f\left([\![\mathbf{u}]\!]_n, \kappa\right) = [\![\mathbf{u}]\!]_n - \kappa \tag{2.37}$$

Algorithm 2.2 Update of internal forces for a cohesive element

Locate the crack intersection on the element's faces
for f=1 to N_{faces} **do**
  If this face, defined with nodes number 1,2, is crossed by the crack
  if $\phi_1 \times \phi_2 < 0$ **then**
    Locate the crack intersection coordinates on this face in the natural coordinates system. For a Q4 element the natural coordinates $(\xi_i, \eta_i)_{i=1..4}$ are $[-1,1] \times [-1,1]$:
$r = \dfrac{\phi_1}{\phi_1 - \phi_2}$
$\zeta_k = \{(1-r)\xi_1 + r\xi_2, (1-r)\eta_1 + r\eta_2\}$
  end if
end for
Triangulate the element using a constrained triangulation (The CGAL Project, 2019) with the boundaries defined by (ξ_i, η_i) and the crack location defined by $(\zeta_k)_{k=1..2}$
For each triangles defined by nodes $(\xi_j, \eta_j)_{j=1..3}$ in the reference element Q4 natural coordinates, transform the 3 Gauss points location from their local natural coordinates gp_{loc} into their coordinates gp_{ref} in the Q4 reference element natural coordinates
for t=1 to $N_{triangles}$ **do**
  For each of the Gauss points
  for gp=1 to 3 **do**
    Evaluate shape function $\mathbf{N}$ at Gauss point gp_{loc}
    Transform the coordinates such that :
$\mathrm{gp}_{ref} = \mathbf{N}_j \times (\xi_j, \eta_j)$
    Evaluate $\det J$ at Gauss point gp_{loc}
    Compute the integration weight :
$w_{\mathrm{gp}\,ref} = \det J \, w_{\mathrm{gp}\,loc}$
  end for
end for
Compute $\mathbf{T}$ and $\mathbf{M}$ with algorithm 2.3
Using $\mathbf{C}_d^{(g)}$ previously saved, the Gauss points and weights computed, update the internal forces $\mathbf{r}$

Opening of the discontinuity is indicated by $f > 0$ and closing by $f < 0$. Upon crack closure $[\![\mathbf{u}]\!]_n = 0$, a penalty stiffness coefficient is assumed. The traction-separation relation for the normal opening is defined such that energy conservation is respected when the transition from the CDM to the XFEM occurs. Thus, the fracture energy in mode I and in mode II should be conserved during transition. Fracture energy in mode I is a well defined parameter. However, in mode II there is no agreement on whether this energy is a real material property or not. In (Carpinteri *et al.*, 1993) it was concluded that mode II fracture energy did not appear to be a material property, and that a cohesive model dissipating energy only in mode I is able to reproduce experimental results with good approximation. In contrast, (Reinhardt & Xu, 2000; Bažant & Pfeiffer, 1986) gives a mode II fracture energy that is 20 to 25 times higher than the mode I fracture energy because shear fracture energy includes not only the energy to create inclined tensile microcracks in the FPZ, but also the energy required to break the shear resistance due to aggregate interlock and other asperities on rough crack surfaces behind the crack front. To simplify the energy conservation during transition and to stay on the conservative side by neglecting aggregate interlock and crack tortuosity, the shear traction t_s will be neglected, therefore, only the traction t_n will be considered.

A typical decaying function is used to compute the normal traction force t_n transmitted across a discontinuity as a function of the history parameter κ :

$$\begin{aligned} t_n &= \alpha e^{-\beta\kappa} \\ t_s &= 0 \\ \mathbf{t} &= t_n\mathbf{n} + t_s\mathbf{m} \end{aligned} \tag{2.38}$$

where α, β are defined in section 3.4.3.

2.6 Proposed transition from continuous damage mechanics to cohesive XFEM

As noted in (Simone *et al.*, 2003), even if enhancement with a discontinuous interpolation is performed at a high damage level, high stresses can still develop. After transition, these stresses will drop to zero and incorrect energy dissipation will occur. Thus, energy conservation will be enforced using mode I energy dissipation. The three conditions required for the conservation of energy during transition are illustrated in figure 2.4. The first condition states that the area Ψ_1 must be equal to Ψ_2 before transition. Similarly, the second condition, states that area Ψ_3 is equal to Ψ_4 after transition. Finally, the initial traction stress of the cohesive surface must be equal to the CDM model stress at the transition strain. These conditions are detailed in the equations presented in the following paragraphs for an example with unit area.

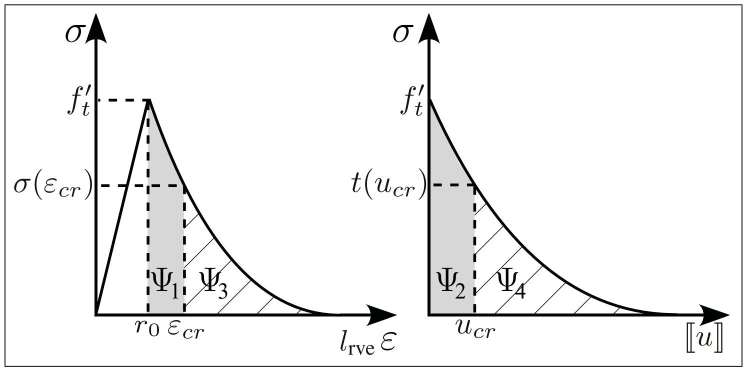

Figure 2.4 Energetic equivalence between CDM (left) and cohesive XFEM (right)

The energy dissipation of the continuous damage mechanics (CDM) approach from damage initiation until the transition strain ε_{cr} occurs must be equivalent to the energy dissipated by the cohesive model from damage initiation until the opening u_{cr} is reached :

$$\Psi_1 = \Psi_2 \Rightarrow \int_{r_0}^{\varepsilon_{cr}} \sigma(\bar{\varepsilon})d\bar{\varepsilon} = \int_0^{u_{cr}} \sigma(u)du \tag{2.39}$$

Considering the CDM approach and a localization band of width l_{rve}, the total energy dissipated until the transition strain ε_{cr} occurs is given by :

$$\int_{r_0}^{\varepsilon_{cr}} \left(l_{\text{rve}}\ f_t' \ \left(\frac{r_0}{\bar{\varepsilon}} \exp\left(-R\left(\bar{\varepsilon} - r_0\right)\right)\right)\right) d\bar{\varepsilon} = \exp\left(Rr_0\right)\ f_t'\ l_{\text{rve}}\ r_0 \left(\Gamma\left[Rr_0\right] - \Gamma\left[R\varepsilon_{cr}\right]\right) \tag{2.40}$$

where $\Gamma[z] = \int_0^\infty t^{z-1} e^{-t} dt$ is the gamma function.

Similarly, for the cohesive model, the energy dissipated from the initiation of the softening until the separation u_{cr} occurs is given by :

$$\int_0^{u_{cr}} \alpha e^{-\beta(u)} du = \frac{\alpha - \alpha e^{-\beta u_{cr}}}{\beta} \tag{2.41}$$

where α and β are two parameters required to adjust the cohesive softening curve. This adjustment concerns the energy that remains to be dissipated until full separation of the material occurs and the initial traction stress of the cohesive surface, which must be equal to the CDM model stress at the transition strain :

$$t(u_{cr}) = \sigma(\varepsilon_{cr}) \tag{2.42}$$

The energy remaining to be dissipated from ε_{cr} by the CDM model to complete material separation must be equal to that of the cohesive model :

$$\Psi_3 = \Psi_4 \Rightarrow \int_{\varepsilon_{cr}}^{\infty} \sigma(\bar{\varepsilon})d\bar{\varepsilon} = \int_{u_{cr}}^{\infty} \sigma(u)du \tag{2.43}$$

The energy dissipation from the transition strain ε_{cr} to complete the separation of the CDM model is given by :

$$\int_{\varepsilon_{cr}}^{\infty} \left(l_{\text{rve}}\, f_t' \, \left(\frac{r_0}{\bar{\varepsilon}} \exp\left(-R\left(\bar{\varepsilon} - r_0\right)\right)\right)\right) d\bar{\varepsilon} = \exp\left(Rr_0\right)\, f_t'\, l_{\text{rve}}\, r_0 \Gamma\left[R\varepsilon_{cr}\right] \tag{2.44}$$

For the cohesive model, the energy that remains to be dissipated at u_{cr} is given by :

$$\int_{u_{cr}}^{\infty} \alpha e^{-\beta(u)} du = \frac{\alpha e^{-\beta u_{cr}}}{\beta} \tag{2.45}$$

By equating equations 2.40 and 2.41, equations 2.44 and 2.45 and by using equation 2.42, the three unknowns α, β and u_{cr} of the cohesive traction separation law can be determined. Algorithm 2.3 is given to compute these unknowns as well as the cohesive force matrix.

2.7 Crack tracking technique

The use of the rotating damage approach allows any initial misprediction of the crack direction to be corrected as a crack grows. Because the discontinuity is introduced after a certain critical damage has been reached, it is expected that the macroscopic crack path will be improved by this correction. Numerical stab1 :ility is also improved because enriching and de-enriching of a node during a non-linear resolution may provide instab1 :ility to the numerical algorithm.

Algorithm 2.3 Compute the cohesive force matrix

If the element damage exceeds the threshold for the first time
if ParamsComputed = false **then**
  Set $\varepsilon_{cr} = \tilde{\varepsilon}_1$
  $f_1 = \dfrac{\alpha - \alpha e^{-\beta u_{cr}}}{\beta} - e^{Rr_0}\, f_t'\, l_{\mathrm{rve}}\, r_0 \left(\Gamma\left[Rr_0\right] - \Gamma\left[R\varepsilon_{cr}\right]\right)$
  $f_2 = \dfrac{\alpha e^{-\beta u_{cr}}}{\beta} - \exp\left(Rr_0\right)\, f_t'\, l_{\mathrm{rve}}\, r_0 \Gamma\left[R\varepsilon_{cr}\right]$
  $f_3 = \dfrac{f_t' r_0}{\varepsilon_{cr}} e^{-R(\varepsilon_{cr} r_0)} - \alpha e^{-\beta u_{cr}}$
  while $||f|| \geqslant 10^{-8}$ **do**
    $-\begin{bmatrix} \dfrac{\partial f_1}{\partial \alpha}, \dfrac{\partial f_1}{\partial \beta}, \dfrac{\partial f_1}{\partial u_{cr}} \\ \dfrac{\partial f_2}{\partial \alpha}, \dfrac{\partial f_2}{\partial \beta}, \dfrac{\partial f_2}{\partial u_{cr}} \\ \dfrac{\partial f_3}{\partial \alpha}, \dfrac{\partial f_3}{\partial \beta}, \dfrac{\partial f_3}{\partial u_{cr}} \end{bmatrix}^{-1} \begin{Bmatrix} f_1 \\ f_2 \\ f_3 \end{Bmatrix} = \begin{Bmatrix} \Delta\alpha \\ \Delta\beta \\ \Delta u_{cr} \end{Bmatrix}$
    $\alpha = \alpha + \Delta\alpha,\ \beta = \beta + \Delta\beta,\ u_{cr} = u_{cr} + \Delta u_{cr}$
    Update f_i
  end while
  Save α, β
  Set ParamsComputed=true
end if
Evaluate the crack normal $\mathbf{n}$ at step $k+1$
Evaluate the crack normal opening $[\![\mathbf{u}]\!]_n^{k+1}$
Evaluate the damage loading function :
$f\left([\![\mathbf{u}]\!]_n, \kappa^{k+1}\right) = [\![\mathbf{u}]\!]_n^{k+1} - \kappa^k$
if $f \geq 0$ **then**
  $\kappa^{k+1} = [\![\mathbf{u}]\!]_n^{k+1}$
else
  $\kappa^{k+1} = \kappa^k$
end if
  Evaluate the cohesive force matrix :
$\mathbf{T} = \left(\alpha e^{-\beta \kappa^{k+1}}\right) \mathbf{n} \otimes \mathbf{n}$
  Evaluate the shape functions $\mathbf{M}$ on the Gauss points located on Γ_d

To simplify the energy transfer between the CDM and the XFEM approach, the damage will be localized as much as possible over a minimal number of finite element rows. Hence, the crack tracking algorithm will enforce this localization. It is known that the width of the localized damage band has a negligible influence on the results of structural analysis provided that the energy dissipation per unit length in a narrow damage band is the same as that of a band of finite width (Bažant & Planas, 1997). However, the diffusion of damage over a width of several element sizes helps to avoid directional finite element mesh bias. The present algorithm can not benefit from this advantage ; the crack tracking algorithm therefore makes use of a stress based nonlocal method (Giry *et al.*, 2011).

The position of the crack within the element can be evaluated with level-sets (Osher & Sethian, 1988). This ensures the continuity of the crack between the elements and once the level of damage has reached a certain threshold, these level-sets can directly be used for the XFEM formulation.

2.7.1 Location of a new potential crack tip

We first make the assumption that cracks initiate along boundaries. Thus a potential crack tip can be identified by a tensile energy criterion on the boundary mesh, similar to that of reference (Bhattacharjee & Léger, 1994) :

$$\frac{1}{2}\sigma_1\tilde{\varepsilon}_1 \geq \gamma\left(\frac{1}{2}f_t' r_0\right) \tag{2.46}$$

where γ is a threshold factor to identify potential elements. If γ is close to one, then more Newton iterations will be required for convergence in a load step because the crack will advance element by element. On the other hand, if γ is set too low, many elements will be identified and there is a chance that the crack diffusion will be high. From our numerical experiments we have found that $\gamma = 0.85$ works well. When multiple elements on the boundary exceed the criterion, the one that has the greatest tensile energy is selected as the crack tip for that iteration. Once a cracked element tip is selected, the coordinates of the crack origin $o(x,y)$ is computed. We make the assumption that the origin is located at the center of the element edge located on the boundary. If more than one edge is in contact with the boundaries, the centroid of the element is selected as the origin. Knowing the origin point and the crack normal $\vec{n}$, the level-set ϕ can be defined. In this work, the non local principal stress direction cosine is taken as the crack normal direction. The level-set, defined by the signed distance (point-plane distance) can be evaluated for all of the potential cracked element nodes. For example, at node i with coordinates $p(x,y)$ the signed distance ϕ_i is given by the relation :

$$\phi_i = \frac{\vec{n} \cdot (p(x,y) - o(x,y))}{||\vec{n}||} \tag{2.47}$$

2.7.2 Potential crack propagation

With the crack tip element located and its level-set computed, the identification of the potential crack path can be defined. The neighboring element whose edge respects the condition $\min(\phi_i) \times \max(\phi_j) < 0$ is selected (its minimal level-set times its maximal one is less than zero). If this neighbor element's energy threshold, as given by equation 2.46, is exceeded, than the not-yet computed element nodes' level sets can be evaluated by point-plane distance as previously reported. Particular attention must be taken to scale the level sets at these nodes. The signed distance is evaluated by the point-plane distance. Hence, the element nodes do not necessarily lie at the same signed distance of two different planes, as illustrated in figure 2.5. In this figure, ϕ_1 and ϕ_2 have already been defined whereas ϕ_3 and ϕ_4 must be computed using a different plane. Consequently, the ratio of the level-set at a pre-defined node, ϕ_2, with the level-set it would have if it were computed with the new plane, ϕ_2', is the scaling factor to apply to the newly-defined level-sets ϕ_3 and ϕ_4 for this element. The potential crack propagation can be cycled until the element in the neighborhood of the crack tip does not respect the threshold defined in equation 2.46. This is detailed in algorithm 2.4.

2.7.3 Stress-based non local method

The main difference between the original nonlocal approach and the stress-based nonlocal method (Giry *et al.*, 2011) is that instead of considering what a point **x** can receive, one considers what a point located at **s** can distribute. Hence point **s** distributes its internal stress and strain

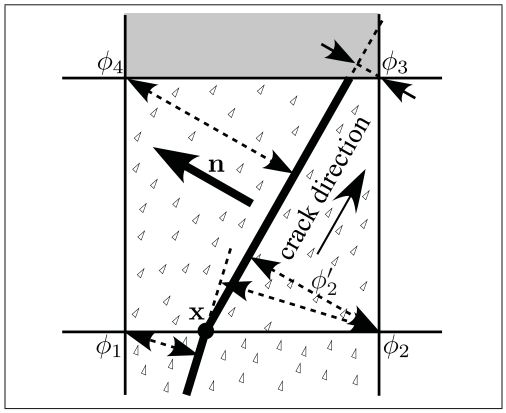

Figure 2.5 Level set scaling

field to neighboring points according to the magnitude and direction of the principal stresses. The area of influence of a point is defined such that it creates an ellipse that is defined by the principal stress direction cosines. Hence, using the principal stress σ_1, σ_2 direction cosines $\mathbf{u}_1$ and $\mathbf{u}_2$ associated with point $\mathbf{s}$, an ellipse can be defined using polar coordinates :

$$\rho\left(\mathbf{x},\sigma_{\text{princ}}(\mathbf{s})\right)^2 = \frac{(\mathbf{u}_1(\mathbf{s})\cdot\mathbf{u}_2(\mathbf{s}))^2}{f_t'^2\left((\mathbf{u}_2(\mathbf{s})\cos(\theta))^2+(\mathbf{u}_1(\mathbf{s})\sin(\theta))^2\right)} \tag{2.48}$$

where

$$\cos(\theta) = \frac{\mathbf{u}_1(\mathbf{s})\odot(\mathbf{x}-\mathbf{s})}{||(\mathbf{x}-\mathbf{s})||} \tag{2.49}$$

$$\sin(\theta) = \frac{||\mathbf{u}_1(\mathbf{s})\otimes(\mathbf{x}-\mathbf{s})||}{||(\mathbf{x}-\mathbf{s})||} \tag{2.50}$$

The amplitude of $\rho\left(\mathbf{x},\sigma_{\text{princ}}(\mathbf{s})\right)$ scaled by the tensile strength f_t' is such that it is limited to 1. An example of this ellipse is given in figure 2.6. Using the Gauss distribution, the weight function can be defined by :

$$\psi(\mathbf{x}-\mathbf{s}) = \exp\left(-\left(\frac{2||\mathbf{x}-\mathbf{s}||}{R_a\rho\left(\mathbf{x},\sigma_{\text{princ}}(\mathbf{s})\right)}\right)^2\right) \tag{2.51}$$

Algorithm 2.4 Crack tracking algorithm

1: For each crack c
2: **for** c=1 to N_{crack} **do**
3: Loop over the tip element's faces
4: **for** f=1 to N_{faces} **do**
5: If this face defined, with nodes number 1,2, is crossed by the crack
6: **if** $\phi_1 \times \phi_2 < 0$ **then**
7: Locate the crack intersection coordinates on this face : $r = \dfrac{\phi_1}{\phi_1 - \phi_2}$
8: $o(x,y) = \{(1-r)x_1 + rx_2, (1-r)y_1 + ry_2\}$
9: Locate the element el adjacent to face f
10: Check if the energy threshold of element el is exceeded
11: **if** $\frac{1}{2}\sigma_1^{av}\varepsilon_1^{av} \geq \gamma\left(\frac{1}{2}f_t' r_0\right)$ **then**
12: Get crack normal $\vec{n}$ using algorithm 2.5
13: Check if a node has ϕ already defined
14: **for** n=1 to N_{nodes} **do**
15: **if** ϕ_n is defined **then**
16: $s = \dfrac{\phi_n}{\phi}$
17: Go to 20
18: **end if**
19: **end for**
20: Loop over element el nodes n defined by coordinates $p_n(x,y)$
21: **for** n=1 to N_{nodes} **do**
22: **if** ϕ_n is not defined **then**
23: $\phi_n = s\dfrac{\vec{n}\cdot(p_n(x,y) - o(x,y))}{||\vec{n}||}$
24: **end if**
25: **end for**
26: Return to 3 with element el being the crack tip
27: **else**
28: Stop crack propagation
29: **end if**
30: **end if**
31: **end for**
32: **end for**

where R_a is the interaction radius, often directly related to the characteristic length l_c. l_c is a material property that governs the minimum possible width of a zone of strain-softening damage in a nonlocal continuum, or the minimum possible spacing of cracks in discrete fracture

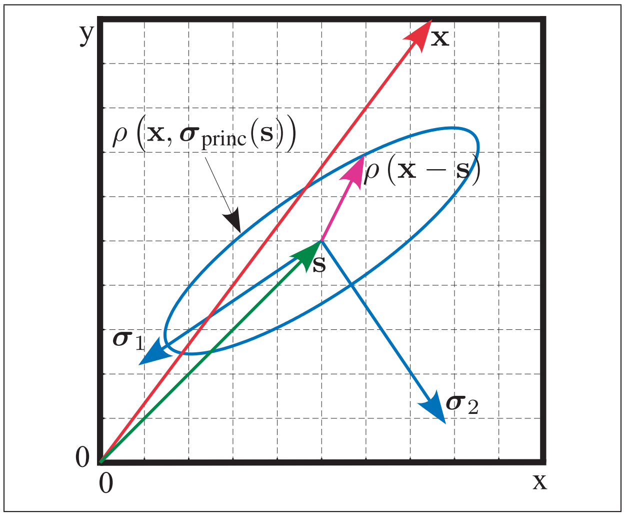

Figure 2.6 Stress-based non local model

models (Bažant & Cabot, 1989). The effective length of the FPZ, c_f, is often related to the characteristic length. This parameter can be estimated with the relation :

$$c_f = \frac{EG_F}{{f'_t}^2} \tag{2.52}$$

c_f and l_c can be related such that $c_f \approx 4l_c \approx 12d_a$ (Bažant & Oh, 1983). Typically, l_c is defined as $l_c \approx 3d_a \approx R_a$, where d_a is the maximum aggregate size. (Bažant & Oh, 1983; Bažant & Cabot, 1989; Denarie *et al.*, 2001).

For the situation presented in figure 2.6, the weight function is plotted in figure 2.7. The point s has a larger influence area in the direction of its first principal stress.

One can deduce that a point with a small state of stress will have a marginal effect on the nodes located in its vicinity. On the other hand, if a point has a principal stress close to the tensile strength, the points located at a distance R_a in the direction of this principal stress will be influenced by this point. Finally, a point located outside the principal stress isocontour's gradient caused by a crack tip will not attract much the crack towards itself.

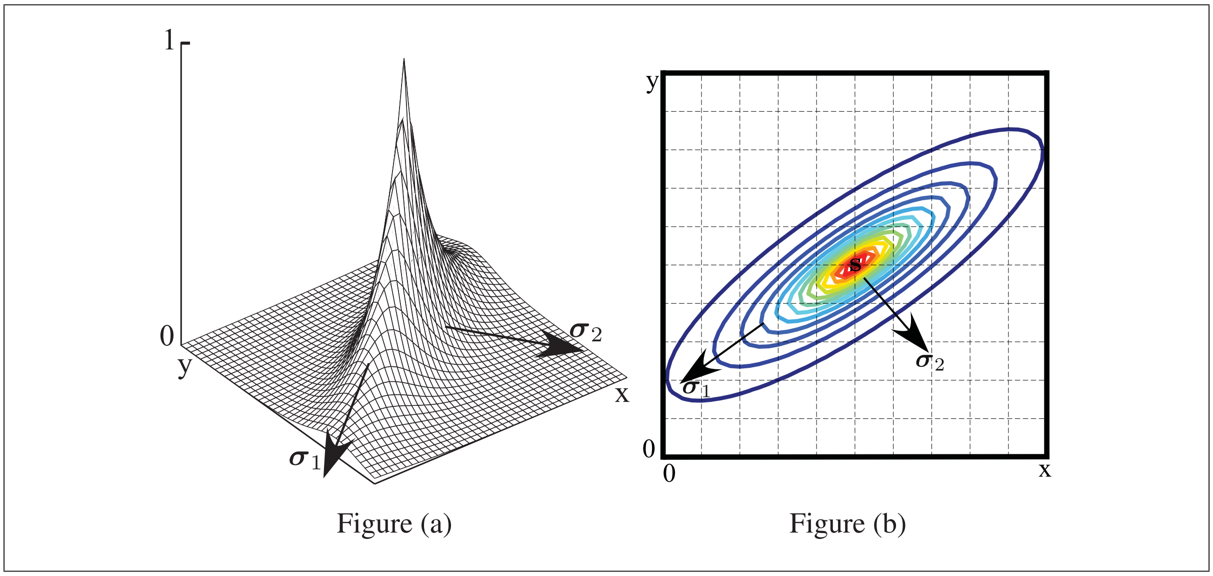

Figure 2.7 (a) Influence of the distributing point **s**, (b) isocontours of the distributing point influence

The nonlocal stresses $\tilde{\sigma}(\mathbf{x})$ at point **x** are given by :

$$\tilde{\sigma}(\mathbf{x}) = \frac{\int_\Omega \psi(\mathbf{x}-\mathbf{s})\,\sigma(\mathbf{s})\mathrm{d}\mathbf{s}}{\int_\Omega \psi(\mathbf{x}-\mathbf{s})\,\mathrm{d}\mathbf{s}} \tag{2.53}$$

Algorithm 2.5 gives the main lines in order to compute the stress based non local crack normal.

2.7.4 Predictor corrector

The element can sustain damage as presented in section 2.4 if it respects the condition $\min(\phi_i) \times \max(\phi_j) < 0$. In a rotating crack model, the initial normal direction used to compute the level-sets is susceptible to change until the level-sets are fixed when $d > d_{crit}$. Therefore, the potential crack path is predicted as indicated in section 2.7.2 and is corrected according to the damage sustained by the elements crossed by the crack by cycling through the propagation algorithm at each Newton iteration. To preserve the robustness of the Newton-Raphson solution procedure, an XFEM discontinuity is introduced at the end of a load increment in the elements ahead of the crack tip if the damage index exceeds the parameter $d > d_{crit}$. The selection of d_{crit} is discussed in the validation examples. Figure 2.8, give the steps in the predictor corrector algorithm. In

Algorithm 2.5 Stress based nonlocal algorithm

Using a nearest neighbour algorithm seek for Gauss points with coordinates $\mathbf{s}$ located in radius R_a from the element centroid $\mathbf{x}$ ($||\mathbf{x}-\mathbf{s}|| < R_a$)
For all source points $\mathbf{s}$ found assign contribution to the stress tensor σ
for gp=1 to N_{gp} **do**
    Compute Gauss point's principal stresses $\sigma_1(\mathbf{s})$ and $\sigma_2(\mathbf{s})$ and direction cosines $\mathbf{u}_1(\mathbf{s})$ and $\mathbf{u}_2(\mathbf{s})$
    Set $\cos(\theta) = \dfrac{\mathbf{u}_1(\mathbf{s}) \odot (\mathbf{x}-\mathbf{s})}{||(\mathbf{x}-\mathbf{s})||}$
    Set $\sin(\theta) = \dfrac{||\mathbf{u}_1(\mathbf{s}) \otimes (\mathbf{x}-\mathbf{s})||}{||(\mathbf{x}-\mathbf{s})||}$
    Set $\rho = \sqrt{\dfrac{(\sigma_1(\mathbf{s})\sigma_2(\mathbf{s}))^2}{{f'_t}^2\left((\sigma_2(\mathbf{s})\cos(\theta))^2 + (\sigma_1(\mathbf{s})\sin(\theta))^2\right)}}$
    if $\rho R_a < l_{rve}$ **then**
        Set $\rho R_a = l_{rve}$
    end if
    Evaluate the weight function :
$\psi(\mathbf{x}-\mathbf{s}) = \exp\left(-\left(\dfrac{2||\mathbf{x}-\mathbf{s}||}{\rho R_a}\right)^2\right)$
    Evaluate the determinant $\det J_{gp}$ and the weight w_{gp} of the Gauss point gp
    Evaluate $\mathrm{Sum} = \mathrm{Sum} + w_{gp}\det J_{gp}\psi(\mathbf{x}-\mathbf{s})$
    Evaluate $\sigma = \sigma + \sigma_{gp} w_{gp} \det J_{gp} \psi(\mathbf{x}-\mathbf{s})$
end for
Evaluate $\sigma = \dfrac{\sigma}{\mathrm{Sum}}$
Compute principal stresses direction cosines of tensor σ
The direction cosine corresponding to the largest principal stress is the crack normal $\vec{n}$

2.8a, the elements located in the crack path and respecting condition 2.46 are selected. During the Newton-Raphson iterations, if the initiation criterion is fulfilled, the elements located in the crack path get damaged, while the crack path gets corrected as in figure 2.8b. At the end of the Newton-Raphson iteration, if $d > d_{crit}$ for any element located in the crack path, an XFEM discontinuity is introduced (figure 2.8c). This predictor corrector algorithm is detailed in algorithm 2.6.

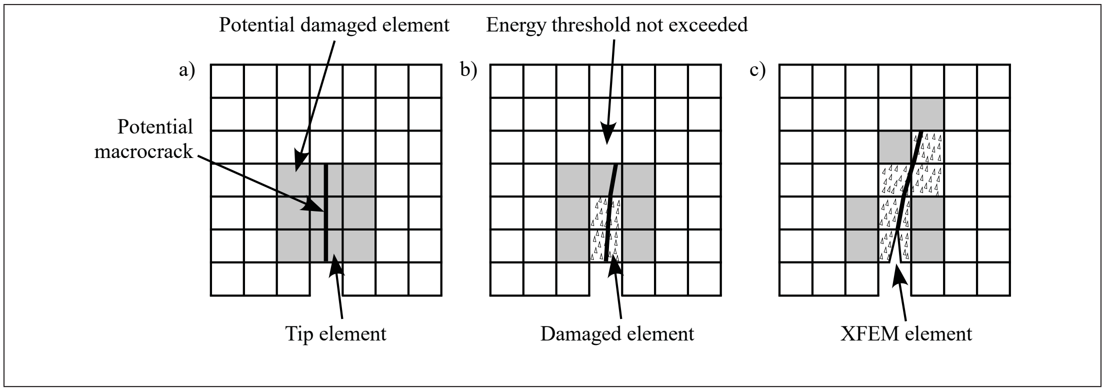

Figure 2.8 Crack tracking algorithm : a) potential damaged elements, b) damaged elements in the crack path, c) introduction of macrocrack with XFEM

2.8 Validation examples

The computer implementation of this model is achieved in a parallel object oriented C++ code. The solver and parallel data structure is provided by the package Trilinos (Heroux *et al.*, 2005). Five validation examples are presented in this section. The simple three-point beam test of Bažant and Pfeiffer (Bažant & Pfeiffer, 1987), the shear beam with single notch test of Arrea and Ingraffea (Arrea & Ingraffea, 1981), the tension-shear specimen test of Nooru-Mohamed (Nooru-Mohamed, 1992), and two concrete gravity dams (Carpinteri *et al.*, 1994; Gioia *et al.*, 1992) are used for the validation of the proposed model. The problems are discretized using four node elements with bilinear interpolation, with the addition of the incompatible mode formulation (Taylor *et al.*, 1976).

2.8.1 Three point beam

The beam in figure 2.9 tested by Bažant and Pfeiffer (Bažant & Pfeiffer, 1987) with d =0.3048 m and a thickness of 0.038 m is considered for the first validation example. The material properties are given in table 2.1. The nonlocal interaction radius is given by $R_a = 3d_a$. Displacement control has been performed by applying a displacement increment $\Delta u = 4\times10^{-6}$ m at the two nodes adjacent to the center line of the beam. In the experiment, the ultimate average load resistance was $P_u = 7784$N. Using elastic bending theory, the load that causes the tensile stress

Algorithm 2.6 General algorithm

Loop over load steps
for ls=1 to N_{steps} **do**
    Define load vector $\mathbf{F}$ and $\Delta\mathbf{F} = \mathbf{F}$
    while $\dfrac{||\Delta\mathbf{F}||}{||\mathbf{F}||} > \varepsilon$ **do**
        Solve $\mathbf{K}\Delta\mathbf{u} = \Delta\mathbf{F}$
        $\mathbf{u} = \mathbf{u} + \Delta\mathbf{u}$
        Loop over elements
        for e=1 to N_{elem} **do**
            If the element is enriched
            if $\max\phi_i \times \min\phi_i < 0$ **then**
                Compute $\mathbf{r}$ using algorithm 2.2
            else
                Compute $\mathbf{r}$ using algorithm 2.1
            end if
        end for
        $\Delta\mathbf{F} = \mathbf{F} - \mathbf{r}$
        Update the crack path using algorithm 2.4
    end while
    $N_{enrich} = 0$
    Loop over all elements
    for e=1 to N_{elem} **do**
        If the criterion d_{crit} is exceeded
        if $d_1 \geqslant d_{crit}$ **then**
            Enrich the element's e nodes
            $N_{enrich} = N_{enrich} + 1$
        end if
    end for
    if $N_{enrich} > 0$ **then**
        Update the graph for matrix assembly to add the new DOFs
    end if
end for

at the crack tip is 6206 N. Four different Q4 plane stress meshes were used to study the results independence with regards to the mesh refinement. The computed ultimate loads are 6940 kN, 6560 kN, 7231 kN and 7579 kN, for $h_c = d/6$, $d/12$, $d/24$ and $d/36$, respectively. The ultimate loads computed are between the elastic bending theory and the experimental approach. Given that the finest mesh is six times more refined than the coarsest one, the results are nearly mesh independent. The force-displacement curve for the case where $h_c = d/36$ is given in figure

Tableau 2.1 Material properties for the three-point beam specimen

E (MPa)	f'_t (MPa)	f'_c (MPa)	ν	G_F (N/m)	d_a (mm)
27413	2.886	34.0	0.18	40.29	12.7

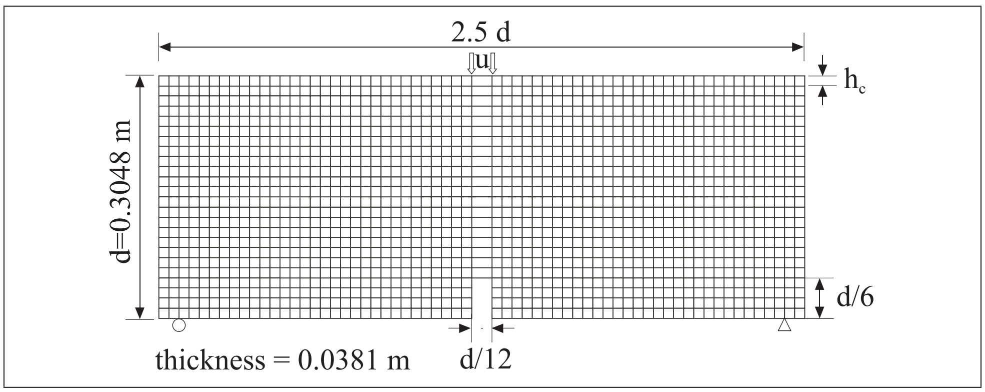

Figure 2.9 Notched three-point beam specimen dimensions (mesh $h_c = d/24$)

2.10a. Continuum damage model ($d_{crit} = 1.0$) results are compared with the CDM+XFEM model with different transition damage criteria. The ultimate load for the range $d_{crit} = [0.5\ 0.7]$ are close to 7650 N and for $d_{crit} = [0.8\ 1.0]$ the ultimate load is 7246 N. For the models with $d_{crit} = [0.5\ 0.7]$, the transition to the XFEM model occurs before the peak load has been reached. Thus, the cohesive model predicts a slightly higher ultimate load. The beam's energy response is shown in figures 2.10b and 2.10c. Figure 2.10b gives the difference in energy dissipation for different transition criteria. It is possible to observe that the strain energy for $d_{crit} = [0.8\ 1.0]$ is exactly the same. Given that the ultimate load is greater for $d_{crit} = [0.5\ 0.7]$, both the work done and the energy dissipation are larger for these transition criteria. In figure 2.10c, the difference in energy response is shown for a case where the energy transfer is carried out and for a case where there is no special treatment of energy transfer during transition at $d_{crit} = 0.5$. For the model not considering energy transfer, the maximum elastic energy stored in the beam before dissipation by cracking occurs is below that of the models in figure 2.10b.

It is shown that even if the transition occurs at a low damage level, if the energy transfer between the CDM and the cohesive XFEM model is carried out, the beam energy response will be treated in a satisfactory manner. What can be concluded with this pure mode I example

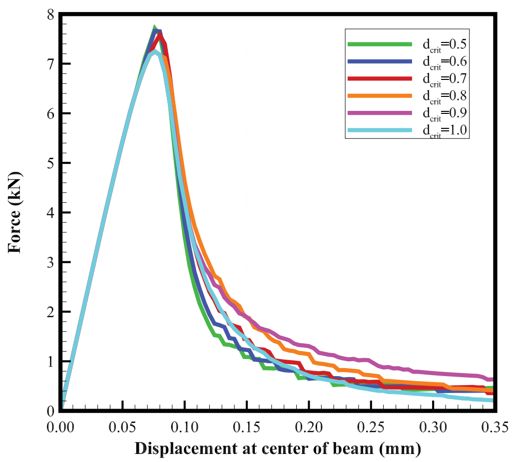

Figure (a) Force-displacement beam response

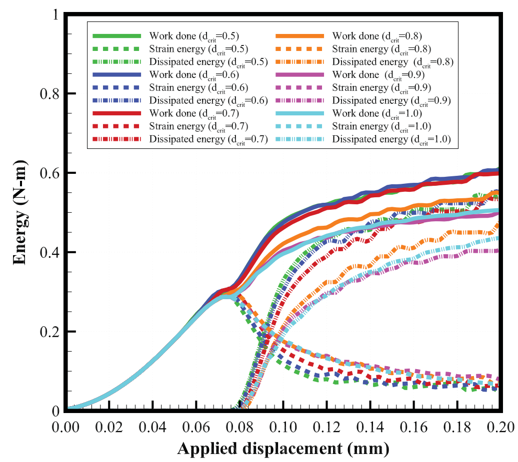

Figure (b) Energy response for different transition criteria for the three-point beam specimen

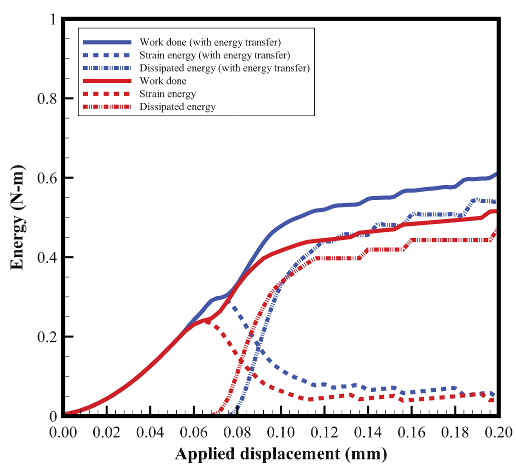

Figure (c) Difference in energy response for $d_{crit} = 0.5$ with and without energy transfer for the three-point beam specimen

Figure 2.10 Three point beam results

is that if transition occurs before the peak load, the cohesive XFEM model will predict higher peak load than the CDM model and the work done will be similar, regardless of this transition criterion.

2.8.2 Shear beam with single notch

A single-notched shear beam illustrated in figure 2.11 and tested by Arrea and Ingraffea (Arrea & Ingraffea, 1981) is used as a second validation example. This case shows the opening as well as sliding (mixed-mode) that occurs during crack-propagation. Therefore, the effect of the energy transfer done in mode I during transition from CDM to cohesive XFEM will be validated. Most smeared crack solutions are unable to predict full separation and softening down to zero (Rots, 1988). The transition from damage mechanics to XFEM should be able to alleviate this problem. The crack mouth sliding displacement (CMSD) is used as a feed-back signal to control the load applied and capture the snap-back beam response. The material properties are given in table 2.2. The nonlocal interaction radius is given by $R_a = 3d_a$. The beam model meshed with Q4 plane stress elements is used to compute the force-CMSD response of the shear beam.

Tableau 2.2 Material properties for the shear beam specimen

E (MPa)	f'_t (MPa)	f'_c (MPa)	ν	G_F (N/m)	d_a (mm)
24800	2.80	45.5	0.18	100	2

The force-deflection of point A's response curves are presented in figure 2.12a for $d_{crit} = [0.5\ 1.0]$ and compared with the discrete crack model results given in reference (Rots, 1988). Force-CMSD results are presented in figure 2.12b and compared with experimental results (Arrea & Ingraffea, 1981) (shaded grey). Only the models with $d_{crit} = [0.5\ 0.8]$ are capable of predicting the peak load and able to soften down to zero. The model using the criteria $d_{crit} = 0.9$ has the same peak load as the CDM model ($d_{crit} = 1.0$), thus transition occurs after the peak

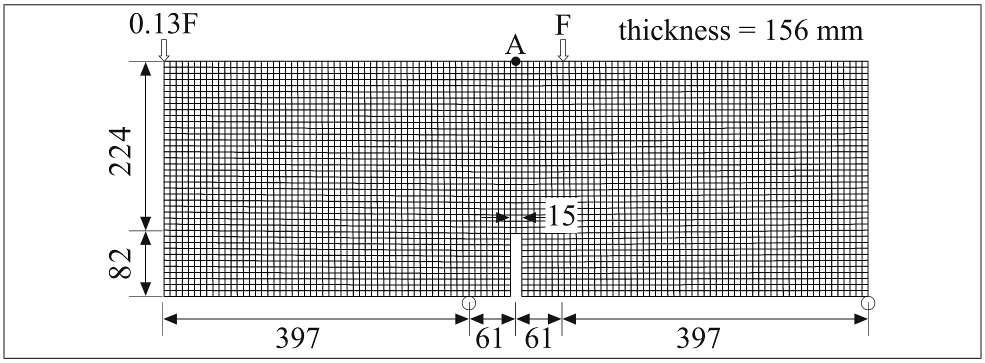

Figure 2.11 Shear beam with single notch specimen dimensions

load has been reached. Both models suffer from stress locking. Moreover, the CDM model is unable to soften down to zero, and in addition, the force tends to increase rather than decrease after snap-back. The beam's energy response is given in figure 2.12c. At approximately 0.2 mm of displacement from point A, the energy added to the beam is almost completely dissipated for the models where $d_{crit} = [0.5\ 0.8]$ indicating that the crack has reached the top part of the beam. For $d_{crit} = [0.5\ 0.7]$, the energy response is similar whereas for $d_{crit} = 0.8$ the model has a tendency to have small spurious stress transfer after snap-back. Figure 2.12d illustrates the effect of energy transfer on the energy response for $d_{crit} = 0.5$. If the transfer is not made during the transition from CDM to cohesive XFEM, the irrecoverable energy corresponds to approximately half the work done. For the three point beam the work done for the model with $d_{crit} = 0.5$ with no energy transfer during transition was similar to that of the CDM model (figure 2.10c). Based on the results obtained for the single-notched shear beam, this appears to be a coincidence. Finally, the absence of mode II fracture energy dissipation in the cohesive XFEM model does not seem to affect the results in a significant manner. In fact, in this case transition to XFEM helps avoid the spurious stress transfer experienced with the CDM model. From the results, the ideal values of d_{crit} should be between 0.6 or 0.7 to avoid spurious stress transfer.

The path is compared with the profile observed in the laboratory and used by Rots (Rots, 1988) for the discrete crack analysis performed by introducing interface elements on the *a priori*

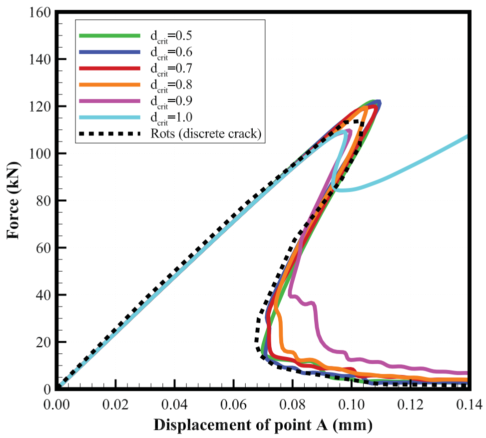

Figure (a) Force-deflection of point A of the shear beam

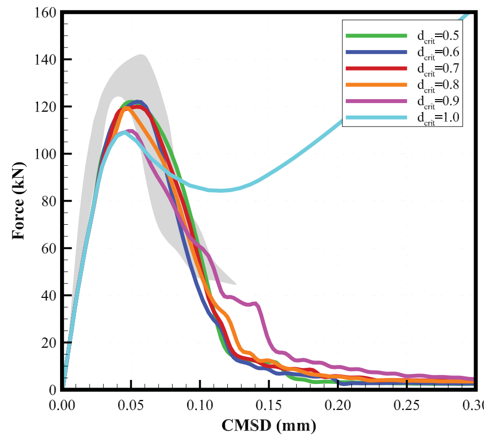

Figure (b) Force-CMSD of the shear beam

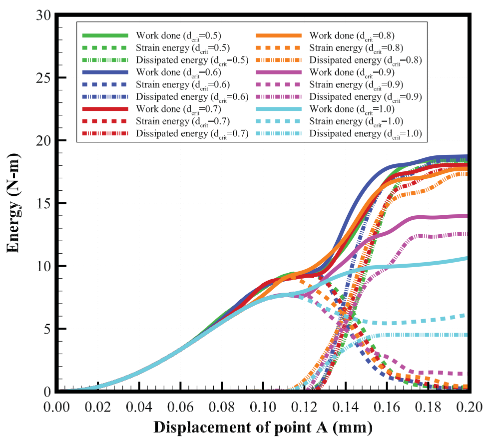

Figure (c) Energy response for different transition criteria for the tension-shear specimen

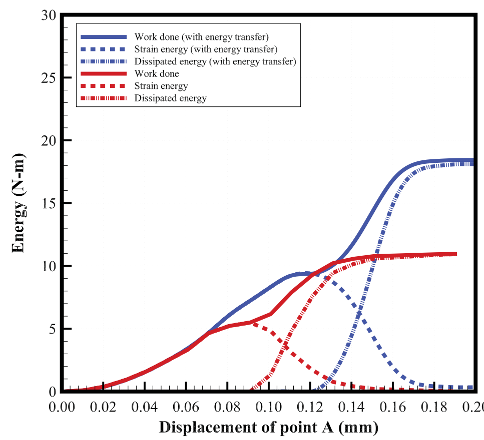

Figure (d) Difference in energy response for $d_{crit} = 0.5$ with and without energy transfer for the tension-shear specimen

Figure 2.12 Shear beam Force-CMSD and energy response

known crack path. Figure 2.13 gives the profile computed with the crack tracking technique. That crack path is almost identical to the experimental one.

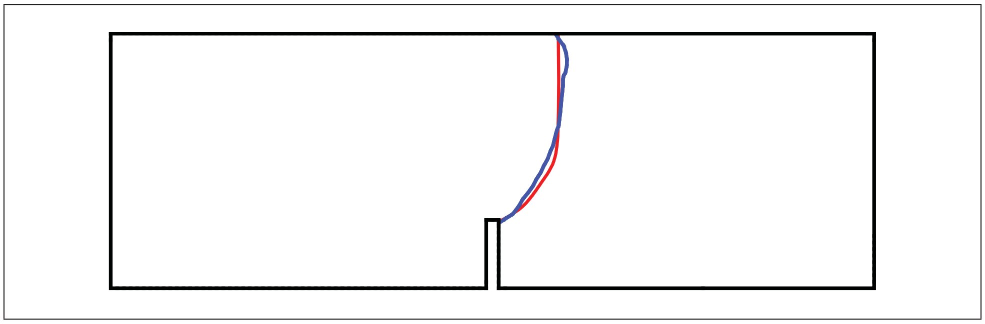

Figure 2.13 Crack path predicted for the single-notched shear beam (blue) compared with reference (Rots, 1988) (red)

2.8.3 Double-edge notched specimen

A double-edge notched specimen (DEN) made of concrete and tested experimentally by Nooru-Mohamed (Nooru-Mohamed, 1992) is taken as the third validation example to demonstrate the applicability of the model. The geometry, the loading and the boundary conditions of the panel are presented in figure 2.14. The material parameters, similar to those used in reference (Meschke & Dumstorff, 2007), are given in table 2.3. Loading is applied via prescribed displacements along the left edge and along the top edge of the panel. The prescribed u_x displacement on the left edge is applied in a manner to have the shear force P_s constant at all times and the displacement on the top edge is varied continuously. The model is meshed with Q4 plane stress elements and the nonlocal interaction radius is given by $R_a = 3d_a$. For cases 4a and 4b, the shear load P_s is applied from the beginning using displacement control u_s. u_s is adjusted continuously to keep P_s constant. The traction force P_n, is applied gradually using displacement control with increments of $\Delta u_n = 1 \times 10^{-6}$ m. For case 4c, the shear force must be applied gradually keeping the top edge free of axial forces. To simplify the numerical model, instead of having the top edge free of axial forces, it is forced to remain horizontal during application of the shear load, such that constraint equations are applied to maintain the edge at the horizontal level. When the full shear load is applied this constraint is removed and replaced with imposed displacements. A coarse mesh (figure 2.14) and a fine mesh (figure 2.15) will be used to assess the independence of the crack path with regards to the mesh alignment and fineness. Load-displacement responses for loading paths 4a to 4c are presented in figures 2.16b,

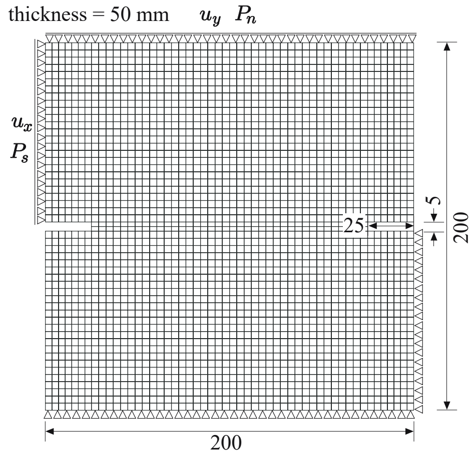

Figure 2.14 Double-edge notched specimen dimensions (coarse mesh)

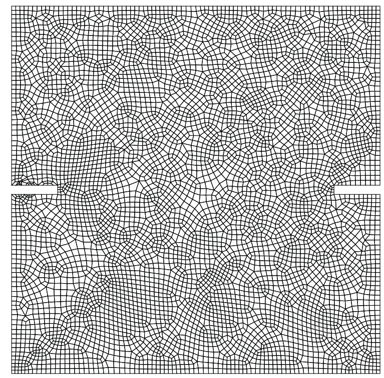

Figure 2.15 Double-edge notched specimen (fine mesh)

Tableau 2.3 Material properties for the tension-shear specimen

E (MPa)	f'_t (MPa)	f'_c (MPa)	ν	G_F (N/m)	d_a (mm)
30000	3.00	30.0	0.20	110	2

2.16d and 2.16f, and are compared with the experimental results (Nooru-Mohamed, 1992) (4a-sample : 48-03, 4b-samples : 46-05 and 47-01, 4c-sample : 47-06) and those of the reference (Meschke & Dumstorff, 2007). The ultimate loads for loading paths 4a and 4b are similar to that of reference (Meschke & Dumstorff, 2007). For path 4c, traction load is present during the application of the shear load. This is caused by the constraint equation applied on the top edge. There is no information about how the top edge is treated in reference (Meschke & Dumstorff, 2007), but the traction force of 5 kN is similar to that obtained with their model. Compared to the experiments, the numerical model overestimates the ultimate load. The first observation is that in the linear region, the numerical model is more flexible than the experimental one, so the modulus could be adjusted to obtain the same slope. It should be emphasized that when the same parameters as reference (Meschke & Dumstorff, 2007) are used, the numerical results are in agreement.

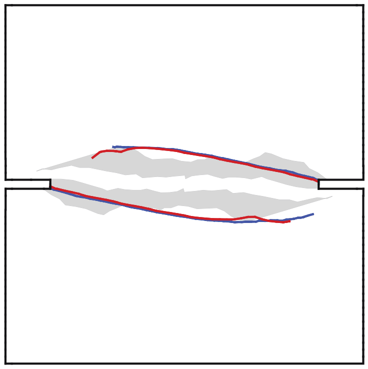

Figure (a) Computed crack path for loading path 4a (P_s=5kN)

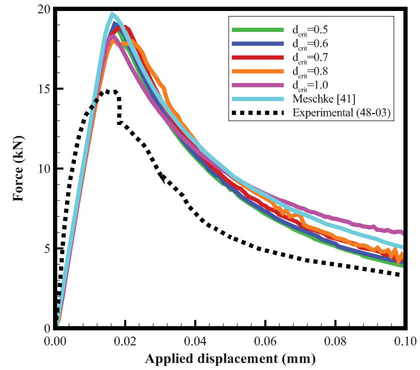

Figure (b) Load-displacement for loading path 4a (P_s=5kN)

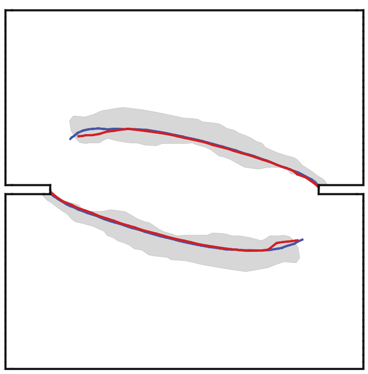

Figure (c) Computed crack path for loading path 4b (P_s=10kN)

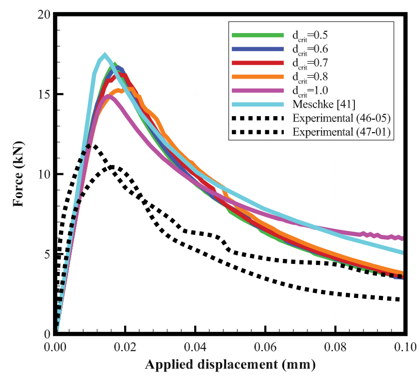

Figure (d) Load-displacement for loading path 4b (P_s=10kN)

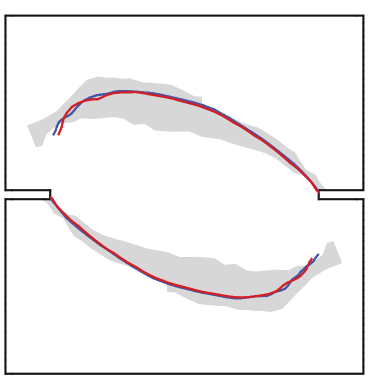

Figure (e) Computed crack path for loading path 4c (P_s=27.5kN)

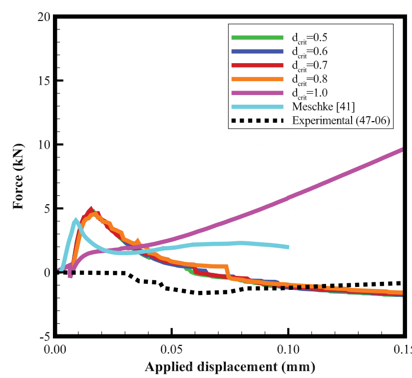

Figure (f) Load-displacement for loading path 4c (P_s=27.5kN)

Figure 2.16 Force response of the DEN specimen

The computed crack trajectories are given in figures 2.16a, 2.16c and 2.16e and compared with the experimental results (shaded grey). The red line corresponds to the computed trajectory with the coarse mesh, while the blue line corresponds to the results obtained with the fine mesh. The numerical results are in agreement with those of the experiment. Furthermore, as per these results, it is clear that the crack path is independent of the mesh. Thus, the non local tracking algorithm coupled with an anisotropic damage model is a sufficient condition to avoid mesh-induced directional bias.

2.8.4 Crack propagation in a reduced scale gravity dam

A reduced scale gravity dam (1 :40) subjected to equivalent hydraulic and weight loading tested by Carpinteri (Carpinteri *et al.*, 1994) is considered as the fourth validation example. Material properties are given in table 2.4. The geometry, the loading and the boundary conditions of the dam are presented in figure 2.17.

Tableau 2.4 Material properties for the reduced scale gravity-dam

E (MPa)	f'_t (MPa)	f'_c (MPa)	ν	G_F (N/m)	ρ (kg/m^3)	d_a (mm)
35700	3.60	45.0	0.10	184	2400	25

Figure 2.18 gives the crack paths for different nonlocal radius. The shaded area corresponds to the experimental crack path of the front and rear faces of the dam. Figure 2.19 gives the force as a function of the crack mouth opening displacement (CMOD) for different transition criteria. The ultimate predicted load of approximately 625 kN is lower than the load measured during the experiment. However, it is obvious that in the linear region, the numerical model is more flexible than the experimental one. Similar behavior was observed in (Bhattacharjee & Léger, 1994; Ghrib & Tinawi, 1995; Gunn, 1998; Cai, 2007). In these references, the posistion of the imposed loads were measured from datum B (figure 2.17) instead of datum A corresponding to the dimensions provided in (Carpinteri *et al.*, 1994). Thus, the numerical results using datum B

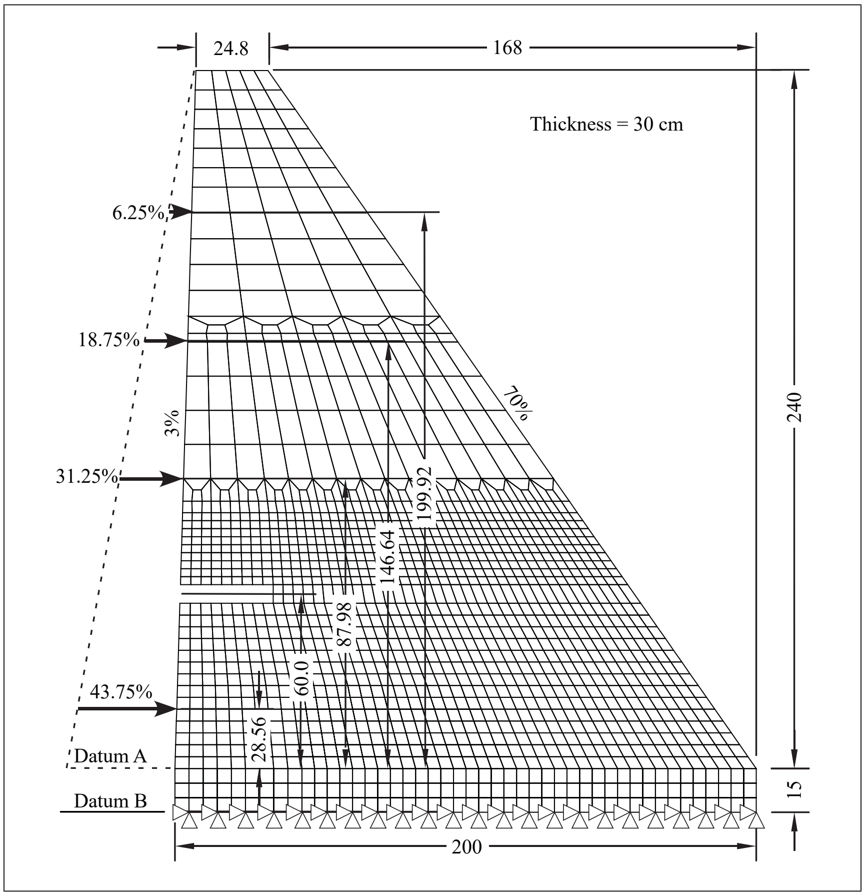

Figure 2.17 Gravity dam specimen dimensions

are added to figure 2.19. The slope in the linear zone is similar as well as the ultimate predicted load of 736 kN, that is close to the experimental load of approximately 720 kN.

Also note that references (Bhattacharjee & Léger, 1994; Ghrib & Tinawi, 1995; Gunn, 1998; Cai, 2007) fail to predict the correct experimental crack path. Based on the numerical results presented in figure 2.18, the crack paths computed with $R_a < 10\, d_a$ emerge on the downstream side of the dam. Using $R_a \geq 10\, d_a$ leads to a convergence of crack paths that are in agreement with the numerical results.

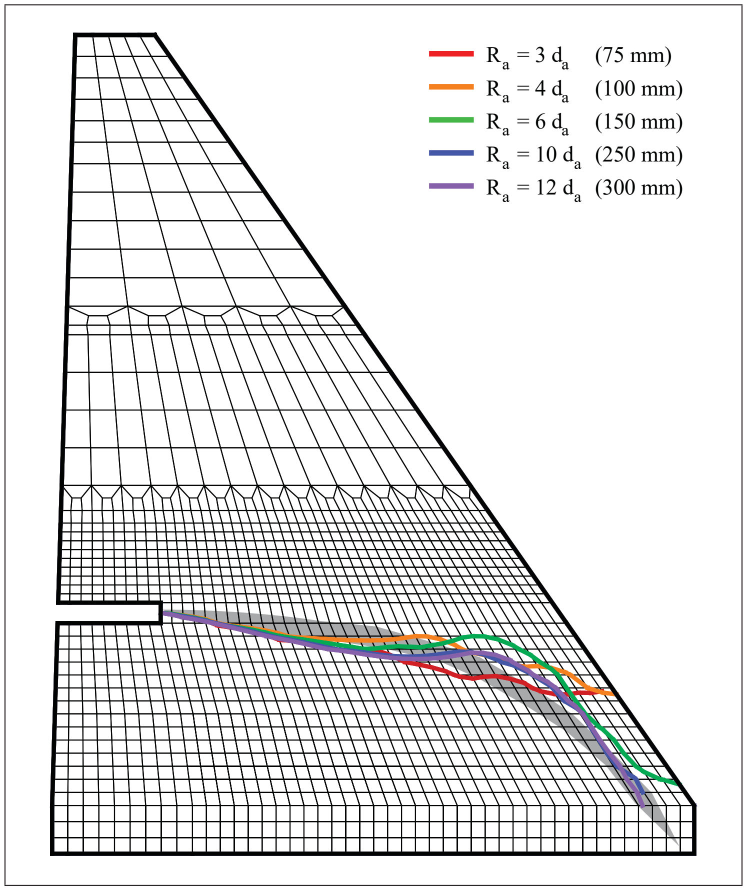

Figure 2.18 Crack path for the reduced scale gravity dam ($d_{crit} = 0.6$)

2.8.5 Crack propagation of a full scale gravity dam subjected to reservoir overpressure

Koyna Dam is a 103-m-high concrete gravity dam in India widely used as a benchmark model for seismic analysis. There is also a static analysis case study that was analyzed using a plasticity-based model and linear fracture mechanics under reservoir overflow (Gioia *et al.*, 1992). This case study has not been validated experimentally, however numerous authors have published numerical results using the same geometry and material parameters (Bhattacharjee & Léger, 1994; Ghrib & Tinawi, 1995; Cai, 2007). Material parameters and geometric configuration adapted from (Chopra & Chakrabarti, 1972) are presented in table 2.5 and figure 2.20 respectively. The initial notch facing the change of slope on the downstream face has a depth that corresponds to 10% of the dimension d, and is included in the model by dis-

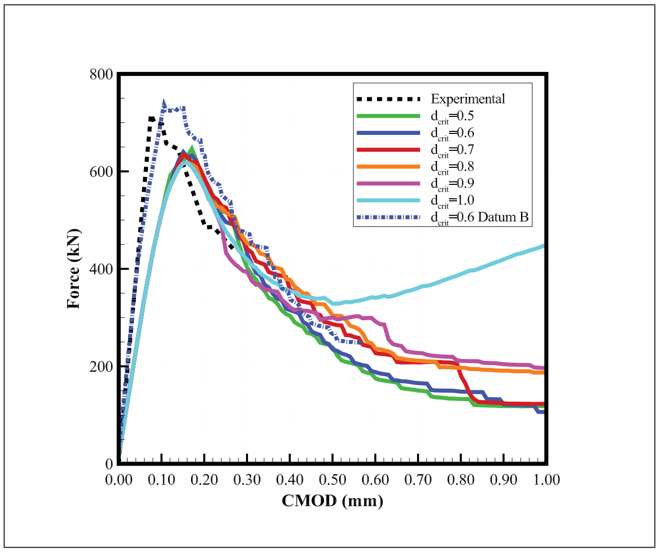

Figure 2.19 Load as a function of crack mouth opening displacement for the gravity dam ($R_a = 6d_a$)

connecting the nodes of the elements underlying the notch (the red line in figure 2.20). The maximum aggregate dimension is not specified, hence using equation 2.52 and the relation $c_f \approx 4l_c \approx 12d_a$, the nonlocal interaction radius equal to $3d_a$ is given by $R_a = c_f/4 = 0.625$ m.

Tableau 2.5 Material properties for the full scale gravity-dam

E (MPa)	f'_t (MPa)	f'_c (MPa)	ν	G_F (N/m)	ρ (kg/m^3)
25000	1.00	10.0	0.20	100	2450

A Q4 plane stress model, subjected to gravity, hydrostatic pressure of a full reservoir level and overflow pressure is considered. The water pressure inside the cracks is neglected. Only a fine mesh with a transition criteria of d_{crit}=0.6 has been considered. The response of the structure is represented by the overflow height versus the horizontal displacement at the crest in figure 2.21. It is compared with results based on the plasticity theory (Gioia *et al.*, 1992), on smeared

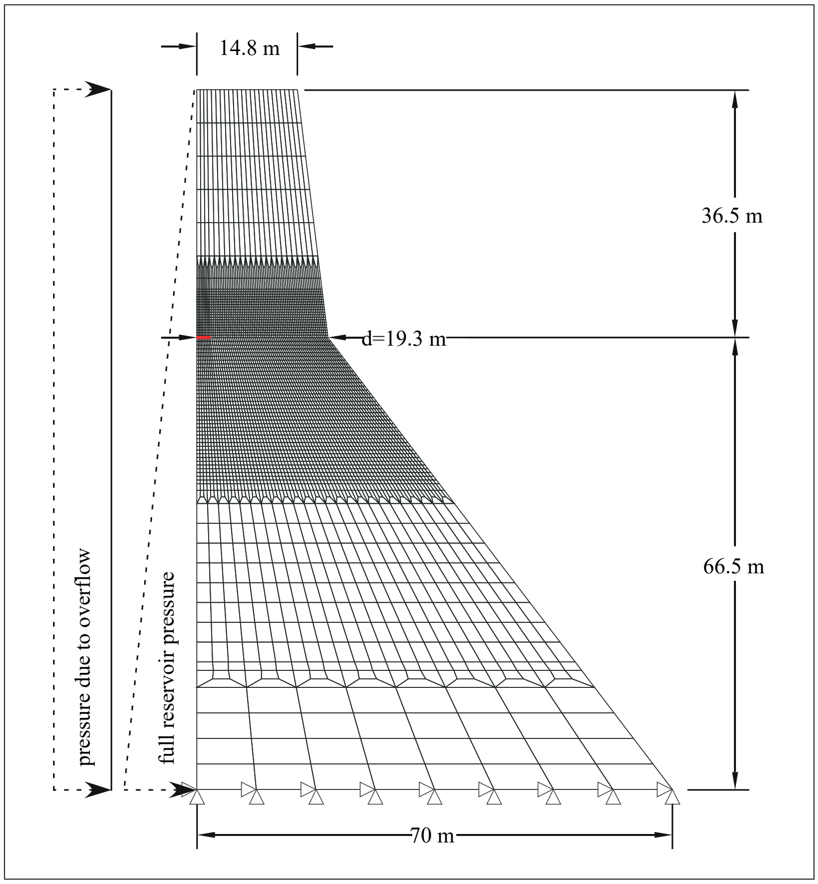

Figure 2.20 Full scale gravity-dam specimen dimensions

cracks (Bhattacharjee & Léger, 1994; Cai, 2007), and on damage mechanics (Ghrib & Tinawi, 1995). With the exception of the plasticity model, the results are in agreement. The crack path illustrated in figure 2.22a is compared with those given in the previous references. All the crack paths are within a small bandwidth. The reservoir overflow increases compressive stresses on the downstream face of the dam and drives the crack downward. Figure 2.22b shows that overturning of the top part of the dam is the principal consequence of cracking in this region.

2.9 Discussion about the influence of the nonlocal interaction radius

The correct crack path for the reduced scale gravity dam (section 2.8.4) was predicted by modifying the procedure used to compute the nonlocal interaction radius. For that particular test,

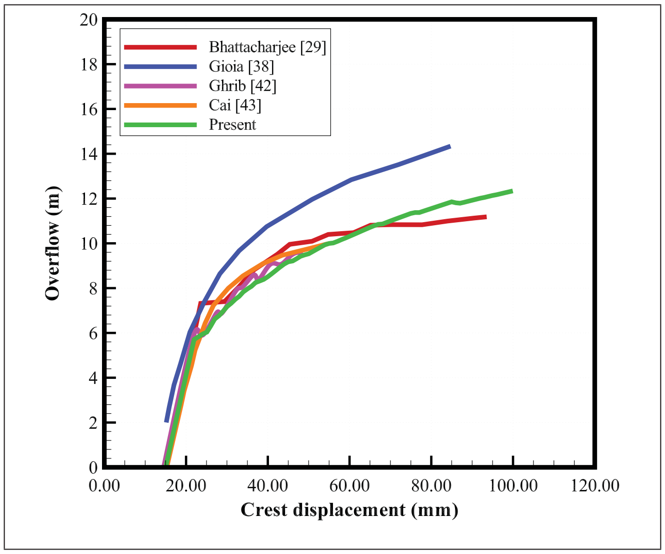

Figure 2.21 Load as a function of crest displacement

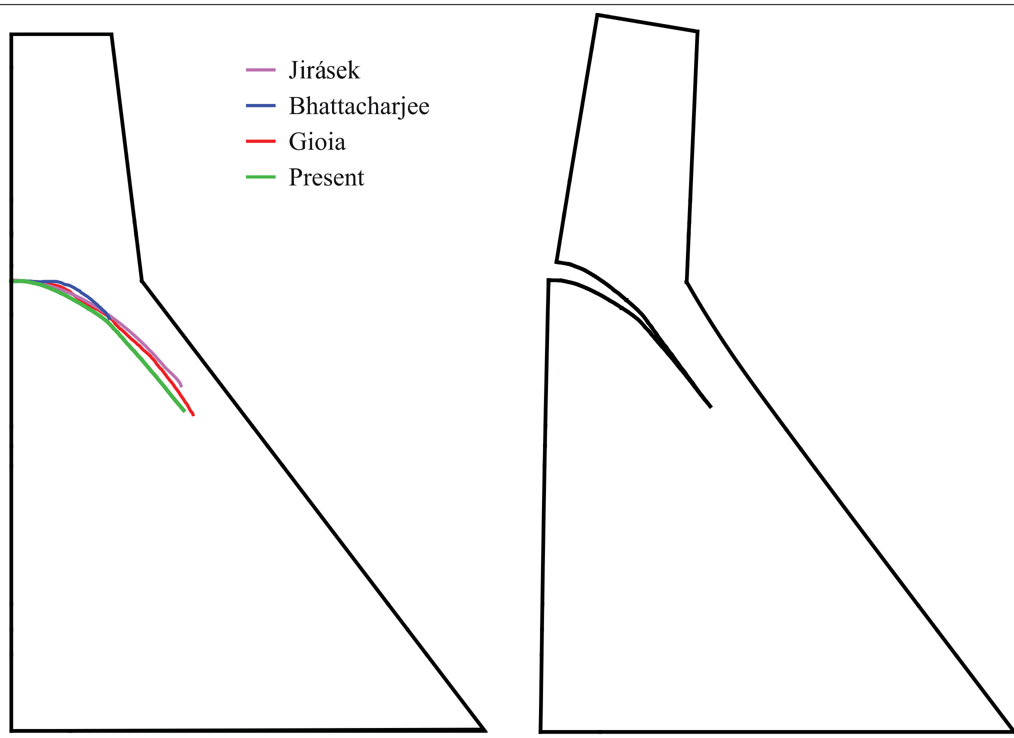

Figure (a) Crack path full scale gravity-dam

Figure (b) Deformed configuration of the full scale gravity-dam (amplified 100x)

Figure 2.22 Full scale gravity-dam results the results are dependent on the parameter R_a up to a certain limit. A constitutive model must be able to provide objective results. If a model does not provide objective results with regards to mesh refinement or some parameters, then it is impossible to rely on its results regarding its predictive capabilities. Thus, in this section, the influence of the nonlocal interaction radius will be discussed by comparing the crack paths computed with $R_a = 3d_a$ with those computed with $R_a = 12d_a$ for the examples presented earlier.

For the shear beam case, the crack paths computed with $R_a = 3d_a$ and $R_a = 12d_a$ and given in figure 2.23 are exactly the same as well as the failure loads. Thus, the results are fully independant on parameter R_a.

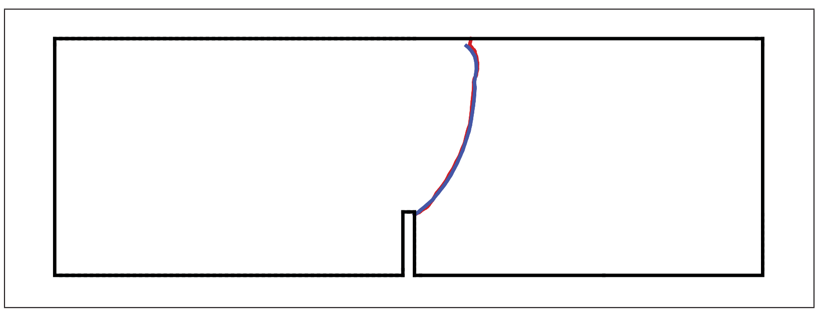

Figure 2.23 Crack path for the shear beam computed with $R_a = 3\ d_a$ (red) and $R_a = 12\ d_a$ (blue)

Similar to the previous case, the DEN specimen using loads configuration 4a (figure 2.24a), 4b (figure 2.24b) and 4c (figure 2.24c) obtained results nearly independant on the paramater R_a. However, when the crack is close to a boundary, the results are slightly different.

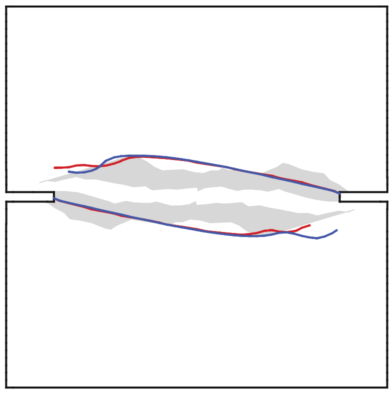

Figure (a) Crack path for the DEN specimen 4a computed with $R_a = 3\ d_a$ (red) and $R_a = 12\ d_a$ (blue)

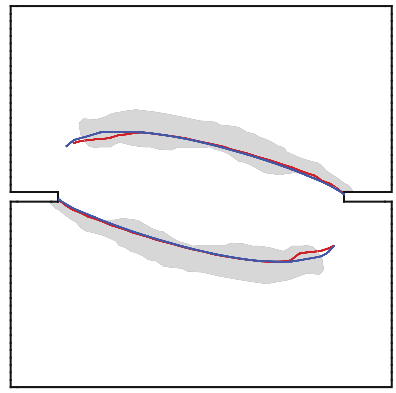

Figure (b) Crack path for the DEN specimen 4b computed with $R_a = 3\ d_a$ (red) and $R_a = 12\ d_a$ (blue)

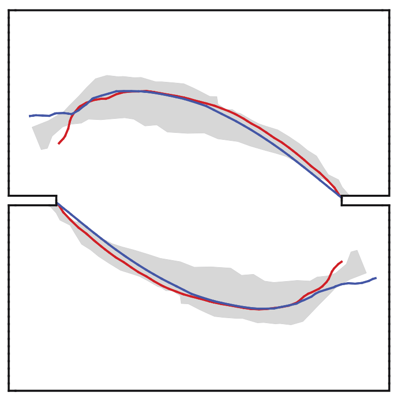

Figure (c) Crack path for the DEN specimen 4c computed with $R_a = 3\ d_a$ (red) and $R_a = 12\ d_a$ (blue)

Figure 2.24 Influence of the nonlocal interaction radius on the crack path for the DEN specimen

Finally, the effect of R_a on the crack path for the full scale gravity dam is given in figure 2.25. Similar to the shear beam, the crack path is fully independant on this parameter.

Based on these results and those obtained on the reduced scale gravity dam, the nonlocal interaction radius should be chosen as $R_a = 10d_a$ to obtain numerical results that are in agreement with the experimental results for all the validation examples presented. Although the interaction radius should be related to the microstructure of the material, a direct link to any measurable microscopic material property has not yet been estab1 :lished. As stated earlier, certain theories

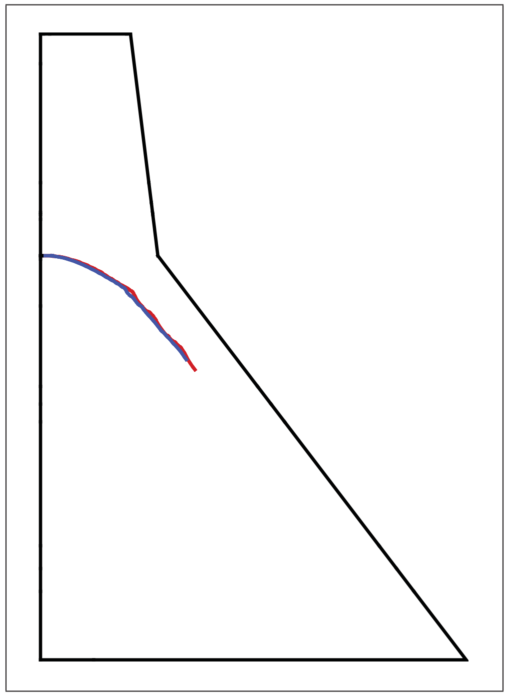

Figure 2.25 Crack path for the full scale gravity dam computed with $R_a = 3\ d_a$ (red) and $R_a = 12\ d_a$ (blue)

give a fixed ratio between R_a and the maximum aggregate size (Bažant & Cabot, 1989). Other studies suggest that this internal length scale is dependent on the stress or strain field in the neighbourhood of a point (Giry *et al.*, 2011). Other investigations indicate that the shape and width of the fracture process zone in concrete varies with the specimen size (Bažant & Ozbolt, 1990). From this study, the use of the stress based nonlocal method to predict the crack path shows that for large interaction radius the crack path converges to a single path, thus assessing the model predictive capabilities.

2.10 Conclusions

The crack model presented in this paper couples the benefits of the damage mechanics approach and the extended finite element method. Before transition occurs between the models, damage mechanics is used as a predictor for the determination of the crack path. A crack-tracking technique is developed to propagate the crack path along a single row of finite elements as a function of the stress-based nonlocal method. During transition from CDM to XFEM, energy conservation is enforced using mode I energy dissipation. The proposed model has shown the following features :

- The localized cracks predicted by the proposed tracking technique are consistent with the ones experienced in structures. The cracks develop along a single row of finite elements and a minimum level of damage diffusion is observed ;
- The transition to XFEM when the damage is significant alleviates the locking phenomenon often observed in smeared type models ;
- The model has the ability to predict the crack path with a damage mechanics model, and, because the rotating crack model is used, the crack direction can be corrected ;
- The crack paths and the ultimate loads predicted are independent of the mesh used ;
- The energy transfer between the continuum damage model and the cohesive XFEM model is approximated with a method that does not add additional parameters to the model ; and
- The validation examples have shown the efficiency and the robustness of the model.

It can be concluded that a nonlocal tracking algorithm coupled with an anisotropic damage model is a sufficient condition to avoid mesh-induced directional bias. Moreover, the absence of mode II fracture energy dissipation in the cohesive XFEM model does not affect the results in a significant manner. Finally, from the results obtained, the ideal values of d_{crit} should be between 0.6 and 0.7 to avoid spurious stress transfer.

Extension to the present model could include crack branching as well as the introduction of fluid pressure inside the cracks. For use in dam safety assessment, the introduction of the construction joints in the model could be formulated using the cohesive XFEM model. This would allow assessing whether safety factors are different than those computed with conventional gravity methods in the case where cracks plunge downwards, instead of spreading along construction joints.

2.11 Résumé et liens avec la problématique de recherche

Cet article répond partiellement à la première problématique de la thèse qui est d'établir une méthode afin de résoudre des problèmes tridimensionnels de propagation de fissures en formulant un modèle de fissure qui couple les avantages de l'approche de la mécanique continue de l'endommagement avec ceux de la méthode des éléments finis étendus. Le chapitre a présenté le développement bidimensionnel d'une nouvelle méthode numérique pour représenter la fissuration en intégrant la mécanique non linéaire de la rupture à l'aide d'un modèle de fissuration diffuse dans la zone d'élaboration de la fissure avec un modèle XFEM dans la zone où il y a coalescence des microfissures. Avant que la transition se produise entre les deux modèles, la mécanique continue de l'endommagement est utilisée comme prédicteur afin de déterminer la trajectoire de fissure. Lors de la transition, la conservation d'énergie est appliquée en assurant que la dissipation d'énergie en mode I est conservée. Ce modèle a démontré une très bonne capacité à reproduire les trajectoires de fissures ainsi que les courbes de résultats expérimentaux pour de nombreux cas de simulation. De plus, il a été démontré que ces résultats sont indépendants du maillage utilisé, confirmant l'objectivité du modèle. Afin de répondre entièrement à la première problématique soulevée dans la thèse et à satisfaire la seconde problématique, le modèle est étendu en 3D dans le chapitre suivant ou il est question de modéliser la fissuration hydromécanique fortement couplée dans des structures tridimensionnelles en béton de grandes dimensions en utilisant l'approche proposée dans le chapitre 2.

CHAPITRE 3

STRONGLY COUPLED XFEM FORMULATION FOR NON-PLANAR THREE-DIMENSIONAL SIMULATION OF HYDRAULIC FRACTURING WITH EMPHASIS ON CONCRETE DAMS

Simon-Nicolas Roth[1], Pierre Léger[2], Azzeddine Soulaïmani[3]

[1] Hydro-Québec, 75 boul. René-Lévesque Ouest, Montréal, Québec, Canada, H2Z 1A4
[2] École Polytechnique de Montréal, Department of Civil, Geological and Mining Engineering, C.P. 6079, succ. Centre-Ville, Montréal Québec, Canada, H3C 3A7
[3]École de Technologie Supérieure, Department of Mechanical Engineering, 1100, rue Notre-Dame Ouest, Montréal, Québec, Canada, H3C 1K3

Article publié dans la revue « Computer Methods in Applied Mechanics and Engineering » en mai 2020.

3.1 Abstract

This paper presents a novel and robust three-dimensional plain concrete cracking model applicable to the study of structural stability of large structures, such as dams, while considering the presence of pressurized water in propagating cracks. When leaving the elastic range, there is a transition from a continuum approach to a XFEM approach. This mechanical model is coupled with a poro-damage model where the permeability is increased as micro-cracks coalesce into macro-cracks. The crack opening computation during continuum damage is based on a local XFEM formulation without the need for a reference length in a strongly coupled hydro-mechanical formulation to update the uplift pressures. The 3D crack path computation is adapted from an analogy to the heat conduction problem to draw the envelope of the discontinuities' tangent vector field. Six benchmark problems available from the literature, including a 96m-high arch dam, are considered and indicate the very good performance of the proposed model as well as its applicability to real industrial structures.

Keywords : Plain concrete, 3D crack propagation, XFEM, Continuum damage, Hydro-mechanical coupling, Hydrofracturation, Dam

3.2 Introduction

In recent years, different numerical approaches have been proposed for the solution of crack representation and propagation. Within the framework of the FEM, there are two approaches, namely discrete and diffuse, to represent the discontinuity. In the discrete models, the crack is a geometric discontinuity. This can be modeled explicitly by an interface element (Dechaumphai *et al.*, 2003), which separates two solid elements. As the interface moves, the mesh should be adapted, which requires powerful adaptive meshing techniques (Dechaumphai *et al.*, 2003; Areias *et al.*, 2016; Bouchard *et al.*, 2003), especially for 3D problems. In implicit discontinuity models such as in the extended finite element method (XFEM) (Moës *et al.*, 1999), the crack is tracked by using a level set function while the mesh is fixed ; the zero-level represents the discontinuity. The elements crossed by this interface have their displacements interpolations enriched by discontinuous functions thanks to the partition of unity method (Babuška & Melenk, 1997). In (Rabczuk *et al.*, 2007) a local partition of unity enriched mesh-free method is developed to simulate crack initiation and propagation (including joining cracks) in non-linear three-dimensional solids.

In the diffuse crack models such as phase-field methods (PFM), a scalar field variable is introduced to : first, distinguish between the damaged and the undamaged phases and second, track the crack paths by an evolution equation over a fixed mesh (Bourdin *et al.*, 2008, 2000; Francfort & Marigo, 1998; Miehe *et al.*, 2016, 2010). The phase-field approach has received a great interest in the recent years due to its appealing advantages : crack initiation, propagation, multiple joining and branching are automatically determined. A review on phase-fields models can be found in (Ambati *et al.*, 2015; Hirshikesh *et al.*, 2019). However, these models are computationally demanding as they require extremely fine meshes to resolve accurately the diffused crack (Patil *et al.*, 2018) and because the staggered numerical algorithms typically used are slowly converging (Ambati *et al.*, 2015). A hybrid XFEM-Phase field method is proposed in (Giovanardi *et al.*, 2017), where XFEM and phase-field method are coupled to simulate crack propagation in brittle materials. The discrete element method has been also proposed to crack propagation and branching for brittle biopolymers (Hedjazi *et al.*, 2012).

Large 3D plain concrete structures, such as dams, must be assessed for structural safety, considering crack initiation and non-planar propagation in the presence of pressurized water under usual, unusual and extreme loads. For these structures, the failure mode is most often triggered by a few dominant discrete cracks. Robust and efficient algorithms are required to track and characterize discontinuities' opening as they evolve from micro cracks into the continuum to discrete cracks. Without the a priori knowledge of the crack location, an efficient strategy to avoid remeshing and to follow crack propagation is the XFEM. 3D XFEM constitutive models for concrete structures were proposed in (Fries & Baydoun, 2011; Linder & Zhang, 2013), and 3D XFEM algorithms have also been proposed in the context of hydro-fracturing (Becker *et al.*, 2010; Gordeliy *et al.*, 2018). Even though the results presented in the literature are applied to 3D problems, the XFEM has not been applied to quasi-brittle material problems of significant size, such as those encountered in industrial context.

One objective of this paper is to extend to 3D our previous work (Roth *et al.*, 2015c) combining damage mechanics with the XFEM to characterize the discontinuity permeability and hydraulic conductivity. Another objective is to improve crack opening computation during continuum damage by using a local XFEM formulation. The advantage of this novel approach is that there is no need for a reference length at the element level. A key aspect to implement the XFEM is to have an efficient discontinuity tracking strategy. Several algorithms have been proposed to define the discontinuity geometry at the element level and to track nonplanar crack surfaces in 3D (Gravouil *et al.*, 2002; Oliver *et al.*, 2002; Gasser & Holzapfel, 2005; Sukumar *et al.*, 2008; Ferté *et al.*, 2016). However, most of these algorithms were only validated using small test problems. We show that it is possible to adapt the marching cube algorithm in combination with the solution of a global analogous heat conduction problem at each mechanical step to effectively draw the envelope of the discontinuities' tangent vector field where the crack path exhibits fairly sharp changes of direction. The third objective is to apply the XFEM to a complex large-scale 3D cracking problem. To this end, the simulation of an arch dam is considered to demonstrate that the proposed method is applicable to a complex large-scale cracking problem.

This paper is organized as follows. In section 3.3 we consider fluid transport in a porous continuum and the discontinuities with which to develop the matrix form of the coupled hydro-mechanical formulation. Section 3.4 describes the 3D strategy utilized to perform the transition from the continuum damage mechanics to the XFEM formulation. Section 3.6 proposes a novel approach to compute crack openings in the continuous damage model using a local XFEM solution. Section 3.5.2 presents the implementation of the marching cube algorithm to define the surface discontinuity within a finite element. Section 3.5.1 develops the algorithm for non-planar crack path computation using the global solution of an analogous heat conduction problem to draw the envelope of the discontinuities' tangent vector field. A Unified Modeling Language activity diagram summarizing the global solution algorithm using Newton-Raphson iteration for a typical load step is given in section 3.7. Section 3.8 first compares the load-displacement response and crack patterns from the proposed computational framework with three 3D small-scale plain concrete benchmark problems available in the literature. The computed crack pattern for a large scale 96m high arch dam, for which the model test data are available, are then presented to demonstrate the very good performance of the proposed solution strategy for real industrial structures. Section 3.9 presents the solutions of a wedge splitting test problem in the presence of pressurized water for structured and unstructured meshes to show the robustness and objectivity of the formulation in hydro-fracturing simulations. Finally, the computed hydro-mechanical response of a 41m high masonry dam is compared with previously published results.

3.3 Coupled hydro-mechanical problem

The Biot model of a porous material saturated with a fluid assumes that the solid skeleton is permeated by an interconnected network of pores filled with a moving fluid. The description of stress in the fluid is limited to its hydrostatic component. Therefore, the total stress σ in Voigt notation is related to the effective stress σ' and to the liquid pressure p such that :

$$\sigma = \sigma' - \mathbf{m}p \tag{3.1}$$

$\mathbf{m}$ is defined for isotropic behavior as $\mathbf{m}^T = b\{1\ 1\ 1\ 0\ 0\ 0\}$, with $b\,(0 \leq b \leq 1)$ the Biot coefficient. Because the main application of this work is to model hydromechanical problems applied to dam engineering, it is assumed that there is an infinite amount of water in contact with the material. Therefore, the coupled hydro-mechanical problem can be expressed in terms of balances of momentum and fluid mass for steady state pressure in Ω as follows :

$$\nabla \cdot \sigma + \mathbf{b} = 0 \tag{3.2}$$

$$\nabla \cdot \mathbf{v} = 0 \tag{3.3}$$

where Ω denotes the computed domain ($\Omega \subset \mathbb{R}^n$), σ is the Cauchy stress tensor, $\mathbf{b}$ are the body loads and $\mathbf{v}$ is the fluid velocity vector. The following boundary conditions are added to complete the mathematical description of the poroelastic problem :

$$\begin{aligned} \mathbf{u} &= \mathbf{u}_b && \text{on } \Gamma_u \\ p &= p_b && \text{on } \Gamma_p \\ \sigma \cdot \mathbf{n}_t &= \bar{\mathbf{t}} && \text{on } \Gamma_t \\ \sigma \cdot \mathbf{n}_d &= \mathbf{t}_d && \text{on } \Gamma_d \end{aligned} \tag{3.4}$$

where Γ_u, Γ_p, Γ_t and Γ_d are respectively the boundaries having displacements, pressure, traction and traction in the discontinuities imposed. In the presence of a discontinuity, equation (3.2) is solved using a combined XFEM-damage mechanics approach (Roth *et al.*, 2015c) for which the three dimensional formulation is given in section 3.4.

The transport process with regard to the averaged motion of the fluid involves molecular diffusion. The molecular diffusion and viscous flow are dissipative. The positivity of the dissipation associated with the viscous flow of the fluid through the porous solid can be written in the form ($-\nabla p \cdot \mathbf{v} \geq 0$) (Coussy, 2010). The fluid movement is governed by the law relating the velocity vector $\mathbf{v}$ to the driving force $-\nabla p$ producing the flow. Linearly relating $\mathbf{v}$ to $-\nabla p$ and neglecting body loads is the simplest form that this law can take and leads to the expression of

Darcy's law :

$$\mathbf{v} = -\mathbf{K}\nabla p, \tag{3.5}$$

where $\mathbf{K} = \delta_{ij}k/\mu$ is the permeability coefficient matrix, in which k is the intrinsic permeability and μ the fluid viscosity. Hence, the fluid transport in the interstitial space, defined as $\Omega\backslash\Omega_c$, where Ω_c are the discontinuities channels, is described by replacing the velocity in the continuity equation (3.3) by Darcy's law leading to :

$$\nabla \cdot (-\mathbf{K}\nabla p) = 0 \ \in \Omega\backslash\Omega_c \tag{3.6}$$

3.3.1 Weak form of the coupled hydro-mechanical problem

The displacements of the solid and the interstitial pressure are the unknowns of the problem. Therefore, two trial function spaces, $\mathscr{U}$ and $\mathscr{P}$ and two weighting function spaces, $\delta\mathscr{U}$ and $\delta\mathscr{P}$ are introduced as follows :

$$\begin{aligned}
\mathscr{U} &= \{\mathbf{u} \mid \mathbf{u} \in W^1, \mathbf{u} = \mathbf{u}_b \text{ on } \Gamma_u\},\\
\mathscr{P} &= \{p \mid p \in W^1, p = p_b \text{ on } \Gamma_p\},\\
\delta\mathscr{U} &= \{\delta\mathbf{u} \mid \delta\mathbf{u} \in W^1, \delta\mathbf{u} = 0 \text{ on } \Gamma_u\},\\
\delta\mathscr{P} &= \{\delta p \mid \delta p \in W^1, \delta p = 0 \text{ on } \Gamma_p\}
\end{aligned} \tag{3.7}$$

where $W^1 = H^1(\Omega\backslash\Gamma_d)$ is a first order Sobolev space of functions. Using the Galerkin method to construct the approximation of the weak form, the trial spaces $\mathscr{U}$ and $\mathscr{P}$ and the weighting spaces $\delta\mathscr{U}$ and $\delta\mathscr{P}$ are replaced respectively by their finite approximation $\mathscr{U}^h$, $\mathscr{P}^h$, $\delta\mathscr{U}^h$ and $\delta\mathscr{P}^h$. Hence, $\mathbf{u}$, p, $\delta\mathbf{u}$ and δp are replaced in the weak form by their approximations $\mathbf{u}^h \in \mathscr{U}^h$, $p^h \in \mathscr{P}^h$, $\delta\mathbf{u} \in \delta\mathscr{U}^h$ and $\delta p \in \delta\mathscr{P}^h$, respectively. Using the Bubnov-Galerkin method, the trial functions and the test functions are discretized in the same space, therefore, the matrix form requires the representation of $\mathbf{u}^h$, p^h in terms of shape functions such that :

$$\begin{aligned} \mathbf{u}^h &= \mathbf{N}\bar{\mathbf{u}} \\ p^h &= \mathbf{N}p \end{aligned} \tag{3.8}$$

Accordingly, the gradients of $\mathbf{u}^h$ and p^h are given by :

$$\begin{aligned} \nabla\mathbf{u}^h &= \mathbf{B}\bar{\mathbf{u}} \\ \nabla p^h &= \mathbf{H}p \end{aligned} \tag{3.9}$$

Within the framework of the extended finite element method, discontinuities can be modelled by enriching the displacement interpolation of the element crossed by the discontinuity with special purpose functions and by introducing an additional unknown $\hat{\mathbf{u}}$ to the problem :

$$\mathbf{u}^h = \sum_{\forall I} N_I \bar{\mathbf{u}}_I + \sum_{J \in S_H} N_J \psi_J(\phi_\xi)\hat{\mathbf{u}}_J \tag{3.10}$$

with $\bar{\mathbf{u}}$ the standard displacement degrees of freedom of the problem, and $\hat{\mathbf{u}}$ the additional degrees of freedom. The variable ϕ_ξ is the level-set function evaluated at the natural coordinate ξ and S_H represents the set of nodes that are enriched because the discontinuity passes through the element to which they belong. To represent a strong discontinuity such as a crack, the Heaviside function ($\mathscr{H}$) can be used for $\psi(\phi)$:

$$\mathscr{H}(\phi) = \begin{cases} 1, & \phi > 0 \quad (\text{in } \Omega^+ \subset \Omega) \\ 0, & \text{else} \quad (\text{in } \Omega^- \subset \Omega) \end{cases} \quad \Omega = \Omega^+ \cup \Omega^- \tag{3.11}$$

To treat differently only those elements crossed by the discontinuity and avoid blending elements, the enrichment function is shifted so that the product of the shape function N_J and the enrichment function cancels out at each node such that :

$$\psi_J(\phi) = [\mathscr{H}(\phi) - \mathscr{H}(\phi_J)] \tag{3.12}$$

with ϕ_J the level-set function of node J. With the additional degrees of freedom, the admissible test function $\delta\mathbf{u}$ is decomposed into two independent admissible test functions :

$$\delta\mathbf{u} = \delta\bar{\mathbf{u}} + \mathscr{H}\delta\hat{\mathbf{u}} \tag{3.13}$$

The weak form of the problem is obtained by multiplying equation 3.1 by δu and integrating over Ω, where Ω is an open subset of R^n :

$$\int_{\Omega} (\delta\bar{\mathbf{u}} + \mathscr{H}\delta\hat{\mathbf{u}})\,(\nabla\cdot\sigma + \mathbf{b})\ \mathrm{d}\Omega = 0 \tag{3.14}$$

Applying the divergence theorem for the discontinuous problems, the following set of equations can be obtained

$$\begin{aligned}
\int_{\Omega} \nabla\delta\bar{\mathbf{u}} : \sigma\ \mathrm{d}\Omega &= \int_{\Gamma} \delta\bar{\mathbf{u}}\cdot\bar{\mathbf{t}}\ \mathrm{d}\Gamma + \int_{\Omega} \delta\bar{\mathbf{u}}\cdot\mathbf{b}\ \mathrm{d}\Omega \\
\int_{\Omega^\star} \nabla\delta\hat{\mathbf{u}} : \sigma\ \mathrm{d}\Omega^\star + \int_{\Gamma_d} \delta\hat{\mathbf{u}}\cdot\mathbf{t}_d\ \mathrm{d}\Gamma_d &= \int_{\Gamma} (\mathscr{H}\delta\hat{\mathbf{u}})\cdot\bar{\mathbf{t}}\ \mathrm{d}\Gamma + \int_{\Omega^\star} \delta\hat{\mathbf{u}}\cdot\mathbf{b}\ \mathrm{d}\Omega^\star
\end{aligned} \tag{3.15}$$

It must be noted that $\mathscr{H}$ has been eliminated by changing the integration domain from Ω to $\Omega^\star$, and $\Omega^\star$ is the set of enriched discontinuous elements.

3.3.2 Fluid transport

To complete the mathematical description, the weak form of equation 3.6 must be defined. The pressure field in the discontinuity can be modeled by enriching the pressure to take into account its discontinuity across Γ_d (Abellan *et al.*, 2005). This discontinuity arises from the leak-off of the fluid from the discontinuity towards the surrounding medium through its surface boundaries. One can also assume that no membrane effect exists meaning that the permeability of the discontinuity surfaces is infinite. For this case, $p^+ = p^-$, therefore the pressure field is continuous across the Ω^+ and Ω^- domains (Armero & Callari, 1999; Jox *et al.*, 2006). With the assumptions that there is a large amount of water in contact with the discontinuity and that the fluid percolation time in the discontinuity is negligible compared to the life of the structure, pressure continuity will be assumed. Therefore, the weak form of the continuity equation including the bulk material and the crack channel is given by :

$$\int_{\Omega\backslash\Omega_c} (\nabla\delta p \cdot \mathbf{K}\nabla p)\ \mathrm{d}\Omega + \int_{\Omega_C} \left(\nabla\delta p \cdot \mathbf{m}_{\Gamma_d}\right) \frac{k_{cr}}{\mu} \left(\nabla p \cdot \mathbf{m}_{\Gamma_d}\right)\ \mathrm{d}\Omega_C = 0 \tag{3.16}$$

where μ the fluid viscosity, k_{cr} is given by equation 3.43, $\nabla p \cdot \mathbf{m}_{\Gamma_d}$ is th gradient in the direction of the channel, $\mathbf{m}_{\Gamma_d}$ is the orientation of the channel defined in equation 3.40, and Ω_C is the discontinuity channel. The first term of this equation correspond to the flow in the bulk material, while the last term is the flow in the crack channel.

In addition, this form of the continuity equation will be developed for the flow in damaged material in the presence of microcracks in section 3.4.4.

3.3.3 Matrix form

Replacing the trial spaces $\mathbf{u}$, p and the weighting spaces $\delta\mathbf{u}$ and δp in the weak form with the shape function of their approximations $\mathbf{u}^h$ and p^h leads to :

$$\begin{gathered}
\int_{\Omega} \mathbf{B}^{\mathrm{T}}\sigma\ \mathrm{d}\Omega = \int_{\Gamma} \mathbf{N}^{\mathrm{T}}\bar{\mathbf{t}}\ \mathrm{d}\Gamma + \int_{\Omega} \mathbf{N}^{\mathrm{T}}\mathbf{b}\ \mathrm{d}\Omega \\
\int_{\Omega^\star} \mathbf{B}^{\mathrm{T}}\sigma\ \mathrm{d}\Omega^\star + \int_{\Gamma_d} \mathbf{M}^{\mathrm{T}}\mathbf{t}_d\ \mathrm{d}\Gamma_d = \int_{\Gamma} \mathscr{H}\mathbf{N}^{\mathrm{T}}\bar{\mathbf{t}}\ \mathrm{d}\Gamma + \int_{\Omega^\star} \mathbf{N}^{\mathrm{T}}\mathbf{b}\ \mathrm{d}\Omega^\star \\
\int_{\Omega\backslash\Omega_c} \mathbf{H}^T\mathbf{K}\mathbf{H}^T\ \mathrm{d}\Omega + \int_{\Omega_C} \mathbf{H}^T\mathbf{m}_{\Gamma_d}^T \frac{k_{cr}}{\mu}\mathbf{m}_{\Gamma_d}\mathbf{H}\ \mathrm{d}\Omega_C = 0
\end{gathered} \tag{3.17}$$

in which $\mathbf{M}$ comprises the shape functions $\mathbf{N}$ evaluated on Γ_d. Substituting the stress relation 3.1 in the preceeding system of equations, thereby decoupling the total stress in effective stress and liquid pressure, leads to the formulation of the global discrete system of an enriched element :

$$\begin{bmatrix} \int_{\Omega} \mathbf{B}^{\mathrm{T}}\mathbf{C}_d^{(g)}\mathbf{B}\,\mathrm{d}\Omega & \int_{\Omega^\star} \mathbf{B}^{\mathrm{T}}\mathbf{C}_d^{(g)}\mathbf{B}\,\mathrm{d}\Omega^\star & \int_{\Omega} \mathbf{B}^{\mathrm{T}}\mathbf{m}^T\mathbf{N}\,\mathrm{d}\Omega \\ \int_{\Omega^\star} \mathbf{B}^{\mathrm{T}}\mathbf{C}_d^{(g)}\mathbf{B}\,\mathrm{d}\Omega^\star & \int_{\Omega^\star} \mathbf{B}^{\mathrm{T}}\mathbf{C}_d^{(g)}\mathbf{B}\,\mathrm{d}\Omega^\star + \int_{\Gamma_d} \mathbf{M}^{\mathrm{T}}\mathbf{T}\mathbf{M}\,\mathrm{d}\Gamma_d & \int_{\Omega^\star} \mathbf{B}^{\mathrm{T}}\mathbf{m}^T\mathbf{N}\,\mathrm{d}\Omega^\star \\ 0 & 0 & \int_{\Omega\backslash\Omega_c} \mathbf{H}^T\mathbf{K}\mathbf{H}^T\,\mathrm{d}\Omega + \int_{\Omega_C} \mathbf{H}^T\mathbf{m}_{\Gamma_d}^T\frac{k_{cr}}{\mu}\mathbf{m}_{\Gamma_d}\mathbf{H}\,\mathrm{d}\Omega_C \end{bmatrix}$$

$$\begin{Bmatrix} \bar{\mathbf{u}} \\ \hat{\mathbf{u}} \\ p \end{Bmatrix} = \begin{Bmatrix} f_{\bar{u}}^{ext} + f_{\bar{u}}^{body} \\ f_{\hat{u}}^{ext} + f_{\hat{u}}^{body} \\ 0 \end{Bmatrix} \tag{3.18}$$

where $f_{\bar{u}}^{ext}$ and $f_{\hat{u}}^{ext}$ contain the external loads and $f_{\bar{u}}^{body}$ and $f_{\hat{u}}^{body}$ contain the body loads. $\mathbf{T}$ contains the cohesive force and is detailed in section 3.4.2. The stress-strain constitutive relation $\mathbf{C}_d^{(g)}$ which takes into account the material damage is defined in section 3.4.1. To achieve the coupling between the fracture and the porous medium, the interfacial force vector f^{int} due to the fluid pressure exerted on the discontinuity faces can be discretized as :

$$f_{\hat{u}}^{int} = -\int_{\Gamma_d} \mathscr{H}\mathbf{N}^T p \cdot \mathbf{n}_{\Gamma_d}\,\mathrm{d}\Gamma_d \tag{3.19}$$

3.4 Three-dimensional discontinuity model using a transition from CDM to XFEM

A strategy based on a transition from a continuum approach to a kinematic XFEM approach for cohesive crack propagation is used. This process allows the benefits of the continuum damage approach to be combined with the benefits of the cohesive extended finite element method. The regularized local anisotropic continuum damage approach (Roth *et al.*, 2015c) is used to describe the first stage of the fracture process zone (FPZ) formation. When the damage has reached a critical value, a switch to the cohesive XFEM model is achieved by ensuring that the energy that remains to be dissipated by the continuous damage model (CDM) is transferred to the XFEM model. The model has the benefit of not adding any additional parameters during the energy transfer between the CDM and the cohesive XFEM models.

3.4.1 Continuous damage model

The non-linear behavior of concrete under monotonic loading is described using an anisotropic formulation. The behavior of a damaged material results in the constitutive relations of an undamaged material in which the usual stress is replaced by the effective stress by invoking the principle of energy equivalence (Cordebois & Sidoroff, 1982). The effective stress $\tilde{\sigma}$ is defined as :

$$\tilde{\sigma} = \mathbf{D}^{-1}\sigma \tag{3.20}$$

where $\mathbf{D}$ is an anisotropic damage tensor with its index in each damage direction equal to zero when the material is undamaged, and equal to one when it is completely damaged. With the energy equivalence concept, the local damaged constitutive tensor $\mathbf{C_d}^{(l)}$ is given by :

$$\mathbf{C_d}^{(l)} = \mathbf{D}^{-1}\mathbf{C_0}\left(\mathbf{D}^{-1}\right)^T \tag{3.21}$$

where $\mathbf{C_0}$ is the undamaged stress-strain constitutive relation tensor. The damage tensor is a function of the internal scalars κ_i ($i \in [1,3]$). This parameter initially equals the damage threshold r_0 and is defined as the largest recorded value of the principal strains ε_i^{avg} during the damage process. This evolution is governed by the Kuhn-Tucker condition, given as a loading function f_i such that :

$$f_i\left(\varepsilon_i^{avg}, \kappa_i\right) = \varepsilon_i^{avg} - \kappa_i \tag{3.22}$$

Loading is indicated by $f_i \geq 0$ and unloading by $f_i < 0$. The unloading behavior can be modeled using the secant stiffness $\mathbf{C_d}$. Damage is initiated when a tensor norm is greater than the initial threshold r_0. One suitable norm that considers the effect of compressive strains (Paas *et al.*, 1993; Ghrib & Tinawi, 1995) can be written as follows :

$$\bar{\varepsilon} = \sqrt{\sum_{i=1}^{3} \left(\langle \varepsilon_i^{av} \rangle^2 + m \langle -\varepsilon_i^{av} \rangle^2 \right)} \tag{3.23}$$

where $\langle \ldots \rangle$ are the Macaulay brackets : $\langle \varepsilon_i^{av} \rangle = \varepsilon_i^{av}$ if $\varepsilon_i^{av} > 0$, $\langle \varepsilon_i^{av} \rangle = 0$ if $\varepsilon_i^{av} < 0$ and $m = \left(\frac{f_t}{f_c}\right)^2$ with f_t, the tensile strength, f_c the compressive strength and ε_i^{av} is defined in equation 3.31.

The damage evolution law is proposed in (Gunn, 1998) :

$$d = 1 - \sqrt{\frac{r_0}{\bar{\varepsilon}} \exp\left(-R\left(\bar{\varepsilon} - r_0\right)\right)} \tag{3.24}$$

where $r_0 = \frac{f_t}{E_0}$ is the initial threshold defined in terms of the tensile strength and the elastic modulus E_0. Mesh objectivity requirements are satisfied adequately by introducing a regularization based on the energy equivalence. Thus, the derivation of R in equation (3.24) is done so that it satisfies the mesh objectivity requirements and is defined as :

$$R = \frac{2E_0 f_t l_{rve}}{2E_0 G_F - {f_t}^2 l_{rve}} \geq 0 \tag{3.25}$$

where G_F is the fracture energy and l_{rve} is the representative volume element characteristic length. To satisfy the requirements that $R \geq 0$, l_{rve} must be smaller than $l_{\text{rve}} \leq \frac{2E_0 G_F}{{f_t}^2}$.

The damage evolution is based on the principal strains exceeding the damage threshold r_0 :

$$\text{if } \kappa_i > r_0 \text{ then } d_i = d \qquad i \in [1,3] \tag{3.26}$$

The anisotropic damage tensor (Gunn, 1998) can now be defined by :

$$\mathbf{M} = \begin{bmatrix} M_{11}^{-1} & 0 \\ 0 & M_{22}^{-1} \end{bmatrix} \tag{3.27}$$

with

$$M_{11}^{-1} = \begin{bmatrix} (1-d_1)^2 & (1-d_1)(1-d_2) & (1-d_1)(1-d_3) \\ (1-d_1)(1-d_2) & (1-d_2)^2 & (1-d_2)(1-d_3) \\ (1-d_1)(1-d_3) & (1-d_2)(1-d_3) & (1-d_3)^2 \end{bmatrix}, \qquad M_{22}^{-1} = \begin{bmatrix} \chi_{12} & 0 & 0 \\ 0 & \chi_{23} & 0 \\ 0 & 0 & \chi_{13} \end{bmatrix}$$

$$\chi_{ij} = \frac{2(1-d_i)^2(1-d_j)^2}{(1-d_i)^2+(1-d_j)^2}$$

Damage in either of the principal directions leads to a reduction of the shear resistance by the scalar coefficient χ similar to that found in smeared crack models. The damage tensor is valid in the local reference frame (aligned with the principal strains directions). Hence, in the global reference frame, this tensor must be rotated by the transformation matrix given by :

$$\mathbf{T} = \begin{bmatrix} l_1^2 & m_1^2 & n_1^2 & l_1m_1 & m_1n_1 & l_1n_1 \\ l_2^2 & m_2^2 & n_2^2 & l_2m_2 & m_2n_2 & l_2n_2 \\ l_3^2 & m_3^2 & n_3^2 & l_3m_3 & m_3n_3 & l_3n_3 \\ 2l_1l_2 & 2m_1m_2 & 2n_1n_2 & l_1m_2+l_2m_1 & m_1n_2+n_1m_2 & l_1n_2+l_2n_1 \\ 2l_2l_3 & 2m_2m_3 & 2n_2n_3 & l_2m_3+l_3m_2 & m_2n_3+n_2m_3 & l_2n_3+l_3n_2 \\ 2l_1l_3 & 2m_1m_3 & 2n_1n_3 & l_1m_3+l_3m_1 & m_1n_3+n_3m_1 & l_1n_3+l_1n_3 \end{bmatrix} \tag{3.28}$$

with $\{l_i, m_i, n_i\}$ the cosines of the i^{th} eigen vector. The transformation of the damaged constitutive tensor from the local to the global reference frame is given by :

$$\mathbf{C}_d^{(g)} = \mathbf{T}^{\mathrm{T}}\mathbf{C}_d^{(l)}\mathbf{T} \tag{3.29}$$

Finally, the damage is considered to be distributed on a representative volume element l_{rve}. Therefore, this measure is given by the relation :

$$l_{\mathrm{rve}} = \sqrt[3]{V_e} = \sqrt[3]{\sum_{i=1}^{n_{int}} w_i \det{}_i} \tag{3.30}$$

where V_e is the element volume, n_{int} the number of integration points, w the weight and det the determinant associated with the Gauss point. Similarly, the strain tensor ε is averaged over the volume and given by :

$$\varepsilon^{av} = \frac{1}{V_e} \int_{\Omega_e} \varepsilon \, \mathrm{d}\Omega \simeq \frac{\sum_{i=1}^{n_{int}} \varepsilon_i w_i \det_i}{\sum_{i=1}^{n_{int}} w_i \det_i} \tag{3.31}$$

Using eigen decomposition, ε^{av} is decomposed to obtain the principal strains noted as ε_i^{avg}. These averaged principal strains are used to evaluate the loading/unloading function (3.22).

3.4.2 Cohesive forces in the discontinuity

The computation of the cohesive forces is based on (Tvergaard, 2003; Unger *et al.*, 2007). The normal T_n and the tangential T_t forces along the interface are evaluated considering that the interface constitutive relations are derived from a potential specified by :

$$\phi(u_n, u_t) = \int_0^{\lambda} \sigma(\lambda') \, \mathrm{d}\lambda' \tag{3.32}$$

where $\sigma(\lambda')$ is the traction separation relation and λ is introduced such that :

$$\lambda = \sqrt{u_n^2 + (\alpha u_t)^2} \tag{3.33}$$

with u_n and u_t respectively the normal opening and the tangential sliding of the discontinuity surface and where α is a material parameter that controls the weighting between the normal and tangential openings. Using parameter λ a loading/unloading function can be defined as :

$$f(\lambda, \kappa(t)) = \lambda - \kappa(t), \text{ with } \kappa(t) = \max_{\tau \leq t} (\lambda(\tau)) \tag{3.34}$$

where $\kappa(t)$ is an internal variable characterizing the maximum value of parameter λ reached in the history of the interface. Using the potential defined earlier, the normal and tangential forces per unit area can be defined as :

$$
\begin{aligned}
T_n &= \frac{\partial \phi(u_n, u_t)}{\partial u_n} = \sigma\left(\kappa(t)\right)\frac{u_n}{\kappa(t)} \\
T_t &= \frac{\partial \phi(u_n, u_t)}{\partial u_t} = \sigma\left(\kappa(t)\right)\frac{\alpha^2 u_t}{\kappa(t)}
\end{aligned}
\tag{3.35}
$$

The relations 3.35 apply if $f(\lambda, \kappa(t)) \geq 0$ corresponding to a loading condition. If $f(\lambda, \kappa(t)) < 0$ corresponding to unloading, a linear elastic path is used to represent the partly damaged interface. In this case $\kappa(t)$ is the largest reached scalar value as given by 3.34. Finally, if contact occurs ($u_n \approx 0$), the contact condition is approximated by a penalty stiffness :

$$
T_n = K_p u_n \tag{3.36}
$$

and frictional sliding at the interface is given by :

$$
T_t = -\operatorname{sign}(\dot{u}_t)\tan(\phi)\,T_n \tag{3.37}
$$

where ϕ is the friction angle of concrete. As specified in (Unger *et al.*, 2007), the assumption that equivalent fracture energies for mode I and mode II is considered. Fracture energy in mode I is a well-defined parameter. It is generally accepted that mode II fracture energy is greater than that of mode I by a ratio of between 20 and 25 (Reinhardt & Xu, 2000; Bažant & Pfeiffer, 1986). This includes the energy required to create the inclined tensile micro cracks in the FPZ as well as the energy required to break the shear resistance due to aggregate interlock and other asperities on rough crack surfaces behind the crack front. The assumption that mode I and mode II energies are equivalent is therefore on the conservative side.

The traction-separation law is computed using a typical decaying function related to the history parameter κ :

$$
\sigma(\kappa(t)) = \alpha \exp^{-\beta\kappa(t)} \tag{3.38}
$$

where α, β are the parameters stemming from the CDM to XFEM transition. Finally, the cohesive force matrix is given by :

$$\mathbf{T} = T_n \left(\mathbf{n}_{\Gamma_d} \otimes \mathbf{n}_{\Gamma_d}\right) + T_t \left(\mathbf{m}_{\Gamma_d} \otimes \mathbf{m}_{\Gamma_d}\right) \tag{3.39}$$

with

$$\mathbf{m}_{\Gamma_d} = \mathbf{n}_{\Gamma_d} - \frac{\mathbf{w}}{||\mathbf{w}||} \tag{3.40}$$

and

$$\mathbf{w} = \sum_{J \in S_H} N_J(x)\hat{\mathbf{u}}_j \tag{3.41}$$

Algorithm 3.1 gives a pseudo-code to implement this traction-separation relation for a 3D problem. One key element is the definition of the triangles required to integrate on the discontinuity surface. Details about the method used to extract these triangles are given in section 3.5.2.

3.4.3 Transition from continuous damage mechanics to cohesive XFEM

Following the approach proposed in (Roth *et al.*, 2015c), energy conservation during the transition from CDM to XFEM is enforced using mode I energy dissipation. The three conditions required for energy conservation during the transition are :

- The energy dissipation of the continuous damage mechanics approach from damage initiation until the transition strain occurs must be equivalent to the energy dissipated by the cohesive model from damage initiation until the transition opening is reached ;
- The energy remaining to be dissipated from the transition strain in the CDM model to complete material separation must be equal to that of the cohesive model ; and
- The initial traction stress of the cohesive surface must be equal to the CDM model stress at the transition strain.

Using these conditions, the parameters α and β can be defined using the approach proposed in (Roth *et al.*, 2015c). The transition from CDM to XFEM is achieved when $d > d_{crit}$.

Algorithm 3.1 Integration of the cohesive force over the discontinuity surface

GETISOSURFACETRIANGLES() ▷ Get the triangles defining the isosurface (see section 3.5.2)
Define the crack normal $\mathbf{n}_{\Gamma_d}$ using the smallest eigenvalue of equation 3.54
for $t = 1 \rightarrow N_{triangles}$ **do** ▷ For each triangles
  for $gp = 1 \rightarrow N_{gausspoint}$ **do** ▷ For each gauss point in the triangle
    Get the triangle determinant and position of the triangle gauss point in the reference element natural coordinates system ξ_t
    Get the reference element shape function at the triangle gauss point $\mathbf{M}(\xi_t)$
    Compute the crack opening $\mathbf{w}$ (equation 3.41)
    Compute the tangent vector $\mathbf{m}_{\Gamma_d}$ (equation 3.40)
    Using the normal and tangent vectors compute the normal opening u_n and tangential sliding u_t
    if $u_n \approx 0$ **then** ▷ If the crack is closing
      Define T_n and T_t using equations 3.36 and 3.37
    else
      if $f(\lambda, \kappa(t)) \geq 0$ **then** ▷ Check the loading/unloading function (equation 3.34)
        Update T_n, T_t and $\kappa(t)$
      end if
    end if
    Compute $\mathbf{T}_{gp} = T_n \left(\mathbf{n}_{\Gamma_d} \otimes \mathbf{n}_{\Gamma_d}\right) + T_t \left(\mathbf{m}_{\Gamma_d} \otimes \mathbf{m}_{\Gamma_d}\right)$
    $\mathbf{T} += \int_{\Gamma_d} \mathbf{M}^{\mathrm{T}} \mathbf{T}_{gp} \mathbf{M} \, \mathrm{d}\Gamma_d$
  end for
end for

3.4.4 Poro-damage model

A parallel between material damage and increasing permeability in the porous flow model can be achieved. Indeed, damaged concrete has a large number of pores that can be filled in the liquid phase. This observation may be represented mathematically by modifying the permeability and/or the Biot coefficient as a function of the damage level.

According to (Picandet *et al.*, 2001) changes in concrete permeability can be split in two parts. The first part is where micro cracking linked to low-level damage (0 to 15%) occurs, and the second is where macro-cracks occurs beyond the peak load. Based on experimental results, this reference frame gives a damaged-permeability relationship in the prepeak phase of concrete (valid for damage values between 0 and 0.18) as an exponential function :

$$k_D = k_0 \exp\left((\alpha d_1)^{\beta}\right) \tag{3.42}$$

with $\alpha = 11.3$, $\beta = 1.64$ and d_1 is the first principal tensile damage scalar. For serious damage, the permeability of a crack is given by the Hele-Shaw flow (equation (3.43)) (also called the plane-Poiseuille flow) :

$$k_{cr} = \frac{g w_{cr}^2}{12\nu} \tag{3.43}$$

where g is the acceleration due to gravity, w_{cr} is the crack opening and ν is the fluid kinematic viscosity. The crack opening computation remains a challenge when continuous damage models are used. A novel method to compute crack opening is proposed in section 3.6.

A single mathematical law, based on the law of mixtures which makes it possible to describe the evolution of permeability from the initiation of micro cracks until the opening of the macro crack (Pijaudier-Cabot *et al.*, 2009; Bouhjiti *et al.*, 2018).

$$\log(k_m) = (1 - d_1)\log\left(k_D^F\right) + d_1 \log\left(k_{cr}\right) \tag{3.44}$$

where k_D^F is a limited Taylor expansion of the exponential relation. Assuming that the permeability change in the damaged material is isotropic, the permeability matrix from equation (3.16) is given by $\mathbf{K} = \delta_{ij} k_m/\mu$. Similarly, the Biot coefficient increases such that :

$$b = b_0 + (1 - b_0) d_1 \tag{3.45}$$

with b_0 the initial Biot coefficient.

3.5 Algorithm for 3D non-planar crack path computation

3.5.1 Computation of the level-set function

The XFEM method requires the discontinuity paths to be identified to capture the displacement jump. Discontinuity paths identification is a complex challenge to address. In (Saloustros *et al.*, 2018), a thorough review of the challenges involved is given. Three dimensional discontinuity path identification is not as trivial as the two dimensional case. Extension of the discontinuity surface requires, for each element in the discontinuity tip, the definition of the location of the discontinuity in the element in front of the tip as well as in the elements located in its immediate neighborhood. Many algorithms have been proposed to track crack paths. These can be classified in five categories : local methods, non-local methods, global tracking methods, level set methods and implicit methods. The three first methods were compared for 3D extruded-type applications in (Jäger *et al.*, 2008). In fact, most of the algorithms developed were tested on 2D or pseudo 3D problems, where a 2D geometry is extruded. Hence, the discontinuity surface is simple to describe and the elements in the crack front are aligned. For applications in more complex problems where the discontinuity is described by a 3D surface, numerous methods developed to track the discontinuity either fail or more development would be required to apply them. To our knowledge, there are very few references dealing with real three dimensional discontinuity surfaces applied to concrete problems.

A short survey of three-dimensional concrete problems with non-planar discontinuities computed using the five tracking categories listed above is presented here. The local discontinuity tracking strategy was used on the Brokenshire test (Brokenshire, 1996) in (Fries & Baydoun, 2011). An explicit description of the crack was employed to define the direction of propagation using the surface tangential direction and the maximum circumferential (hoop) stress. The non-local strategy (Gasser & Holzapfel, 2005, 2006) was applied to the Brokenshire test. Because the local method (element by element algorithm) may yield a non-unique discontinuity surface depending on the order in which the elements are treated, a smoothing algorithm is proposed in this reference to ensure a unique description of the discontinuity surface and to force its continuity across the elements. A similar tracking algorithm is used (Gasser, 2007) to model a three-dimensional benchmark called PCT3D (Feist & Hofstetter, 2007). The global tracking strategy is applied to the Brokenshire test (Linder & Zhang, 2013) and to the PCT3D case (Feist, 2004). The level-set method (Gravouil *et al.*, 2002) and a special case of the level-set method, the fast marching method (Sukumar *et al.*, 2008), are used to model an inclined penny crack. An implicit method where the crack propagation is embedded in the unknowns of the problem is proposed in (Ferté *et al.*, 2016). The numerical results of a three-point bending test with an initial skew crack (made of PMMA (Plexiglas)) and the Brokenshire test are solved using the implicit approach.

The pull out test is often used to validate 3D non planar discontinuity tracking algorithms. Even if this test is not an extrusion of a 2D geometry (this test is discussed in section 3.8.3), it is considered here as a 2D profile revolved around an axis, and which does not yield a complex discontinuity surface. Therefore this case was not considered as a true 3D complex geometry surface in this short review.

Based on the above references, it is possible to draw the following conclusions. First, there are few reference cases to validate crack tracking algorithms with complex surfaces. Second, few works deal with real 3D applications of tracking algorithms using either PUFEM (Melenk & Babuška, 1996) (Partition of Unity Finite Element Method), XFEM, GFEM (Duarte *et al.*, 2000) (Generalized Finite Element Method) or SDA (Oliver, 1996) (Strong Discontinuity Approach). Although these methods were first published around twenty years ago, they have not yet been successfully deployed in the industry. One of the reason is probably the challenges inherent when dealing with non-planar discontinuities tracking.

The global strategy proposed in (Oliver *et al.*, 2002) is applied herein. Beginning with a brief description of the method, details of the implementation are then presented to provide more information on how to follow complex cracking surfaces.

The main idea of this tracking strategy is to draw the envelopes of the discontinuities tangent vector field. An analogy to a heat conduction-like problem is used to compute the nodal isovalues (temperatures) used to draw the envelopes. A steady heat conduction problem with no internal heat source can then be solved with prescribed Dirichlet and Neumann boundary conditions.

The direction normal to the plane of propagation of the discontinuity can be defined as $\mathbf{N}(\mathbf{x})$ at every point $\mathbf{x}$ in the domain Ω and vectors $\mathbf{S}(\mathbf{x})$, $\mathbf{T}(\mathbf{x})$ as unit vectors orthogonal to $\mathbf{N}$ so that :

$$\mathbf{S}\cdot\mathbf{N} = \mathbf{T}\cdot\mathbf{N} = 0 \tag{3.46}$$

Introducing a function $\theta(\mathbf{x})$, where the isosurfaces are tangent to vectors $\mathbf{S}$ and $\mathbf{T}$ allows the isosurfaces S_i to be described by the function $\theta(\mathbf{x})$ passing through point P such that :

$$S_i = \{\mathbf{x} \in \Omega \mid \theta(\mathbf{x}) = \theta_P\} \tag{3.47}$$

Hence, the isosurfaces of function $\theta(\mathbf{x})$ must satisfy these conditions $\mathbf{T}\cdot\nabla\theta = 0$ and $\mathbf{S}\cdot\nabla\theta = 0$. The solution that satisfies the conditions can be found by solving the heat-conduction like problem with adiabatic boundary conditions and no internal heat source :

$$\nabla\cdot\mathbf{q} = 0 \text{ in } \Omega \tag{3.48a}$$

$$\mathbf{q} = -\mathbf{K}_{ls}\cdot\nabla\theta \text{ in } \Omega \tag{3.48b}$$

$$\mathbf{q}\cdot\mathbf{n} = 0 \text{ on } \Gamma_q \tag{3.48c}$$

$$\theta = \theta_p \text{ on } \Gamma_\theta \tag{3.48d}$$

where the anisotropic conductivity tensor $\mathbf{K}_{ls}$ is given by :

$$\mathbf{K}_{ls} = \mathbf{T}\otimes\mathbf{T} + \mathbf{S}\otimes\mathbf{S} + \zeta\mathbf{I} \tag{3.49}$$

where $\otimes$ denotes the tensor product and ζ is a small isotropic perturbation term (10^{-6}) introduced to avoid the ill-posedness of the conduction problem. The envelopes of the vector field provides C^0 continuous surfaces. The vectors $\mathbf{S}$, $\mathbf{T}$ are the eigenvectors orthogonal to the eigenvector associated with the largest strain eigenvalue. These eigenvalues/eigenvectors can be computed using either the local or the nonlocal strain tensor. The nonlocal strain provides smoother discontinuity surfaces, but at the cost of losing the local support of the finite element and with the additional complexity of having to implement the method in parallel computing. This avenue was investigated during this work, however it was not pursued in depth because the global tracking method already provides path smoothing. To eradicate the perturbation term, the heat convective-diffusion problem (Riccardi *et al.*, 2017) can be solved instead of the conduction problem. Although this method seems to alleviate the problems associated with the loss of crack-path continuity, the discontinuities predicted on coarse meshes seems to be less precise that those calculated with the standard global method.

The solution of 3.48 provides the scalar values of θ at each node. To build the isosurfaces, a method similar to the one given in section 3.5.2 is used. The algorithm presented in section 3.5.2 was an application of the marching cube method at the element level. It must be extended to track multiple isosurfaces crossing numerous elements in the numerical model. The method is implemented using two “classes” :

- **Class 1** (*GlobalTracking*) : deals with the solution of equations 3.48, identifies the possible starting locations of the discontinuities and instantiates the second class for each possible discontinuity found ;
- **Class 2** (*CrackInstance*) : manages discontinuity tracking and assigns the crack position using the same nomenclature as the level-set method. This class is instantiated for each discontinuity in the model.

Every call to the tracking algorithm is dealt with the class *GlobalTracking* (pseudo-algorithm 3.2). This class is used to solve equations 3.48. First, the boundary conditions on the nodes attached to the elements crossed by discontinuities are imposed such that the scalar field is fixed around the discontinuity so that it cannot change position and direction. If no discontinuities are present, θ must be imposed on at least two points. After computing θ for each node, the possible discontinuity starting locations are computed (algorithm 3.3) by determining the elements exceeding the energy threshold in the numerical model, defined as :

$$\frac{1}{2}\sigma_1\varepsilon_1^{av} \geq \gamma\left(\frac{1}{2}f_t'r_0\right) \tag{3.50}$$

where σ_1, ε^{av}, f_t', r_0, were defined in section 3.4.1 and γ is a threshold factor to identify potential elements. If γ is close to one, then more Newton iterations will be required for convergence in a load step because the discontinuity will advance element by element. On the other hand, if γ is set too low, many elements will be identified and there is a chance that the discontinuity diffusion will be too high. From our numerical experiments we have found that $\gamma = 0.90$ is optimal. The discontinuity starting point is located on the mesh boundary, therefore at each call of the global tracking algorithm, the elements on the boundaries exceeding the criterion are used as possible discontinuity initiation points (the class 2 is instantiated for each possible discontinuity). To satisfy the condition that there is a minimum spacing between discontinuities (Bažant & Cabot, 1989), only one discontinuity in a sphere R_a is allowed. This verification is made by using the element exceeding the threshold as the center of a sphere and a NearTree algorithm (Andrews & Bernstein, 2016) to find the elements within the sphere.

Thereafter, for each new instantiation of the *CrackInstance* class, the discontinuity start point must be defined. The coordinates of the discontinuity origin $o(x,y,z)$ is defined at the center of the element face located on the boundary. If more than two faces are on the boundary, the origin is defined as the element's centroid. To define the isosurface, the value of θ_P in a point P located on the isosurface must be defined using the shape functions :

$$\theta_P = \sum_{i=1}^{n} N_i(\xi)\theta_i \tag{3.51}$$

where ξ are the natural coordinates of the discontinuity origin. The tracking algorithm is used only for the few isosurfaces that must be followed to track the discontinuities. Hence, starting from the elements initiating the discontinuity, each of the neighboring elements to the faces crossed by the isosurface are used in turn to follow the isosurfaces (pseudo-algorithm 3.4). The extension of the isosurface is stopped at the elements not exceeding the energy threshold.

The level-sets are defined at each nodes of the elements crossed by the isosurface. Level-set functions are scalar functions within the domain whose zero-level is interpreted as the discontinuity. The domain Ω is therefore divided into two subdomains Ω^+ and Ω^- on either side of the discontinuity where the level-set functions are respectively positive or negative such that :

$$\phi_i = \theta_i - \theta_P \tag{3.52}$$

where θ_P is the value of θ at the zero level-set of the considered discontinuity surface S_i. The nodes on one side of the isosurface will have negative values of θ while the nodes on the other side will have positive values. Note that the global method is often classified as a method requiring significant computational effort. Dealing with partial-domain tracking algorithms has been proposed (Feist & Hofstetter, 2006a), where the discontinuities are tracked through the solution of a boundary value problem within a sub-domain rather than in the whole domain. The present algorithm has been optimized to handle the entire domain for multiple reasons. First, the effort to solve the problem using parallel computing is quite small compared to the complexity of dealing with partial-domain tracking algorithms. Second, the communication time required to synchronize the multiple MPI processes can cancel all possible gains related to the partial-domain algorithm. Finally, using a conjugate gradient method with an incomplete Cholesky factorization preconditionner, very few iterations (3-5) are required to reach a convergence of 10^{-8}.

Algorithm 3.2 Global tracking method

```
Add boundary conditions for the heat transfer problem onto the nodes that belong to the
  elements crossed by the discontinuity
Solve the heat transfer equation (equation 3.48)
GETROOTELEMENT()                          ▷ Find if a discontinuity must be initiated
for all CrackInstance do
    UPDATELEVELSETS()
end for
```

Algorithm 3.3 Get discontinuity root element

function GETROOTELEMENT()
    for $e = 1 \to N_{elements}$ **do** ▷ For each elements located on the boundaries
        $\Xi = \frac{1}{2}\sigma_1 \varepsilon_1^{av}$
        if $\Xi > \gamma\left(\frac{1}{2} f_t' r_0\right)$ and $\Xi > \Xi_{max}$ **then** ▷ Get the element with the largest energy
            Using a NearTree algorithm (Andrews & Bernstein, 2016), get the elements in a sphere of radius R_a and located at the current element centroid
            if No element in the sphere has a discontinuity **then**
                $\Xi_{max} = \Xi$ ▷ New largest value of the energy
                $E_{id} = e$ ▷ Element number with the largest energy
            end if
        end if
    end for
    if One element exceeding the energy threshold has been found **then**
        Create a new *CrackInstance*
    end if
end function

Algorithm 3.4 Discontinuity path tracking

function UPDATELEVELSETS
    Get the isovalue θ_p located on the discontinuity
    GETELEMENTS(*TipElementList*, *SweepElementList*, *DummyArg*) ▷ Get all the elements crossed by the discontinuity adjacent to the crack tip elements
    while List *SweepElementList* is not empty **do** ▷ For each element retrieved from the previous list
        for $n = 1 \to N_{nodes}$ **do** ▷ For each node of the element
            $\phi_n = \theta_n - \theta_p$ ▷ Assign the level-set function
        end for
        GETELEMENTS(*CurrentElement*, *SweepElementList*, *DummyArg*) ▷ Get the elements adjacent to the current element in the extension of the discontinuity
        Remove the current element from the list *SweepElementList*
        The element is crossed by the discontinuity and is added to the *CrossedElementList* list
    end while
    GETELEMENTS(*CrossedElementList*, *DummyArg*, *TipElementList*) ▷ Define the crack tip elements
end function

Algorithm 3.5 Function to define the crack tip elements and the elements extending the discontinuity

function GETELEMENTS(*ElementList*, *SweepElementList*, *TipElementList*)
    for $e = 1 \rightarrow N_{elements}$ **do** ▷ For each elements in *ElementList*
        for $f = 1 \rightarrow N_{face}$ **do** ▷ For each face of the element
            for $n = 1 \rightarrow N_{nodes}$ **do** ▷ For each node of the face
                $\phi_{min} = \min(\phi_{min}, \phi_n)$
                $\phi_{max} = \max(\phi_{max}, \phi_n)$
            end for
            if $\phi_{min} \times \phi_{max} < 0$ **then** ▷ If the level sets changes sign, the face is crossed by a discontinuity
                Find the neighbor element adjacent to the face currently being processed
                if $\frac{1}{2}\sigma_1 \varepsilon_1^{av} < \gamma \left(\frac{1}{2} f_t' r_0 \right)$ **then** ▷ Check if the element adjacent to the face exceeds the threshold
                    Add the element currently being processed to the list *TipElementList*
                else ▷ Threshold exceeded : the adjacent element must be treated by the path tracking algorithm
                    Add the element adjacent to the face currently being processed to the list *SweepElementList*
                end if
            end if
        end for
    end for
end function

3.5.2 Definition of the discontinuity at the element level

To determine the crack position at the zero level-set ($\phi = 0$) and to integrate over the discontinuity surface, the isosurface triangulation defined by the level-sets must be constructed. The marching cube method (Lorensen & Cline, 1987) is probably the most commonly used method for isosurfacing extraction and is widely applied in many application areas, including medical visualization (CT scans and MRI). The marching cube method constructs a triangulated isosurface by processing the data set in a sequential cube-by-cube or element by element order. During this processing, each element that has at least one node with an isovalue equal to or greater than an isovalue (marked node) and one node with an isovalue below the isovalue (unmarked node) is intersected by the isosurface. The intersection points with the isosurface are computed using a linear interpolation of the isovalue for all the element's edges that have one marked and one unmarked node. Because each node of an element can be either marked or unmarked, there are $2^8 = 256$ possible marking scenarios that encode a cube-isosurface intersection pattern. Note that by using reflective and rotational symmetry is possible to limit the possible marking scenarios to 15.

Pseudo-algorithm 3.6 is given for the marching cube method applied to isosurfacing extraction computation within a finite element. Marking scenarios can be found in many references (Newman & Yi, 2006). Note that the standard marching cube method does not guarantee correctness or topological consistency. In fact, it can produce topologically inconsistent isosurfaces caused by facetization ambiguity. Multiple disambiguation approaches have been proposed, such as the use of extended lookup tables for marking scenarios and element decomposition into subelements. According to a small sample of tests, elements exhibit face ambiguity at a rate that is typically 3% (Wilhelms & Van Gelder, 1990). To avoid this type of problem, decomposition to tetrahedra is used in this work as it provides an efficient method to have isosurface consistency. The hexahedron is divided into five tetrahedra (Dompierre *et al.*, 1999) such that the elements' connectivities (shown in figure 3.1) are given by : $\{n_1,n_2,n_3,n_6\},\{n_1,n_3,n_8,n_6\},\{n_1,n_3,n_4,n_8\},\{n_1,n_6,n_8,n_5\},\{n_3,n_8,n_6,n_7\}$. Instead of using the hexahedron lookup tables, the tetrahedron lookup table should be used to construct the isosurface. This reduces the possible marking scenarios to $2^4 = 16$. In complex problems where the mesh is built with a hexa-dominant algorithm, hexahedra, wedges, pyramids and tetrahedra are all present. All these elements are divided into a number of tetrahedra (Dompierre *et al.*, 1999) in the pseudo-algorithm 3.6.

From the different isosurfaces encoded in the marching cube method, it is obvious that 3D discontinuity propagation in solids leads to non-planar crack surfaces. To simplify numerical integration over the element and the discontinuity, an artificial planar surface is constructed following the method proposed in (Linder & Zhang, 2013). Hence, a unique crack normal is computed for the discontinuity and the position is defined by minimizing the distances between the computed crack intersection with the element edges defined by the level-set functions and a

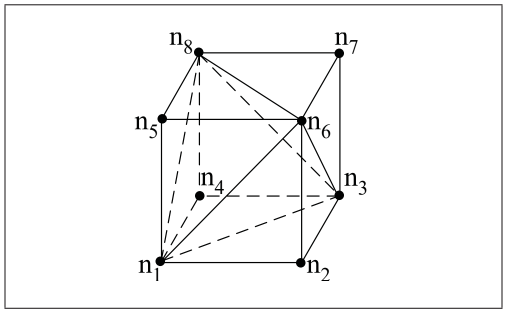

Figure 3.1 Hexaedron division
into five tetrahedra

unique internal element discontinuity plane. This minimization leads to an eigenvalue problem defined by :

$$(\mathbf{M}-\lambda\mathbf{I})\,\mathbf{v}=0 \tag{3.54}$$

where

$$\mathbf{M}=\frac{1}{n_{in}}\sum_{i=1}^{n_{in}}(\mathbf{x}_i-\bar{\mathbf{x}})\otimes(\mathbf{x}_i-\bar{\mathbf{x}}) \tag{3.55}$$

with n_{in} the number of intersection points between the discontinuity and the element, and :

$$\bar{\mathbf{x}}=\frac{1}{n_{in}}\sum_{i=1}^{n_{in}}\mathbf{x}_i \tag{3.56}$$

is the discontinuity plane position. To fully define the discontinuity, its normal must be defined. The vector $\mathbf{n}_{\Gamma_d}$ corresponding to the minimal eigenvalue λ is the discontinuity normal and the two other eigenvectors are tangential directions.

3.6 Proposed crack opening computation in the continuous damage model

Computing crack opening in damage material is not trivial when continuous damage models are used. The strain must somehow be scaled by a reference length. This length can be determined analogously to the characteristic length or the localization limiter required for the so-called mesh-adjusted softening modulus technique or crack band approach. Often, this length is computed with the volume of the representative element ($l_{rve}=\sqrt[3]{V}$). However, more ela-

Algorithm 3.6 Computation of the crack isosurface

function GETISOSURFACETRIANGLES()
  Divide the base element into tetrahedra
  For each of the N_{tetra} a tetrahedron is defined using the global coordinates $\mathbf{x}$ and natural coordinates η corresponding to the base element natural coordinates.
  for $t = 1 \rightarrow N_{tetra}$ **do** ▷ For each of the tetrahedra
    Mark the nodes if the level-set value is negative
    for $n = 1 \rightarrow N_{nodes}$ **do**
      if $\phi_n < 0$ **then**
        TetraIndex |= 2^{n-1}
      end if
    end for
    Using the TetraIndex, look up the marching tetrahedron edge table to find the segments cut by the isosurface
    for for each segment **do**
      Get the intersection point using a linear interpolation. If $\mathbf{v}_1$ and $\mathbf{v}_2$ are segment's vertices global coordinates, η_1 and η_2 are the segment's vertices natural coordinates (provided by the isoparametric base element) and ϕ_1 and ϕ_2 are the scalar values of the level-set at each vertex, then the intersection point in global coordinates $\mathbf{x}$ and natural coordinates η is given by :

$$\begin{aligned} \mu &= -\phi_1/(\phi_2 - \phi_1) \\ \mathbf{x} &= \mathbf{v}_2 + \mu(\mathbf{v}_2 - \mathbf{v}_1) \\ \eta &= \eta_2 + \mu(\eta_2 - \eta_1) \end{aligned} \tag{3.53}$$

    end for
  end for
  Using the TetraIndex, look up the marching tetrahedron segment table and construct the triangular facets to represent the isosurface within the base element using the global and natural coordinates (provided by the isoparametric base element).
end function

borated reference lengths can be computed taking into account the crack direction using the approaches found in (Oliver, 1989; Sanjay *et al.*, 1995; Slobbe *et al.*, 2013; Morenon, 2017). In this work, it is proposed to compute the crack opening of the damaged element using a local XFEM solution. The displacement solution of the standard FEM solution is used to constrain the displacements of the element (figure 3.2) while the formulation of the local stiffness matrix is computed using XFEM. Hence, the additional unknowns stemming from the discontinuous functions at the element nodes can be computed. Using these unknowns, it is possible to com-

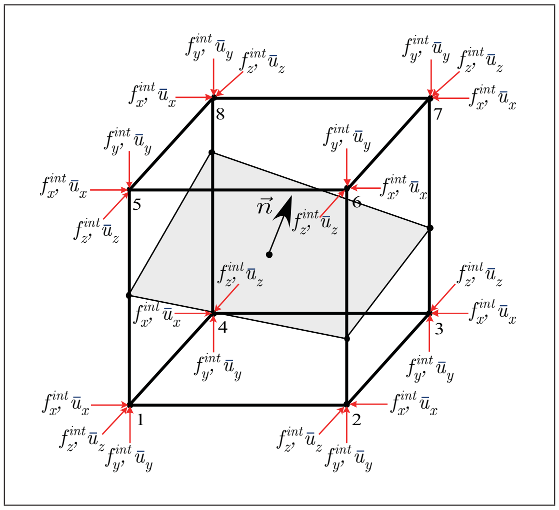

Figure 3.2 Constrained element for crack opening computation

pute the crack opening without introducing a reference length. The system of equations to solve at the element level is given by :

$$\begin{bmatrix} \int_{\Omega} \mathbf{B}^{\mathrm{T}}\mathbf{C}_0\mathbf{B}\ \mathrm{d}\Omega & \int_{\Omega^\star} \mathscr{H}\mathbf{B}^{\mathrm{T}}\mathbf{C}_0\mathbf{B}\ \mathrm{d}\Omega^\star \\ \int_{\Omega^\star} \mathscr{H}\mathbf{B}^{\mathrm{T}}\mathbf{C}_0\mathbf{B}\ \mathrm{d}\Omega^\star & \int_{\Omega^\star} \mathscr{H}\mathbf{B}^{\mathrm{T}}\mathbf{C}_0\mathbf{B}\ \mathrm{d}\Omega^\star + \int_{\Gamma_d} \mathbf{M}^{\mathrm{T}}\mathbf{T}\mathbf{M}\ \mathrm{d}\Gamma_d \end{bmatrix} \begin{Bmatrix} \bar{u} \\ \hat{u} \end{Bmatrix} = \begin{Bmatrix} f_{\bar{u}}^{int} \\ 0 \end{Bmatrix} \tag{3.57}$$

The stress-strain constitutive relation $\mathbf{C}_0$ is computed using the undamaged material and $\mathbf{T}$ contains the cohesive force evaluated on the discontinuity (see algorithm 3.1 for evaluation of this integral). Instead of using the traction-separation law given in section 3.3.1, the damage parameter from the continuous damage model (d_1) is used directly to avoid an iterative process when evaluating the damage parameter, which is dependent upon the crack opening. Therefore, the traction separation relation $\sigma(\lambda)$ is replaced by :

$$\sigma(\lambda) = (1 - d_1) f_t \tag{3.58}$$

The parameter $\alpha = 0$ is considered such that tangential sliding is neglected. As the crack flow is not affected by the crack sliding according to 3.43, the cohesive law used for crack opening computation only considers mode I cracks. Finally, the internal loads $f_{\bar{u}}^{int}$ (the right hand side of 3.57) are evaluated using the relation $f_{\bar{u}}^{int} = \mathbf{B}^{\mathrm{T}}\sigma$.

The crack position is computed using the algorithm presented in section 3.5.1. However, crack path computation is seldom done when continuous damage models are used. In that case, the discontinuity at the element level can be placed at the element centroid and oriented with the eigenvector $\left\{ \varepsilon_{1\,x}, \varepsilon_{1\,y}, \varepsilon_{1\,z} \right\}^T$ of the largest principal strain $\max(\lambda(\varepsilon))$.

Algorithm 3.7 Computation of the crack opening

Compute the undamaged stress-strain constitutive tensor relation $\mathbf{C}_0$
if no tracking algorithm is used **then**
    Assign the nodal level-set with $\vec{n} = \left\{ \varepsilon_{1\,x}, \varepsilon_{1\,y}, \varepsilon_{1\,z} \right\}^T$
    for $n = 1 \rightarrow N_{nodes}$ **do** ▷ For every element nodes
        $\phi_n = \vec{n} \cdot (c_n - \bar{c})/||\vec{n}||$ ▷ c_n and $\bar{c}$ are respectively the coordinates of the node n and the element centroid
    end for
end if
Compute the crack plane (see section 3.5.2)
Integrate the traction-separation law over the crack plane (using algorithm 3.1)
Compute the other terms in the matrix given in equation 3.57
Reduce the sytem of equations by applying the boundary conditions ($\bar{u}$ and $f_{\bar{u}}^{int}$)
Solve the system of equations 3.57 to determine $\hat{u}$
Compute the crack opening

$$w_{cr} = ||\sum_{j=1}^{N_{nodes}} N_j(x)\hat{u}_j||,\ x \in \Gamma_d$$

3.7 Global solution algorithm

The computer implementation of this model is achieved in a parallel object oriented C++ code. The solver and parallel data structure is provided by the package Trilinos (Heroux *et al.*, 2005). Figure 3.3 presents the UML activity diagram of the global solution algorithm described here. Steps 1 and 2 update the element stiffness matrix using the method described in section 3.4.1 and 3.4.2. If the element is enriched, the permeability matrix is computed according to equation 3.16 in step 3 ; if the element is damaged, the crack opening must be computed using the algorithm given in section 3.6 (steps 4 and 5) and the permeability coefficient is computed using section 3.4.4. The solution of the matrix system is then computed. Using the updated principal stresses, the heat transfer problem can be solved in step 7 (figure 3.3) and the isosurface for each discontinuity is tracked using the algorithms defined in section 3.5.1. Three numerical solution algorithms were tested to model hydraulic fracturing :

1. The Newton-Raphson algorithm is iterated until convergence is reached. The discontinuities are propagated using the CDM. In this case the CDM-XFEM switching threshold can be exceeded. When the solution is converged, the CDM-XFEM switching threshold is verified. If there are elements exceeding the threshold, the nodes are enriched, the matrix system is rebuilt and the Newton-Raphson algorithm is continued. This process is repeated as long as there are elements reaching the CDM-XFEM switching threshold. When this process is completed, the next load step is computed ;
2. During the Newton-Raphson iteration, as soon as an element reaches the CDM-XFEM switching threshold, the matrix system is rebuilt once the nodes are enriched (by increasing the number of degrees of freedom). This process is repeated as long as there are elements reaching the CDM-XFEM switching threshold. When this process is completed, the next load step is computed ;
3. All the nodes have seven degrees of freedom $(\bar{u}_x, \bar{u}_y, \bar{u}_z, \hat{u}_x, \hat{u}_y, \hat{u}_z, p)$ with the enriched degrees of freedom considered as imposed and null. The imposition of constraints on these nodes is removed when the elements connected to these nodes are crossed by a discontinuity. This avoids matrix resizing during the Newton-Raphson iterations, at the cost of having a larger system to solve.

These solution algorithms are illustrated in figure 3.3. The second algorithm is less stable than the first, as the solution used to update the discontinuity position is not converged. Although the switching threshold of the first algorithm can be exceeded, it has been found to yield stable and accurate results. For problems without hydromechanical coupling and with relatively small imposed load or displacement changes, the switching threshold is respected, while for hydromechanical problems with brittle behavior, the threshold can be exceeded more importantly. Note that for hydraulic fracturing problems on isostatic models where the crack is in contact with a high pressure boundary condition (typical for gravity dams), the discontinuity propagates rapidly and the model exhibits brittle fracture. This behavior is more ductile for hyperstatic problems (typical for arch dams) where the loads are redistributed differently during cracking. Finally, the third algorithm is being implemented in another version of the code using the user programmable features (UPF) of the ANSYS commercial finite element package, and so it is still under investigation.

Step 10 is performed by an algorithm similar to algorithm 3.4. To ensure continuity of the enriched elements in the discontinuity, the enrichment is done progressively, from an initiation of the discontinuity (root elements) to the crack tip. The nodes located on the face adjacent to the row of elements not exceeding the switching threshold are not enriched to better define the crack tip.

The algorithm presented in the UML activity diagram is iterated until convergence. The convergence criterion of the Newton-Raphson method is taken such that the imbalance force norm is less than 0.1% of the external loads norm and that the XFEM switching threshold is not exceeded by any element.

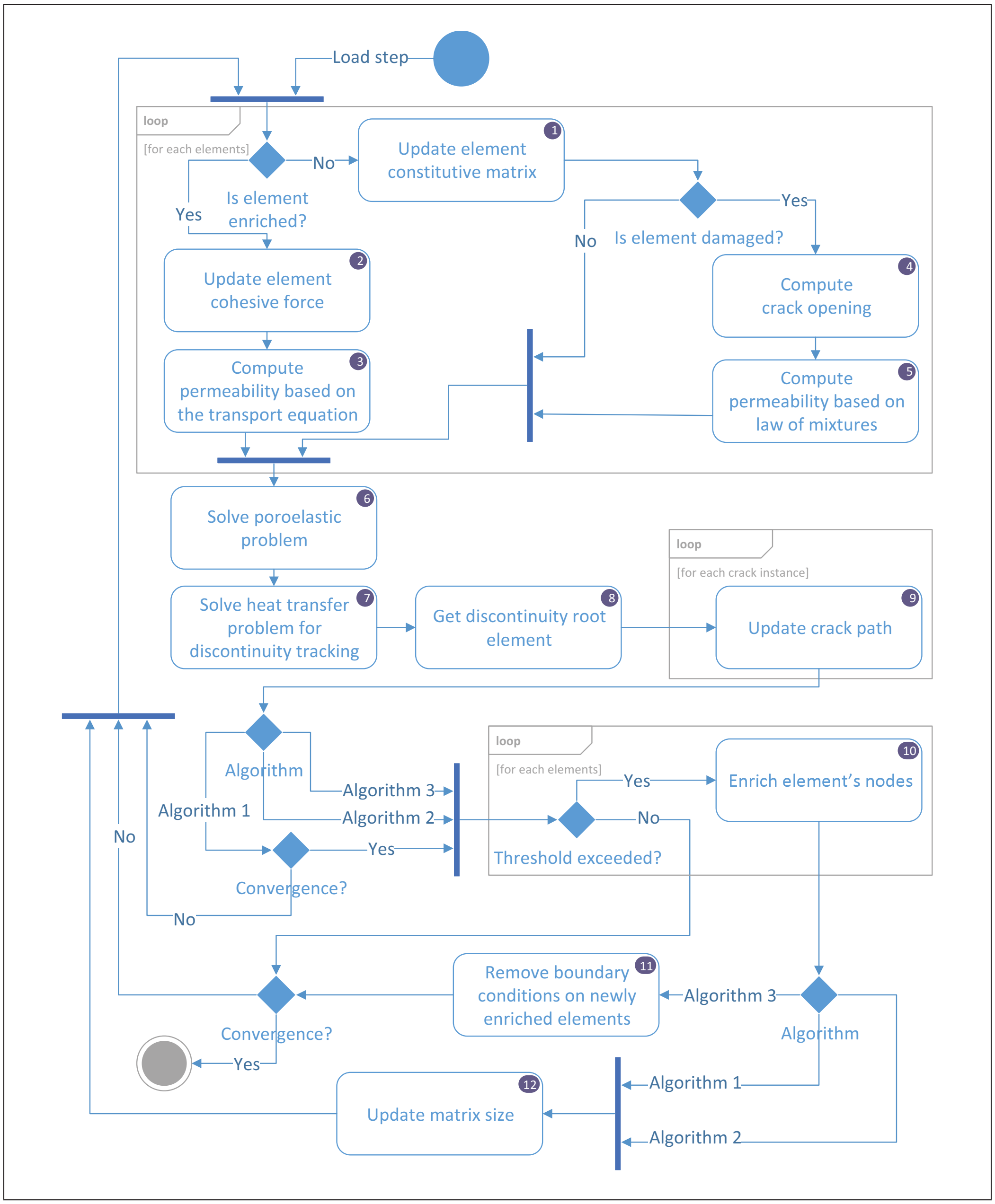

Figure 3.3 UML activity diagram of the algorithm for the Newton-Raphson iteration for one load step

3.8 Numerical examples for non-planar three-dimensional concrete fracturing

For all the validation example presented in this section, the parameter that controls the weighting between the normal and tangential opening is taken as $\alpha = 1$, the concrete friction angle is given by $\phi = 45$ and the CDM-XFEM transition threshold is considered to be 0.6 (the effect of this parameter on the results is given in (Roth *et al.*, 2015c)). The problems are discretized using eight nodes elements with tri-linear interpolation, with the addition of the enhanced strain formulation (Simo *et al.*, 1993b).

3.8.1 Brokenshire test

The first validation example is taken from the experimental study (Brokenshire, 1996) of different plain concrete specimens under torsion. The detailed description of the experimental procedure is given in (Jefferson *et al.*, 2004). This validation test was performed numerically, applying different approaches including damage, plasticity, embedded and XFEM crack models (Jefferson *et al.*, 2004; Gasser & Holzapfel, 2006; Gürses & Miehe, 2009; Fries & Baydoun, 2011; Linder & Zhang, 2013; Bilbao *et al.*, 2015; Zhan & Meschke, 2016; Benedetti *et al.*, 2017; Kaczmarczyk *et al.*, 2017; Dias *et al.*, 2018). Two geometries were experimentally tested, but only the prismatic version of the geometry (shown in figure 3.4) is used here.

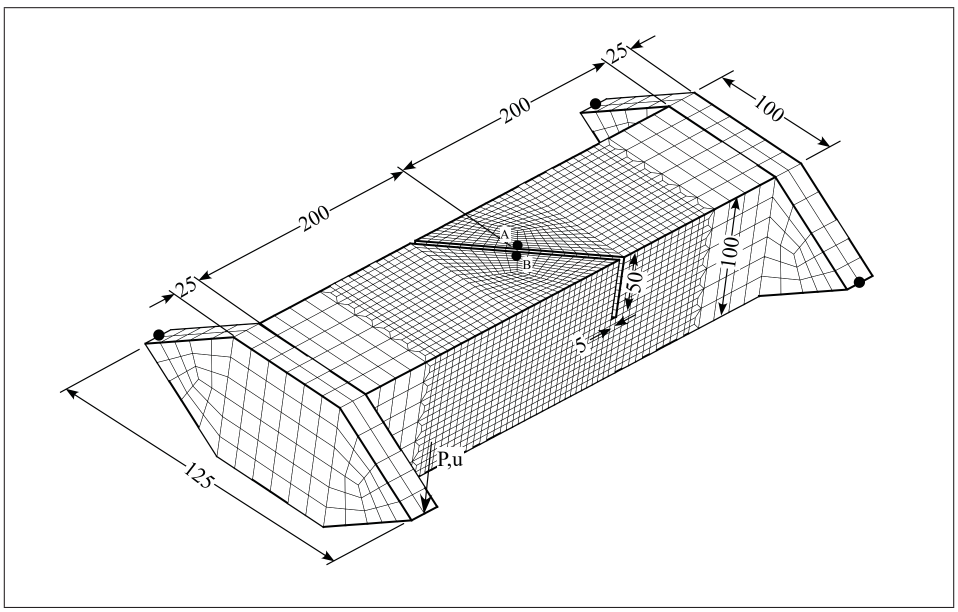

Figure 3.4 Brokenshire case (dimensions in mm)

Tableau 3.1 Material properties for the Brokenshire test

E (MPa)	f'_t (MPa)	f'_c (MPa)	ν	G_F (N/m)	b	k
35000	2.3	32.0	0.20	80	0.2	10^{-8}

The references cited above use material properties that are within a fairly limited range (note that the material properties are not given in some references). The material properties used here are taken from (Jefferson *et al.*, 2004) and given in table 3.1. The crack mouth opening displacement between points A and B is used to control the applied load.

Figure 3.5 gives the force-CMOD of the beam. The results are in agreement with the experimental result up to CMOD=0.50 mm. At this CMOD, the solution begins to be unstable resulting in a gradual force response slope change. This may be due to the discontinuity reaching the bottom surface of the beam. Once most of the elements on the bottom surface are crossed by a discontinuity, the force response suddenly drops and the solution gradually returns to the experimental value. This “bump” in the force response is not physical and must be further investigated. Perhaps the coefficient of friction or the weighting between the normal and the tangential aperture may explain this behavior. Figure 3.6 shows the predicted crack evolution at different CMOD stages. The crack starts to reach the bottom surface at CMOD=0.6 mm, which corresponds to the “bump” discussed earlier. Finally, figure 3.7 gives the comparison between the numerical and the experimental results once the specimen is fully cracked.

3.8.2 PCT3D test

The series of experimental tests carried out on a 180 mm square-shaped beam with an eccentric load resulting in a bending and torsion load is considered as the second validation example. This series of tests called PCT3D (Plain Concrete Test in 3D) was performed experimentally (Feist, 2004; Feist & Hofstetter, 2007) and numerically (Feist, 2004) for the validation of crack models for 3D stress states. It was conducted in the objective of the "Integrity Assessment

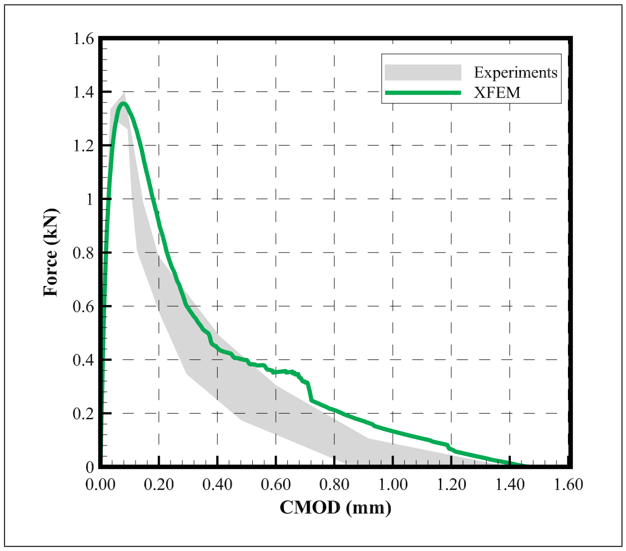

Figure 3.5 Brokenshire case force-CMOD results

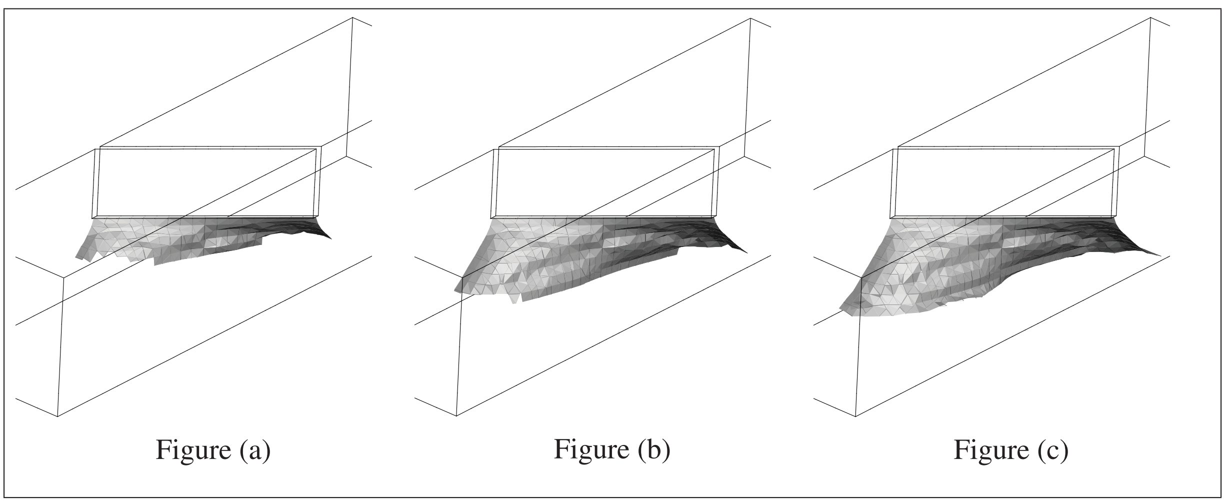

Figure 3.6 Evolution of the discontinuity surface (a) CMOD=0.044 mm, (b) CMOD=0.127 mm, (c) CMOD=0.600 mm

of Large Concrete Dams" (IALAD) working group to provide an experimental database to systematically compare different material models for ordinary concrete cracking.

The geometry and the boundary conditions are sketched in figure 3.8. The black circles located on both sides of the beam represent the axes of support. The load is applied eccentrically as

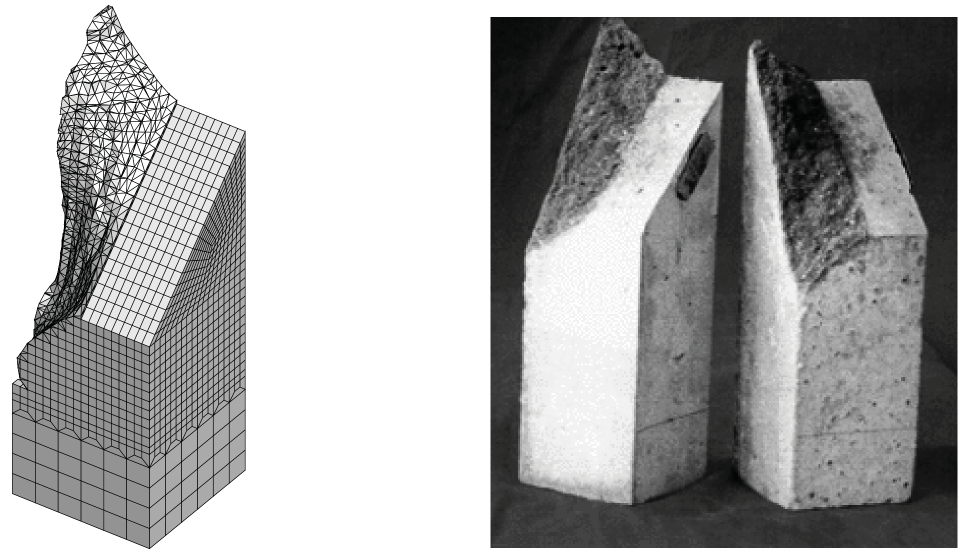

Figure (a) Figure (b)

Figure 3.7 (a) Numerical result, (b) Experimental result

a point displacement obtained by means of a steel bar located 75 mm from the beam center.

Material properties were carrefully tested (Feist, 2004) using multiple specimens specially

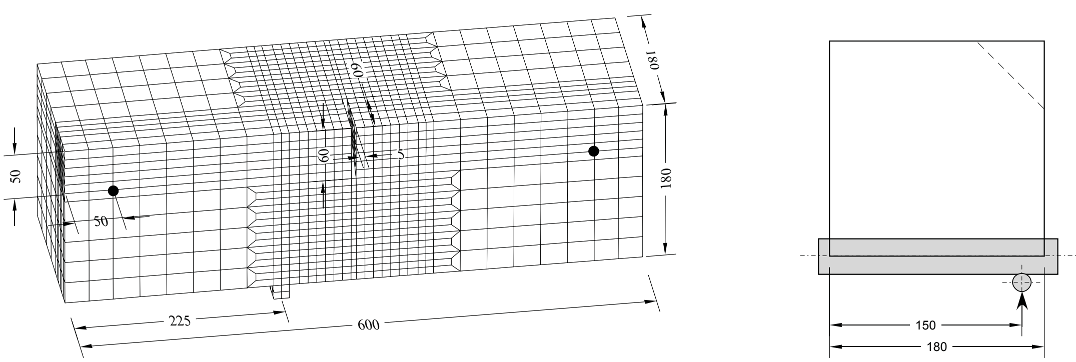

Figure (a) Figure (b)

Figure 3.8 PCT3D case (dimensions in mm)

made to determine the materials' properties. Uniaxial tensile and compressive strength, density, Young's modulus, Poissons's ratio, flexural and splitting tensile strength and fracture energy were tested with at least three samples per test. The average material properties mesured are given in table 3.2 except for the tensile strength parameter. A sensitivity analysis was performed on this parameter (using 2.03 MPa, 2.83 MPa and 4.83 MPa) as the measured value of 4.83 MPa appears too large considering the value of the compressive strength, as noted in (Feist, 2004). The solution is computed using a displacement controlled algorithm, where the increment of

Tableau 3.2 Material properties for the PCT3D test

E (MPa)	f'_t (MPa)	f'_c (MPa)	ν	G_F (N/m)
37292.6	2.03 - 2.83 - 4.83	32.12	0.1927	75

the CMOD is used to constrain the solution. The CMOD is defined as the relative displacement between the points on both sides of the notch.

The load-CMOD results are compared with the experimental results in figure 3.9 for the three strength parameters. The results computed with the strength parameters in the range 2.03 to 2.83 MPa are similar to the experimental envelope which confirms that the measured value of 4.83 MPa is out of range. This is in agreement with the results computed in (Feist, 2004; Gasser, 2007). During the simulation it was noted that the steel bar modulus also has an influence on the results. These analyses used a modulus of 200 GPa and a Poisson ratio of 0.3. Increasing the steel modulus has the same effect as reducing the concrete tensile strength. Moreover, using a square steel section may also have influenced the response curve. Figure 3.10 shows the predicted crack with crack mouth opening displacements of CMOD=0.02, 0.06, 0.20 mm. This figure clearly illustrates that the 3D stress state of the PCT3D test causes a double curved crack, similar to experimental observations. To compare the numerical and the experimental results, the discontinuity profile isolines are shown in figure 3.11 (positive values indicate the discontinuity profile moves towards the steel bar). Knowing that the concrete maximum aggregate size is 8 mm, it is clear that these isolines are in agreement.

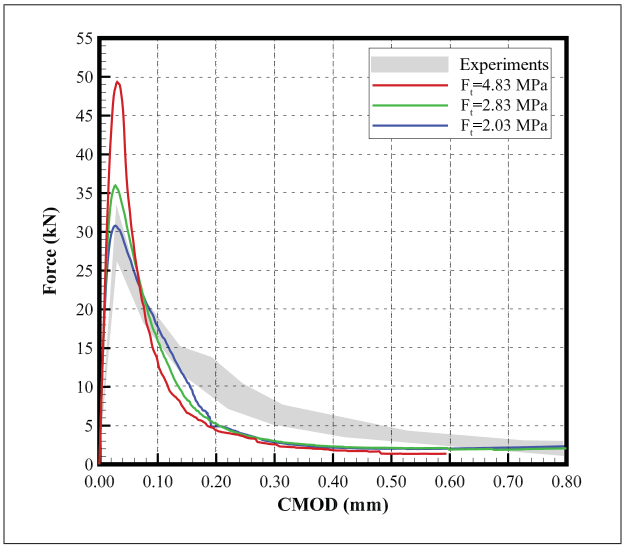

Figure 3.9 PCT3D force-CMOD results

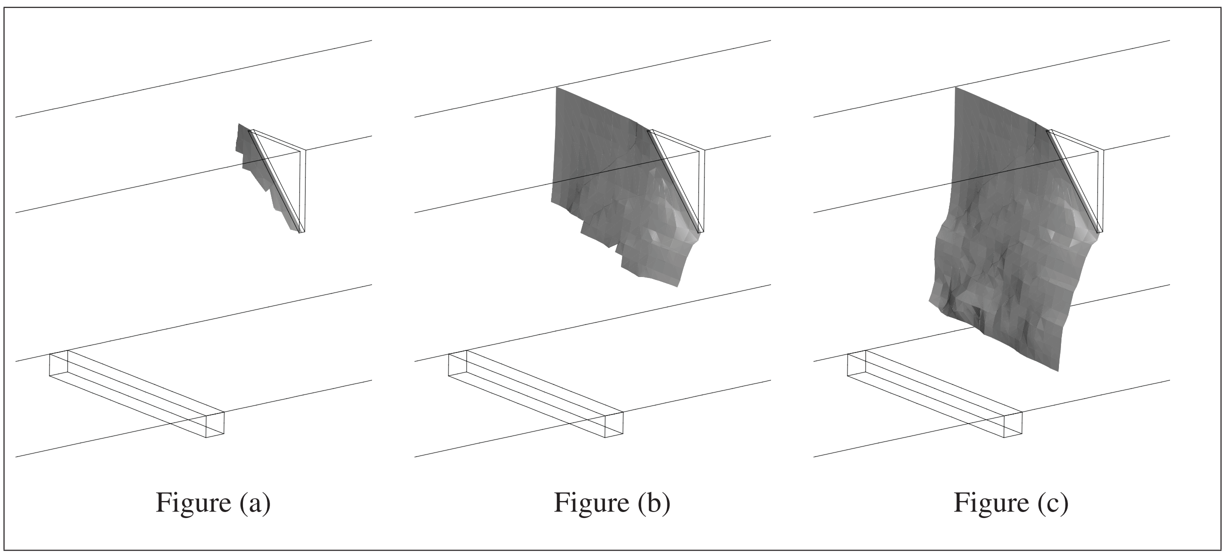

Figure 3.10 Evolution of the discontinuity surface (a) CMOD=0.02 mm, (b) CMOD=0.06 mm, (c) CMOD=0.20 mm

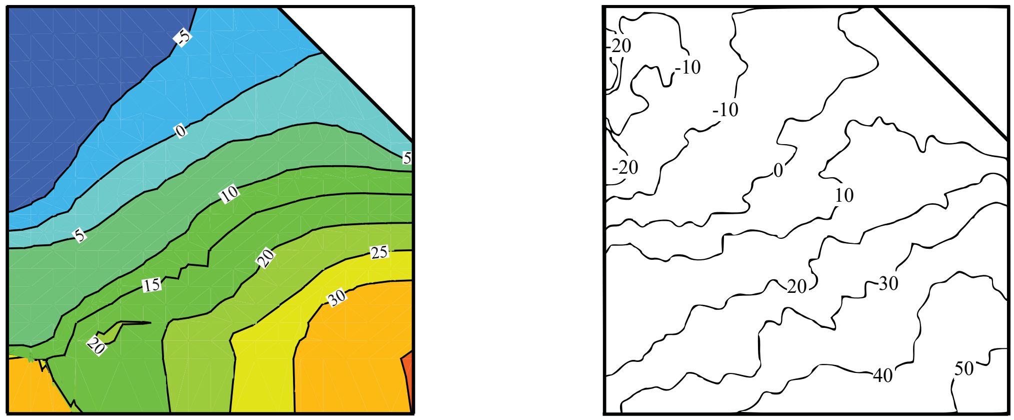

Figure (a) Figure (b)

Figure 3.11 Discontinuity profile in mm (a) Numerical result, (b) Experimental result

3.8.3 Anchorage structure

This validation example models the pull-out of a steel anchor embedded in concrete. This is a test commonly used to illustrate the performance of 3D numerical methods, especially in applications involving a curved discontinuity surface, as considered in (Areias & Belytschko, 2005; Benedetti *et al.*, 2017; Gasser & Holzapfel, 2005; Duan *et al.*, 2009; Feist & Hofstetter, 2006b; Armero & Kim, 2012). This test has also been computed in 2D using axisymmetric finite elements (de Borst, 1986; Rots, 1988; Benedetti *et al.*, 2017) as the 3D discontinuity surface is the result of a revolved 2D profile.

Only a quarter of the cylinder is modeled to simplify the problem with symmetrical boundary conditions applied on the face along the x and y axes. The geometric dimensions of the model are given in figure 3.12. It is assumed that the concrete cylinder is supported by an annular ring (illustrated in figure 3.12 using shaded elements in the 70 mm thick ring) along its upper perimeter and the anchor is being pulled out centrically. The disc is assumed to be infinitely stiff so that the displacements can be prescribed on the disc–concrete interface. This assumption is used by most of the references cited above.

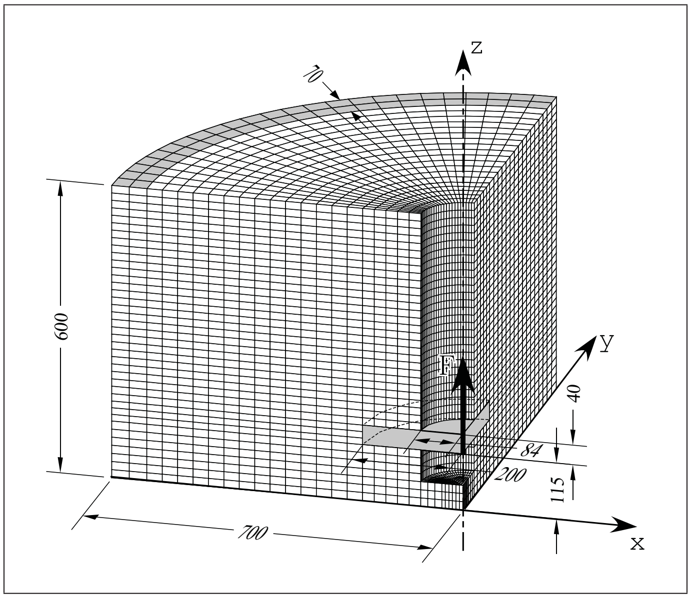

Figure 3.12 Anchorage structure (dimensions in mm)

Tableau 3.3 Material properties for the pullout test

E (MPa)	f'_t (MPa)	f'_c (MPa)	ν	G_F (N/m)
30000	3.00	30.0	0.20	106

The material parameters given in table 3.3 are taken from (Areias & Belytschko, 2005). The computed discontinuity surface is shown in figure 3.13. The angle formed between the discontinuity and the horizontal plane is approximately 35°. No angles are given in the cited references ; however, they appear to be qualitatively similar. The load-displacement response is given in figure 3.14 along with a compilation of the results from the cited references. Comparing these results, it is obvious that those obtained in (Areias & Belytschko, 2005; Benedetti *et al.*, 2017) have a different slope in the linear part. This may be due to different boundary conditions applied to the numerical model or because of secondary cracks developing in the model. The other results are in a similar range and show a re-increase of the load at an average displacement of approximately 0.25 mm. This may be caused by the discontinuity going below the annular ring support.

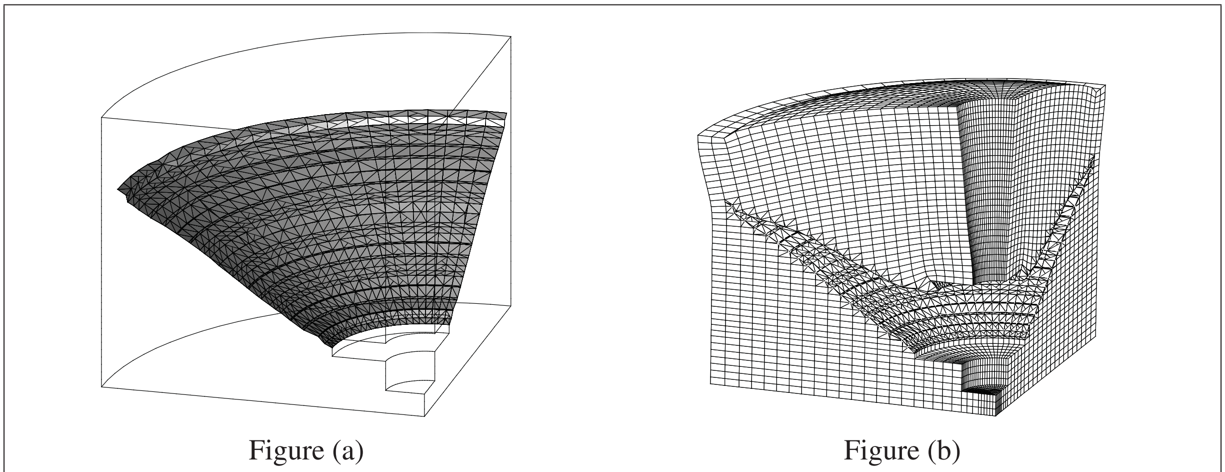

Figure 3.13 (a) Crack surface, (b) Deformed result

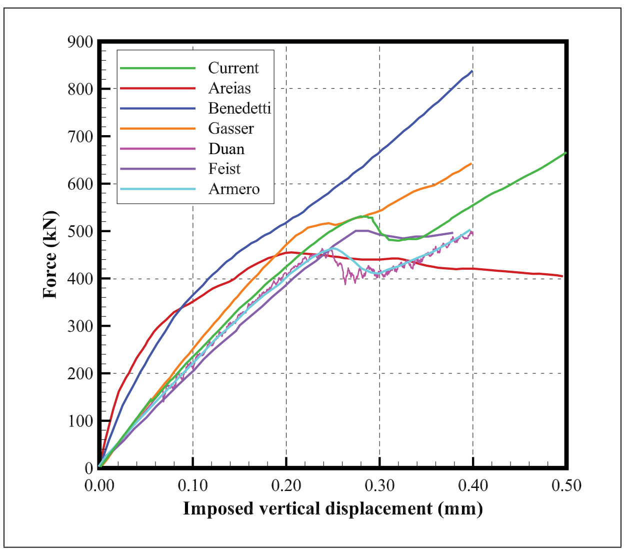

Figure 3.14 Anchorage structure load-displacement response

3.8.4 Arch Dam

To assess whether the CDM-XFEM method developed in this work can be applied to industrial problems, a real arch dam model was computed. The Alqueva arch dam, built on the Guadiana River, is located in Portugal near the Spanish border. It was completed in 2002, creating the largest freshwater reserve dammed by artificial methods in Europe. It is a 96-meters high double-curvature arch dam with a crest length of 458 meters. The thickness at its base is between 32 and 33 meters and the thickness at its crest is 7 meters. A fault located in the ground under the foundation which forms an angle of approximately 25.5° with the vertical plane of symmetry of the dam was one of the most important issue to address during the dam's construction. The dam geometric definition is given in figure 3.15.

To analyze the safety of the Alqueva dam, a landslide scenario of the left bank is considered. The imposed displacement applied in the fault is decomposed into tangential and normal components to the fault where the normal component is three quarters of the tangential component. This hypothesis was considered to be able to compare the numerical results with the experimental results obtained in scale models (LNEC, 1999). In the experimental test, a 1 :250 model built in mortar was reproduced. A joint, was added in the foundation to experimentally reproduce a landslide. Although the experimental data was obtained from the scale model, the numerical analysis is computed using the real dam dimensions. One of the differences between the numerical model and the real model is that the vertical construction joints were neglected. The rock-concrete interface was also considered to be completely solidary.

The boundary conditions are shown graphically in figure 3.16. On the downstream face of the right bank foundation, the nodes displacements are fixed in the upstream/downstream direction. For the face located on the right bank of the foundation, the nodes displacements are fixed in the left bank / right bank directions. All the nodes located below the foundation have their vertical displacements fixed. The boundary conditions in the left bank fault are applied using an x, y component vector to provide the required tangential and normal components. These displacements are applied gradually to capture the crack propagation. The self-weight is applied

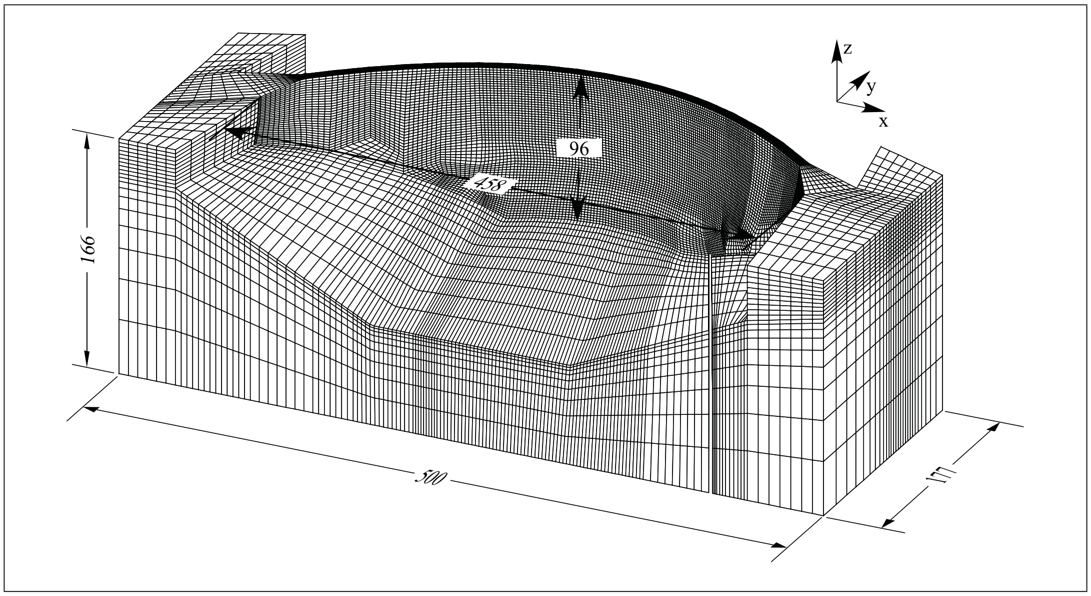

Figure 3.15 Alqueva case (dimensions in m)

on the dam by imposing a density and a vertical acceleration ; however the foundation has already had some settlement, therefore a zero density is imposed on the foundation. Finally, the water pressure is imposed on the dam's and foundation's upstream faces. The water level is 1 meter below the crest, therefore the nodes located under the water level on the dam upstream face, and on the top of the upstream foundation have a pressure imposed using a linear gradient with $\gamma = 9806.65 N/m^3$. The same materials as those defined in (Ibáñez, S. B., 2006) are used and are given in table 3.4. The computed crack surface is given in figure 3.17a corresponding

Tableau 3.4 Material properties for the Alqueva arch dam

Material	E (MPa)	f'_t (MPa)	f'_c (MPa)	ν	G_F (N/m)	ρ (kg/m^3)
Dam	35000	3.5	25.5	0.20	80	2400
Rock	35000	-	-	0.20	-	0

to the displacement given in figure 3.17b. The complexity of the three-dimensional discontinuity surface clearly shows the robustness of the crack tracking algorithm. The discontinuity

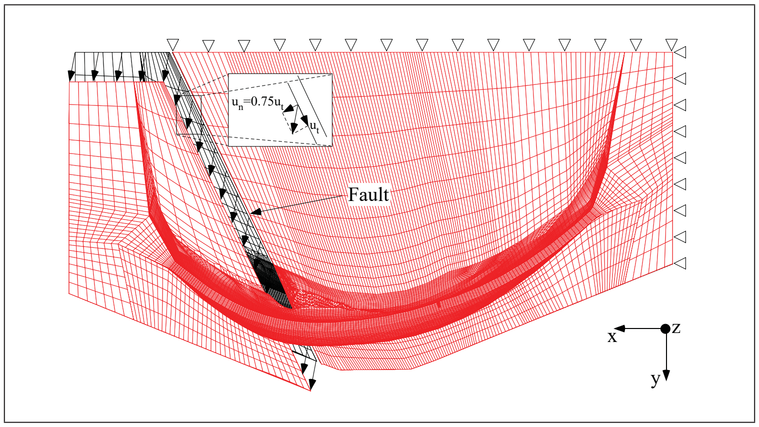

Figure 3.16 Boundary conditions for the Alqueva case

initiates vertically and quickly turns towards the right bank. It then goes horizontally until it reaches the dam's center. From there, the discontinuity turns to become vertical up to the crest. The crack does not cross the dam in the upstream/downstream direction. It is only visible on the downstream surface until it reaches the crest where it crosses the dam body and moves down vertically. The reason it does not cross the dam body is illustrated in figure 3.18. This figure plots the normal stresses (arch stresses) extracted from points near the upstream and downstream faces and located in the first 1/3 of the dam height as a function of the fault displacement magnitude. It is clear that on the upstream face, the compression stress increases as the fault moves. The opposite happens on the downstream face. Hence, this result is similar to the one computed in (Azevedo & de Lemos, 2010) and obtained experimentally. The computed crack trace on the upstream and downstream faces is given in figure 3.19 and can be compared with photos of the crack trace obtained experimentally on the reduced model in figure 3.20b. It can be concluded that the computed crack trajectory is in agreement with the experimental one.

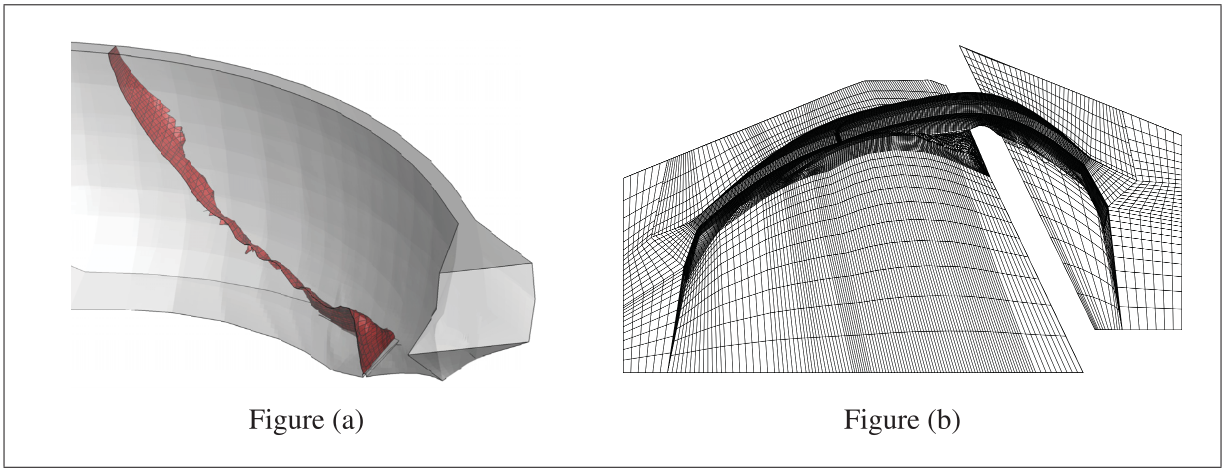

Figure 3.17 (a) Crack surface, (b) Deformed results (amplified x100)

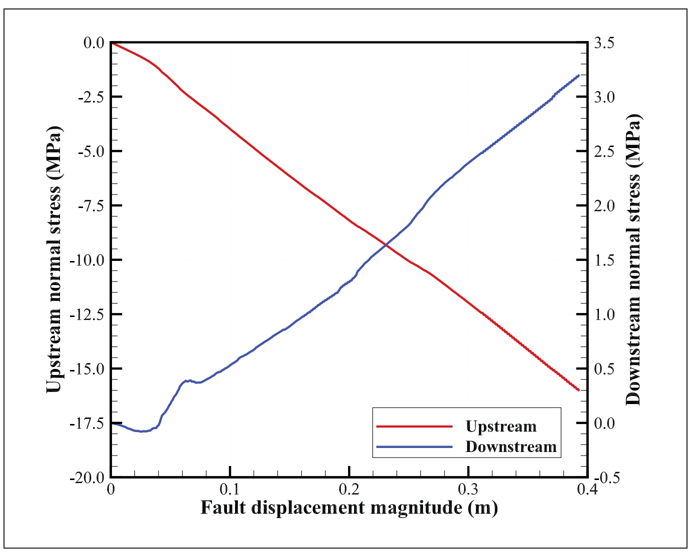

Figure 3.18 Alqueva upstream and downstream normal stress as a function of fault displacement magnitude

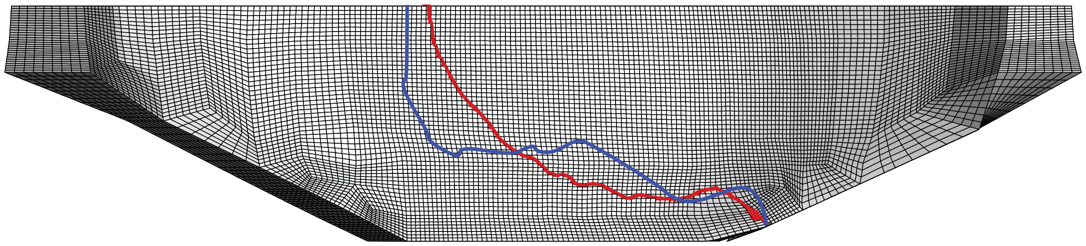

Figure (a)

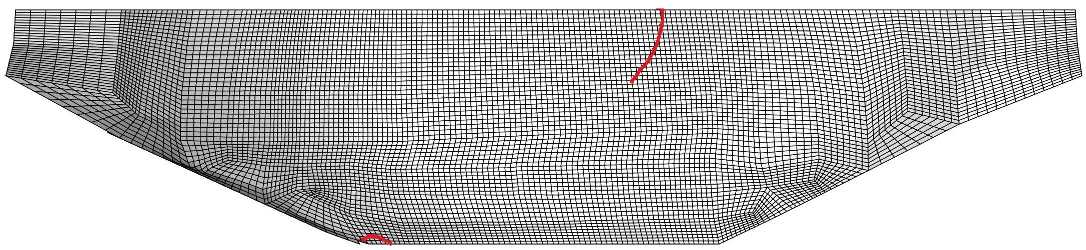

Figure (b)

Figure 3.19 Computed results (red) compared to experimental results (blue)
(a) Downstream face, (b) Upstream face

Figure (a)

Figure (b)

Figure 3.20 Experimental result (a) Downstream face, (b) Upstream face

3.9 Numerical examples for hydraulic fracturing

3.9.1 Brühwiler wedge splitting test

The wedge-splitting device tested in (Brühwiler & Saouma, 1995) and simulated numerically in (Bhattacharjee *et al.*, 1995) is used as a validation example of the crack opening algorithm in the continuous damage model (CDM). The geometry and material properties are given in figure 3.21a and table 3.5, respectively. Pressure boundary condition is imposed on the nodes in contact with the zone marked in red in figure 3.21a. With the exception of the front and back faces as well as the horizontal face in contact with the notch, zero pressure is applied on the other seven faces. The crack mouth opening displacement between points A and B is used to control the applied pressure.

Tableau 3.5 Material properties for the wedge-splitting specimen

E (MPa)	f'_t (MPa)	f'_c (MPa)	ν	G_F (N/m)	b	k
24320	2.54	25.4	0.20	182	0.2	10^{-8}

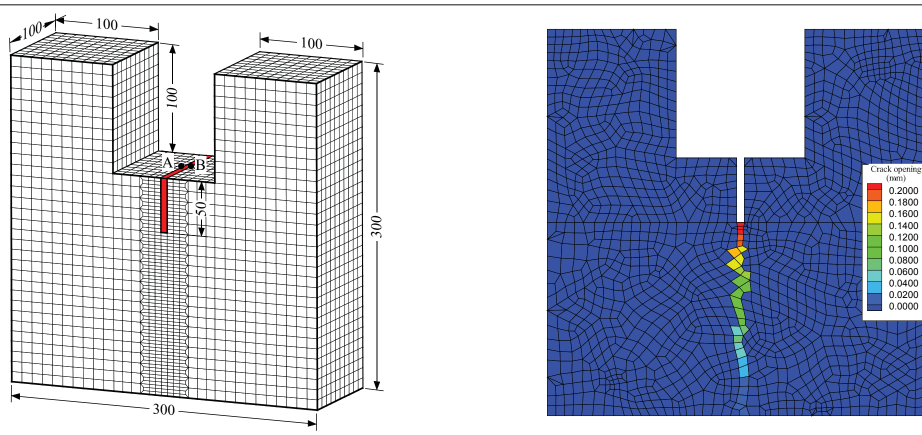

Figure (a)

Figure (b)

Figure 3.21 (a) Wedge-splitting finite element model (dimensions in mm), (b) Wedge-splitting finite element model unstructured mesh

To show the effectiveness of the proposed method, structured (figure 3.21a) and unstructured (figure 3.21b) meshes are used. The proposed method is compared with three other methods :

- Multiplication of the representative element length defined as $l_{rve} = V^{1/3}$ with the largest principal strain ;
- Multiplication of the projected element characteristic length (Morenon, 2017) with the largest principal strain. The projected element characteristic length, illustrated in figure 3.22, is defined as :

$$l_{rve} = \max(\phi_i) - \min(\phi_i) \tag{3.59}$$

  where ϕ_i are the signed distances defined as $\phi_i = \dfrac{\mathbf{n}_{\Gamma_d} \cdot (\mathbf{c}_i - \bar{\mathbf{x}})}{||\mathbf{n}_{\Gamma_d}||}$, with $\mathbf{c}_i$ is the nodal coordinate of node i, $\bar{\mathbf{x}}$ and $\mathbf{n}_{\Gamma_d}$ are respectively the discontinuity plane position and normal (defined in section 3.5.2) ;
- Use of the CDM-XFEM method proposed herein.

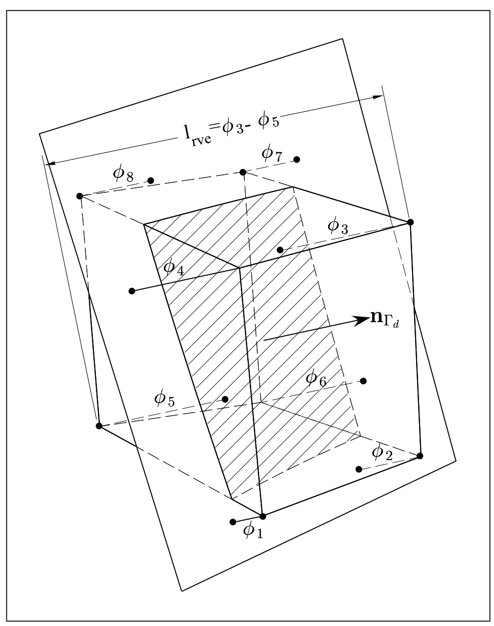

Figure 3.22 Projected characteristic length

The maximum pressure computed is 1.50 MPa on the unstructured mesh and 1.36 MPa on the structured mesh, which is comparable with the 1.30 MPa coumputed in (Bhattacharjee *et al.*, 1995). Figure 3.23 gives the crack opening distribution along the discontinuity center for a CMOD of 0.3 mm. For the results computed with the unstructured mesh (figure 3.23a), only the proposed crack opening algorithm is consistent with the CDM-XFEM results. The other two methods show oscillations that are not physical. The results computed using the structured mesh (figure 3.23b), with the exception of those computed with the method using the cubic root of the element volume as the characteristic length, are similar for the other three methods. The proposed crack opening computation algorithm is therefore able to compute the crack opening with a good accuracy, even if the discontinuity passes through elements of different sizes, shapes and orientations.

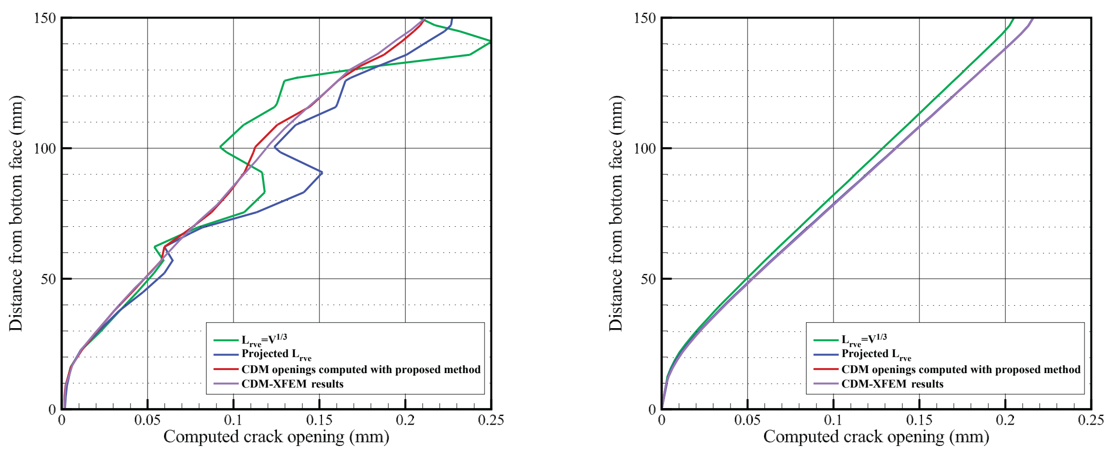

Figure (a)　　　Figure (b)

Figure 3.23　Crack opening distribution for CMOD=0.30 mm (a) Unstructured mesh, (b) Structured mesh

3.9.2 Ternay dam

Modeling interstitial pressures in hydraulic structures combined with a constitutive model for concrete, including cracking represents a major challenge for performing nonlinear computation in the field of dams. Cracks in dams have a high probability to initiate along a weak construction joint. After a certain distance along the joints, the cracks ususally develop in a diagonal profile leading to failure, a mechanism that was observed at the Bouzey dam (Léger *et al.*, 1997). The pressure inside the cracks and in the interstitial space should not be neglected when performing a stability assessment. The case study presented in this section treats the Ternay masonry dam. This case was already treated in (Léger *et al.*, 1997; Fauchet, 1991) in which poro-elastic models were used to compute the hydrostatic loading required to reach dam failure. The pressure hydrostatic loading is thus gradually increased until the dam becomes unstable. To increase the stability of the numerical solution, crest displacement is used to control the hydrostatic loading. Hence, if the crest suddenly moves towards downstream, the control algorithm will decrease the hydrostatic load.

The geometry of the 41 m Ternay masonry dam is given in figure 3.24.The dam was treated in 2D in (Léger *et al.*, 1997; Fauchet, 1991), whereas it will be treated in 3D in this work (extrusion of the 2D profile for a total thickness of 10 m.). The displacement boundary conditions are imposed on the rock foundation, where the nodes located upstream, downstream and on the bottom are considered to be fixed. A zero pressure boundary condition is imposed on the nodes located on the dam's downstream face, on the crest and on the foundation top downstream face. Finally, the nodes located under the water level on the upstream dam face and those on the top of the upstream foundation have a linear pressure gradient imposed with $\gamma = 9806.65N/m^3$. Nodes on the upstream dam face located above the water level have a zero pressure applied. Self-weight is applied on the dam by imposing a density and a vertical acceleration.

The material parameters, similar to those used in (Léger *et al.*, 1997), are given in table 3.6. The only difference is that isotropic hydraulic permeability is considered in the dam, whereas the reference used a horizontal permeability of (10^{-7} m/s) and a vertical permeability of (10^{-8} m/s) to consider the effect of the masonry construction process. The final cracking pattern is given in figure 3.25. In this figure, number ① indicates the location of the first crack and then number ② indicates the second and main crack that causes the dam to be unstable. The pressure isocontours are shown in this figure to reveal how water penetration inside the cracks changes the pressure pattern drastically. As expected, the pressure isocontours are parallel to the discontinuity. Figures 3.26a and 3.26b present the results obtained by the two other references. The

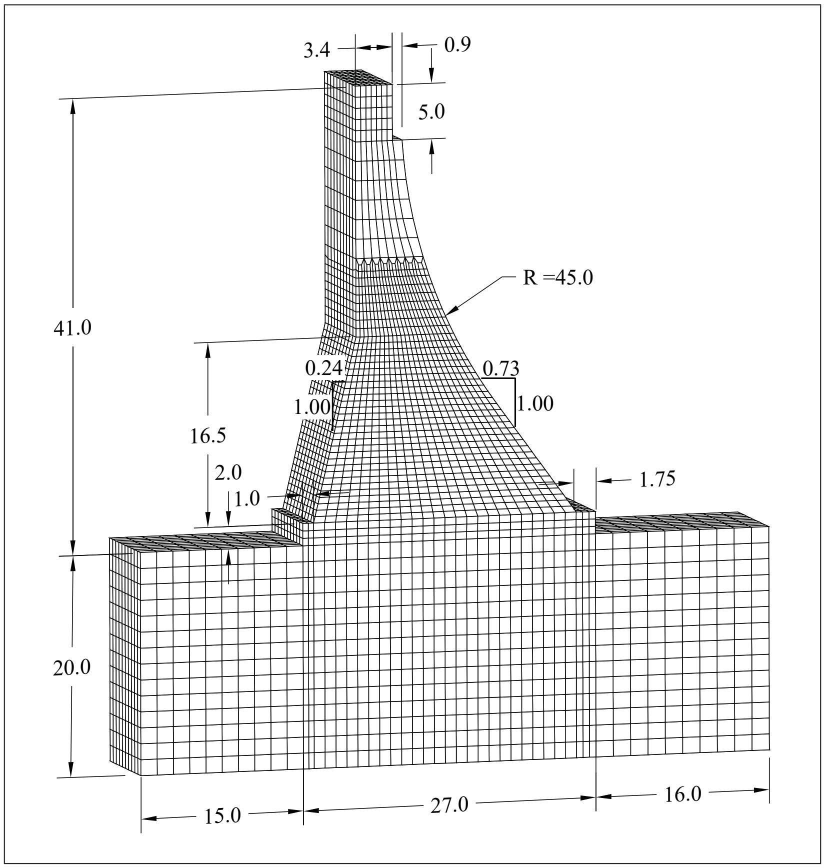

Figure 3.24 Ternay dam (dimensions in m)

Tableau 3.6 Material properties for the Ternay dam

Material	E (MPa)	f'_t (kPa)	f'_c (kPa)	ν	G_F (N/m)	ρ (kg/m^3)	b	k
Dam	14000	78	800	0.15	15	2400	0.4	10^{-8}
Rock	18000	-	-	0.15	-	0	0.2	10^{-4}

predicted water level at failure of 35.25m is very close to the 35.6m and the 36.4m values reported by (Léger *et al.*, 1997) and (Fauchet, 1991) respectively. The cracking profile is similar to that computed in (Léger *et al.*, 1997). Two cracks appear, one at the dam heal and one with initiation located at 13.5 m above the foundation. A similar cracking pattern was computed in (Léger *et al.*, 1997) where the second crack initiation location is 14.7m, which is 1.2 m above the present results. Both of these predicted cracking profiles are very localized compared to the one predicted in (Fauchet, 1991) where the cracks are diffused over a significant portion of the dam. Finally, the failure mode computed for the Ternay masonry dam is similar to the one observed for the Bouzey dam (figure 3.26c).

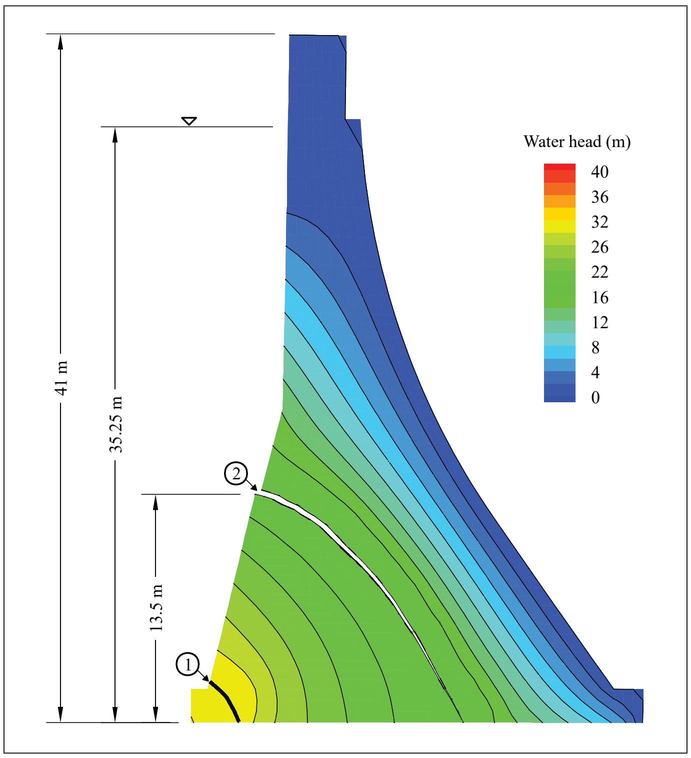

Figure 3.25 Final crack pattern of the Ternay masonry dam

The crack openings and the water levels as a function of crest displacement are shown in figure 3.27.The relationship between the reservoir level and the displacement at the dam crest is nonlinear. This is a consequence of the interstitial pressure causing displacements of the dam body. The first crack appears when the water level reaches 31.4 m. Its opening increases progressively until the second crack appears and propagates deep into the dam. The second crack appears at a water level of 35 m and at 35.25 m this crack propagates rapidly until it reaches the rock-concrete interface. During the propagation of this main crack, the first crack opening reduces considerably. In conclusion it can be seen from this test case that the hydrofracturation of dams where tensile strength and fracture energy are small is a brittle process.

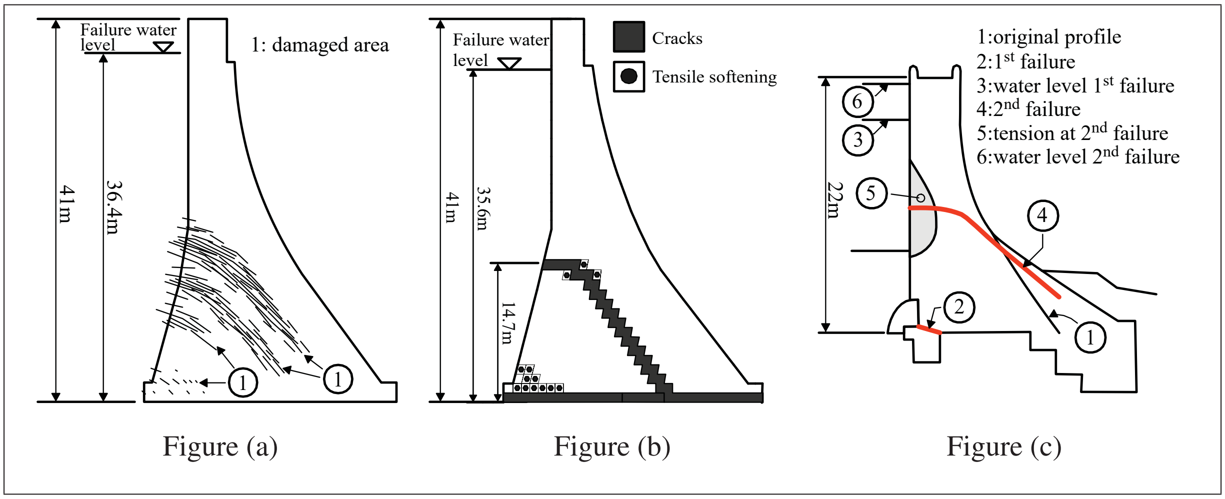

Figure 3.26 (a) Crack pattern from ref. (Fauchet, 1991), (b) Crack pattern from ref. (Léger *et al.*, 1997), (c) Bouzey dam failure

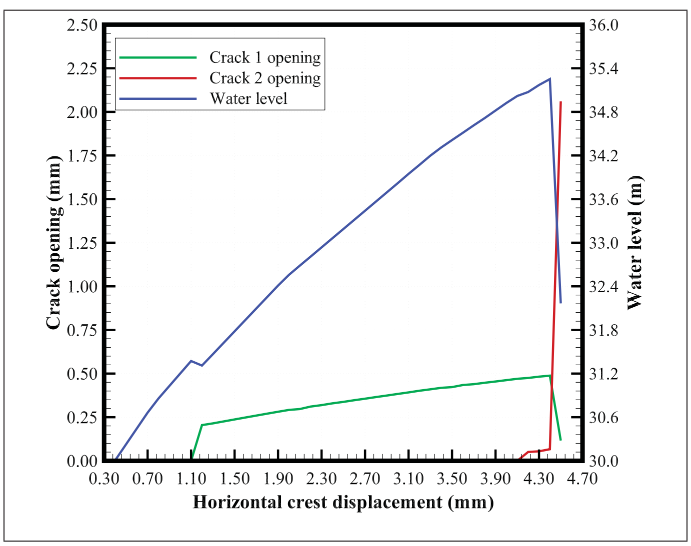

Figure 3.27 Crack opening as a function of crest displacement

3.10 Conclusions

This contribution has proposed a combined mechanical damage - XFEM approach for coupled hydro-mechanical computation applied to hydraulic fracturing problems. Our work has shown that the proposed method is able to simulate the propagation of non-planar fractures with complex 3D geometries. The paper provides the algorithms' details required to effectively implement the approach. A key ingredient of this method is the discontinuity tracking algorithm. The so-called global method is used to follow discontinuities. This method has been applied by other authors, but here it is extended to much larger problems. Another important aspect is the approach proposed to define the crack opening for discontinuities computed using a continuum damage method. This aspect is extremely relevant for the simulation of hydraulic fractures and for evaluating reinforcement effects in shear loading. The crack opening computed using a local XFEM solution at the element level was compared to other methods commonly used in the literature and has shown its superiority when computing discontinuity openings across elements of different sizes, shapes and orientations. Several different examples involving the propagation of non-planar and non-smooth crack surfaces were solved with our coupled XFEM approach. The performance of the proposed model in the analysis of load-induced cracks and hydraulically induced cracks was demonstrated using reference problems. The XFEM was first published around twenty years ago, but it has not yet been successfully deployed in the industry to model quasi brittle materials. The challenges inherent when dealing with non-planar discontinuities' tracking still exist. Commercial software do not offer the possibility to fully compute implicit discontinuities in non-planar 3D problems using XFEM. Many new extended discretization methods have been proposed since the first appearance of the XFEM method. However, to date none have been able to compute complex, large-scale cracking problems ; further research is needed before these methods become mature enough to compute alkali-silicate reaction (ASR) induced cracking for problems the size of a dam. Both of these topics are the subject of ongoing research by the authors.

3.11 Résumé et liens avec la problématique de recherche

Ce chapitre répond aux deux premières problématiques soulevées dans la thèse. Le modèle de fissuration développé en deux dimensions dans le chapitre 2 a été étendu pour un contexte tridimensionnel. Il a été déterminé que pour que la méthode fonctionne en 3D, l'algorithme de suivi des discontinuités est d'une importance considérable. La méthode dite globale est utilisée pour suivre les discontinuités. Celle-ci a été appliquée par d'autres auteurs, mais dans le chapitre 3 elle a été étendue à des problèmes de taille importante avec des géométries de fissures complexes. Une contribution importante a été réalisée afin de calculer l'ouverture de fissure dans le contexte de la mécanique continue de l'endommagement. Il est commun de définir une sorte de longueur caractéristique afin de relier la déformation dans la direction principale avec une ouverture de fissure. Or, il a été démontré que dans le cas où un maillage irrégulier est utilisé, l'ouverture de fissure présente des oscillations non réalistes le long de la fissure et donne des résultats très approximatifs. La méthode proposée, basée sur une formulation XFEM locale et sur l'équilibre des forces, vient régler cette problématique. Cet algorithme a notamment été utilisé dans un cas de fissuration hydromécanique où la perméabilité, liée à l'ouverture de fissure, est augmentée lors de la progression de l'endommagement. Maintenant qu'une méthode robuste a été développée afin de modéliser l'hydrofracturation en 3D, la troisième problématique soulevée peut-être résolue en ajoutant au modèle proposé la prise en compte d'un écoulement complexe et de la présence de drainage dans les discontinuités en plus des conditions de saturation partielles. Ceci est le sujet du chapitre suivant.

CHAPITRE 4

FULLY-COUPLED HYDRO-MECHANICAL CRACKING USING XFEM IN 3D FOR APPLICATION TO COMPLEX FLOW IN DISCONTINUITIES INCLUDING DRAINAGE SYSTEM

Simon-Nicolas Roth[1], Pierre Léger[2], Azzeddine Soulaïmani[3]

[1] Hydro-Québec, 75 boul. René-Lévesque Ouest, Montréal, Québec, Canada, H2Z 1A4
[2] École Polytechnique de Montréal, Department of Civil, Geological and Mining Engineering, C.P. 6079, succ. Centre-Ville, Montréal Québec, Canada, H3C 3A7
[3]École de Technologie Supérieure, Department of Mechanical Engineering, 1100, rue Notre-Dame Ouest, Montréal, Québec, Canada, H3C 1K3

Article soumis dans la revue « Computer Methods in Applied Mechanics and Engineering » en janvier 2020.

4.1 Abstract

The presence of uplift pressures in cracked plain concrete hydraulic structures is a major concern for their durability, serviceability and stability. To assess the performance of cracked structures several mechanical and hydraulic response parameters must be computed. This paper presents the development, implementation and application of a new nonlinear combined segregated fully-coupled hydro-mechanical model for application to non-planar 3D hydraulic fractures where complex flow is occurring. The eXtended Finite Element Method (XFEM) formulation is used, as it facilitates the computation of the crack aperture as well as the application of water pressure on crack surfaces for the simulation of hydraulic fracture initiation and propagation. To take into consideration the effects of drainage in numerical modelling and simulation, two coupled (multi-physics) finite element models are used ; (1) one for the uplift pressures where a hydraulic mesh with refinement around drains is used, and (2) one for the mechanical response coupled with the computation of the unsaturated interstitial seepage problem. The two subproblems are solved using a partitioned procedure, as they have different resolution requirements. Finally, the mechanical mesh and the hydraulic mesh have non-matching discrete interfaces that must be coupled while respecting the equilibrium of the

applied loads. Applications of the proposed hydro-mechanical constitutive model and numerical solution strategy to different problems are presented on a wedge splitting test and a full scale gravity dam including multiple drainage configurations. A case study adapted from a real dam is also given with a complex 3D non-planar discontinuity surface.

Keywords : Fully Coupled Hydro-Mechanical model, Hydraulic fracturing, Extended Finite Element Method, Drainage

4.2 Introduction

The flow problem in deforming porous media has been a popular research topic for a considerable time. Interest in the role of these coupled diffusion-deformation mechanisms was initially motivated by the problem of consolidation. Terzaghi's theory of one-dimensional consolidation can be considered as the first study in deformable porous media, which led to a one-dimensional consolidation theory on the basis of the effective stress concept Terzaghi (1923). Terzaghi's theory was extended to three-dimensional cases by Biot Biot (1935, 1941),who formulated the basic linear theory of poroelasticity, and it has since been reformulated several times Biot (1955, 1956); Verruijt (1969); Rice & Cleary (1976). Biot's theory was in turn extended to three-phase conditions with pore air as the third phase Fredlund & Morgenstern (1977); Chang & Duncan (1983). This multiphase flow is particularly important when computing the decrease in liquid-water content during the drying process in concrete. This drying process is associated with capillary effects that can induce shrinkage Bažant & Najjar (1972); Wittmann (1973). Non-uniform drying induces tensile stresses that may be much larger than the concrete tensile strength and eventually cause cracking Bisschop & van Mier (2002). The equations to correctly model the drying phenomena must be derived from thermodynamic principles Baroghel-Bouny *et al.* (1999); Mainguy *et al.* (2001).

Flow in damaged porous media has received more attention since the 1990's. The presence of damage, cracks, joints or faults, can noticeably change the physical behavior of the porous medium. The flow within the discontinuities with higher permeability is of different nature than the flow within the deforming interstitial medium. Depending on the problem being investigated, the interaction between the discontinuities and its surroundings, especially in the vicinity of the crack tip where a fluid lag can be observed Advani *et al.* (1993), can be important.

The simulation of hydraulically-driven fractures in poroelastic materials can be achieved using different approaches. A partitioned solution procedure to solve a finite element approximation to a poroelasticity problem in conjunction with a finite difference approximation for modelling fluid flow along the fracture is proposed in Boone & Ingraffea (1990). Using the Strong Discontinuities Approach (SDA) in fully saturated porous media with the incorporation of the local effects of surfaces discontinuity in the displacement field is presented in Armero & Callari (1999). The proposed framework involves the solution of the coupled conservation equation of the fluid mass and seepage through the porous solid via Darcy's law, taking into account a continuous pressure field with discontinuous gradients, and leading to discontinuous fluid flow vectors across strong discontinuities. Similar assumptions are used within the eXtended Finite Element Method (XFEM) framework in Jox *et al.* (2006), and using the Partition of Unity Finite Element Method (PUFEM) in Réthoré *et al.* (2007). The pressure field in the discontinuity can also be modeled by enriching the pressure to take into account its discontinuity across the domains Abellan *et al.* (2005) and thereby consider the membrane effect. Coupling schemes for modelling hydraulic fracture propagation using XFEM for the two-dimensional Khristianovic–Geertsma–de Klerk (KGD) model is proposed in Gordeliy & Peirce (2013). A fully coupled hydromechanical numerical method with a partial, modified adaptation of the XFEM to include pre-existing intersecting fractures is proposed in Watanabe *et al.* (2012). XFEM is also applied for partially saturated porous media including cohesive cracks in Mohammadnejad & Khoei (2013). Finally, the phase-field method was applied Wheeler *et al.* (2014); Yoshioka & Bourdin (2016); Wilson & Landis (2016) for fracture problem coupled to diffusion of fluids.

To better understand hydraulic fracturing in complex, layered, naturally fractured reservoirs, fully 3D models must be developed. An early three-dimensional work, in which an inclined borehole is simulated during the early stages of the hydraulic fracturing process, was applied in the oil industry Morales *et al.* (1993). More recently, a three-dimensional numerical model based on the XFEM for the simulation of cohesive cracks in cementitious materials, such as concrete, in a hydromechanical framework was presented in Becker *et al.* (2010). Simulations of 3D non-planar fracture propagation using an adaptive Generalized Finite Element Method (GFEM) are given in Gupta & Duarte (2014). Rungamornrat *et al.* (2005) developed a computational technique for simulating the non-planar evolution of hydraulic fractures in 3D elastic media, making use of a symmetric Galerkin boundary element method to treat the elasticity problem associated with a fracture in an unbounded domain. A three-dimensional GFEM formulation is proposed in Meschke & Leonhart (2015), where physically motivated enrichment functions are used to approximate the liquid pressure near discontinuities.

Seepage problems with complex drainage systems are commonly encountered in civil engineering. To numerically include the effect of their presence in the interstitial media, Fipps *et al.* (1986) proposed including the drainage effects using logarithmically-varied adjustment factors to modify the hydraulic conductivity and by incorporating a modified mesh in the vicinity of the drain to produce accurate drain flow estimates. A numerical solution combining the substructure technique with a variational inequality formulation of Signorini's type is proposed in Chen *et al.* (2008) to include the effect of drainage.

In this paper, we present a combined segregated, fully-coupled hydromechanical model for application to non-planar 3D hydraulic fractures in which there are complex flows. To describe a discontinuity such as a crack, the cohesive XFEM is used. The XFEM formulation allows the crack aperture's progress to be calculated, as well as the water pressure on the crack surfaces to simulate hydraulic fracture initiation and propagation. Two coupled (multi-physics) finite element models are used to account for the effects of drainage in numerical modelling : (1) one for the uplift pressures, incorporating a hydraulic mesh with refinement around the drains ; and (2) one for the mechanical response coupled with the computation of the unsaturated interstitial seepage problem. These two sub-problems are solved using a partitioned procedure, as they have different resolution requirements. The mechanical mesh and the hydraulic mesh have non-matching discrete interfaces that must be coupled while respecting the equilibrium of the applied loads.

This paper is organized as follows. Section 4.3 presents the strong form of the partial differential equations governing the propagation of hydraulic fractures in a porous medium. This section describes equations governing solid skeleton deformation, fluid transport in a coupled unsaturated interstitial medium and the fluid transport in discontinuities. Section 4.4 gives the weak form of the conservation equation required to solve the coupled hydromechanical problem. The discretization using the Bubnov-Galerkin method is presented in section 4.5. A solution algorithm for discontinuity path computation and hydraulic mesh generation is given in section 4.6. The hydraulic mesh is automatically generated on the crack surface with the possible inclusion of drains, with a particular emphasis on the fact that this surface is not known a priori. A key aspect when solving a partitioned problem with computational domains that have non-matching discrete interfaces is the transfer of the structural crack apertures to the hydraulic mesh, and the transfer of the hydraulic pressures to the mechanical problem by respecting the applied load equilibrium. This algorithm is presented in section 4.7. In section 4.8, the embedded drain approach used to model the effect of the presence of drains on the pressure distribution in the solid skeleton is detailed. Drains are not geometrically present in the mechanical mesh, and so geometric manipulations must be performed to integrate them into the hydraulic mesh. Hence, the drainage in the discontinuity achieved by discretizing the drains' geometry in the hydraulic mesh is also presented in this section. Finally, section 4.10 presents applications of the proposed hydromechanical constitutive model and numerical solution strategy to different problems. The wedge splitting test, including a multiple drainage configuration, is given first. Next, the Koyna dam (103-m-high concrete gravity dam) is used as a benchmark model to show that the proposed method can be used to optimize the drainage configuration. A case study which has a complex 3D non-planar discontinuity surface adapted from a real dam is presented. Three drainage configurations are compared to show the effects of drainage on crack propagation. The case study demonstrates how the proposed hydromechanical constitutive model can be applied in an industrial context. This section also presents a case that includes the effects of unsaturated moisture transport in a discontinuity of a three-point beam. The paper concludes with a summary of the results and recommendations for future work.

4.3 Strong form of the coupled hydromechanical problem

Partial differential equations governing the propagation of hydraulic fractures in a porous medium involve the coupling of various physical phenomena. The system of equations must be able to (i) describe the deformation of the solid skeleton, (ii) represent the pore fluid flow in the interstitial medium, and (iii) describe the fluid flow in fracture. The fluid exchange between the fracture and the surrounding porous medium must also be taken into account.

4.3.1 Description of the solid skeleton deformation

Biot's model of a porous fluid-filled material is constructed on the conceptual model of a solid skeleton and a freely moving pore fluid where the solid and fluid phases are fully connected. Two kinematic quantities must be computed : the movement of the porous solid with respect to a reference configuration and the fluid movement with respect to the solid. The description of stress in the fluid is limited to its hydrostatic component. Therefore, the total stress σ in Voigt notation is related to the effective stress σ' and the liquid pressure p such that :

$$\sigma = \sigma' + \mathbf{m}p \tag{4.1}$$

where $\mathbf{m}$ is defined for isotropic behavior as $\mathbf{m}^T = b\,\{1\ 1\ 1\ 0\ 0\ 0\}$, with $b\,(0 \leq b \leq 1)$ as the Biot coefficient. Under the hypothesis of small displacements, the elastostatic problem to describe the deformation of the solid skeleton is governed by the following equilibrium equations, boundary conditions and initial conditions :

$$
\begin{aligned}
\nabla \cdot \sigma + \mathbf{b} &= 0 && \text{in } \Omega = \Omega^{+} \cup \Omega^{-} \\
\mathbf{u} &= \bar{\mathbf{u}} && \text{on } \Gamma_u \\
p &= \bar{p} && \text{on } \Gamma_p \\
\sigma \cdot \mathbf{n}_t &= \bar{\mathbf{t}} && \text{on } \Gamma_t \\
[[\sigma \cdot \mathbf{n}_{\Gamma_d}]] &= \mathbf{t}_d && \text{on } \Gamma_d \\
\mathbf{u} &= \mathbf{u}_0 && \text{at } t = 0 \\
p &= p_0 && \text{at } t = 0
\end{aligned}
\tag{4.2}
$$

defining $\mathbf{n}_t$ and $\mathbf{n}_{\Gamma_d}$ respectively the unit normal vectors to Γ_t and Γ_d. In the presence of a

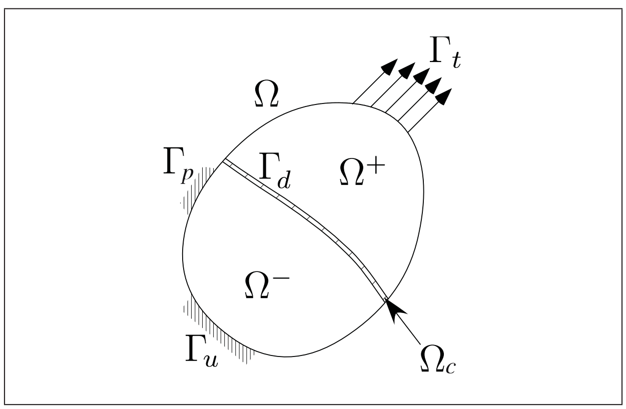

Figure 4.1 Notation for solid skeleton

discontinuity Γ_d, system (4.2) is solved using the XFEM approach.

4.3.2 Description of the fluid transport in the coupled interstitial medium

To describe the fluid flow in an interstitial medium, two hypotheses are considered ; (i) a fully saturated medium, and (ii) an unsaturated medium. Under the hypothesis of fully saturated medium, the fluid movement is governed by the law relating the velocity vector $\mathbf{v}$ to the driving force $-\nabla p_l$. In this section p is replaced by the liquid pressure p_l to explicitly differentiate the different pressures of constituents of an unsaturated medium. Linearly relating $\mathbf{v}$ to $-\nabla p_l$ and neglecting body loads is the simplest form that this law can take which leads to the expression of Darcy's law :

$$\mathbf{v} = -\frac{k}{\mu_l}\nabla p_l, \tag{4.3}$$

where k is the permeability and μ_l the fluid viscosity. For a fully saturated porous medium, the constitutive equation expressed in terms of the balance of fluid mass for unsteady state pressure leads to :

$$S_s\frac{\partial p_l}{\partial t} + b\nabla\cdot\frac{\partial \mathbf{u}}{\partial t} = \nabla\cdot\left(\frac{k}{\mu_l}\nabla p_l\right) \tag{4.4}$$

where the specific storage S_s is given by Bear (1972) :

$$S_s = \rho_l g\left(\frac{\phi}{E_l} + \frac{1-\phi}{E_s}\right) \tag{4.5}$$

with ρ_l the water density, g the gravitational acceleration, E_l and E_s the bulk modulus of water and the solid skeleton, respectively, and where ϕ represents the porosity. For an unsaturated medium, the relation between the velocity vector and the driving force is nonlinear and depends on the saturation level. An unsaturated porous medium such as concrete and soil is composed of three constituents : a solid skeleton, a liquid-water phase (index l), and a gas phase (index g). The gas phase is composed of water vapor (index v) and dry air (index a). To define the conservation equation in an unsaturated medium, the flow velocity $\mathbf{w}$ for each constituent must be defined Mainguy *et al.* (1999) :

$$\mathbf{w}_l = -\rho_l\frac{k}{\mu_l}k_{rl}(S_l)\nabla p_l \tag{4.6a}$$

$$\mathbf{w}_v = -\rho_v\frac{k}{\mu_g}k_{rg}(S_l)\nabla p_g - \left(\frac{M_v}{RT}\right)D_{va}(T,p_g)f(S_l,\phi)\nabla C_v \tag{4.6b}$$

$$\mathbf{w}_a = -\rho_a\frac{k}{\mu_g}k_{rg}(S_l)\nabla p_g - \left(\frac{M_a}{RT}\right)D_{va}(T,p_a)f(S_l,\phi)\nabla C_a \tag{4.6c}$$

where R is the ideal gas constant, T the absolute temperature, M_α the molar mass of constituent α, C_α the molar fraction of constituent α, ρ_α the density of constituent α and p_α is the pressure of constituent α. The permeability of constituent α is reduced by a relative permeability factor $k_{r\alpha}(S_l)$, which is a function of the degree of saturation S_l. The diffusion coefficient of water vapor in wet air D_{va} (cm/s) is given by :

$$D_{va}(T, p_g) = 0.217 p_{atm} \left(\frac{T}{T_0}\right)^{1.88} \tag{4.7}$$

with T_0 the reference temperature (273 K) and $p_{atm} = 101325$ Pa. The function $f(S_l, \phi)$ represents the resistance factor to gaseous diffusion in a porous medium compared to the case of free diffusion and takes the form Millington (1959) :

$$f(S_l, \phi) = \phi^{4/3} (1 - S_l)^{10/3} \tag{4.8}$$

The saturation degree S_α of constituent α is defined by :

$$S_\alpha = \frac{\phi_\alpha}{\phi}; \qquad \sum_\alpha S_\alpha = 1 \tag{4.9}$$

where ϕ denotes the total porosity through which fluid flow occurs and ϕ_α the fraction occupied by $\alpha =$ {liquid, vapor, air}. The mass conservation equations of each constituent together with the state equations form the modelling basis of water transfer in unsaturated porous media. Solving this system of highly nonlinear equations makes the development of numerical models complex. Therefore, depending on the solid material involved in the water transfer, some assumptions can be made to simplify the model. Assuming the gas pressure remains constant and equals to the atmospheric pressure during the transport process greatly simplifies the equations. This assumption is based on the fact that due to the high conductivity of the vapor-air phase, any change in its pressure, disappears almost immediately as air transport occurs almost instantaneously compared to the time scale of all other phenomena Mainguy *et al.* (2001). Moreover, for low permeability materials, drying is ultimately achieved by transporting moisture in its liquid form. The diffusion of the vapor quickly becomes inactive for the transport of moisture Mainguy *et al.* (2001). Hence only the conservation equation formulated as the moisture transport in liquid form is required :

$$\frac{\partial \phi \rho_l S_l(p_l)}{\partial t} = -\nabla \cdot \mathbf{w}_l \tag{4.10}$$

This yields the final non linear diffusion equation, formulated in u-p form for application to low permeability materials at constant gas pressure :

$$\phi \frac{\partial S_l(p_l)}{\partial t} + b\nabla \cdot \frac{\partial \mathbf{u}}{\partial t} = \nabla \cdot \left(k_{rl}(S_l) \frac{k}{\mu_l} \nabla p_l \right) \tag{4.11}$$

An expression of the often-admitted relative water permeability factor $k_{rl}(S_l)$ is given by the model of Mualem van Genuchten (1980) :

$$k_{rl}(S_l) = S_l^{1/2} \left(1 - \left(1 - S_l^{1/m}\right)^m\right)^2 \tag{4.12}$$

with m a material parameter. The imposition of liquid pressure boundary conditions requires a relation between the relative humidity h_r and the degree of saturation achieved using Kelvin's law (4.13) :

$$\frac{\rho_l RT}{M_v} \ln h_r = -p_c \qquad h_r = \frac{p_v}{p_{vs}} \tag{4.13}$$

with p_c the capillary pressure, p_v the vapor pressure and p_{vs} the saturation vapor pressure. At the macroscopic scale, the capillary pressure between two fluids is introduced as the pressure difference between the non-wetting fluid and the wetting fluid due to the phenomenon of surface tension. In our case, the wetting fluid is water and the non-wetting fluid is the gas. Therefore, the capillary pressure is defined as :

$$p_c = p_g - p_l \tag{4.14}$$

The expression linking the liquid saturation to the capillary pressure depends on the material, the saturating fluids and the temperature. The relationship is not the same when the material is adsorbing or desorbing water. This phenomenon results in a sorption curve that differs from the desorption curve. A model often used in the literature for desorption can be found by using the Mualem model van Genuchten (1980) :

$$p_c(S_l) = a\left(S_l^{-1/m} - 1\right)^{1-m} \tag{4.15}$$

The values of the parameters are $a = 18.6$ MPa and $m = 0.44$ for a standard concrete with a compressive strength f_c'=50 MPa Baroghel-Bouny *et al.* (1999). From this equation, for a 90% degree of saturation, the capillary pressure is 9 MPa. In comparison, the pressure of the gas phase is approximately 0.1 MPa. It is therefore possible to make the assumption that :

$$p_c \approx -p_l \tag{4.16}$$

Solving equation 4.11 with the relations 4.12, 4.15, 4.16, and imposing the liquid pressure at the boundaries using 4.13 and 4.16, allows to compute the water transfer in unsaturated porous media inside a structure as a function of time.

The equation system composed of 4.2, of 4.4 or 4.11 and the fluid transport in the discontinuities can be solved using either a segregated or a coupled algorithm. The coupled problem leads to the solution of an unsymmetrical and often ill-conditioned matrix system that may demand considerable computational efforts, especially when the solved system is nonlinear. To simplify the solution process, it is common to make the assumption of a laminar and incompressible flow between two smooth parallel plates for the computation of the fluid flow through discontinuities. However, by using a segregated algorithm, it is possible to solve the nonlinear flow problem in the discontinuity with fewer assumptions and without affecting the overall solution procedure. This method is presented in the next section.

4.3.3 Description of the fluid transport in discontinuities

Starting with the Navier-Stokes equations and using the assumptions that the flow velocity through the crack wall is negligible compared to that in the tangent direction and that the inertial forces are negligible compared to the viscous forces one can derive the general equation for flow in the discontinuities as :

$$S_d \frac{\partial H}{\partial t} = \nabla \cdot (w_{cr} k_{cr} \nabla H) \tag{4.17}$$

with w_{cr} the crack opening, k_{cr} the hydraulic conductivity coefficient and H the total water head. The crack opening considered in this section corresponds to the average mechanical crack opening which is a measure of the void between the surfaces of the crack, while the hydraulic opening is an equivalent opening where the fluid flow can take place. Numerous experimental tests compiled in Barton & de Quadros (1997) have clearly shown that hydraulic opening is considerably smaller than the mechanical opening. This is mainly caused by the surface roughness and the tortuosity of the crack. Other parameters influencing this aperture reduction are shown in Figure 4.2.

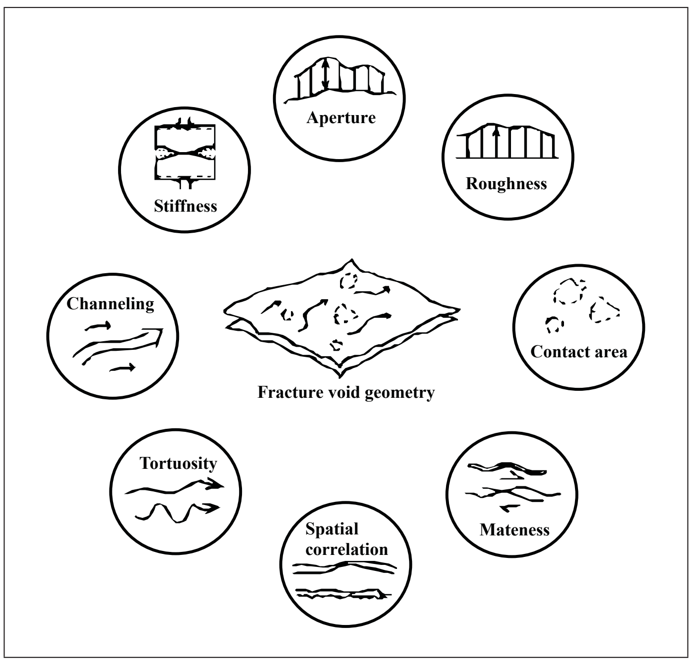

Figure 4.2 Factors affecting flow in a discontinuity (Hakami, 1995)

An expression linking the mechanical opening $w_{cr}^{(m)}$ to the hydraulic opening $w_{cr}^{(h)}$ is given by Barton *et al.* (1985) :

$$w_{cr}^{(h)} = \frac{{w_{cr}^{(m)}}^2}{JRC^{2.5}} \text{ with } \frac{w_{cr}^{(m)}}{w_{cr}^{(h)}} \geq 1 \tag{4.18}$$

where *JRC* is the joint roughness coefficient of the surface and $w_{cr}^{(h)}, w_{cr}^{(m)}$ are in units of microns (μm). The *JRC* is not easy to define for real applications. Therefore, computing flow rates using mechanical opening gives an upper limit and defining the hydraulic opening prior to compute flow rates remains a challenging task.

In equation 4.17, the specific storage capacity given by :

$$S_d = \rho g \left(\frac{1}{K_n} + w_{cr}\beta \right) \tag{4.19}$$

where g is the gravity, ρ the fluid density, K_n the normal crack stiffness given by $K_n = -\dfrac{\partial \sigma_n}{\partial w_{cr}}$, β the fluid compressibility and σ_n is the normal effective stress in the discontinuity. The total water head is given by :

$$H = z + \frac{p}{\rho g} + \frac{\mathbf{v}_{cr}^2}{2g} \tag{4.20}$$

with $\mathbf{v}_{cr}$ the velocity of the fluid in the crack. The hydraulic conductivity coefficient k_{cr} is related to the flow profile inside the crack. For example, for a parallel laminar flow where the velocity profile is parabolic, the hydraulic conductivity coefficient is given as :

$$k_{cr} = \frac{g w_{cr}^2}{12\nu} \tag{4.21}$$

corresponding to the Hele-Shaw flow, with ν the fluid kinematic viscosity. For other types of flow profiles, the results of several authors were recorded Louis (1969) and a series of five flow laws with their associated validity ranges were defined. A parameter h_a/D_h refered to as the "relative roughness" is used to define the crack roughness, where h_a is the average asperity height in the crack and D_h is the hydraulic diameter (equals to two times the crack opening width). By definition, the relative roughness of a crack is zero for a smooth crack and 0.5 for a rough crack with asperities the size of the crack opening. Flow in a crack is considered parallel for low values of relative roughness ($h_a/D_h < 0.033$), whereas for $h_a/D_h \geq 0.033$, the flow will be non-parallel.

The flow velocity distribution made by Louis Louis (1969), taking into account the roughness of the crack is given by :

$$\mathbf{v}_{cr} = k_{cr} |\nabla H|^{\alpha - 1} \nabla H \tag{4.22}$$

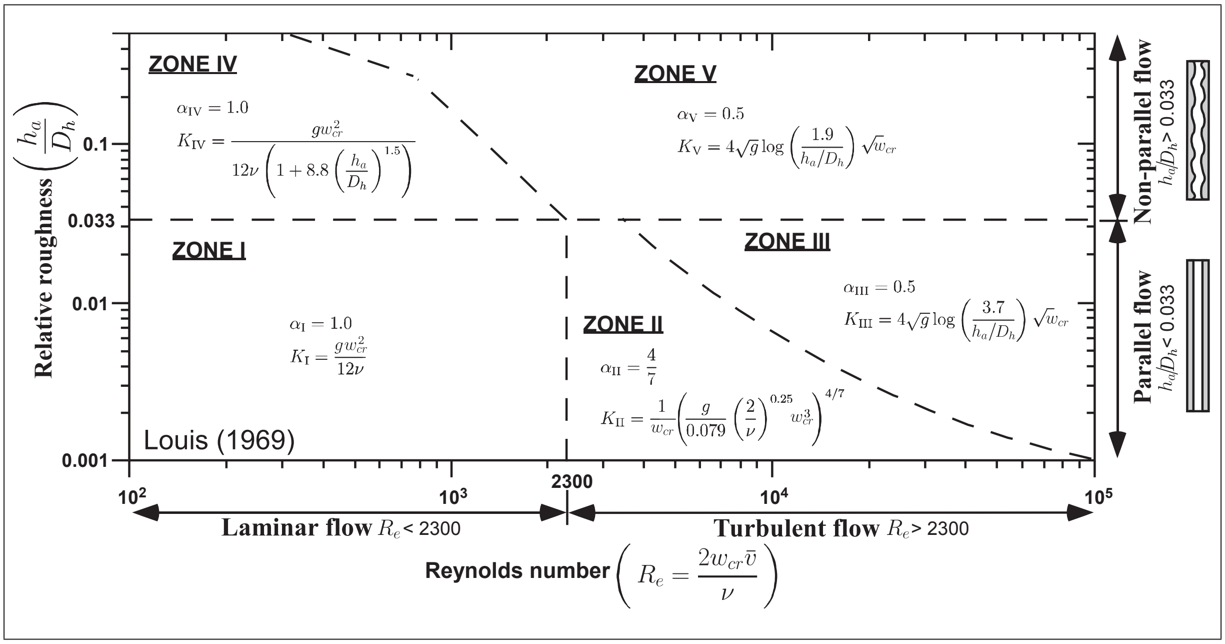

Figure 4.3 Compilation of the different flow laws and their ranges of validity [after (Louis, 1969)]

The values of hydraulic conductivity k_{cr} and the exponent α depend on the type of flow as described in Figure 4.3. For hydraulically-smooth parallel flow the transition from laminar to turbulent flow occurs at approximately $R_e = 2300$, with the Reynolds number defined by :

$$R_e = \frac{2w_{cr}||\mathbf{v}_{cr}||}{\nu} \tag{4.23}$$

Adding boundary conditions (water head H at the boundaries), equation (4.17) can solve the flow problem in the discontinuity. If turbulent flow conditions are encountered (zones II, III, and V), the velocity is not proportional to the hydraulic gradient and the formulation of the problem leads to a nonlinear equation.

4.4 Weak form of the hydromechanical problem

4.4.1 Coupled hydromechanical problem

The three conservation equations required to solve the coupled hydromechanical problem (4.2, 4.4 or 4.11) were given in their strong form in the previous section. Two types of equations will be solved using their weak forms : balance of momentum (equation 4.2) and diffusion equations (4.4, 4.11).

Starting with the momentum equation, the trial function space $\mathscr{U}$ and the weighting function space $\delta\mathscr{U}$ are introduced as :

$$\begin{aligned} \mathscr{U} &= \{\mathbf{u} \mid \mathbf{u} \in W^1, \mathbf{u} = \mathbf{u}_b \text{ on } \Gamma_u\}, \\ \delta\mathscr{U} &= \{\delta\mathbf{u} \mid \delta\mathbf{u} \in W^1, \delta\mathbf{u} = 0 \text{ on } \Gamma_u\} \end{aligned} \tag{4.24}$$

where $W^1 = H^1(\Omega \backslash \Gamma_d)$ is a first order Sobolev space of functions. Within the framework of the extended finite element method, cracks can be modelled by enriching the displacement interpolation of the element crossed by the discontinuity with special purpose functions and by introducing additional test functions on the displacement jump to the problem. Hence, the admissible test function $\delta\mathbf{u}$ is decomposed into two independent admissible test functions :

$$\delta\mathbf{u} = \delta\bar{\mathbf{u}} + \mathscr{H}\delta\hat{\mathbf{u}} \tag{4.25}$$

with $\mathscr{H}$, the Heaviside function defined as :

$$\mathscr{H}(\phi) = \begin{cases} 1, & \phi > 0 \quad (\text{in } \Omega^+ \subset \Omega) \\ 0, & \text{else} \quad (\text{in } \Omega^- \subset \Omega) \end{cases} \quad \Omega = \Omega^+ \cup \Omega^- \tag{4.26}$$

The weak form of the problem is obtained by multiplying equation 4.2 by δu and integrating over Ω, where Ω is an open subset of R^n :

$$\int_{\Omega} (\delta\bar{\mathbf{u}} + \mathscr{H}\delta\hat{\mathbf{u}})(\nabla\cdot\sigma + \mathbf{b})\ \mathrm{d}\Omega = 0 \tag{4.27}$$

Applying the divergence theorem for the problems, the following set of equations can be obtained

$$\begin{aligned} \int_{\Omega} \nabla\delta\bar{\mathbf{u}} : \sigma\ \mathrm{d}\Omega &= \int_{\Gamma_t} \delta\bar{\mathbf{u}}\cdot\bar{\mathbf{t}}\ \mathrm{d}\Gamma_t + \int_{\Omega} \delta\bar{\mathbf{u}}\cdot\mathbf{b}\ \mathrm{d}\Omega \\ \int_{\Omega^\star} \nabla\delta\hat{\mathbf{u}} : \sigma\ \mathrm{d}\Omega^\star + \int_{\Gamma_d} \delta\hat{\mathbf{u}}\cdot\mathbf{t}_d\ \mathrm{d}\Gamma_d &= \int_{\Gamma} (\mathscr{H}\delta\hat{\mathbf{u}})\cdot\bar{\mathbf{t}}\ \mathrm{d}\Gamma + \int_{\Omega^\star} \delta\hat{\mathbf{u}}\cdot\mathbf{b}\ \mathrm{d}\Omega^\star \end{aligned} \tag{4.28}$$

It must be noted that $\mathscr{H}$ has been eliminated by changing the integration domain from Ω to $\Omega^\star$, and $\Omega^\star$ is the set of enriched elements. Thus, the integration is performed only on the body parts where $\hat{\mathbf{u}}$ is non-zero due to the Heaviside function. The surface integral on the discontinuity Γ_d comes from the boundary condition (4.2) defined earlier ($\left[\left[\sigma\cdot\mathbf{n}_{\Gamma_d}\right]\right] = \mathbf{t}_d$ on Γ_d). This integral can be expanded by defining the unit normal vectors on both sides of the discontinuity as $\mathbf{n}_{\Gamma_d^+}$ and $\mathbf{n}_{\Gamma_d^-}$ directed respectively towards Ω^- and Ω^+. Note that the unit normal is taken as $\mathbf{n}_{\Gamma_d} = \mathbf{n}_{\Gamma_d^-} = -\mathbf{n}_{\Gamma_d^+}$.

Hence, the fluid transport in the interstitial space, defined as $\Omega\backslash\Omega_c$, where Ω_c are the discontinuities channels, can be defined by introducing the trial function space $\mathscr{P}$ and the weighting function space $\delta\mathscr{P}$ for the diffusion problem such that :

$$\begin{aligned} \mathscr{P} &= \{p \mid p \in W^1, p = p_b \text{ on } \Gamma_p\}, \\ \delta\mathscr{P} &= \{\delta p \mid \delta p \in W^1, \delta p = 0 \text{ on } \Gamma_p\} \end{aligned} \tag{4.29}$$

then allows the weak form to be obtained by multiplying the governing equation by the weighting function and integrating over the volume using the divergence theorem to get :

$$\int_{\Omega\backslash\Omega_c} \left(c\frac{\partial\Phi}{\partial t} + b\nabla\frac{\partial\mathbf{u}}{\partial t}\right)\delta p\ \mathrm{d}\Omega + \int_{\Omega\backslash\Omega_c} (\nabla\delta p\mathbf{K}\nabla p)\ \mathrm{d}\Omega = 0 \tag{4.30}$$

with $\mathbf{K} = \delta_{ij}k$ and $c = \{S_s, \phi\}$, $\Phi = \{p, S_l(p)\}$ for the weak form of the fluid transport in : (i) the fully saturated porous medium (equation 4.4), and in (ii) the unsaturated porous medium (equation 4.11), respectively.

4.4.2 Fluid transport problem in the discontinuities

The weak form of the fluid transport in discontinuities (equation 4.17) is similar to the diffusion problem in the preceding section (without the coupling with the solid skeleton deformation rate), however the trial function space and the weighting function space are respectively formulated in terms of total water head H and δH instead of pressure, yielding :

$$\int_{\Omega_c} \left(S_d \frac{\partial H}{\partial t} \right) \delta H \; \mathrm{d}\Omega_c + \int_{\Omega_c} \left(\nabla \delta H \left(w_{cr} k_{cr} \right) \nabla H \right) \; \mathrm{d}\Omega_c = 0 \tag{4.31}$$

4.5 Numerical development of the hydromechanical problem

4.5.1 Coupled hydromechanical problem

Replacing $\mathbf{u}$, p, $\delta\mathbf{u}$ and δp in the weak form by their approximations $\mathbf{u}^h \in \mathscr{U}^h$, $p^h \in \mathscr{P}^h$, $\delta\mathbf{u} \in \delta\mathscr{U}^h$ and $\delta p \in \delta\mathscr{P}^h$, respectively and using the Bubnov-Galerkin method, where the trial functions and the test functions are discretized in the same space, requires the representation of $\mathbf{u}^h$ and p^h in terms of shape functions and their gradients to produce the matrix form of the problem such that :

$$\begin{aligned} \mathbf{u}^h &= \mathbf{N}\bar{\mathbf{u}} + \mathbf{N}\mathscr{H}\hat{\mathbf{u}}, & \nabla\mathbf{u}^h &= \mathbf{B}\bar{\mathbf{u}} + \mathbf{B}\mathscr{H}\hat{\mathbf{u}} + \delta_D \hat{\mathbf{u}} \otimes \mathbf{n}_d \\ p^h &= \mathbf{H}p, & \nabla p^h &= \nabla\mathbf{H}p \end{aligned} \tag{4.32}$$

where δ_D is the Dirac distribution. Replacing the trial spaces and the weighting spaces in the weak form with the shape function of their approximations $\mathbf{u}^h$ and p^h leads to :

$$\begin{aligned}
\int_{\Omega} \mathbf{B}^{\mathrm{T}} \sigma \,\mathrm{d}\Omega &= \int_{\Gamma} \mathbf{N}^{\mathrm{T}} \bar{\mathbf{t}} + \int_{\Omega} \mathbf{N}^{\mathrm{T}} \mathbf{b} \,\mathrm{d}\Omega \\
\int_{\Omega^\star} \mathbf{B}^{\mathrm{T}} \sigma \,\mathrm{d}\Omega^\star + \int_{\Gamma_d} \mathbf{M}^{\mathrm{T}} \mathbf{t}_d \,\mathrm{d}\Gamma_d &= \int_{\Gamma} \mathscr{H} \mathbf{N}^{\mathrm{T}} \bar{\mathbf{t}} \,\mathrm{d}\Gamma + \int_{\Omega^\star} \mathbf{N}^{\mathrm{T}} \mathbf{b} \,\mathrm{d}\Omega^\star \\
\int_{\Omega \setminus \Omega_c} \mathbf{H}^T c \frac{\partial \Phi}{\partial t} \,\mathrm{d}\Omega + \int_{\Omega \setminus \Omega_c} \mathbf{H}^T b \nabla \cdot \frac{\partial \mathbf{u}}{\partial t} \,\mathrm{d}\Omega &+ \int_{\Omega \setminus \Omega_c} \nabla \mathbf{H}^T \mathbf{K} \nabla p \,\mathrm{d}\Omega = 0
\end{aligned} \tag{4.33}$$

in which $\mathbf{M}$ comprises the shape functions $\mathbf{N}$ evaluated on Γ_d and where $\mathbf{t}_d$ is the cohesive force. In equation 4.33 the enrichment functions should be shifted so that the product of the shape functions and the enrichment functions cancels out at each node, as proposed in Belytschko *et al.* (2001). Therefore, only those elements that are crossed by the discontinuity should be treated differently. Using relation 4.1 in the preceding system of equations, thereby decoupling the total stress in effective stress and liquid pressure, leads to the formulation of the matrix system of an enriched element :

$$
\begin{bmatrix}
0 & 0 & 0 \\
0 & 0 & 0 \\
\int_{\Omega} \mathbf{B}^{\mathrm{T}}\mathbf{m}^{T}\mathbf{H}\,\mathrm{d}\Omega & \int_{\Omega^{\star}} \mathbf{B}^{\mathrm{T}}\mathbf{m}^{T}\mathbf{H}\,\mathrm{d}\Omega^{\star} & \int_{\Omega\backslash\Omega_c} \mathbf{H}^{\mathrm{T}}c\mathbf{H}\,\mathrm{d}\Omega
\end{bmatrix}
\begin{Bmatrix} \dot{\bar{\mathbf{u}}} \\ \dot{\hat{\mathbf{u}}} \\ \dot{p} \end{Bmatrix} +
$$

$$
\begin{bmatrix}
\int_{\Omega} \mathbf{B}^{\mathrm{T}}\mathbf{C}\mathbf{B}\,\mathrm{d}\Omega & \int_{\Omega^{\star}} \mathbf{B}^{\mathrm{T}}\mathbf{C}\mathbf{B}\,\mathrm{d}\Omega^{\star} & \int_{\Omega} \mathbf{B}^{\mathrm{T}}\mathbf{m}^{T}\mathbf{N}\,\mathrm{d}\Omega \\
\int_{\Omega^{\star}} \mathbf{B}^{\mathrm{T}}\mathbf{C}\mathbf{B}\,\mathrm{d}\Omega^{\star} & \int_{\Omega^{\star}} \mathbf{B}^{\mathrm{T}}\mathbf{C}\mathbf{B}\,\mathrm{d}\Omega^{\star} + \int_{\Gamma_d} \mathbf{M}^{\mathrm{T}}\mathbf{T}\mathbf{M}\,\mathrm{d}\Gamma_d & \int_{\Omega^{\star}} \mathbf{B}^{\mathrm{T}}\mathbf{m}^{T}\mathbf{N}\,\mathrm{d}\Omega^{\star} \\
0 & 0 & \int_{\Omega\backslash\Omega_c} \nabla\mathbf{H}^{T}\mathbf{K}\nabla\mathbf{H}^{T}\,\mathrm{d}\Omega
\end{bmatrix}
\begin{Bmatrix} \bar{\mathbf{u}} \\ \hat{\mathbf{u}} \\ p \end{Bmatrix}
$$

$$
= \begin{Bmatrix} f_{\bar{u}}^{ext} + f_{\bar{u}}^{body} \\ f_{\hat{u}}^{ext} + f_{\hat{u}}^{body} \\ q_{\hat{u}}^{ext} \end{Bmatrix} - \begin{Bmatrix} f_{\bar{u}}^{int} \\ f_{\hat{u}}^{int} \\ q_{\hat{u}}^{int} \end{Bmatrix} \tag{4.34}
$$

where $f_{\bar{u}}^{ext}$ and $f_{\hat{u}}^{ext}$ contain the external loads and $f_{\bar{u}}^{body}$ and $f_{\hat{u}}^{body}$ contain the body loads. To achieve the coupling between the fracture and the porous medium, the interfacial force vector $f_{\hat{u}}^{int}$ due to the fluid pressure exerted on the discontinuity faces can be discretized as :

$$
f_{\hat{u}}^{int} = \int_{\Omega^{\star}} \mathbf{B}^{\mathrm{T}}\sigma\,\mathrm{d}\Omega^{\star} + \int_{\Gamma_d} \mathbf{N}^{T}\mathbf{t}_d\,\mathrm{d}\Gamma_d - \int_{\Gamma_d} \mathscr{H}\mathbf{N}^{T} p\mathbf{n}_{\Gamma_d}\,\mathrm{d}\Gamma_d \tag{4.35}
$$

The cohesive force matrix is given by :

$$
\mathbf{T} = T_n\left(\mathbf{n}_{\Gamma_d} \otimes \mathbf{n}_{\Gamma_d}\right) + T_t\left(\mathbf{m}_{\Gamma_d} \otimes \mathbf{m}_{\Gamma_d}\right) \tag{4.36}
$$

where $\mathbf{n}_{\Gamma_d}$ and $\mathbf{m}_{\Gamma_d}$ are the orientation (respectively the normal and tangent directions) of the channel defined. The normal T_n and tangential T_t forces per unit area are defined as Tvergaard (2003); Unger *et al.* (2007) :

$$\begin{aligned} T_n &= \sigma\left(\kappa(t)\right) \frac{u_n}{\kappa(t)} \\ T_t &= \sigma\left(\kappa(t)\right) \frac{\beta^2 u_t}{\kappa(t)} \end{aligned} \tag{4.37}$$

The traction-separation law is computed using a typical decaying function related to the history parameter $\kappa(t)$, characterizing the maximum value of parameter λ reached in the history of the interface :

$$\sigma(\kappa(t)) = f_t \exp^{-\frac{f_t}{G_F}\kappa(t)} \tag{4.38}$$

where G_F is the fracture energy and corresponds to the area under the complete softening stress-strain curve and f_t the uniaxial tensile strength. Using $\lambda = \sqrt{u_n^2 + (\beta u_t)^2}$, u_n and u_t as the normal opening and the tangential sliding, respectively, of the discontinuity surface, and β a material parameter that controls the weighting between the normal and tangential openings, a loading/unloading function can be defined as :

$$f\left(\lambda, \kappa(t)\right) = \lambda - \kappa(t), \text{ with } \kappa(t) = \max_{\tau \leq t}\left(\lambda(\tau)\right) \tag{4.39}$$

The relations 4.37 apply if $f\left(\lambda, \kappa(t)\right) \geq 0$ corresponding to a loading condition. If $f\left(\lambda, \kappa(t)\right) < 0$ corresponding to an unloading condition, a linear elastic path is used to represent the partly damaged interface. Finally, if contact occurs ($u_n \approx 0$), the contact condition is approximated by a penalty stiffness :

$$T_n = K_p u_n \tag{4.40}$$

and frictional sliding at the interface is given by :

$$T_t = -\operatorname{sign}(\dot{u}_t) \tan\left(\phi\right) T_n \tag{4.41}$$

where ϕ is the friction angle of the uncracked concrete.

4.5.2 Fluid transport problem in discontinuities

Assuming that no membrane effect exists in a discontinuity, meaning that the permeability of the discontinuity surfaces is infinite, the fluid transport problem in the discontinuities can be modeled using a collection of triangular elements located in a 3D space. The velocity profile transverse to the discontinuity is averaged and the permeability relation is computed using the relations found in figure 4.3. Hence, one can define an open set Ω in the space $\mathbb{R}^2$ where one seeks to solve equation (4.17) discretized into a collection of planar linear T3 triangular elements. The mesh is in the $\mathbb{R}^2$ space only locally, namely, it is on a surface in space $\mathbb{R}^3$, but when solving the problem, the element is transferred to a local coordinate system in the $\mathbb{R}^2$ space. The use of linear T3 triangle simplifies the evaluation of the conductivity matrix in the local coordinate system as it ensures that the element is planar. Because the total hydraulic load is independent of the coordinate system used (similar to a potential function), it is not necessary to transpose the conductivity matrix in the global coordinate system. Using this type of formulation, care must be taken to add the effect of total water head as a function of the discontinuity surface elevation variation.

For a triangular element (figure 4.4) located in a 3D space and defined with three nodes with shape functions $\{N_1 = 1 - \xi - \eta,\, N_2 = \xi \text{ and } N_3 = \eta\}$, its local coordinates x, y and z can be related to the global coordinates X, Y and Z by :

$$\begin{Bmatrix} x \\ y \\ z \end{Bmatrix} = [Q]^T \begin{Bmatrix} X \\ Y \\ Z \end{Bmatrix} \tag{4.42}$$

with

$$\Big[Q\Big] = \Big[\vec{t}_1 \quad \vec{t}_2 \quad \vec{n}\Big] \tag{4.43}$$

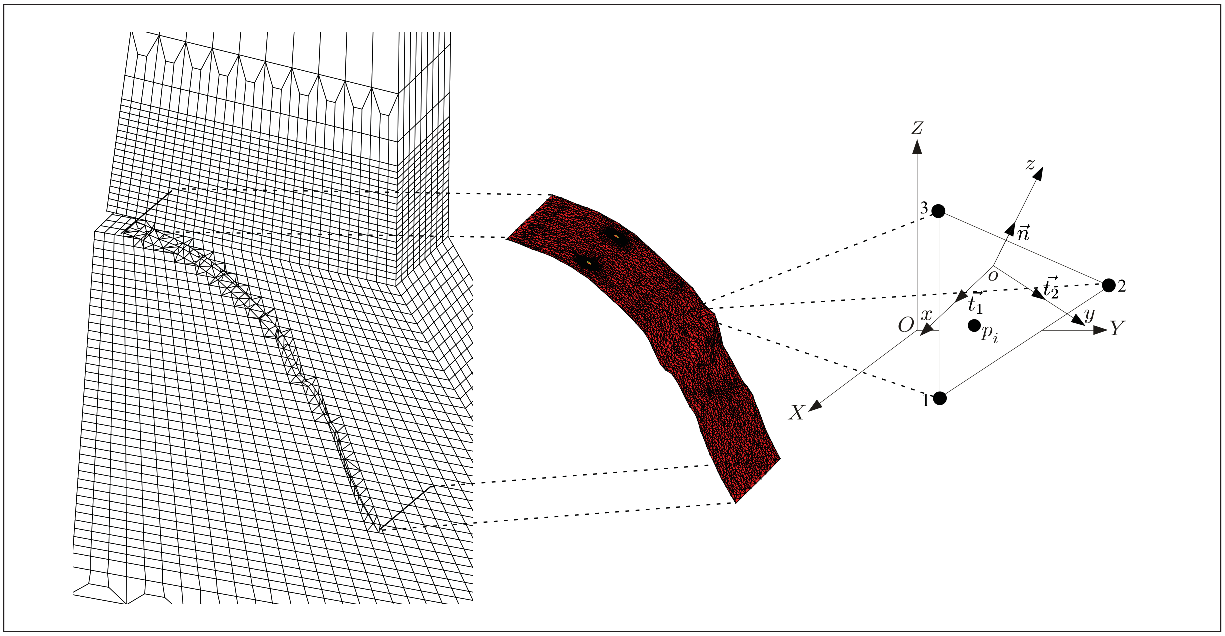

Figure 4.4 Hydraulic mesh (in red) generated in the discontinuity located at the zero level-set (illustrated on the left) constituted with a collection of T3 elements whose local coordinates (x, y, z) are located in the global space (X, Y, Z)

and

$$\vec{t}_1 = \begin{Bmatrix} \vec{n}_z + a\vec{n}_y^2 \\ -a\vec{n}_x\vec{n}_y \\ -\vec{n}_x \end{Bmatrix} \qquad \vec{t}_2 = \begin{Bmatrix} -a\vec{n}_x\vec{n}_y \\ \vec{n}_z + a\vec{n}_x^2 \\ -\vec{n}_y \end{Bmatrix} \qquad \vec{n} = \frac{\vec{a}_1 \otimes \vec{a}_2}{||\vec{a}_1 \otimes \vec{a}_2||} \tag{4.44}$$

where $a = 1/(1+\vec{n}_z)$. For $a = 0$, $\vec{t}_1 = \begin{Bmatrix} 1 & 0 & 0 \end{Bmatrix}^T$ and $\vec{t}_2 = \begin{Bmatrix} 0 & -1 & 0 \end{Bmatrix}^T$. The vectors $\vec{a}_1$ and $\vec{a}_2$ at point (ξ, η) are defined as :

$$\begin{aligned} \vec{a}_1 &= \sum_{i=1}^{3} \left(\frac{\partial \mathbf{N}_i(\xi, \eta)}{\partial \xi} \mathbf{X}_i \right) \\ \vec{a}_2 &= \sum_{i=1}^{3} \left(\frac{\partial \mathbf{N}_i(\xi, \eta)}{\partial \eta} \mathbf{X}_i \right) \end{aligned} \tag{4.45}$$

After the geometric transformation, the triangular element in the local system is parallel with the plane $x \circ y$. The Jacobian is computed using :

$$[\mathbf{J}] = \begin{bmatrix} \vec{t}_1 \odot \vec{a}_1 & \vec{t}_2 \odot \vec{a}_1 \\ \vec{t}_1 \odot \vec{a}_2 & \vec{t}_2 \odot \vec{a}_2 \end{bmatrix} \tag{4.46}$$

Using a one point Gauss integration $(\xi = 1/3, \eta = 1/3)$ the conductivity matrix for a T3 element is given by :

$$\mathbf{C} = \frac{1}{4}\mathbf{B}^T \mathbf{K}_{cr} \mathbf{B} \det\left[\mathbf{J}(\xi,\eta)\right] \tag{4.47}$$

with $\mathbf{K}_{cr} = \delta_{ij} w_{cr} k_{cr}$ and $\mathbf{B} = [\mathbf{J}(\xi,\eta)]^{-1} \nabla_{\xi,\eta} \mathbf{N}(\xi,\eta)$. After consistent linearization the non-linear system to solve using the Newton-Raphson method is :

$$[\mathbf{S} + \Delta t \mathbf{C}]_{n+1} \{\mathbf{H}\}_{n+1} = [\mathbf{S}] \{\mathbf{H}\}_n \tag{4.48}$$

with $\mathbf{S} = \mathbf{N}^T S_d \mathbf{N} \det\left[\mathbf{J}(\xi,\eta)\right]$. The hydraulic conductivity k_{cr} is computed using the relations in figure 4.3 with the fluid velocity computed using relation 4.22. Note that the fluid velocity in the global coordinate system is computed using relation 4.42. Algorithm 4.1 gives the information to process the conductivity matrix. Finally, the velocity extrapolation from the Gauss point to the nodes is achieved using the SPR (superconvergent patch recovery) technique Zienkiewicz & Zhu (1992).

4.6 Solution algorithm for discontinuity path computation and hydraulic mesh generation

4.6.1 Discontinuity path computation

Following the global method proposed in Oliver *et al.* (2002), the search for isosurfaces of a scalar field θ tangent to a direction field such that it satisfies the conditions $\mathbf{T}\nabla\theta = 0$ and $\mathbf{S}\nabla\theta = 0$ where the vectors $\mathbf{S}$ and $\mathbf{T}$ are the eigenvectors orthogonal to the eigenvector associated with the largest strain eigenvalue. Therefore, one solves the heat-conduction like problem

Algorithm 4.1 Formulation of the element conductivity matrix to compute the fluid transport problem in discontinuities

1. Evaluate the element shape functions derivative at the Gauss point
2. Compute vectors $\vec{a}_1$ and $\vec{a}_2$ using equation 4.45
3. Compute vectors $\vec{t}_1$, $\vec{t}_2$ and $\vec{n}$ using equation 4.44
4. Computation of the local to global transformation matrix Q using equation 4.42
5. Transform the shape functions derivative into global coordinates x, y, z
6. Create the matrix $\mathbf{B}$
7. Compute the fluid velocity using equation 4.3 discretized as $\mathbf{v}_{cr} = -k_{cr}\mathbf{BH}$
8. Transform the fluid velocity from local to global coordinates using equation 4.42
9. Compute the Reynolds number using equation 4.23 : $R_e = 2w_{cr}||\mathbf{v}_{cr}||/\nu$;
10. Using the Reynolds number computed and the relative roughness parameter define α and K using figure 4.3
11. Compute $k_{cr} = K||\mathbf{v}_{cr}||^{\alpha-1}$
12. Compute the matrix $\mathbf{K}_{cr} = \delta_{ij}w_{cr}k_{cr}$
13. Compute the conductivity matrix $\mathbf{C}$ using equation 4.47

with adiabatic boundary conditions and no internal heat source :

$$\nabla \cdot \mathbf{q} = 0 \text{ in } \Omega \tag{4.49a}$$

$$\mathbf{q} = -\mathbf{K}_p \nabla \theta \text{ in } \Omega \tag{4.49b}$$

$$\mathbf{q} \cdot \mathbf{n} = 0 \text{ on } \Gamma_q \tag{4.49c}$$

$$\theta = \theta_p \text{ on } \Gamma_\theta \tag{4.49d}$$

The anisotropic conductivity matrix is given by :

$$\mathbf{K}_p = \mathbf{T} \otimes \mathbf{T} + \mathbf{S} \otimes \mathbf{S} + \zeta \mathbf{I} \tag{4.50}$$

with ζ a small perturbation term (10^{-6}) to avoid matrix singularity Vectors $\mathbf{S}$ and $\mathbf{T}$ are computed using the nonlocal strain tensor. The nonlocal counterpart $\tilde{f}(x)$ of the local strain component $f(x)$ located at position x is given by :

$$\tilde{f}(x) = \int_V \alpha(x, \xi) f(\xi) \mathrm{d}\xi \tag{4.51}$$

with ξ the location of the strain in the radius of influence R_a and :

$$\alpha(x,\xi) = \frac{\alpha_0(||x-\xi||)}{\int_V \alpha_0(||x-\xi||)\mathrm{d}\zeta} \text{ and } \alpha_0(r) = \left\langle 1 - \frac{r^2}{R_a^2} \right\rangle^2 \text{ and } r = ||x-\xi|| \tag{4.52}$$

Note that R_a will be related to the maximum aggregate size d_a such that $R_a \approx 3d_a$. The isosurfaces of the computed scalar field are therefore "potential" discontinuity surfaces. Once the discontinuity evolves, boundary conditions on the nodes attached to the elements crossed by the discontinuity are imposed such that the scalar field is fixed around the discontinuity so that it cannot change position or direction. The isosurface origin is assumed to be located at the center of an element face located on a boundary. If more than one face is in contact with the boundaries, the centroid of the element is selected as the origin. Using the finite element shape functions, the scalar θ_{iso} must be evaluated at this origin. Finally, the signed distances (level-sets) between the discontinuity surface and the nodes are computed with $\theta_i - \theta_{iso}$, θ_i as the nodal scalar. More detail on the implementation of this method can be found in Roth *et al.* (2020).

4.6.2 Hydraulic mesh generation

The hydraulic mesh on which equation 4.48 is solved (given in red in figure 4.4) is constructed on the zero level-set surface. This is achieved using a surface reconstruction method Cohen-Steiner & Da (2004); The CGAL Project (2019) based on a surface-based Delaunay algorithm that sequentially selects the most plausible triangle in the vicinity of the previously selected triangles for advancing the mesh front using four situations : (1) extension (figure 4.5a), (2) gluing (figure 4.5b), (3) hole filling (figure 4.5c) and (4) ear filling (figure 4.5d). The first step is to generate the points located at the intersection between the mechanical mesh and the zero level-set surface (black dots in figure4.6a). Then, using the surface reconstruction method the mesh is generated. Once the advancing front has connected all the points with triangles, the hydraulic mesh has a refinement similar to that of the mechanical mesh (figure 4.6b). Therefore, a refinement technique using a Delaunay triangulation is applied to generate the final hydrau-

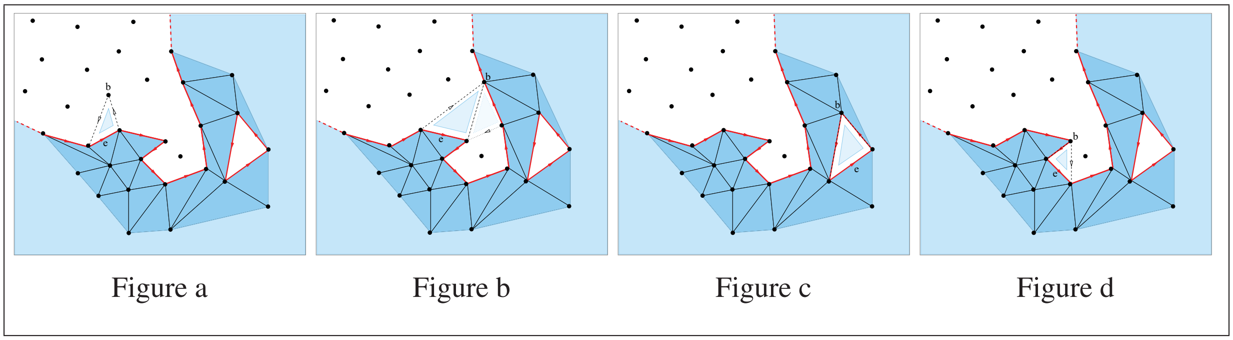

Figure 4.5 Advancing front situations : (a) extension, (b) gluing, (c) hole filling and (d) ear filling (adapted from Cohen-Steiner & Da (2004))

lic mesh (figure 4.6c). Boundary conditions are applied by seeking the points in contact with the mechanical mesh boundary faces. An example of the three steps required to generate the hydraulic mesh is given in figure 4.6. This example is for a planar mesh. However, this algorithm can handle complex three-dimensional discontinuity surfaces. This will be demonstrated in section 4.10.

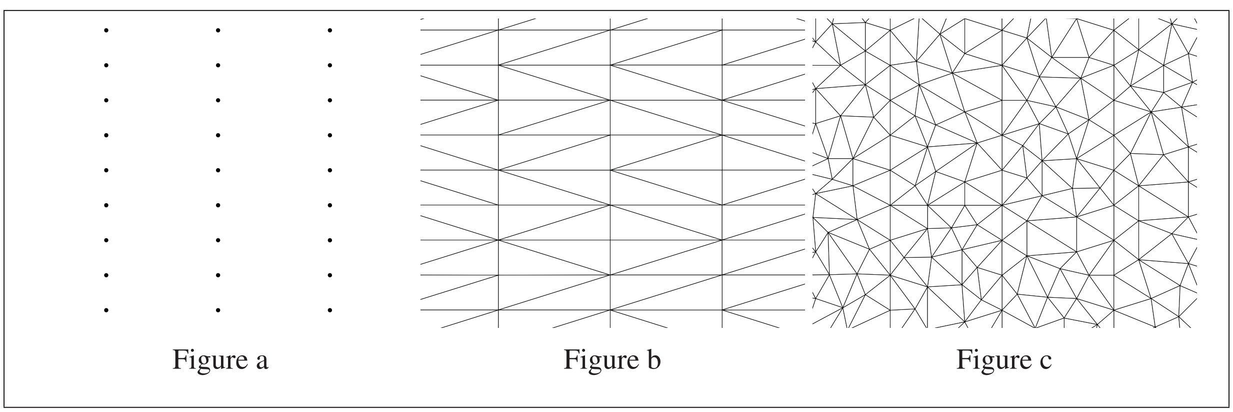

Figure 4.6 (a) Points generated from intersecting the mechanical mesh with the zero level set, (b) Mesh generated using advancing front reconstruction method (c) Final mesh using mesh refinement

4.7 Coupling of fluid-structure interactions with a non-matching interface

When the interface mesh between structural and hydraulic subproblems is identical (each nodes on the hydraulic mesh has an equivalent node located at the same position on the surface of the structure), the transfer of the pressures and of the crack aperture is a trivial operation. However, these sub-problems have different resolution requirements that require the use of different computational domains with non-matching discrete interfaces. Therefore, the hydraulic-structure interface must be coupled. One suitable method is to transfer the variable by taking into account the interpolation functions used by the finite elements as proposed in Farhat *et al.* (1998).

The first step is to pair each node p_i of the fluid Γ_F with the closest element of the structure

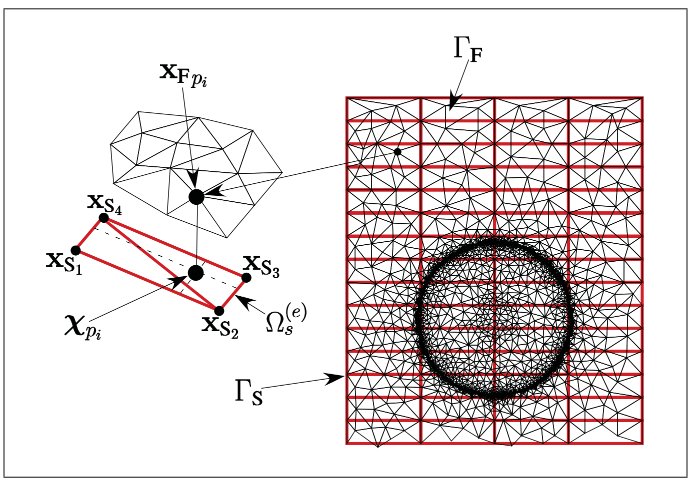

Figure 4.7 Matching fluid node with its structural element

$\Omega_S^{(e)} \in \Gamma_S$ (figure 4.7). The second step is to determine the natural coordinates $\chi_{p_i} \in \Omega_S^{(e)}$ of the fluid node p_i on its projection on the structural element $\Omega_S^{(e)}$. The last step is to determine the interpolation functions $\mathbf{N}_k(\chi_{p_i})$ on $\Omega_S^{(e)}$. Using barycentric coordinates computation, these steps can be performed at once. Hence, the computation of the barycentric coordinates for the projection $P' = \chi_{p_i}$ of a point $P = \mathbf{x}_{F\,p_i}$ into the plane of a triangle (figure 4.8) defined by segments $\vec{u}$, $\vec{v}$ and passing by point Q can be computed using algorithm 4.2. The hydraulic node crack aperture w_{cr} can be interpolated from the associated structural triangular element crack

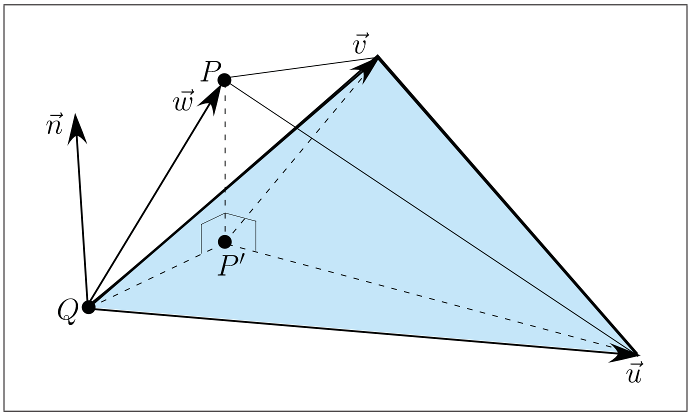

Figure 4.8 Point P projection in triangular element defined by segments $\vec{u}$, $\vec{v}$ and passing by point Q

Algorithm 4.2 Triangular element barycentric coordinates computation

function BOOL = GETINTERSECTION(N_1, N_2, N_3)
  Compute the triangle normal : $\vec{n} = \vec{u} \otimes \vec{v}$ ▷ u and v are vectors representing any of the triangle segments
  Compute vector between point P and Q : $\vec{w} = P - Q$
  Compute the barycentric coordinates :
  $N_1 = (\vec{u} \otimes \vec{w}) \odot \vec{n} / (\vec{n} \odot \vec{n})$
  $N_2 = (\vec{w} \otimes \vec{v}) \odot \vec{n} / (\vec{n} \odot \vec{n})$
  $N_3 = 1 - N_2 - N_1$
  if $0 \leq N_1 \leq 1$ and $0 \leq N_2 \leq 1$ and $0 \leq N_3 \leq 1$ **then**
    return true ▷ Point P' is inside the triangle
  end if
  return false ▷ Point P' is not inside the triangle
end function

aperture at each node $w_{cr}^{i=1..3}$ with the interpolation function computed by using algorithm 4.2 :

$$w_{cr} = \sum_{i=1}^{3} N_i w_{cr}^i \tag{4.53}$$

The inverse procedure is applied for interpolating the hydraulic pressure computed in section 4.3.3 to the structural mesh.

4.8 Consideration of drainage

To control the seepage flow in hydraulic structures, complex drainage systems including drainage galleries and drainage holes are commonly used. However, modelling the seepage problem with a complex drainage system is a challenging problem. Two approaches are presented below, one for the presence of drains in a solid skeleton and one for the presence of drains in the discontinuities.

4.8.1 Drainage in a solid skeleton

The embedded drain approach is used to model the effect of the presence of drains on the pressure distribution in a solid skeleton. This approach accounts for the presence of the drain within a parent element. The drain is independent of the mesh from the parent element. The drain can intersect the parent element in any direction, however the start and endpoint of the drain is restricted to an element face. No additional degrees of freedom are added to the problem ; however, the elements crossed by drains have their conductivity matrix modified by the presence of drains. To specify the location of the drains, geometric line elements are used

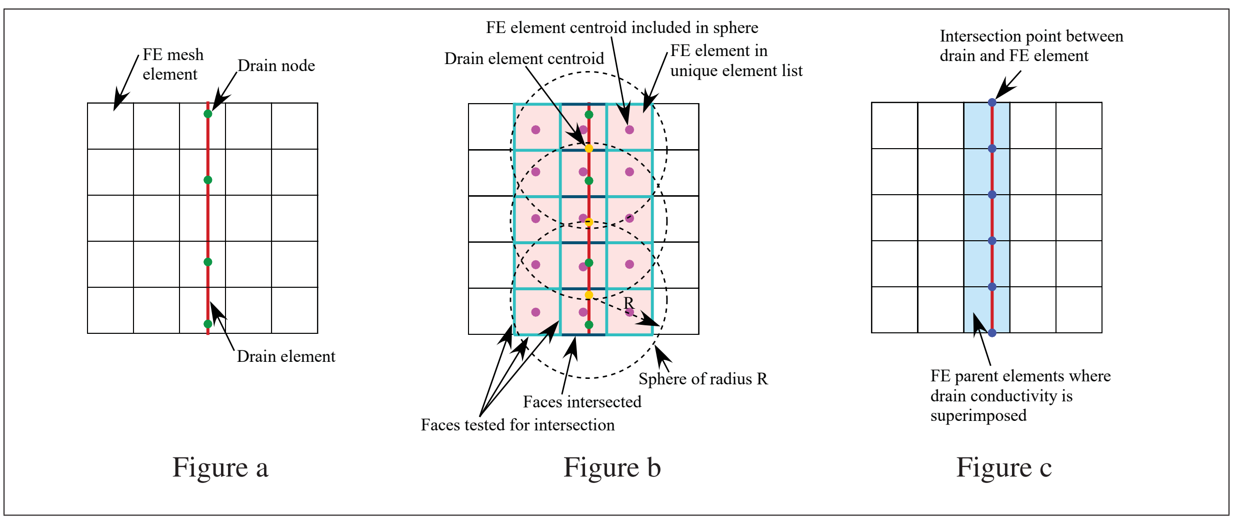

Figure 4.9 Computation of the intersection points between the FE elements and the drains ; (a) drain discretization, (b) creation of the unique element list and faces tested for intersection, (c) parent elements with their intersection points with the drains

in the finite element model. These lines are discretized using a mesh of similar size as that of the parent structural mesh (this mesh is only used to define the locations of the drains and is illustrated in figure 4.9a).

The initialization step requires locating the drains inside the three-dimensional parent elements (figure 4.9c). When locating parent elements in a problem with a large geometry containing a significant number of drains, an optimized algorithm must be developed. This location is achieved using a NearTree algorithm Andrews & Bernstein (2016) to select the parent elements with their centroid located within a certain distance from the drain using the algorithm 4.3. Line 4 of the algorithm 4.3 is illustrated in the figure 4.9b where the list of unique elements is generated by sweeping each drain element centroid to find the FE elements included in a sphere of radius *R*. Then, each face of the elements contained in this list is tested to define if

Algorithm 4.3 Get the list of parent elements in the vicinity of the drain

```
 1: function GetCloseElements()
 2:     Discretize drain geometry in a set of segments
 3:     for all segments do
 4:         Find the parent elements in a sphere of radius R from the center of the segment
    to the centroid of the
 5:         parent element
 6:         for all parent element found do
 7:             Add element to unique elements list
 8:         end for
 9:     end for
10: end function
```

there is an intersection with the discretized drain elements (the tested faces are illustrated in figure 4.9b). This test is performed using the same approach as that for coupling the fluid nodes with the structural elements presented in section 4.7. Hence, the elements' faces are divided into triangles to generalize this procedure to all element types (hexahedron, pyramid, wedge and tetrahedra). Prior to perform this test, point *P* (figure 4.8) corresponding to one of the two node of the drain segment is projected on a plane tangent to the triangle in the direction of the drain. During this projection, a verification is made to make sure that this projected point is located between the two nodes of the drain segment. Using the proposed approach, if an intersection is found, the intersection points in terms of natural ξ_i and global coordinates $\mathbf{x}_i$, as shown in figure 4.10, can be defined from the shape functions computed using algorithm 4.2 :

$$\xi_{1,2} = \sum_{i=1}^{3} N_i \bar{\xi}_i \qquad \mathbf{x}_{1,2} = \sum_{i=1}^{3} N_i \bar{\mathbf{x}}_i \tag{4.54}$$

where $\bar{\xi}_i$ and $\bar{\mathbf{x}}_i$ are the natural coordinates and the global coordinates, respectively of the parent element. Algorithm 4.4 gives the main steps required to perform this task. The drain

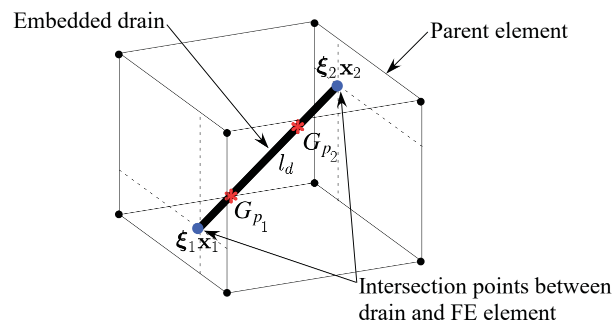

Figure 4.10   Embedded drain in a parent element

conductivity is superimposed on the parent element conductivity. Therefore, the conductivity contribution in equation 4.5.1 is replaced by :

$$\int_{\Omega\backslash\Omega_c} \nabla\mathbf{H}^T \mathbf{K} \nabla\mathbf{H}^T \, \mathrm{d}\Omega = \underbrace{\int_{\Omega\backslash\Omega_c} \nabla\mathbf{H}^T \mathbf{K} \nabla\mathbf{H}^T \, \mathrm{d}\Omega}_{\text{parent}} + \underbrace{\int_{\Omega_d} \nabla\mathbf{H}_d^T k_d \nabla\mathbf{H}_d \, \mathrm{d}\Omega_d}_{\text{drain}} \tag{4.55}$$

with k_d the drain conductivity coefficient and $\Omega_d = A_d l_d$, with A_d the drain area and l_d the drain length. The first integral is the standard form of the parent element conductivity matrix, while the second integral is needed to embed the drain element. The drain conductivity is only available along the drain, and so the integration must be performed along the drain path. Therefore, the parent element shape functions $\mathbf{H}_d$ are evaluated at the Gauss points $G_{p\,i}$ located along the drain path defined as :

$$G_{p\,i} = \xi_1 + \alpha_i(\xi_2 - \xi_1) \tag{4.56}$$

with $\alpha_{1,2} = \left\{ \dfrac{3-\sqrt{3}}{6}, \dfrac{3+\sqrt{3}}{6} \right\}$ for a hexahedral element.

Algorithm 4.4 Computation of the intersection points

for all elements in the list generated using algorithm 4.3 **do**
    for all faces of the considered element **do**
        if face is not triangular **then**
            divide face
        end if
        for all drain segments in the vicinity of the face centroid **do**
            Intersect = COMPUTEINTERSECTION(N_1, N_2. N_3) ▷ Find if segment intersects face
            if Intersect == **true then**
                $\xi_{1,2} = \sum_{i=1}^{3} N_i \bar{\xi}_i$ ▷ Compute the intersection point in natural coordinates
                $\mathbf{x}_{1,2} = \sum_{i=1}^{3} N_i \bar{\mathbf{x}}_i$ ▷ Compute the intersection point in global coordinates
                Save intersection points
            end if
        end for
    end for
    if two intersection points are found **then** ▷ Verify if the element is crossed by the drain
        Save the drain intersection points within the parent element
    end if
end for

4.8.2 Drainage in the discontinuity

Drainage in the discontinuity is achieved by discretizing the geometry of the drains intersecting the discontinuity and by applying proper boundary conditions. This boundary condition can be zero if the drainage system exits the water in a location below the discontinuity or can include a water head if the drain has reduced efficiency or is being connected to a gallery located above the discontinuity. Recalling that drains are not geometrically present in the mechanical mesh, they must be integrated into the hydraulic mesh that is not defined at the beginning of the solution. Geometric manipulations must therefore be performed. The points located around the discretization of the drain geometry must be projected on the mesh generated during the second step given in section 4.6.2 (figure 4.6b). To capture the strong velocity gradients in the vicinity of the drain requires hydraulic mesh refinement. Hence, a series of points projected on the mesh are added (points in gray in figure 4.11a). These points are added inside and outside the drain boundary. Two circles are added inside and outside the drain to gradually increase the mesh spacing. Other nodes are evenly added inside the drain. The triangulation must be recomputed using this set of added points (figure 4.11b) before performing the final mesh refinement (4.11c). Note that the drain geometry can also be partially included in the discontinuity if it is located near the discontinuity tip and not fully included in the discontinuity.

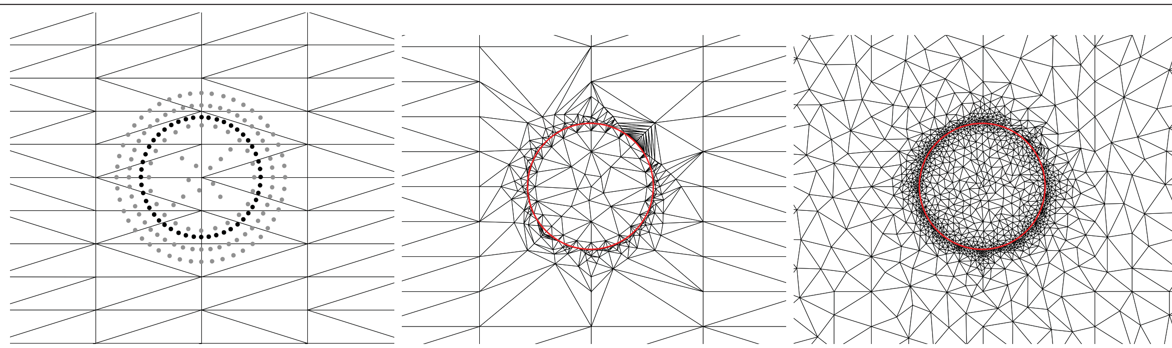

Figure a Figure b Figure c

Figure 4.11 (a) Drain discretization using points (black points) projected on the zero level-set surface with the addition of points (grey points) for mesh refinement in the vicinity of the drain, (b) Remeshing using Delaunay triangulation method (c) Final mesh using mesh refinement

4.9 Global Algorithm Details

Figure 4.12 gives the UML activity diagram of the global solution algorithm. In step 1, the cohesive force is updated if the element is enriched. If there is a discontinuity, the uplift pressure inside it must be updated using the hydraulic mesh. This is achieved in steps 2 to 4 using the proposed segregated method. Once the pressure is updated and transferred to the mechanical mesh, the system of equations (4.5.1) is solved. These steps are repeated until solution convergence. Using this converged solution, the discontinuities paths are computed (section 4.6). Thereafter, for each element located in the extension of the discontinuity, a verification is made to determine if the energy threshold has been exceeded. The energy threshold is defined as :

$$\frac{1}{2}\sigma_1^{av}\varepsilon_1^{av} \geq \gamma\left(\frac{f_t'^{\,2}}{2E}\right) \tag{4.57}$$

where f_t' is the tensile strength and E is the elastic modulus. The principal stress σ_1^{av} averaged over the volume is given by :

$$\sigma_1^{av} = \frac{\sum_{i=1}^{n_{int}} \sigma_1^i w^i \det{}^i}{\sum_{i=1}^{n_{int}} w^i \det{}^i} \tag{4.58}$$

where n_{int} is the number of integration points, w is the weight and det the determinant associated with the Gauss point. The principal strain ε_1^{av} averaged over the volume is analogous to σ_1^{av}. Finally, γ is taken as being equal to 80%. If the element is not enriched and the threshold is reached, the element is enriched. The same verification is done on the elements located on the model boundaries to initiate new discontinuities. If no new enriched element is added, meaning that no crack progression is detected, the solution for this time step is converged. Conversely, if new elements are enriched, the method presented in section 4.6.2 is used to generate the hydraulic mesh in the discontinuities on the points located at the intersection of the discontinuities and the mesh at step 8. At this time, any features such as drains are inserted into the hydraulic mesh. Steps 9 to 11 cover the coupling of the structural mesh with the hydraulic mesh (section 4.7) and compute the initial solution of the flow in the discontinuity (section 4.3.3). The two separate solvers exchange information at each step of the iteration, and so the global solution can use an implicit scheme. Global convergence is based on the solution of the strongly coupled algorithm. Because the pressures computed using the weakly coupled algorithm are introduced as boundary conditions in the strongly coupled problem, they affect the convergence of the latter. Hence, the difficulties related to the definition of partitioned solvers explicit convergence are overcome.

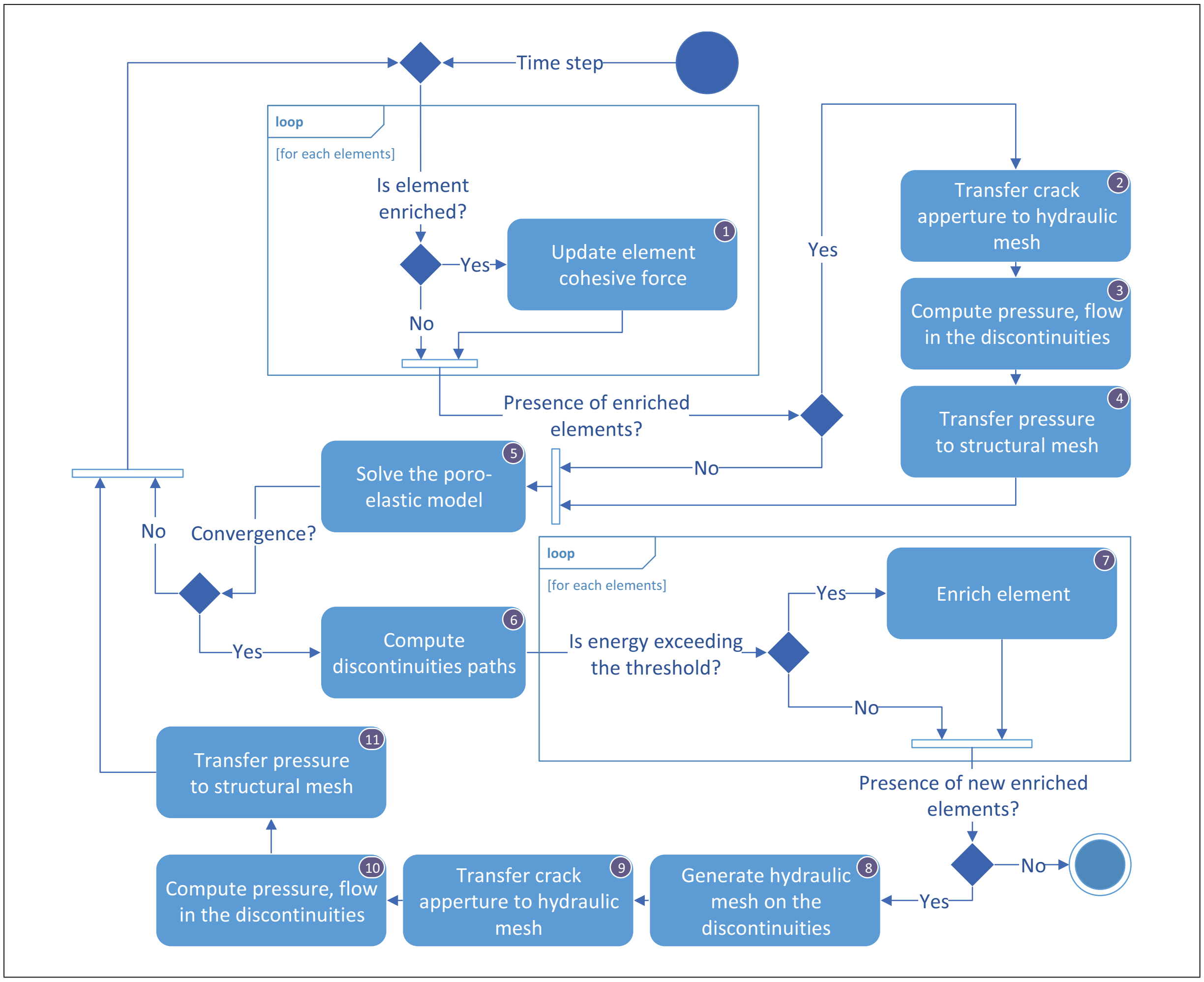

Figure 4.12 UML activity diagram of the algorithm for one load step

4.10 Validation examples

In the context of hydromechanical problems applied to dam engineering, where a large reservoir of water is in contact with the structure, transient effects can be neglected. Therefore, the water entering, initiating and propagating cracks are immediate and generally lead to a brittle cracking process. Using this assumption, a wedge splitting test, a gravity dam and an arch dam validation are used as examples. The transient effects are demonstrated in a fourth validation example. Tri-linear element formulation is used to reduce the number of nodes in problems were large dams are computes. Therefore, enhanced assumed strain (EAS) elements Andelfinger & Ramm (1993) are used to avoid shear locking in all problems solved in the current section.

4.10.1 Wedge splitting test

The wedge-splitting device tested in Brühwiler & Saouma (1995) and simulated numerically in Bhattacharjee *et al.* (1995) is used as a validation example of the algorithm. The geometry and the material properties are given in figure 4.13 and table 4.1 respectively. The mesh is generated using 13k hexahedral linear elements with a total of 15k nodes. Four cases are modeled to show the effect of drainage on the mechanical response. As a reference solution, case 1 does not have any drainage. Case 2 has one 10 mm diameter drain located at the center of the wedge thickness, at a distance of 20 mm below the notch (figure 4.14a, note that the hydraulic mesh given in this figure corresponds to the mesh at the end of the solution and is not defined a priori). Case 3 has two 10 mm diameter drains located at a distance of 20 mm below the notch (Figure 4.14b) and case 4 has the same configuration but the drains' diameters are 20 mm (not illustrated). To simulate hydrofracturation, the pressure applied in the red zone is modified to increase gradually the crack mouth opening displacement (CMOD) between points A and B. The displacement in the thickness direction is fixed for all nodes located at mid depth. Finally the displacement in the other two directions are fixed on the lower surface only for the row of nodes located at mid-span. Figure 4.15 gives the pressure load as a function of the CMOD.

Tableau 4.1 Material properties for the wedge-splitting specimen

E (MPa)	f'_t (MPa)	f'_c (MPa)	ν	G_F (N/m)	b	k (m/s)
24320	2.54	25.4	0.20	182	0.2	10^{-8}

With a maximum pressure of 1.39 MPa, case 1 produces results similar to those in Bhattacharjee *et al.* (1995), where the maximum pressure found is 1.30 MPa. The effectiveness of the drainage is proven when this result is compared with those of cases 2 to 4. Using two drains

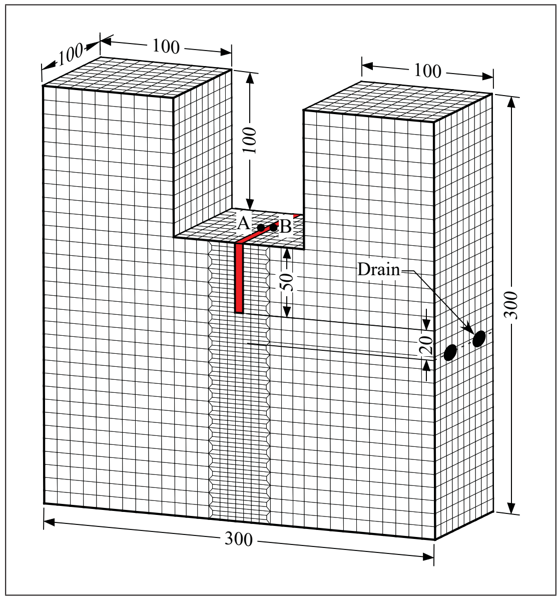

Figure 4.13 Wedge-splitting finite element model (dimensions in mm)

gives a maximum pressure that is 10% higher than that found without drainage when using 10 mm drains, and 20% higher for 20 mm drains. Figure 4.16 gives the pressure distribution at peak load for the three drainage configurations. The configuration with a single drain gives a good idea about the interaction radius of the pressure release. This figure also reveals that the synergy of two drains that are located within a certain range increases this radius of interaction, and that the configuration of two drains of larger size releases the pressure close to zero beyond the drain line. However, it is clear from this figure that the addition of a drain in between two other drains would greatly improve the release of pressure in the center region. The objective of this simulation is not to give a guideline on the positioning of drains, but to qualitatively compare several drainage solutions to demonstrate that the developed method can be used to effectively optimize the efficiency of these drainage configurations. Figure 4.17 gives the velocity vectors as well as their magnitudes for the three drainage configurations at the maximum computed pressure load. Note that the magnitude should not be compared, as the three configurations do not have the same imposed pressure in these figures. The velocity magnitude is close to 4 m/s upstream of the 10 mm drains (1.55 MPa imposed pressure), whereas

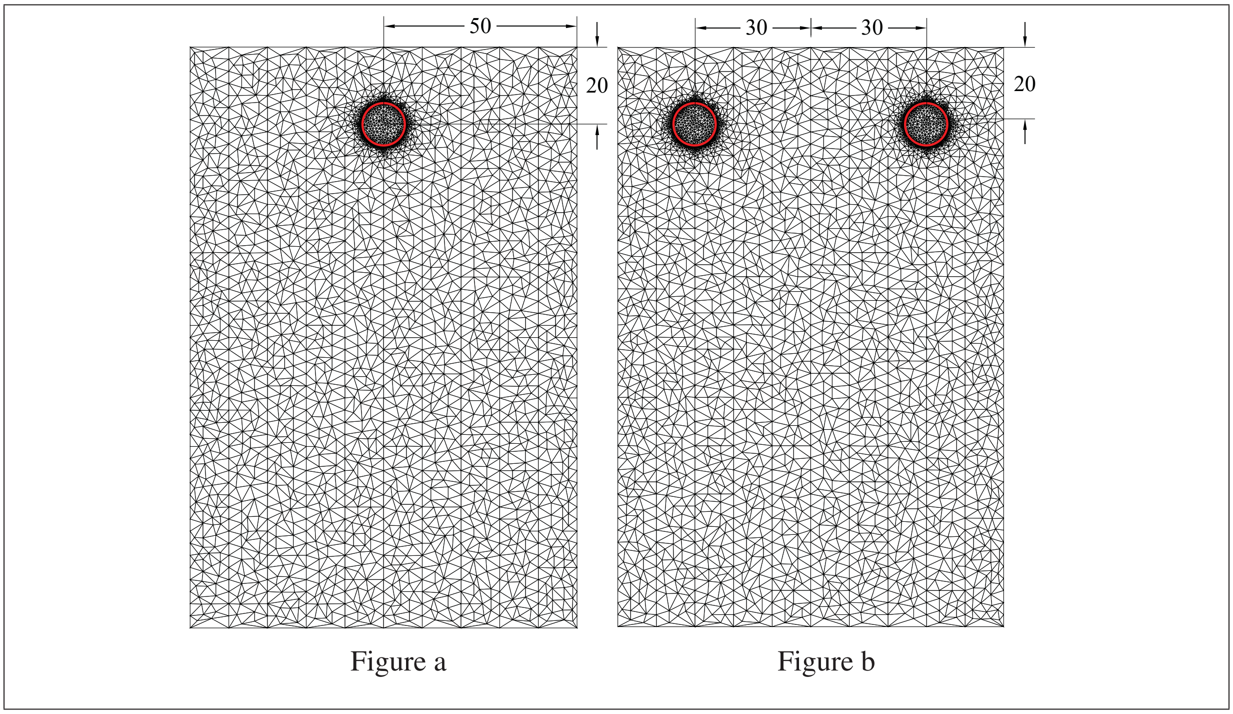

Figure 4.14 (a) Drain location for case 2 (one 10 mm drain), (b) Drains locations for case 3 (two 10 mm drains)

this velocity exceeds 8 m/s in the case of the 20 mm drains (1.65 MPa imposed pressure). To show the embedded drain effect on the pressure distribution within the wedge specimen body, the isosurface at zero pressure is plotted in figure 4.18 for case 3. Nine section cuts are also plotted to give the pressure distribution across the wedge specimen. The interpolated pressure boundary conditions obtained from the hydraulic mesh are clearly visible in the central section. Finally, using an isosurface corresponding to a null pressure reveals the presence of the embedded drains in the porous medium.

4.10.2 Koyna dam

The Koyna dam is a 103 m-high concrete gravity dam located in India that is widely used as a benchmark model for seismic analysis. There is also a static analysis case study that has not been validated experimentally, however numerous authors have published numerical results using the same geometry and material parameters Gioia *et al.* (1992); Bhattacharjee & Léger

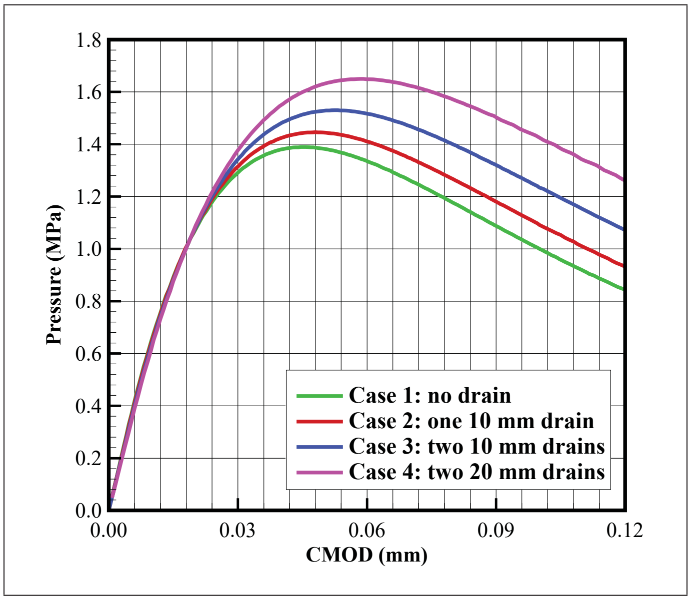

Figure 4.15 Maximum pressure load as a function of the CMOD

(1994); Ghrib & Tinawi (1995); Cai (2007). Some authors have also introduced water pressure inside the crack using different coupling strategies Gioia *et al.* (1992); Bhattacharjee & Léger (1994), which represents the main interest of performing this case analysis.

Material parameters and geometric configuration adapted from Chopra & Chakrabarti (1972) are presented in table 4.2 and figure 4.19, respectively. The mesh is generated using 20k hexahedral linear elements with a total of 23k nodes. The initial notch facing the change of slope on the downstream face has a depth that corresponds to 10% of the dimension d, and is included in the model by disconnecting the nodes of the elements underlying the notch (the red line in figure 4.19). Four configurations are used to demonstrate the effect of drainage : (i) no uplift pressure inside the crack ; (ii) full uplift pressure ; (iii) uplift pressure with one row of 152.4 mm (6") diameter drains located 1 m from the upstream face spaced 1 m apart ; and, (iv) the same as configuration (iii) with the addition of a second row of drains located 1 m away downstream from the first row of drains towards downstream and positioned in a staggered manner (the starting and ending point for each modeled drain is given in table 4.3). Because the notch

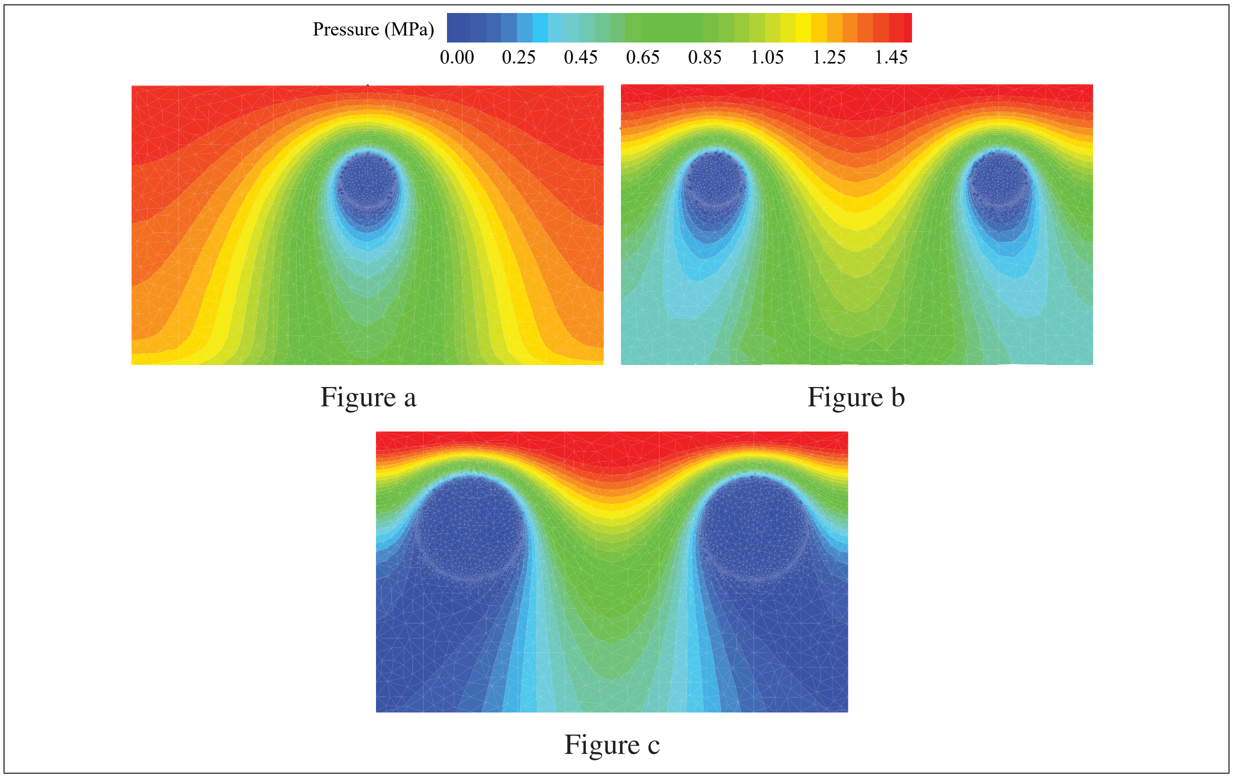

Figure 4.16 Pressure distribution on the hydraulic mesh at peak load for (a) case 2 (one 10 mm drain), (b) case 3 (two 10 mm drains), (c) case 4 (two 20 mm drains)

is initiated at a depth of 1.93 m, the first row of drains is located within an open discontinuity and therefore the flow rate is not zero at the beginning of the computation.

Tableau 4.2 Material properties for the full scale gravity-dam

E (MPa)	f'_t (MPa)	f'_c (MPa)	ν	G_F (N/m)	ρ (kg/m^3)	b	k (m/s)
25000	1.00	10.0	0.20	100	2450	0.2	10^{-8}

The model is subjected to gravity load, hydrostatic pressure corresponding to a full reservoir level (103 m) and overflow pressure. The response is controlled by the crest displacement by varying the overflow pressure. The maximum crest displacement computed is 80 mm with an increment of 0.2 mm per loading step. The response of the structure is represented by the

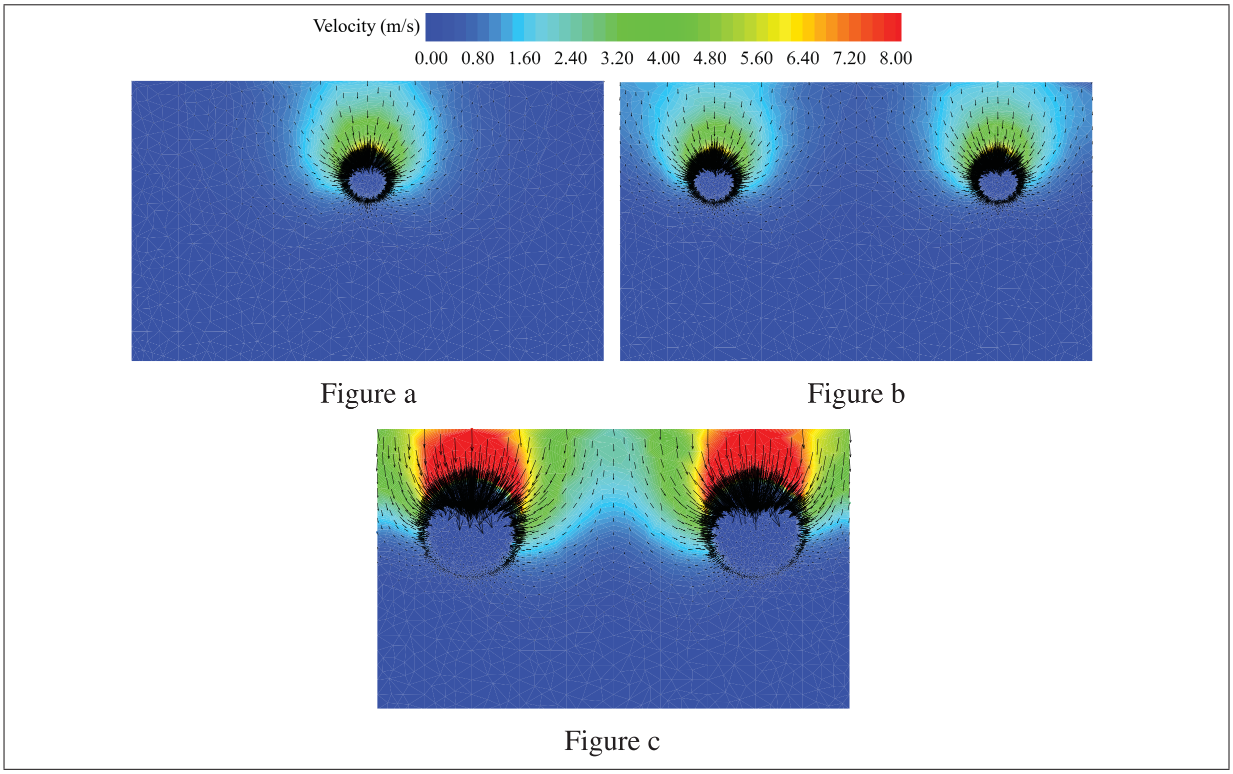

Figure 4.17 Pressure distribution on the hydraulic mesh for (a) case 2 (one 10 mm drain), (b) case 3 (two 10 mm drains), (c) case 4 (two 20 mm drains)

overflow height versus the horizontal displacement at the crest in figure 4.20a for the four computed configurations. The response for the case not considering uplift pressure is similar to that of other authors Bhattacharjee & Léger (1994); Ghrib & Tinawi (1995); Cai (2007), where the nonlinearity of the response starts to occur at an overflow level of approximately 6 m. The case considering full water pressure clearly shows an overturning failure mode of the dam. The crest displacement becomes unbounded and the pressure drops to zero in the solution process. Full crack pressure therefore yields a brittle dam failure. This failure occurs with an overflow pressure of 3.08 m, which is exactly the same water level as that computed in Bhattacharjee & Léger (1994). The addition of drainage in the dam avoids the unstable behavior of the crack when submitted to uplift pressure. The configuration with one row of drains has a significant crest displacement when the water overflow level reaches 3.80 m. When the overflow water level is kept constant, a crest displacement of 33.8 mm occurs. An interesting

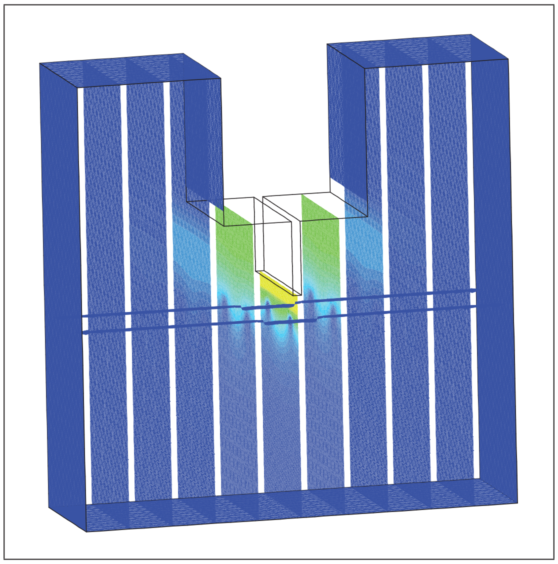

Figure 4.18 Pressure distribution at maximum pressure load for case 3 (two 10 mm drains)

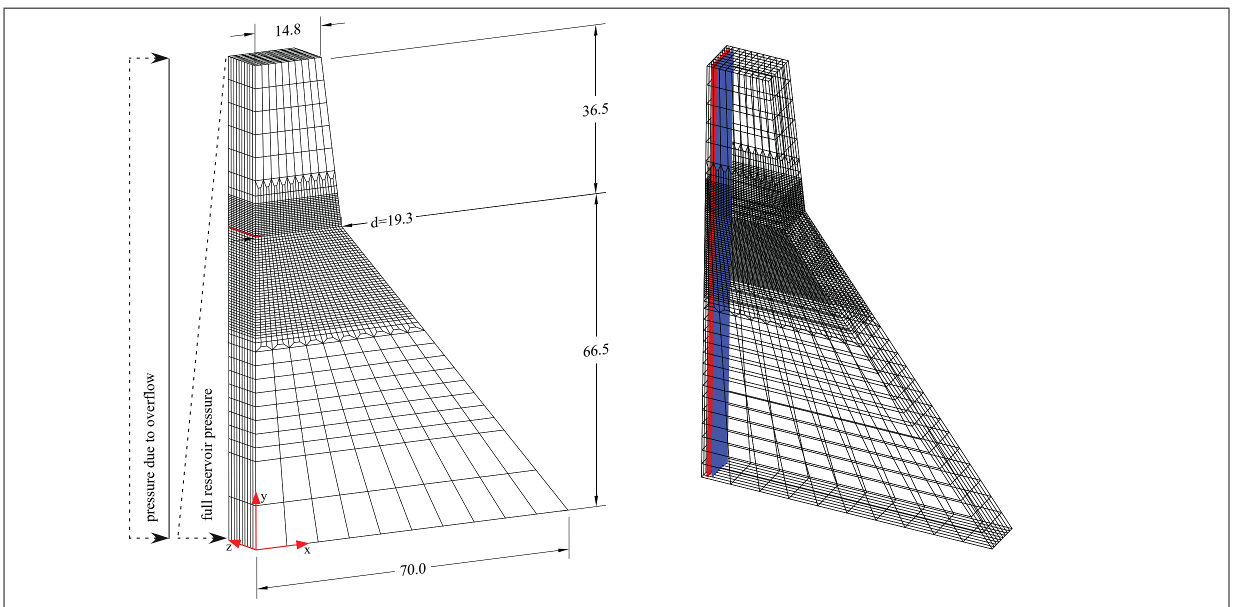

Figure 4.19 Koyna dam (a) geometry (dimensions in m) width is 10 m, (b) drains locations (first row (red), second row (blue))

Tableau 4.3 Drains locations for the full scale gravity-dam

Row	Start point			End point		
	X	Y	Z	X	Y	Z
First row	1.00	103.00	1.00	1.00	9.00	1.00
	1.00	103.00	2.00	1.00	9.00	2.00
	1.00	103.00	3.00	1.00	9.00	3.00
	1.00	103.00	4.00	1.00	9.00	4.00
	1.00	103.00	5.00	1.00	9.00	5.00
	1.00	103.00	6.00	1.00	9.00	6.00
	1.00	103.00	7.00	1.00	9.00	7.00
	1.00	103.00	8.00	1.00	9.00	8.00
	1.00	103.00	9.00	1.00	9.00	9.00
Second row	2.00	103.00	1.50	2.00	9.00	1.50
	2.00	103.00	2.50	2.00	9.00	2.50
	2.00	103.00	3.50	2.00	9.00	3.50
	2.00	103.00	4.50	2.00	9.00	4.50
	2.00	103.00	5.50	2.00	9.00	5.50
	2.00	103.00	6.50	2.00	9.00	6.50
	2.00	103.00	7.50	2.00	9.00	7.50
	2.00	103.00	8.50	2.00	9.00	8.50

conclusion that can be drawn from this analysis is that the failure mode encountered in the case involving full uplift pressure is avoided by the presence of drainage. Using a second row of drains increases the safety margin and significantly reduces the crest displacement when the crack propagates (from 33.8 mm to 5.6 mm). The response after this sudden crest displacement is parallel to the one that does not consider uplift pressure, with an offset of approximately 20 mm of crest displacement. This offset means that the behavior of the dam is similar to the case that does not consider the uplift pressure, but with an additional crest displacement of approximately 20 mm. Figure 4.20b shows the crack opening as a function of crest displacement. The crack opening is between 18 mm and 24 mm for a crest displacement of 80 mm (the full uplift pressure case is not represented in this figure because overturning of the crest takes place as soon as the crack is put under pressure). As expected, the addition of drainage reduces the opening of the cracks, which should be reflected when the flow rate in the drains are compared. Figure 4.20c confirms this fact. The maximum flow rate per drain as a function of crest displacement is given for the two drainage configurations. As explained earlier, the drains are located in the initial notch, and thus the flow rate is not zero at the beginning of the solution when overflow occurs. It is interesting to note that the flow rate is reduced when using a second row of drains. The sum of the flow rate of both rows is less than that of the single row drainage configuration. Therefore, according to these results, adding drains appropriately and optimally helps to reduce crack opening and flow rates. This conclusion still needs to be validated with field experiments. Note that the flow rate were computed with the mechanical opening and yields a large amount of water to be drained inside the dam, an amount that is not acceptable for dam operation. As specified in section 4.3.3, the flow rate computed using the mechanical crack openings is an upper limit and requires to be calibrated. One suggestion could be to calibrate the model using the measured flow rate. This was achieved for this case, were on the right scale of figure 4.20c, the flow rate is divided by a constant factor of 40. This factor is given for information only and is based on the comparison of field data with computed data for a dam that has been grouted (see section 4.10.3).

The contour plots of water pressure and associated drainage efficiency are given in figure 4.21 for the two drainage configurations at 80 mm crest displacement. Note that the water elevation is different for the two configurations. Therefore, to appreciate the effect of drainage, a drainage efficiency coefficient is used. The efficiency is almost independent of the water head and thus it allows the two drainage configurations to be compared. The drainage efficiency is defined as :

$$\text{Efficiency (\%)} = (1 - \frac{\text{Computed water head}}{\text{Imposed water head}}) \times 100\% \tag{4.59}$$

From these figures, one can clearly see that beyond the second row of drains, the drainage efficiency is close to 100% meaning that the uplift pressure falls close to zero. This explains the close behavior between the case where no uplift pressure is present with the case that has two rows of drains. Figure 4.22 gives the crack path for two different crest displacements, 40 mm and 80 mm. The crack trajectory of the case considering the uplift pressure in the crack is not very different from that of the case not taking into account the effect of the uplift pressure. The presence of drainage in the interstitial medium is clearly shown on this contour plot as the internal water pressure is quickly reduced in a narrow band close to the reservoir.

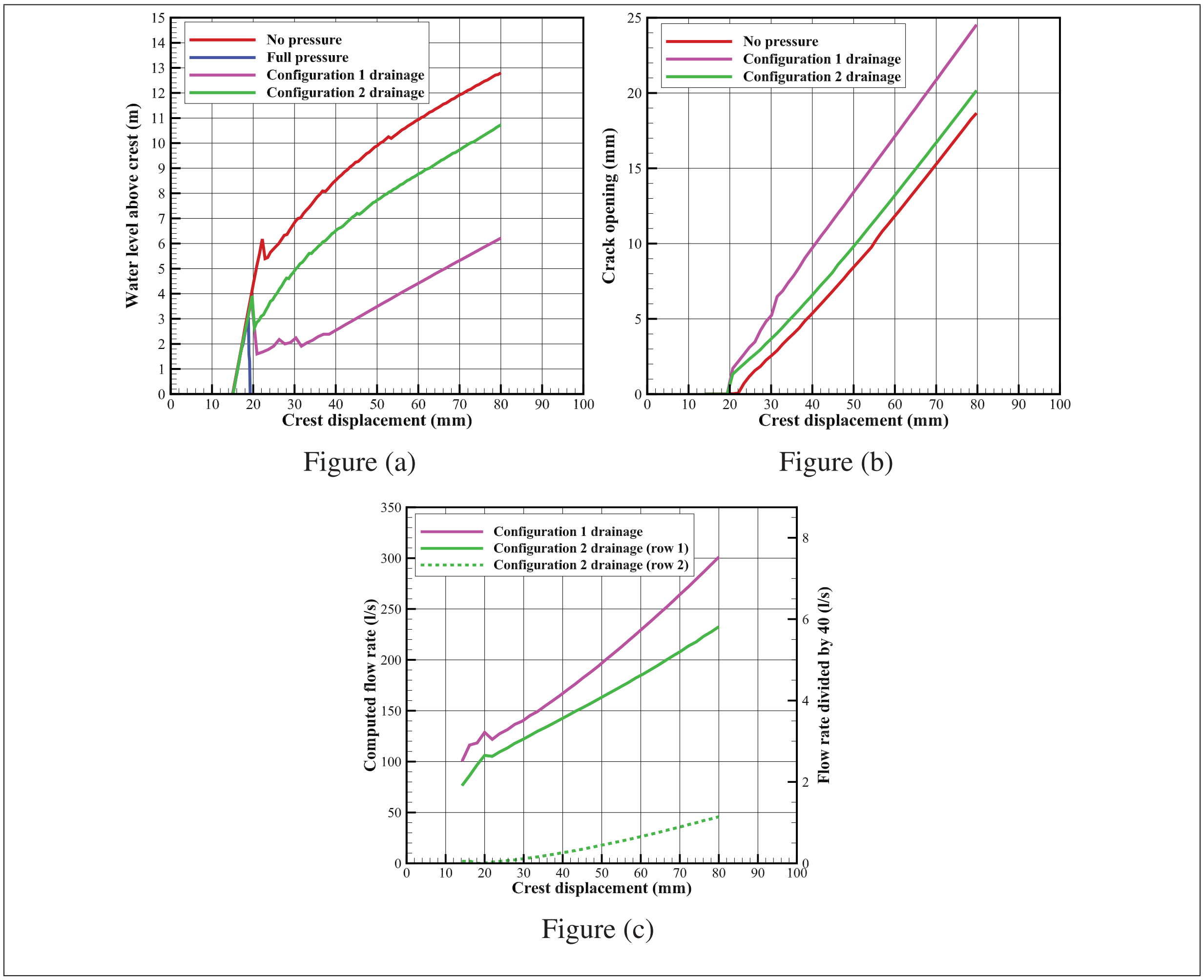

Figure 4.20 Results computed for different drain configurations, (a) Water level above crest as a function of crest displacement, (b) Crack opening as a function of crest displacement, (c) Maximum flow rate per drain as a function of crest displacement

4.10.3 Arch dam hydromechanical cracking

The arch dam material properties and geometry used in this case study are adapted from a real dam. However, changes in the geometry (figure 4.23) were made to simplify the model and promote cracking at the bottom of the dam. The concrete tensile and compressive strengths were also modified (table 4.4). The concrete elastic modulus corresponds to sustained modulus to consider creep effect and the fracture energy is computed using the relation from reference

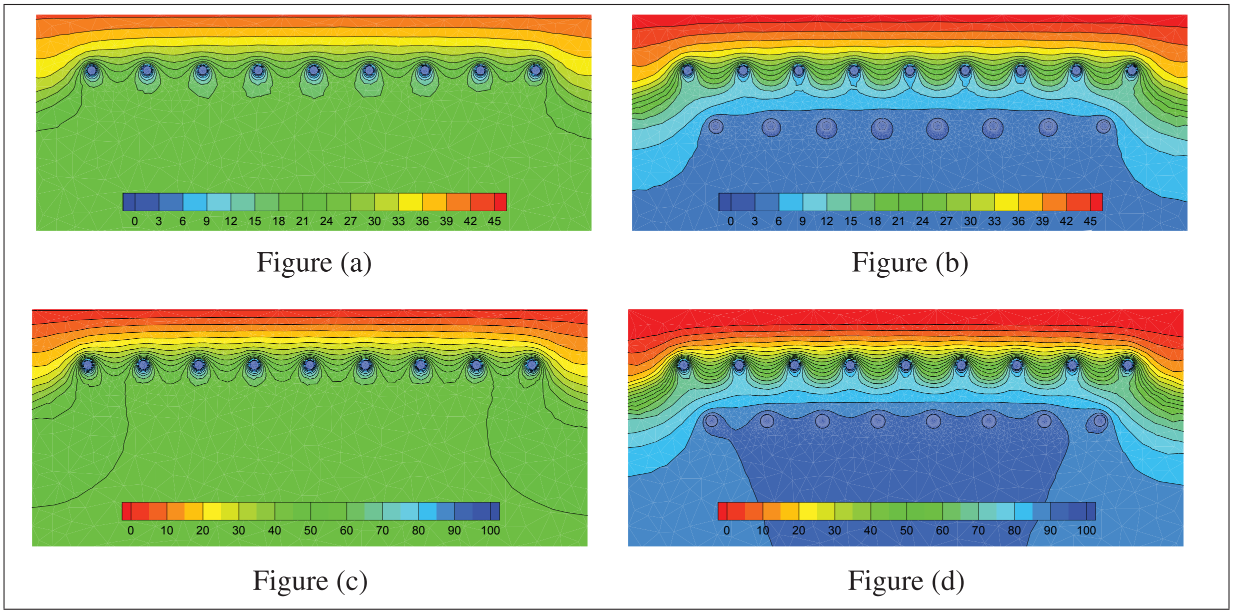

Figure 4.21 Koyna dam hydraulic results contour plots (a) water head (m) inside the crack for the configuration with one row of drains, (b) water head (m) inside the crack for the configuration with two rows of drains, (c) drainage efficiency (%) inside the crack for the configuration with one row of drains, (d) drainage efficiency (%) inside the crack for the configuration with two row of drains

Bažant & Becq-Giraudon (2002) :

$$G_F = 2.5 \times 1.44 \left(\frac{f_c'}{0.062}\right)^{0.43} \left(1 + \frac{d_a}{3.95}\right)^{0.47} \left(\frac{w}{c}\right)^{-0.20} \tag{4.60}$$

where f_c' is in MPa, d_a is the maximum aggregate size (153 mm) and w/c the water cement ratio. The drainage system is modeled (figure 4.24) as it was designed during construction, in which four drains of 152.4 mm (6") diameter per block were planned. These drains are located at a distance of approximately 20% of the thickness of the dam relative to the upstream face. Note that inspection galleries at different elevations are present in the dam however they were omitted in the model, and the collector located near the rock/concrete interface collecting the water from the drains was also omitted.

The dam is discretized using 151k hexahedral linear elements and the rock foundation is discretized using 272k constant strain tetrahedral elements. This gives 161k nodes for the dam

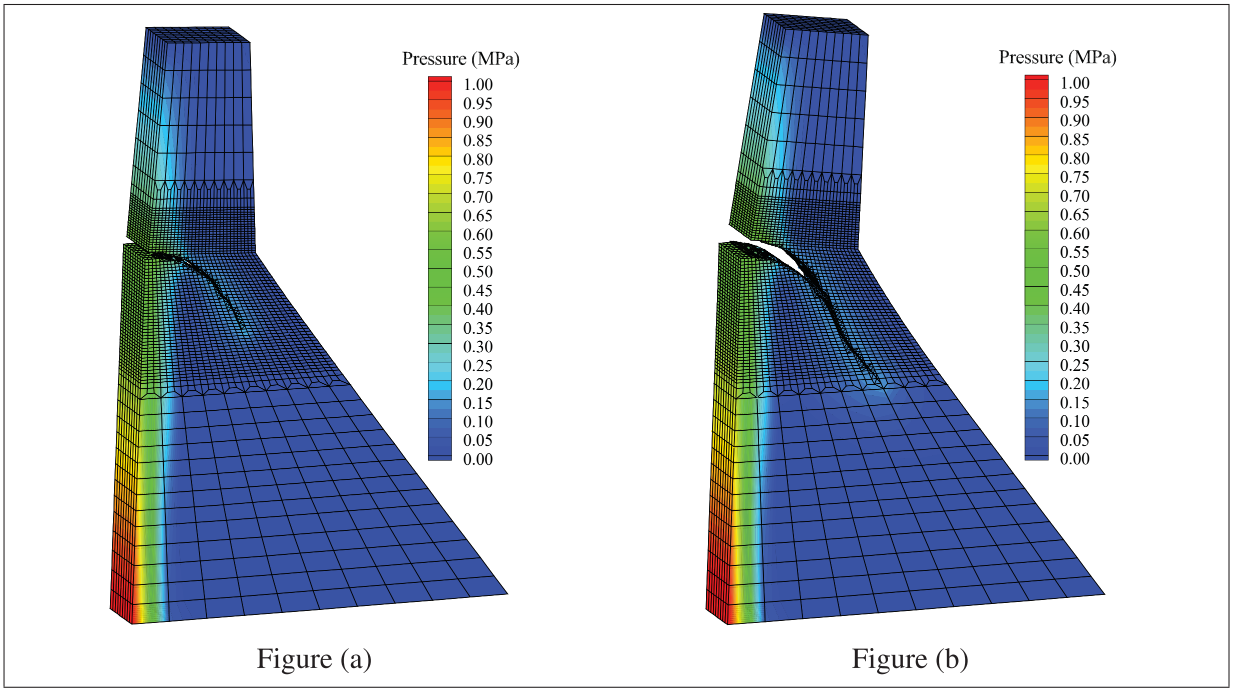

Figure 4.22 Crack progression as a function of crest displacement (a) 40 mm, (b) 80 mm

and 51k nodes for the foundation for a total of 212k nodes. Fixed displacements are applied in the foundation periphery and water pressure (using $\gamma = 9807N/m^3$) is applied on the upstream dam face and on the foundation in contact with the water. Gravity load is applied to the dam only because the foundation has already experienced settlement before the dam was constructed. The crack position was predefined using field data. However, no initial crack was imposed (the dam is initially considered as uncracked). The data came from a drilling campaign that was carried out to characterize the crack and to prepare the dam for grouting. It was not possible to reproduce the loading conditions that caused the cracking at the exact same location (note that the dam geometry used is different than that from the real dam). Consequently, it was considered satisfactory to impose the position of the crack and to predict the dam behavior and crack propagation for an increasing water level.

The numerical simulations aim to compute the plunging crack propagation by gradually increasing the water level. The water level at the beginning of the computation is 30 m below the maximum operating level (360 m) defined during the dam design. Therefore, 30 load steps of

Tableau 4.4 Material properties for the full scale arch dam

Material	E (MPa)	f'_t (MPa)	f'_c (MPa)	ν	G_F (N/m)	ρ (kg/m^3)	b	k (m/s)
Rock	32000	-	-	0.25	-	0	0.2	10^{-12}
Concrete	20700	3.60	35.0	0.20	400	2400	0.2	10^{-12}

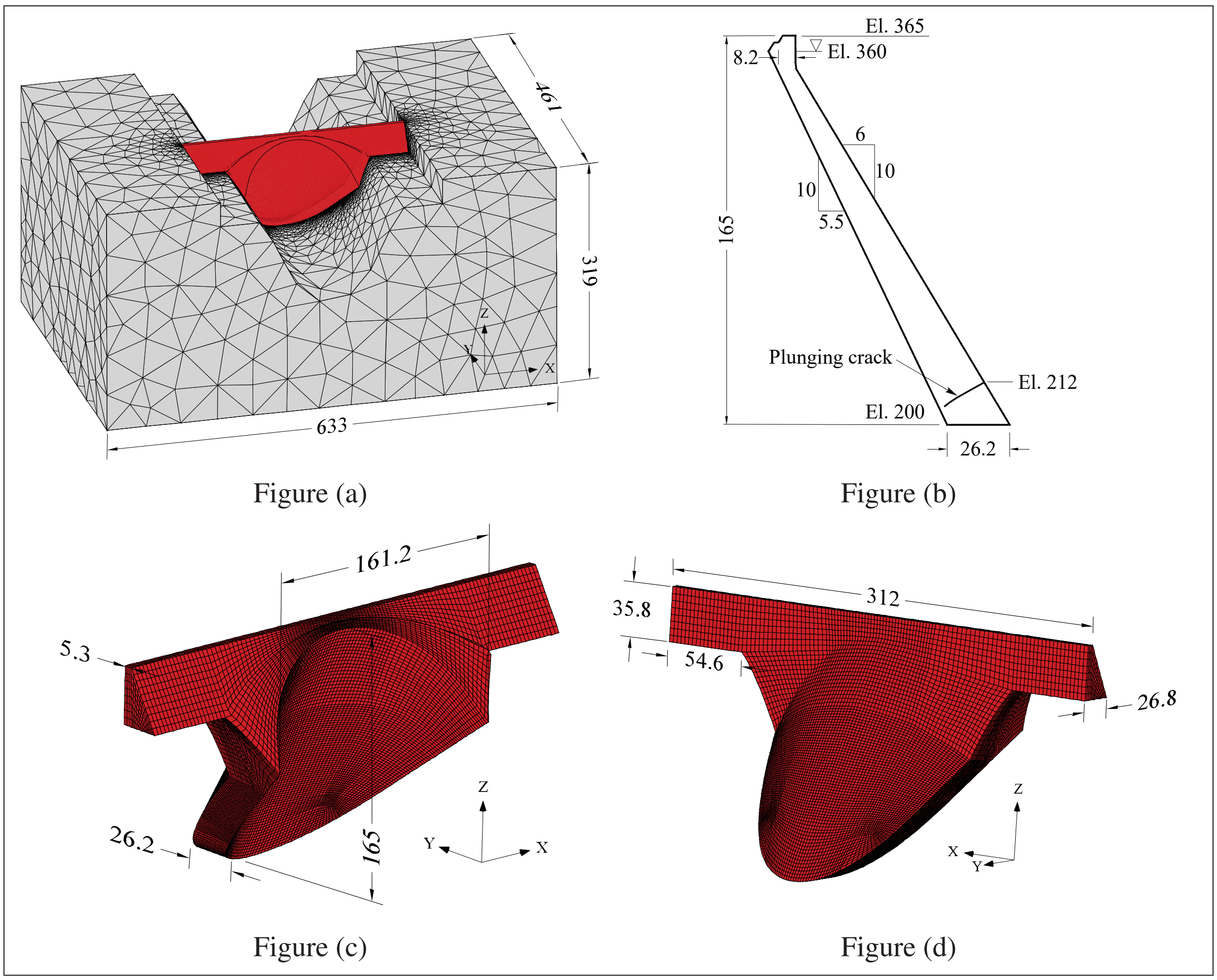

Figure 4.23 Geometry of the arch dam (dimensions in m), (a) finite element model including rock foundation, (b) central cross section, (c) downstream view, (d) upstream view

1 m water level increments were computed. Three drainage configurations were considered to show their effects on the plunging crack propagation : (i) no drainage system, (ii) the original drainage system (figure 4.25a), and (iii) the original drainage system with the addition of a row of drains downstream of the original system and positioned in a staggered way, thereafter called the enhanced drainage system (figure 4.25b).

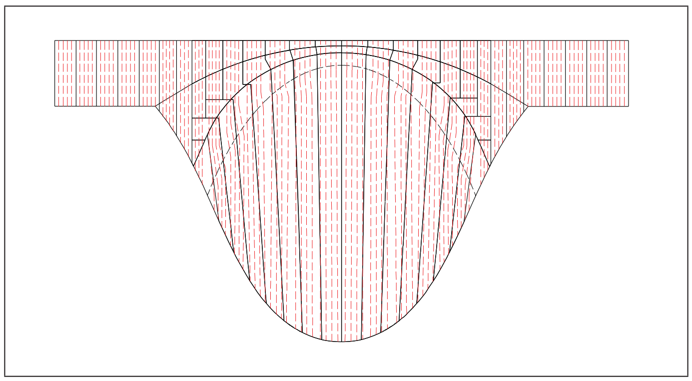

Figure 4.24 Drainage system configuration (downstream view)

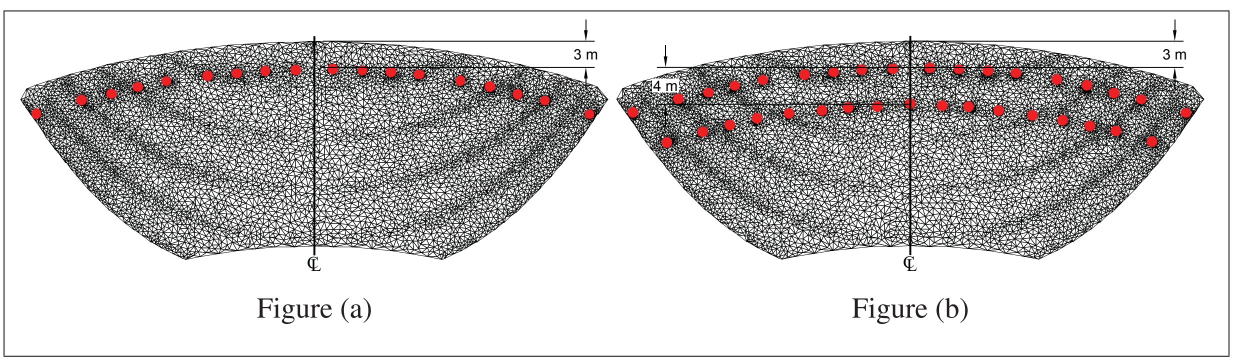

Figure 4.25 Hydraulic mesh for flow computation in the crack and location of the center section (CL) for the XY graphics : (a) original drain configuration, (b) enhanced drain configuration

In figure 4.26, the drainage efficiency contour plots are given for the three drainage configurations. As expected, the configuration without drainage gives a linear pressure reduction between the upstream and the downstream face, as shown in figure 4.26a. The case with a

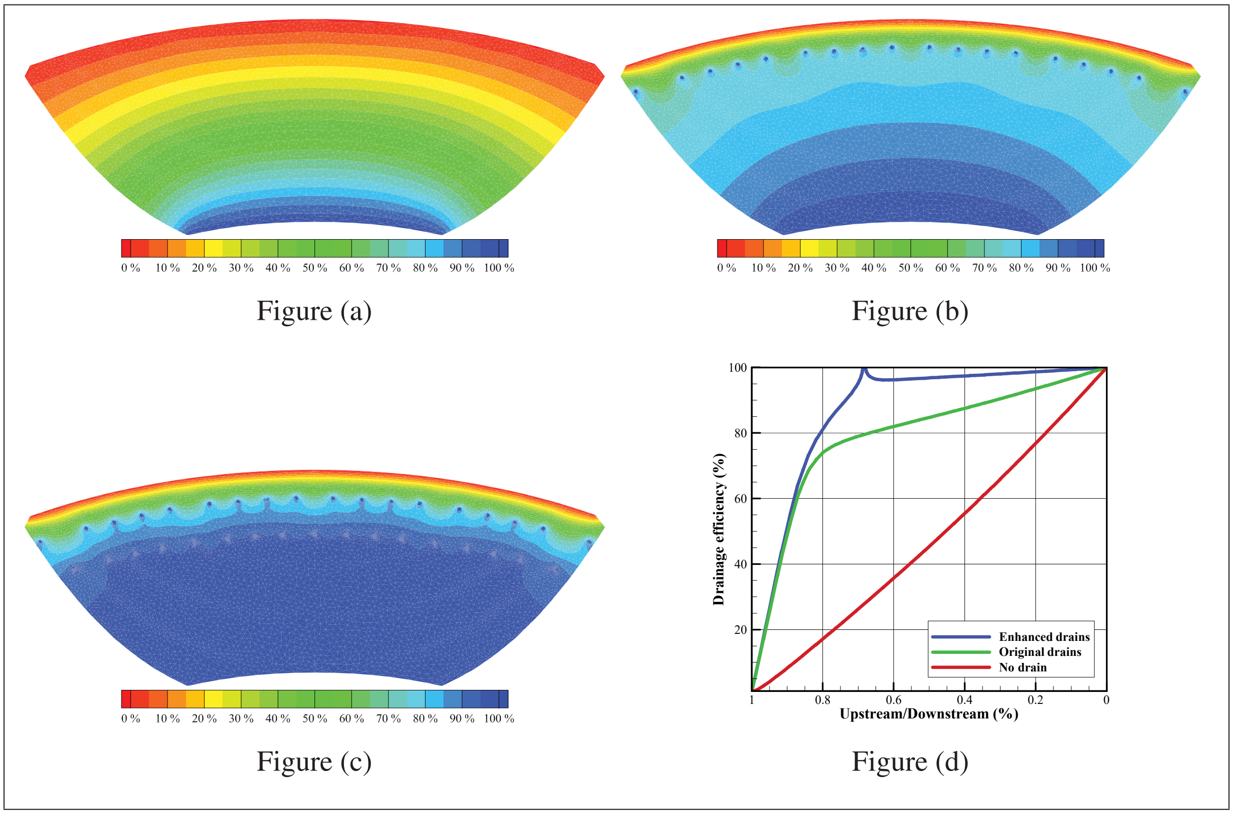

Figure 4.26 Efficiency of the drainage system (uncracked dam) for different configurations : (a) no drainage, (b) original drainage, (c) enhanced drainage, (d) efficiency difference for the different configurations at the center section (CL) (internal pore pressures are proportional to drainage efficiency)

single row of drains shows a rapid decrease in pressure up to the drain axis, followed by a linear decrease up to the downstream face (figure 4.26b). The case with two rows of drains (figure 4.26c) behaves in the same way as the case with one row of drains. However, the presence of the second row of drains reduces the internal water pressure close to zero. The drainage efficiency is given for a section at the center section (CL)(see figure 4.25 for position of CL) in figure 4.26d. It is clear from this analysis that the drainage has a significant effect in reducing the interstitial pressure. However, the assumption of fully saturated concrete is used herein. It is well known that the concrete in a gravity dam may not be saturated over a long distance and that it can take a very long time before it gets fully saturated Bažant (1975). However, for a thin arch dam, saturation is more rapid. If cracking is taking place, the results computed in

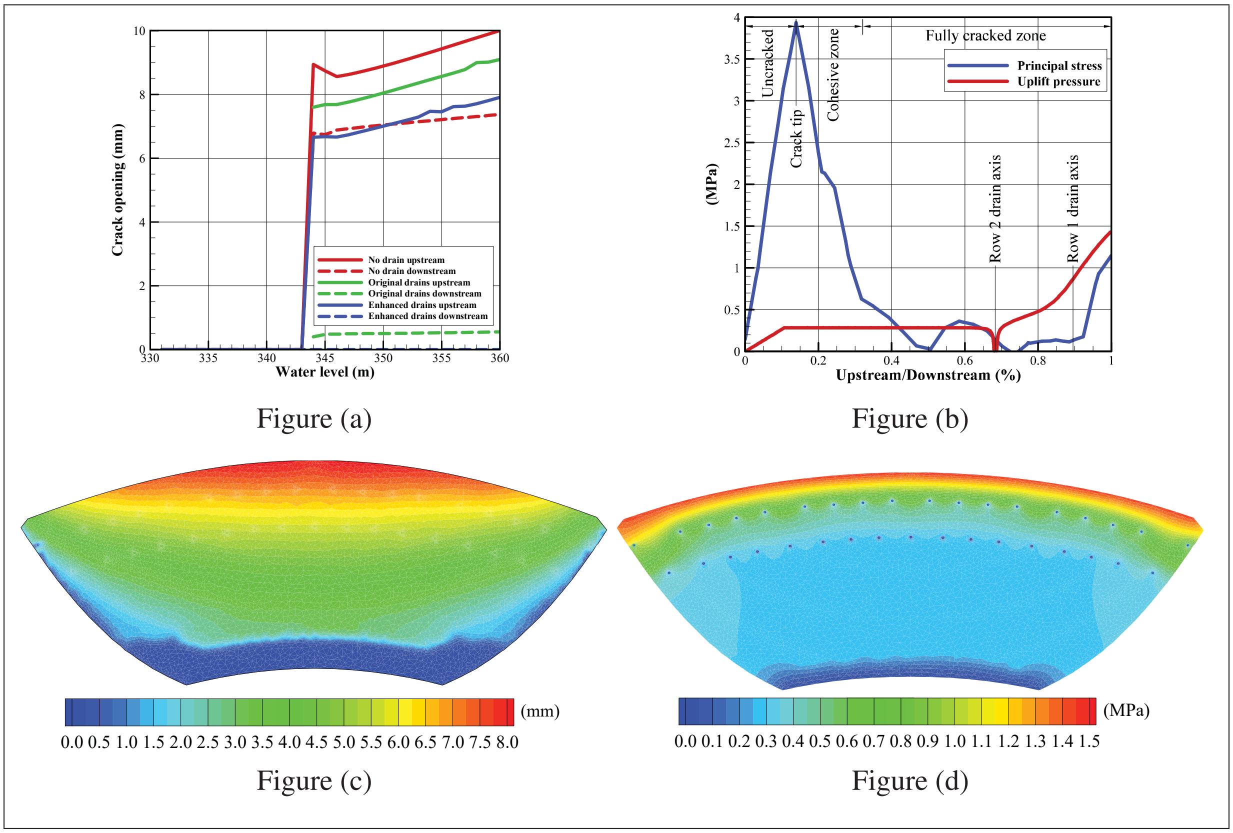

Figure 4.27 (a) Crack openings at the center section (CL) for points located at the upstream and downstream for different water levels, (b) principal stress and uplift pressure distribution at the center section (CL) computed with the enhanced drain configuration at water level 360 m, (c) crack opening contour plot at water level 360m for the enhanced drain configuration, (d) uplift pressure contour plot in the crack

the cracked conditions will be different than those resulting from seepage in a porous drained continuum.

The nonlinear analysis considering a gradual increase in water level clearly shows the benefits of the effects of drainage on the dam structural response. Figure 4.27a gives the crack opening for a point located near the upstream face and for a point located near the downstream face as a function of water level for the three drainage configurations. For all drainage configurations, crack initiation occurs at a water level of 344 m. For the cases without drainage and with the original drainage, the crack opening at the downstream face is more than zero for this water level, which means that the crack reaches the downstream face of the dam. For these two cases, the computed crack openings on the downstream face are 7 mm and 0.5 mm, respectively. For the enhanced drainage configuration, the crack does not propagate to the downstream face. This remains true for all water levels. Another interesting observation is that the addition of drains does necessarily increase the flow rate in the crack, as its opening is decreased due to the reduction in uplift pressure. Figure 4.27c gives the crack opening distribution for water level 360 m. The opening at the upstream center of the crack reaches 8 mm and the uncracked zone (in blue) is clearly visible. In figure 4.27b the corresponding principal stress distribution and the uplift pressure along the center section (CL) are plotted as a function of the distance from the upstream face. The different crack evolution states (uncracked, crack tip, cohesive zone and fully cracked) are also given in this figure. The uncracked concrete ligament is less than 15% of the dam thickness at this location. The stress gradient from the crack tip to the downstream face is important, going from 3.9 MPa to 100 kPa. Therefore, the downstream face is still in tension, but the tensile stress intensity is small compared to the tensile strength. The values presented in this figure are extracted from nodal stresses extrapolated with values at Gauss points and cracking criterion is based on the energy threshold that is averaged over the element volume. Therefore the graphical nodal stresses can sometimes be higher than the tensile strength. The tensile stress in the crack mouth is partly caused by the pressure imposed inside the crack mouth and by extrapolation from Gauss point stresses to points that are virtually inserted in the model to have the results in the discontinuity. Figure 4.27d gives the uplift pressure distribution in the crack.

As written in section 4.10.2, the computed flow rates are upper bounds and ideally, calibration with field data should be performed. For the case study presented, the flow rate computed using mechanical crack aperture with the enhanced drain configuration is 460 l/s with a maximum of 25 l/s in one drain for water level 360 m.

The simulation methodology applied to this case study demonstrates that the proposed numerical method can be applied in an industrial context. The benefits of using such advanced technology allows to make effective decisions regarding the safety of a dam and to minimize costly remedial actions while optimizing drain maintenance or adding new drains. From the results presented here, it is obvious that neglecting the effect of drainage can lead to an underestimation of safety margins. In addition, it has been shown that the addition of a second row of drains positioned in a staggered manner with respect to the first row of drains significantly reduces the uplift pressure and reduces crack propagation.

4.10.4 Hygro-mechanical analysis of a cracked beam

The proposed formulation is applied in this last example to the analysis of moisture transport in a discontinuity of a three point beam Jox *et al.* (2007); Becker *et al.* (2010) of 100 mm x 10 mm with a thickness of 10 mm shown in figure 4.28a. This validation example was not experimentally tested. The mesh is generated using 4k enhanced strain hexahedral linear elements with a total of 4k nodes. The objective is to demonstrate that the proposed hydromechanical model is also able to solve unsaturated problems as described in section 4.3.2. The material properties given in table 4.5 are similar to those given in reference Jox *et al.* (2007), however, the tensile strength, compressive strength and fracture energy are not given in that reference. Therefore, the values used herein are determined such that a crack depth similar to the reference of 3.25 mm is generated by the application of a downward displacement of $u^{\star}$ = 0.56 mm on the top of the beam. After gradually applying a displacement $u^{\star}$ = 0.56 mm on the top of the beam, a drying process at the lower boundary Γ_2 from a liquid saturation of $S_l^{\Gamma_2}$ = 88.2% (p_c = -10 MPa) to a final saturation of $S_l^{\Gamma_2}$ = 58.8% (p_c = -20 MPa) is prescribed, while the liquid saturation $S_l^{\Gamma_1}$ at the upper boundary Γ_1 remains constant. These mechanical and hygral loading histories are given in figure 4.28b.

Tableau 4.5 Material properties for the beam

E (MPa)	f'_t (MPa)	f'_c (MPa)	ν	G_F (N/m)	ρ (kg/m^3)	b	k (m/s)
2000[a]	4.25	20.0	0.20	200	0	1.0	$2.8067 \cdot 10^{-9}$

[a] This value is not common to concrete however it is used in Jox *et al.* (2007).

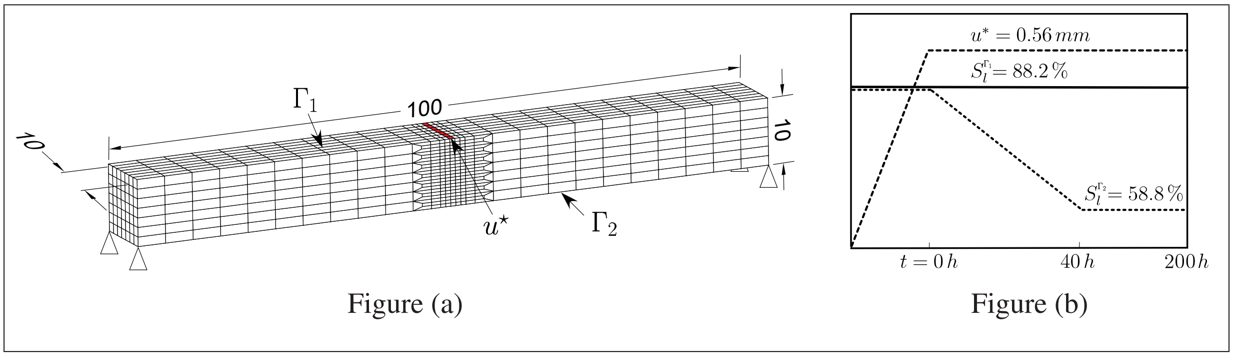

Figure 4.28 (a) Moisture transport problem geometry (in mm) and loading, (b) mechanical and hygral loading history

To maintain similarity with Becker *et al.* (2010), the crack flow is considered laminar and parallel (zone I in figure 4.3) and the permeability k_{cr} in equation 4.31 for an evolving partially filled crack channel is replaced by :

$$k_c(S_l, w_{cr}) = k_{rc}(S_l) k_{cr}(w_{cr}) \tag{4.61}$$

with :

$$k_{rc}(S_l) = 8 \cdot 10^{-6} \exp(11.7 S_l) \tag{4.62}$$

The temporal evolution of the capillary pressure at the center of the beam is given in figure 4.29 and compared to that of reference Becker *et al.* (2010). The results are in agreement. At the beginning, the gradient at the crack tip is of large amplitude and slowly decreases as time increases to get nearly linear between the crack tip and the top beam surface. The contour plots of the capillary pressure are given in figure 4.30 at different time steps. The evolution of capillary pressure around the crack is clearly demonstrated on these plots. The drying process is first concentrated around the crack and then the drying distance increases with time.

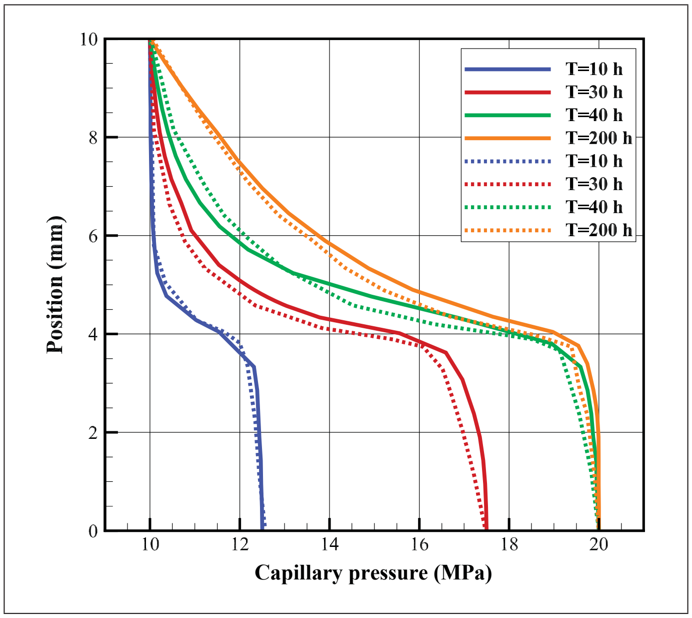

Figure 4.29 Temporal evolution of the capillary pressure at the center of the beam : continuous lines : current results, dashed lines : results of (Becker *et al.*, 2010)

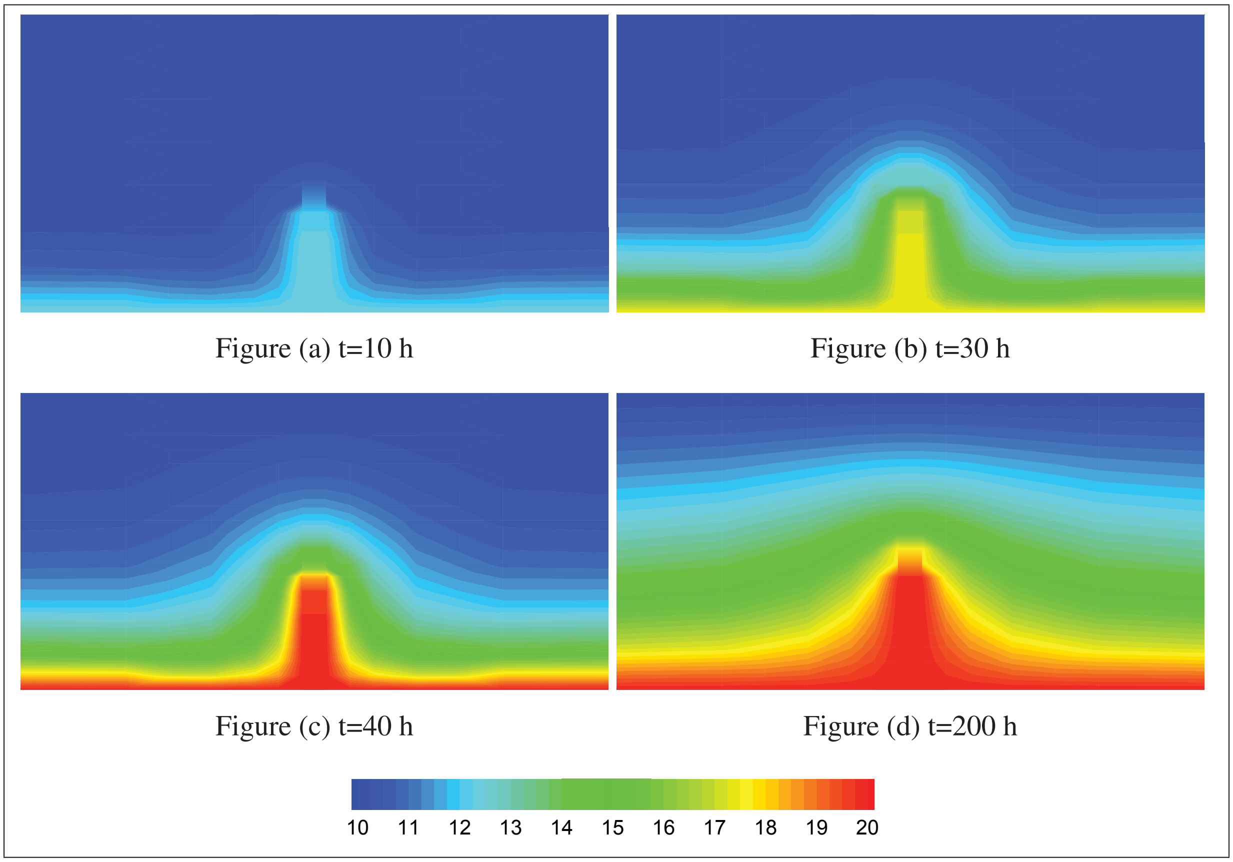

Figure 4.30 Capillary pressure contour plot at different stages (MPa)

4.11 Conclusion

This contribution has proposed a combined segregated fully-coupled 3D hydromechanical method for the computation of complex non-planar hydraulic fracturing problems. The paper provides the algorithms' details required to effectively implement the approach. A key ingredient is the use of a sub-problem in which a hydraulic mesh is used to compute the flow in discontinuities. The complexity of the flow when considering the nonlinearities caused by the different flow regimes in the presence of drains can be computed. The pressure computed using this sub-problem can be transferred to the fully coupled hydromechanical problem. An important aspect of this work is thus the transfer of the structural crack apertures to the hydraulic mesh, and the transfer of the hydraulic pressures to the hydromechanical problem by respecting the applied load equilibrium. The use of XFEM allows the computation of the crack aperture as well as the application of water pressure on the crack surfaces for the simulation of hydraulic fracture initiation and propagation.

Note that the applications herein where limited to Newtonian flow and the drains were used as sinks. Their extension to the numerical simulation of grouting where a Bingham-type fluid is injected in the cracked zones through drain hole could be simulated. The key objective of such simulation would be to estimate the allowable grouting pressure to avoid hydrofracturation.

Moreover, in recent years, natural gas production has increased significantly thanks to advances in the technique of hydraulic fracturing of hydrocarbon-rich shale formations, known as "shale gas" reservoirs. Most of the developments in the numerical simulation of hydraulic fracturing have been related to this industrial sector. The proposed method could be applied using wellbores instead of drains to simulate hydrofracturation.

4.12 Résumé et liens avec la problématique de recherche

Ce chapitre répond à la troisième problématique soulevée dans la thèse. Une méthode hydromécanique 3D fortement couplée pour le calcul de problèmes de fracturation hydraulique complexes et non planaires est proposée. Un ingrédient clé est l'utilisation d'un sous-problème dans lequel un maillage hydraulique est utilisé afin de calculer l'écoulement dans les discontinuités. La complexité de l'écoulement, lié aux non-linéarités causées par les différents régimes d'écoulement et à la présence de drainage, peut être calculée par la méthode proposée. La pression calculée à l'aide de ce sous-problème peut être transférée au problème hydromécanique fortement couplé. Un aspect important à considérer concerne le transfert des ouvertures de fissures de la structure vers le maillage hydraulique et, à l'inverse, le transfert des pressions hydrauliques vers le problème hydromécanique en respectant l'équilibre des charges appliquées. L'utilisation de la XFEM permet le calcul de l'ouverture de fissure ainsi que l'application de la pression sur les surfaces de la fissure pour la simulation de l'amorçage et de la propagation d'une fracture hydraulique. Finalement, les conditions de saturation partielles sont ajoutées en couplant un modèle de diffusion non linéaire prenant en compte l'effet de la saturation par une équation non linéaire variant en temps et en espace.

CONCLUSION ET RECOMMANDATIONS

Afin de statuer si un barrage fissuré a besoin de réhabilitation, il est important d'évaluer de façon efficace si les fissures posent un enjeu réel sur sa stabilité et si celles-ci peuvent se propager. De nombreuses approches ont été développées afin de modéliser la fissuration du béton, cependant peu de celles-ci sont suffisamment robustes pour être applicable sur des structures de grandes dimensions. Selon la mécanique non linéaire de rupture, une zone d'élaboration de fissure est présente en pointe de fissure lors de la propagation de fissure dans un béton de masse. Donc, dans la région de la FPZ, la formation et la croissance de microfissures densément distribuées induisent une réponse non linéaire du matériau avec une dissipation d'énergie importante. À ce stade du processus de rupture, la direction de la fissure n'est pas complètement définie et aucune localisation de déformations n'a lieu. Dans la deuxième étape, la réponse du matériau, à l'échelle macroscopique, devient instable. À la suite de la coalescence des microfissures, les déformations augmentent et se localiseront dans une bande de largeur définie, formant une discontinuité faible avec une orientation connue où les déformations subissent un saut. Par la suite, la largeur de cette bande sur laquelle des forces cohésives sont maintenues tend à se localiser. Finalement, ces forces de cohésion disparaissent et une zone de discontinuité forte sans contrainte apparaît. Ces mécanismes de fissuration doivent correctement être représentés afin de pouvoir prédire le comportement d'un ouvrage fissuré.

En plus du mécanisme de fissuration décrit précédemment, les fissures d'un barrage sont généralement en contact avec le réservoir. Il est donc important de pouvoir modéliser la présence de sous-pressions dans les fissures. Ce calcul amène une complication supplémentaire si celles-ci sont drainées. En l'absence d'une méthode appropriée pour calculer ces pressions, elles sont souvent surestimées et cette surcharge peut occasionner une propagation de fissure non réaliste et amène à des conclusions conservatrices sur la stabilité de l'ouvrage. Il est donc important d'établir une méthode en mesure de réaliser un couplage hydromécanique d'un écoulement complexe afin de modéliser le processus d'hydrofracturation.

En fonction de la problématique générale décrite, trois problématiques spécifiques ont été examinées dans cette thèse à savoir :

1. la résolution des calculs bidimensionnels et tridimensionnels de la propagation de fissures en proposant un modèle de fissure qui couple les avantages de l'approche de la mécanique continue de l'endommagement avec ceux de la méthode des éléments finis étendus ;
2. le calcul de la fissuration hydromécanique fortement couplée dans des structures tridimensionnelles de grandes dimensions en utilisant la XFEM ;
3. la prise en compte d'un écoulement complexe et de la présence de drainage dans les discontinuités dans un modèle hydromécanique couplé ainsi que les conditions de saturation partielles.

5.1 Contributions

Dans cette thèse, nous nous sommes intéressés à la modélisation de la fissuration dans les structures hydrauliques tridimensionnelles en béton non armé de grandes dimensions. Dans ce contexte, le développement d'une nouvelle méthode numérique pour représenter la fissuration en intégrant la mécanique non linéaire de la rupture à l'aide d'un modèle de fissuration diffuse dans la zone d'élaboration de la fissure avec un modèle XFEM dans la zone où il y a coalescence des microfissures a été réalisé en 2D et en 3D. Ce nouveau modèle couple donc les avantages de l'approche de la mécanique continue de l'endommagement avec celle de la méthode des éléments finis étendus. Avant que la transition se produise entre les deux modèles, la mécanique continue de l'endommagement est utilisée comme prédicteur afin de déterminer la trajectoire de fissure. Lors de la transition, la conservation d'énergie est appliquée en assurant que la dissipation d'énergie en mode I est conservée. Ce modèle a démontré une grande capacité à reproduire les trajectoires de fissures ainsi que les courbes de résultats expérimentaux pour de nombreux cas de simulation. De plus, il a été démontré que ces résultats sont indépendants du maillage utilisé, confirmant l'objectivité du modèle. Finalement, sachant que le modèle tient compte uniquement de la conservation d'énergie pour le mode I de rupture, les résultats obtenus pour les cas de simulation de ruptures en cisaillement, en accord avec les résultats expérimentaux, viennent confirmer la remise en question de l'importance du mode II réalisé lors de travaux de recherches expérimentales (Carpinteri *et al.*, 1993; van Mier, 2017).

Le modèle de fissuration développé initialement en deux dimensions a été étendu pour un contexte tridimensionnel. Un ingrédient clé pour que la méthode fonctionne dans ce contexte est l'algorithme de suivi des discontinuités. La méthode dite globale est utilisée pour suivre les discontinuités. Cette méthode a été appliquée par d'autres auteurs, mais dans cette thèse elle a été étendue à des problèmes de taille importante avec des géométries de fissures complexes. Une contribution importante a été réalisée afin de calculer l'ouverture de fissure dans le contexte de la mécanique continue de l'endommagement. Il est commun de définir une sorte de longueur caractéristique afin de relier la déformation dans la direction principale avec une ouverture de fissure. Or, il a été démontré que dans le cas où un maillage irrégulier est utilisé, l'ouverture de fissure présente des oscillations non réalistes le long de la fissure et donne des résultats très approximatifs. La méthode proposée, basée sur une formulation XFEM locale et sur l'équilibre des forces, vient régler cette problématique. Cet algorithme a notamment été utilisé dans un cas de fissuration hydromécanique où la perméabilité, liée à l'ouverture de fissure, est augmentée lors de la progression de l'endommagement. Finalement, une contribution importante a été réalisée en utilisant la XFEM pour la première fois avec succès dans des problèmes d'envergure industrielle dans le secteur du génie civil, malgré que la méthode a été publiée il y a une vingtaine d'années (barrage voûte Alqueva (196m) illustré à la figure 3.15 ; barrage poids Ternay (41m) illustré à la figure 3.24 ; barrage poids Koyna (103m) illustré à la figure 2.20 ; barrage voûte (165m) illustré à la figure 4.23)

Une autre contribution a été réalisée en proposant une méthode hydromécanique 3D fortement couplée pour le calcul de problèmes de fracturation hydraulique complexes et non planaires avec ou sans drains. Un ingrédient clé est l'utilisation d'un sous-problème dans lequel un maillage hydraulique est utilisé afin de calculer l'écoulement dans les discontinuités. La complexité de l'écoulement, lié aux non-linéarités causées par les différents régimes d'écoulement et à la présence de drainage, peut être calculée par la méthode proposée. La pression calculée à l'aide de ce sous-problème peut être transférée au problème hydromécanique fortement couplé. Un aspect important à considérer concerne le transfert des ouvertures de fissures de la structure vers le maillage hydraulique et, à l'inverse, le transfert des pressions hydrauliques vers le problème hydromécanique en respectant l'équilibre des charges appliquées. L'utilisation de la XFEM permet le calcul de l'ouverture de fissure ainsi que l'application de la pression sur les surfaces de la fissure pour la simulation de l'amorçage et de la propagation d'une fracture hydraulique. Les conditions de saturation partielles sont ajoutées au modèle en couplant un modèle de diffusion non linéaire prenant en compte l'effet de la saturation par une équation non linéaire variant en temps et en espace.

5.2 Perspectives

Les défis inhérents au traitement du suivi des discontinuités non planaires existent toujours. À ce jour, aucune des nombreuses nouvelles méthodes de discrétisation étendues n'a été en mesure de calculer des problèmes de fissuration complexes avec présence d'intersections qui peuvent notamment être induites par la réaction alcali-granulat (RAG). Des recherches supplémentaires sont nécessaires avant que ces méthodes ne deviennent suffisamment matures afin de calculer des problèmes de la taille d'un barrage.

Dans les cas de validation proposés pour les écoulements complexes, les applications ont été limitées à un écoulement Newtonien et les drains ont été utilisés comme des puits. L'extension de la méthode développée pour la simulation numérique de l'injection de coulis cimentaire dans une discontinuité, où un fluide de type Bingham est injecté dans les zones fissurées à travers un trou de forage, pourrait être réalisée. L'objectif principal d'une telle simulation serait d'estimer la pression d'injection permise pour éviter l'hydrofracturation. De plus, ces dernières années, la production de gaz naturel a considérablement augmenté grâce aux progrès de la technique de fracturation hydraulique des formations schisteuses riches en hydrocarbures, appelées réservoirs de «gaz de schiste». La méthode proposée pourrait être appliquée, en convertissant les drains en sources, afin de modéliser l'hydrofracturation.

Les présents développements ont été réalisés dans un code autonome écrit en C++ (le code contient approximativement 50000 lignes sans inclure les librairies). Bien que ceci procure plusieurs avantages, puisqu'aucune restriction n'est présente dans l'écriture d'un tel code, elle implique aussi une lourdeur afin d'assurer sa maintenabilité. De plus, afin d'intégrer l'ajout d'éléments tels des contacts, des coques, poutres, l'ajout de la possibilité d'effectuer des analyses dynamiques avec prise en compte des éléments fluides et l'ajout d'une interface graphique nécessite toute une équipe de développeurs dédiés à ce type de développement. Afin de simplifier ceci, il est possible d'intégrer les développements réalisés dans la présente thèse à un logiciel commercial par l'utilisant de fonctions souvent disponibles aux usagers tels que les *User Programmable Features* (UPF) fournies dans le logiciel commercial ANSYS. Afin de rendre les développements disponibles aux ingénieurs avec une interface conviviale, une grande partie des développements ont déjà été intégrés aux logiciels ANSYS. Cependant, il serait appréciable de compléter cette intégration afin d'assurer une pérennité des développements.

L'objectif de la thèse étant le développement d'une méthode pouvant arriver à répondre aux trois problématiques décrites et à vérifier et valider celle-ci par un processus de V&V (Verification & Validation (Oreskes *et al.*, 1994; B.H.Thacker *et al.*)). Un effort important a été consacré au volet validation en modélisant un grand nombre de cas incluant sept cas bidimensionnels, neuf cas tridimensionnels et la proposition d'un nouveau cas tridimensionnel. Il est évident qu'il manque des cas de validation experimental pour les cas les plus complexes, c'est à dire la validation de l'effet du drainage sur les structures. Un programme expérimental sur l'essai de fendage serait certainement une contribution nécessaire afin de fournir des données essentielles sur la réponse d'une structure en présence d'un écoulement complexe dans un milieu fissuré.

Finalement, pour que la thèse ait un impact plus important dans la pratique et donne des indications aux ingénieurs, l'application de la méthode proposée sur des cas génériques pourrait permettre d'élaborer de consignes générales et des approches simplifiées afin d'estimer l'influence de la présence de drains et la prise en compte de la condition de saturation partielle sur le développement de la trajectoire de fissure en présence de joint de levée, etc.

ANNEXE I

LISTE DES PUBLICATIONS

1. Articles présentés dans la thèse

Article 1 : Roth, S.-N., Léger P., Soulaïmani, A. (2014), A combined XFEM - damage mechanics approach for concrete crack propagation, *Computer Methods in Applied Mechanics and Engineering*, 283, 923-955

Article 2 : Roth, S.-N., Léger P., Soulaïmani, A. (2020), Strongly coupled XFEM formulation for non-planar three-dimensional simulation of hydraulic fracturing with emphasis on concrete dams, *Computer Methods in Applied Mechanics and Engineering*, 363, 112899

Article 3 : Roth, S.-N., Léger P., Soulaïmani, A. (2020), Fully-coupled Hydro-Mechanical Cracking using XFEM in 3D for Application to Complex Flow in Discontinuities Including Drainage System, soumis à la revue *Computer Methods in Applied Mechanics and Engineering*

2. Autres publications et présentations pertinentes réalisées durant la thèse

Roth, S.-N., Léger, P., Soulaïmani, A. (2013). XFEM Using a Non Linear Fracture Mechanics Approach for Concrete Crack Propagation in Dam Safety Assessment, dans les comptes rendus de la conférence *VIII International Conference on Fracture Mechanics of Concrete and Concrete Structures (FraMCoS)*, Toledo, Spain.

Roth, S.-N., Lacombe, A., Léger, P., Soulaïmani, A. (2015). Coupled Hydro-Mechanical Cracking of Concrete Arch Dams Considering Drainage Efficiency, dans les comptes rendus de la conférence *Second International Dam World Conference*, Cachan, Paris, France.

Roth, S.-N., Soulaïmani, A., Léger, P. (2015). Combined XFEM-continuous damage mechanics approach for three dimensional concrete crack propagation, dans les comptes rendus de la conférence *Fourth International Conference on Computational Modeling of Fracture and Failure of Materials and Structures (CFRAC)*, Lisbon, Portugal.

Roth, S.-N., Lacombe, A., Léger, P., Soulaimani, A. (2015). Coupled hydro-mechanical cracking of concrete arch dams considering drainage efficiency. *Dam Engineering*, 25(4)

Roth, S.-N., Léger, P., Soulaïmani, A. (2016). Coupled Hydro-Mechanical Cracking of Concrete Using XFEM in 3D, dans les comptes rendus de la conférence *IX International Conference on Fracture Mechanics of Concrete and Concrete Structures (FraMCoS)*, Berkeley, California, USA.

Roth, S.-N., Soulaïmani, A., Léger, P. (2017). Combined Segregated-Fully Coupled Hydro-Mechanical Cracking of Concrete Using XFEM in 3D, dans les comptes rendus de la conférence *U.S. National Congress on Computational Mechanics (USNCCM)*, Montreal, QC, Canada.

Roth, S.-N., Soulaïmani, A., Léger, P. (2017). Combined Segregated-Fully Coupled Hydro-Mechanical Cracking of Concrete Using XFEM in 3D, dans les comptes rendus de la conférence *eXtended Discretization MethodS (XDMS)*, Umeå, Sweden.

Roth, S.-N., Léger, P. (2019). Computation of safety margins of a cracked dam considering drainage efficiency in a coupled hydro-mechanical model, dans les comptes rendus du *Symposium de la Commission internationale des grands barrages (CIGB)*, Ottawa, ON, Canada.

BIBLIOGRAPHIE

Abellan, M.-A., Dangla, P. & Bergheau, J. M. B. (2005). Analysis of Discontinuities in Fluid-Saturated Porous Media. *Turin, Italy*, (International Conference on Fracture (ICF 11)).

Acker, P. & Ulm, F.-J. (2001). Creep and Shrinkage of Concrete: Physical Origins and Practical Measurements. *Nuclear Engineering and Design*, 203(2), 143 - 158. doi: 10.1016/S0029-5493(00)00304-6.

Advani, S. H., Lee, T. S., Dean, R. H., Pak, C. K. & Avasthi, J. M. (1993). Consequences of Fracturing Fluid Lag in Three-Dimensional Hydraulic Fractures. *Denver, Colorado*, (Low Permeability Reservoirs Symposium). doi: 10.2118/25888-MS.

Aifantis, E. C. (1984). On the Microstructural Origin of Certain Inelastic Models. *Journal of Engineering Materials and Technology*, 106(4), 326-330. doi: 10.1115/1.3225725.

Aldea, C., Ghandehari, M., Shah, S. & Karr, A. (2000). Estimation of Water Flow Through Cracked Concrete Under Load. *ACI Structural Journal*, 97(5), 567–575. doi: 10.14359/9289.

Amadei, B., Illangasekare, T., Morris, D. I. & Boggs, H. (1989). Estimation of Uplift in Cracks in Older Concrete Gravity Dams: Analytical Solution and Parametric Study. *Journal of Energy Engineering*, 115(1), 19-38. doi: 10.1061/(ASCE)0733-9402(1989)115:1(19).

Ambati, M., Gerasimov, T. & De Lorenzis, L. (2015). A Review on Phase-Field Models of Brittle Fracture and a New Fast Hybrid Formulation. *Computational Mechanics*, 55(2), 383–405. doi: 10.1007/s00466-014-1109-y.

Andelfinger, U. & Ramm, E. (1993). EAS-Elements for Two-Dimensional, Three-Dimensional, Plate and Shell Structures and Their Equivalence to HR-Elements. *International Journal for Numerical Methods in Engineering*, 36(8), 1311-1337. doi: 10.1002/nme.1620360805.

Andrews, L. & Bernstein, H. J. (2016). NearTree, a Data Structure and a Software Toolkit for the Nearest-Neighbor Problem. *Journal of Applied Crystallography*, 49(3), 756–761.

Areias, P., Msekh, M. & Rabczuk, T. (2016). Damage and Fracture Algorithm Using the Screened Poisson Equation and Local Remeshing. *Engineering Fracture Mechanics*, 158, 116 - 143. doi: 10.1016/j.engfracmech.2015.10.042.

Areias, P. M. A. & Belytschko, T. (2005). Analysis of Three-Dimensional Crack Initiation and Propagation Using the Extended Finite Element Method. *International Journal for Numerical Methods in Engineering*, 63(5), 760-788. doi: 10.1002/nme.1305.

Areias, P. M. & Belytschko, T. (2006). A Comment on the Article "A Finite Element Method for Simulation of Strong and Weak Discontinuities in Solid Mechanics" by

A. Hansbo and P. Hansbo [Comput. Methods Appl. Mech. Engrg. 193 (2004) 3523-3540]. *Computer Methods in Applied Mechanics and Engineering*, 195(9), 1275 - 1276. doi: 10.1016/j.cma.2005.03.006.

Armero, F. & Callari, C. (1999). An Analysis of Strong Discontinuities in a Saturated Poro-Plastic Solid. *International Journal for Numerical Methods in Engineering*, 46(10), 1673-1698. doi: 10.1002/(SICI)1097-0207(19991210)46:10<1673::AID-NME719>3.0.CO;2-S.

Armero, F. & Kim, J. (2012). Three-Dimensional Finite Elements with Embedded Strong Discontinuities to Model Material Failure in the Infinitesimal Range. *International Journal for Numerical Methods in Engineering*, 91(12), 1291-1330. doi: 10.1002/nme.4314.

Arrea, M. & Ingraffea, A. (1981). *Mixed-Mode Crack Propagation in Mortar and Concrete* (Rapport n°81-13). Department of Structural Engineering, Cornell University. Ithaca, New York.

Azevedo, N. M. & de Lemos, J. V. (2010). Modelação De Cenários De Ruptura Em Barragens De Betão Com Um Modelo De Partículas. *Lisbon, Portugal*, (Encontro Nacional Betão Estrutural).

Babuška, I. & Melenk, J. M. (1997). The Partition of Unity Method. *International Journal for Numerical Methods in Engineering*, 40(4), 727–758.

Baroghel-Bouny, V., Mainguy, M., Lassabatere, T. & Coussy, O. (1999). Characterization and Identification of Equilibrium and Transfer Moisture Properties for Ordinary and High-Performance Cementitious Materials. *Cement and Concrete Research*, 29(8), 1225 - 1238. doi: 10.1016/S0008-8846(99)00102-7.

Barton, N., Bandis, S. & Bakhtar, K. (1985). Strength, Deformation and Conductivity Coupling of Rock Joints. *International Journal of Rock Mechanics and Mining Sciences Geomechanics Abstracts*, 22(5), 121-140.

Barton, N. & de Quadros, E. F. (1997). Joint Aperture and Roughness in the Prediction of Flow and Groutability of Rock Masses. *International Journal of Rock Mechanics and Mining Sciences*, 34(3-4), 252.e1–252.e14.

Bary, B. (1996). *Étude Du Couplage Hydraulique-Mécanique Dans Le Béton Endommagé*. (Thèse de doctorat, Thèse dirigée par Gilles Pijaudier-Cabot, Génie civil Cachan, Ecole normale supérieure 1996).

Bažant, Z. P. (1975). Pore Pressure, Uplift, and Failure Analysis of Concrete Dams. *Department of Civil Engineering of the University College, Swansae*, (Int. Simp. Criteria and Assumptions for Numerical Analysis of Dams), 782-802.

Bažant, Z. P. & Becq-Giraudon, E. (2002). Statistical Prediction of Fracture Parameters of Concrete and Implications for Choice of Testing Standard. *Cement and Concrete Research*, 32(4), 529–556. doi: 10.1016/S0008-8846(01)00723-2.

Bažant, Z. P. & Cabot, G. P. (1989). Measurement of Characteristic Length of Nonlocal Continuum. *Journal of Engineering Mechanics (ASCE)*, 115(4), 755–767.

Bažant, Z. P. & Oh, B. (1983). Crack Band Theory for Fracture of Concrete. *Materials and Structures*, 16(3), 155–177. doi: 10.1007/BF02486267.

Bažant, Z. P. & Ozbolt, J. (1990). Nonlocal Microplane Model for Fracture, Damage, and Size Effect in Structures. *Journal of Engineering Mechanics (ASCE)*, 116. doi: 10.1061/(ASCE)0733-9399(1990)116:11(2485).

Bažant, Z. P. & Pfeiffer, P. (1986). Shear Fracture Tests of Concrete. *Materials and Structures*, 19(2), 111–121. doi: 10.1007/BF02481755.

Bažant, Z. P. & Pfeiffer, P. A. (1987). Determination of Fracture Energy from Size Effect and Brittleness Number. *ACI Materials Journal*, 84(6), 463–480.

Bažant, Z. P. & Planas, J. (1997). *Fracture and Size Effect in Concrete and Other Quasibrittle Materials*. Taylor & Francis.

Bažant, Z. P. & Jirásek, M. (2002). Nonlocal Integral Formulations of Plasticity and Damage: Survey of Progress. *Journal of Engineering Mechanics (ASCE)*, 128(11), 1119–1149.

Bažant, Z. P. (1970). Constitutive Equation for Concrete Creep and Shrinkage Based on Thermodynamics of Multiphase Systems. *Materials and Structures*, 3(1), 3–36. doi: 10.1007/BF02475106.

Bažant, Z. & Jirásek, M. (2018). *Creep and Hygrothermal Effects in Concrete Structures*. Springer Netherlands.

Bažant, Z. & Najjar, L. J. (1972). Nonlinear Water Diffusion in Nonsaturated Concrete. *Materials and Structures*, 5(1), 3-20. doi: 10.1007/BF02479073.

Bear, J. (1972). *Dynamics of Fluids in Porous Media*. American Elsevier New York.

Bear, J. (2018). *Modeling Phenomena of Flow and Transport in Porous Media*. Springer International Publishing.

Becker, C., Jox, S. & Meschke, G. (2010). 3D Higher-Order X-FEM Model for the Simulation of Cohesive Cracks in Cementitious Materials Considering Hygro-Mechanical Couplings. *CMES: Computer Modeling in Engineering & Sciences*, 57(3), 245-278.

Belytschko, T. & Black, T. (1999). Elastic Crack Growth in Finite Elements with Minimal Remeshing. *International Journal for Numerical Methods in Engineering*, 45(5), 601–620.

Belytschko, T., Fish, J. & Engelmann, B. E. (1988). A Finite Element with Embedded Localization Zones. *Computer Methods in Applied Mechanics and Engineering*, 70(1), 59–89.

Belytschko, T., Moës, N., Usui, S. & Parimi, C. (2001). Arbitrary Discontinuities in Finite Elements. *International Journal for Numerical Methods in Engineering*, 50(4), 993–1013.

Benedetti, L., Cervera, M. & Chiumenti, M. (2017). 3D Numerical Modelling of Twisting Cracks Under Bending and Torsion of Skew Notched Beams. *Engineering Fracture Mechanics*, 176, 235 - 256. doi: 10.1016/j.engfracmech.2017.03.025.

Bhattacharjee, S., Ghrib, F., Tinawi, R. & Léger, P. (1995). Poro-Fracture Analysis of Concrete Using a Damage Mechanics Model. *ETH Zurich, Switzerland*, (2nd International Conference on Fracture Mechanics of Concrete and Concrete Structures), 1057–1066.

Bhattacharjee, S. S. & Léger, P. (1994). Application of NLFM Models to Predict Cracking in Concrete Gravity Dams. *Journal of Structural Engineering (ASCE)*, 120(4), 1255–1271.

B.H.Thacker, S.W.Doebling, F.M.Hemez, Anderson, M., Pepin, J. & Rodriguez, E. Concepts of Model Verification and Validation. doi: 10.2172/835920.

Bilbao, A. B., Izzuddin, B. & Vollum, R. (2015). Enhanced Nonlinear Analysis of Three-Dimensional Concrete Structures Using Damage Plasticity Modelling. *Czech Republic*, (Proceedings of the Fifteenth International Conference on Civil, Structural and Environmental Engineering Computing).

Biot, M. A. (1935). Le Problèmc De La Consolidation Des Matières Argileuses Sous Une Charge. *Annales de la Société Scientifique de Bruxelles, série B*, 55, 110-113.

Biot, M. A. (1941). General Theory of Three-Dimensional Consolidation. *Journal of Applied Physics*, 12(2), 155-164. doi: 10.1063/1.1712886.

Biot, M. A. (1955). Theory of Elasticity and Consolidation for a Porous Anisotropic Solid. *Journal of Applied Physics*, 26(2), 182-185. doi: 10.1063/1.1721956.

Biot, M. A. (1956). General Solutions of the Equations of Elasticity and Consolidation for a Porous Material. *Journal of Applied Mechanics*, 78, 91-96.

Bisschop, J. & van Mier, J. G. M. (2002). Effect of Aggregates on Drying Shrinkage Microcracking in Cement-Based Composites. *Materials and Structures*, 35(8), 453–461. doi: 10.1007/BF02483132.

Boone, T. J. & Ingraffea, A. R. (1990). A Numerical Procedure for Simulation of Hydraulically-Driven Fracture Propagation in Poroelastic Media. *International Journal for Numerical and Analytical Methods in Geomechanics*, 14(1), 27-47. doi: 10.1002/nag.1610140103.

Bouchard, P., Bay, F. & Chastel, Y. (2003). Numerical Modelling of Crack Propagation: Automatic Remeshing and Comparison of Different Criteria. *Computer Methods in Applied Mechanics and Engineering*, 192(35), 3887 - 3908. doi: 10.1016/S0045-7825(03)00391-8.

Bouhjiti, D. E.-M., Ezzedine El Dandachy, M., Dufour, F., Dal Pont, S., Briffaut, M., Baroth, J. & Masson, B. (2018). New Continuous Strain-Based Description of Concrete's Damage-Permeability Coupling. *International Journal for Numerical and Analytical Methods in Geomechanics*, 42(14), 1671-1697. doi: 10.1002/nag.2808.

Bourdin, B., Francfort, G. & Marigo, J.-J. (2000). Numerical Experiments in Revisited Brittle Fracture. *Journal of the Mechanics and Physics of Solids*, 48(4), 797 - 826. doi: 10.1016/S0022-5096(99)00028-9.

Bourdin, B., Francfort, G. A. & Marigo, J.-J. (2008). The Variational Approach to Fracture. *Journal of Elasticity*, 91(1), 5–148. doi: 10.1007/s10659-007-9107-3.

Brokenshire, D. R. (1996). *Torsional Fracture Tests*. (Thèse de doctorat, Cardiff University, UK).

Brühwiler, E. & Roelfstra, P. E. (1989). Tensile Softening Properties and Structural Response of a Concrete Member. *University of Wales*, (Proceedings, Int. Conf. on Recent Developments in the Fracture of Concrete and Rock).

Brühwiler, E. & Saouma, V. E. (1995). Water Fracture Interaction in Concrete-Part 1: Fracture Properties. *Materials Journal*, 92(3), 296–303.

Brühwiler, E. & Wittmann, F. (1990). Failure of Dam Concrete Subjected to Seismic Loading Conditions. *Engineering Fracture Mechanics*, 35, 565–571. doi: 10.1016/0013-7944(90)90231-5.

Brühwiler, E., Broz, J. J. & Saouma, V. E. (1991). Fracture Model Evaluation of Dam Concrete. *Journal of Materials in Civil Engineering*, 3(4), 235–251.

Burlion, N., Skoczylas, F. & Dubois, T. (2003). Induced Anisotropic Permeability Due to Drying of Concrete. *Cement and Concrete Research*, 33(5), 679 - 687. doi: 10.1016/S0008-8846(02)01039-6.

Cai, Q. (2007). *Finite Element Modelling Of Cracking In Concrete Gravity Dams*. (Thèse de doctorat, University Of Pretoria, South Africa).

Carpinteri, A., Valente, S., Ferrara, G. & Melchiorrl, G. (1993). Is Mode II Fracture Energy a Real Material Property? *Computers & Structures*, 48(3), 397–413. doi: 10.1016/0045-7949(93)90316-6.

Carpinteri, A., Valente, S., Ferrara, G. & Imperato, L. (1994). Experimental and Numerical Fracture Modelling of a Gravity Dam. *Special Publication*, 143, 107-122.

Chang, C. S. & Duncan, J. M. (1983). Consolidation Analysis for Partly Saturated Clay by Using an Elastic-Plastic Effective Stress-Strain Model. *International Journal for Numerical and Analytical Methods in Geomechanics*, 7(1), 39-55. doi: 10.1002/nag.1610070106.

Charmet, J., Guyon, E. & Roux, S. (1989). Disorder and Fracture. *NATO ASI*, 204. doi: 10.1007/978-1-4615-6864-3.

Chen, Y., Zhou, C. & Zheng, H. (2008). A Numerical Solution to Seepage Problems with Complex Drainage Systems. *Computers and Geotechnics*, 35(3), 383 - 393. doi: 10.1016/j.compgeo.2007.08.005.

Chiaia, B., Vervuurt, A. & Mier, J. G. M. V. (1997). Lattice Model Evaluation of Progressive Failure in Disordered Particle Composites. *Engineering Fracture Mechanics*, 57(2). doi: 10.1016/S0013-7944(97)00011-8.

Choińska, M., Dufour, F. & Pijaudier-Cabot, G. (2007). Matching Permeability Law from Diffuse Damage to Discontinuous Crack Opening. (Proc. Fracture Mechanics of Concrete and Concrete Structures), 541-547.

Choinska, M., Khelidj, A., Chatzigeorgiou, G. & Pijaudier-Cabot, G. (2007). Effects and Interactions of Temperature and Stress-Level Related Damage on Permeability of Concrete. *Cement and Concrete Research*, 37(1), 79 - 88. doi: 10.1016/j.cemconres.2006.09.015.

Chopra, A. K. & Chakrabarti, P. (1972). The Earthquake Experience at Koyna Dam and Stresses in Concrete Gravity Dams. *Earthquake Engineering & Structural Dynamics*, 1, 151–164. doi: 10.1002/eqe.4290010204.

Clough, R. W. (1960). The Finite Element Method in Plane Stress Analysis. *Pittsburg, USA*, (Proc. 2nd A.S.C.E. Conf. on Electronic Computation).

Clough, R. W. (1962). *The Stress Distribution of Norfork Dam*. California Univ Berkeley Inst Of Engineering Research.

Cohen-Steiner, D. & Da, F. (2004). A Greedy Delaunay-Based Surface Reconstruction Algorithm. *The Visual Computer*, 20(1), 4-16. doi: 10.1007/s00371-003-0217-z.

Comi, C., Mariani, S. & Perego, U. (2007). An Extended FE Strategy for Transition from Continuum Damage to Mode I Cohesive Crack Propagation. *International Journal for Numerical and Analytical Methods in Geomechanics*, 31(2), 213–238.

Cope, R., Rao, P., Clark, L. & Norris, P. (1980). Modelling of Reinforced Concrete Behaviour for Finite Element Analysis of Bridge Slab. *Swansea*, (Numerical Methods for Nonlinear problem), 457-470.

Cordebois, J. P. & Sidoroff, F. (1982). Damage Induced Elastic Anisotropy. *Mechanical Behavior of Anisotropic Solids / Comportment Méchanique Des Solides Anisotropes*, pp. 761–774.

Coussy, O. (2010). *Mechanics and Physics of Porous Solids*. Chichester, West Sussex, U.K. ; Hoboken, N.J.: Wiley.

Cuvilliez, S., Feyel, F., Lorentz, E. & Michel-Ponnelle, S. (2012). A Finite Element Approach Coupling a Continuous Gradient Damage Model and a Cohesive Zone Model Within the Framework of Quasi-Brittle Failure. *Computer Methods in Applied Mechanics and Engineering*, 237-240(0), 244–259. doi: 10.1016/j.cma.2012.04.019.

de Borst, R. (1991). Simulation of Strain Localization: A Reappraisal of the Cosserat Continuum. *Engineering Computations*, 8(4), 317-332.

de Borst, R. (1986). *Non-Linear Analysis of Frictional Materials*. (Thèse de doctorat, TU Delft, Delft University of Technology).

Dechaumphai, P., Phongthanapanich, S. & Sricharoenchai, T. (2003). Combined Delaunay Triangulation and Adaptive Finite Element Method for Crack Growth Analysis. *Acta Mechanica Sinica*, 19(2), 162–171. doi: 10.1007/BF02487678.

Denarie, E., Saouma, V. E., Iocco, A. & Varelas, D. (2001). Concrete Fracture Process Zone Characterization with Fiber Optics. *Journal of Engineering Mechanics (ASCE)*, 127. doi: 10.1061/(ASCE)0733-9399(2001)127:5(494).

Dias, I. F., Oliver, J. & Lloberas-Valls, O. (2018). Strain-Injection and Crack-Path Field Techniques for 3D Crack-Propagation Modelling in Quasi-Brittle Materials. *International Journal of Fracture*, 212(1), 67–87. doi: 10.1007/s10704-018-0293-8.

Dompierre, J., Labbé, P., Vallet, M.-G. & Camarero, R. (1999). How to Subdivide Pyramids, Prisms, and Hexahedra into Tetrahedra. *Proceedings, 8th International Meshing Roundtable*, pp. 195–204.

Droz, P. (1987). *Modèle Numérique Du Comportement Non-Linéaire D'ouvrages Massifs En Béton Non Armé*. (Thèse de doctorat, Swiss Federal Institute of Technology at Lausanne (EPFL)).

Drucker, D. (1959). A Definition of Stable Inelastic Material. *J. Applied Mech.*, 26, 101-186.

Duan, Q., Song, J.-H., Menouillard, T. & Belytschko, T. (2009). Element-Local Level Set Method for Three-Dimensional Dynamic Crack Growth. *International Journal for Numerical Methods in Engineering*, 80(12), 1520-1543. doi: 10.1002/nme.2665.

Duarte, C., Babuška, I. & Oden, J. (2000). Generalized Finite Element Methods for Three-Dimensional Structural Mechanics Problems. *Computers & Structures*, 77(2), 215 - 232. doi: 10.1016/S0045-7949(99)00211-4.

Eringen, A. C. (1981). On Nonlocal Plasticity. *International Journal of Engineering Science*, 19(12), 1461-1474. doi: 10.1016/0020-7225(81)90072-0.

Eringen, A. C. (1983). Theories of Nonlocal Plasticity. *International Journal of Engineering Science*, 21(7), 741-751. doi: 10.1016/0020-7225(83)90058-7.

Farhat, C., Lesoinne, M. & Le Tallec, P. (1998). Load and Motion Transfer Algorithms for Fluid/structure Interaction Problems with Non-Matching Discrete Interfaces: Momentum and Energy Conservation, Optimal Discretization and Application to Aeroelasticity. *Computer Methods in Applied Mechanics and Engineering*, 157(1-2), 95–114.

Fauchet, B. (1991). *Analyse Poroplastique Des Barrages En Béton Et De Leurs Fondations. Rôle De La Pression Interstitielle*. (Thèse de doctorat, École nationale des ponts et chaussées).

Federal Energy Regulatory Commission (FERC). (2016). *Engineering Guidelines for the Evaluation of Hydroelectric Projects. Chapter III, Gravity Dams*. Federal Energy Regulatory Commission. Office of Hydropower Licensing.

Feist, C. & Hofstetter, G. (2006a). An Embedded Strong Discontinuity Model for Cracking of Plain Concrete. *Computer Methods in Applied Mechanics and Engineering*, 195(52), 7115 - 7138. doi: 10.1016/j.cma.2005.01.028.

Feist, C. & Hofstetter, G. (2006b). Three-Dimensional Fracture Simulations Based on the SDA. *International Journal for Numerical and Analytical Methods in Geomechanics*, 31(2), 189-212. doi: 10.1002/nag.542.

Feist, C. & Hofstetter, G. (2007). Validation of 3D Crack Propagation in Plain Concrete-Part I: Experimental Investigation-The PCT3D Test. *Computers and concrete*, 4(1), 49–66.

Feist, C. (2004). *A Numerical Model for Cracking of Plain Concrete Based on the Strong Discontinuity Approach*. (Thèse de doctorat, Universität Innsbruck).

Ferté, G., Massin, P. & Mo N. (2016). 3D Crack Propagation with Cohesive Elements in the Extended Finite Element Method. *Computer Methods in Applied Mechanics and Engineering*, 300, 347 - 374. doi: 10.1016/j.cma.2015.11.018.

Fipps, G., Skaggs, R. W. & Nieber, J. L. (1986). Drains as a Boundary Condition in Finite Elements. *Water Resources Research*, 22(11), 1613-1621. doi: 10.1029/WR022i011p01613.

Francfort, G. & Marigo, J.-J. (1998). Revisiting Brittle Fracture as an Energy Minimization Problem. *Journal of the Mechanics and Physics of Solids*, 46(8), 1319 - 1342. doi: 10.1016/S0022-5096(98)00034-9.

Fredlund, D. & Morgenstern, N. (1977). Stress State Variables for Unsaturated Soils. *Journal of the Geotechnical Engineering Division*, 103, 447-466.

Fries, T.-P. & Baydoun, M. (2011). Crack Propagation with the Extended Finite Element Method and a Hybrid Explicit-Implicit Crack Description. *International Journal for Numerical Methods in Engineering*, 89(12), 1527-1558. doi: 10.1002/nme.3299.

Gasser, T. C. (2007). Validation of 3D Crack Propagation in Plain Concrete. Part II: Computational Modeling and Predictions of the PCT3D Test. *Computers and Concrete*, 4(1), 67 - 82. doi: 10.12989/cac.2007.4.1.067.

Gasser, T. C. & Holzapfel, G. A. (2005). Modeling 3D Crack Propagation in Unreinforced Concrete Using PUFEM. *Computer Methods in Applied Mechanics and Engineering*, 194(25), 2859 - 2896. doi: 10.1016/j.cma.2004.07.025.

Gasser, T. C. & Holzapfel, G. A. (2006). 3D Crack Propagation in Unreinforced Concrete.: A Two-Step Algorithm for Tracking 3D Crack Paths. *Computer Methods in Applied Mechanics and Engineering*, 195(37-40), 5198–5219.

Gawin, D., Pesavento, F. & Schrefler, B. A. (2002). Simulation of Damage-Permeability Coupling in Hygro-Thermo-Mechanical Analysis of Concrete at High Temperature. *Communications in Numerical Methods in Engineering*, 18(2), 113-119. doi: 10.1002/cnm.472.

Gérard, B. (1996). *Contribution Des Couplages Mécanique-Chimie : Transfert Dans La Tenue À long Terme Des Ouvrages De Stockage De Dechets Radioactifs*. (Thèse de doctorat, Thèse dirigée par Denys Breysse, Génie civil Cachan, Ecole normale supérieure 1996).

Ghrib, F. (1994). *Sur L'analyse De La Fissuration Des Barrages En Béton Par La Mécanique De L'endommagement Continu-Comportement Statique Et Dynamique*. (Thèse de doctorat, Dept. de génie civil, École Polytechnique de Montréal, Montréal, Québec, Canada).

Ghrib, F. & Tinawi, R. (1995). Nonlinear Behavior of Concrete Dams Using Damage Mechanics. *Journal of Engineering Mechanics (ASCE)*, 121. doi: 10.1061/(ASCE)0733-9399(1995)121:4(513).

Gioia, G., Bažant, Z. P. & Pohl, B. (1992). Is No-Tension Dam Design Always Safe? *Dam Engineering*, 3(1), 23–34.

Giovanardi, B., Scotti, A. & Formaggia, L. (2017). A Hybrid XFEM-Phase Field (Xfield) Method for Crack Propagation in Brittle Elastic Materials. *Computer Methods in Applied Mechanics and Engineering*, 320, 396 - 420. doi: 10.1016/j.cma.2017.03.039.

Giry, C., Dufour, F. & Mazars, J. (2011). Stress-Based Nonlocal Damage Model. *International Journal of Solids and Structures*, 48(25-26), 3431–3443. doi: 10.1016/j.ijsolstr.2011.08.012.

Gordeliy, E. & Peirce, A. (2013). Coupling Schemes for Modeling Hydraulic Fracture Propagation Using the XFEM. *Computer Methods in Applied Mechanics and Engineering*, 253, 305 - 322. doi: 10.1016/j.cma.2012.08.017.

Gordeliy, E., Abbas, S. & Peirce, A. (2018). Modeling Nonplanar Hydraulic Fracture Propagation Using the XFEM: An Implicit Level-Set Algorithm and Fracture Tip Asymptotics. *International Journal of Solids and Structures*. doi: 10.1016/j.ijsolstr.2018.09.025.

Granger, L. (1995). *Comportement Différé Du Béton Dans Les Enceintes De Centrales Nucléaires : Analyse Et Modélisation*. (Thèse de doctorat, Thèse dirigée par Jean-Michel Torrenti, Sciences appliquées, École nationale des ponts et chaussées, (France) 1995).

Grassl, P. & Bolander, J. (2016). Three-Dimensional Network Model for Coupling of Fracture and Mass Transport in Quasi-Brittle Geomaterials. *Materials*, 9(9). doi: 10.3390/ma9090782.

Gravouil, A., Moës, N. & Belytschko, T. (2002). Non-Planar 3D Crack Growth by the Extended Finite Element and Level Sets-Part II: Level Set Update. *International Journal for Numerical Methods in Engineering*, 53(11), 2569-2586. doi: 10.1002/nme.430.

Griffith, A. A. (1921). The Phenomena of Rupture and Flow in Solids. *Philosophical Transactions of the Royal Society of London*, 221, 163-197.

Griffith, A. A. (1924). The Theory of Rupture. *Proceedings of the First International Conference for Applied Mechanics*, pp. 55-63.

Gunn, R. M. (1998). *Non-Linear Analysis of Arch Dams Including an Anisotropic Damage Mechanics Based Constitutive Model for Concrete*. (Thèse de doctorat, University of Brighton).

Gupta, P. & Duarte, C. A. (2014). Simulation of Non-Planar Three-Dimensional Hydraulic Fracture Propagation. *International Journal for Numerical and Analytical Methods in Geomechanics*, 38(13), 1397-1430. doi: 10.1002/nag.2305.

Gürses, E. & Miehe, C. (2009). A Computational Framework of Three-Dimensional Configurational-Force-Driven Brittle Crack Propagation. *Computer Methods in Applied Mechanics and Engineering*, 198(15), 1413 - 1428. doi: 10.1016/j.cma.2008.12.028.

Hakami, E. (1995). *Aperture Distribution of Rock Fractures*. (Thèse de doctorat, Royal Institute of Technology).

Hansbo, A. & Hansbo, P. (2002). An Unfitted Finite Element Method, Based on Nitsche's Method, for Elliptic Interface Problems. *Computer Methods in Applied Mechanics and Engineering*, 191(47-48), 5537–5552. doi: 10.1016/S0045-7825(02)00524-8.

Hansbo, A. & Hansbo, P. (2004). A Finite Element Method for the Simulation of Strong and Weak Discontinuities in Solid Mechanics. *Computer Methods in Applied Mechanics and Engineering*, 193(33), 3523 - 3540. doi: 10.1016/j.cma.2003.12.041.

Hedjazi, L., Martin, C., Guessasma, S., Valle, G. D. & Dendievel, R. (2012). Application of the Discrete Element Method to Crack Propagation and Crack Branching in a Vitreous

Dense Biopolymer Material. *International Journal of Solids and Structures*, 49(13), 1893 - 1899. doi: 10.1016/j.ijsolstr.2012.03.030.

Hegen, D. (1996). Element-Free Galerkin Methods in Combination with Finite Element Approaches. *Computer Methods in Applied Mechanics and Engineering*, 135(1-2), 143–166.

Heroux, M. A., Bartlett, R. A., Howle, V. E., Hoekstra, R. J., Hu, J. J., Kolda, T. G., Lehoucq, R. B., Long, K. R., Pawlowski, R. P., Phipps, E. T., Salinger, A. G., Thornquist, H. K., Tuminaro, R. S., Willenbring, J. M., Williams, A. & Stanley, K. S. (2005). An Overview of the Trilinos Project. *ACM Trans. Math. Softw.*, 31(3), 397–423. doi: http://doi.acm.org/10.1145/1089014.1089021.

Hillerborg, A., Modéer, M. & Petersson, P.-E. (1976). Analysis of Crack Formation and Crack Growth in Concrete by Means of Fracture Mechanics and Finite Elements. *Cement and Concrete Research*, 6(6), 773-781.

Hillerborg, A. (1983). Analysis of One Single Crack. Dans Wittmann, F. H. (Éd.), *Fracture Mechanics of Concrete (Developments in civil engineering)* (pp. 223–249). Elsevier.

Hirshikesh, Natarajan, S. & Annabattula, R. K. (2019). A FEniCS Implementation of the Phase Field Method for Quasi-Static Brittle Fracture. *Frontiers of Structural and Civil Engineering*, 13(2), 380–396. doi: 10.1007/s11709-018-0471-9.

Huespe, A. & Oliver, J. (2011). Crack Models with Embedded Discontinuities. Dans Hofstetter, G. & Meschke, G. (Éds.), *Numerical Modeling of Concrete Cracking* (vol. 532, pp. 99-159). Springer Vienna. doi: 10.1007/978-3-7091-0897-0_3.

Ibáñez, S. B. (2006). *Contribuciones a La Simulación Numérica Del Fallo Material En Medios Tridimensionales Mediante La Metodología De Discontinuidades Fuertes De Continuo*. (Thèse de doctorat, Universitat Politècnica de Catalunya).

Inglis, C. E. (1913). Stresses in a Plate Due to the Presence of Cracks and Sharp Corners. *Transactions of the Institution of Naval Architects*.

Ingraffea, A. R. (2004). Computational Fracture Mechanics. Dans *Encyclopedia of Computational Mechanics*. John Wiley and Sons, Ltd. doi: 10.1002/0470091355.ecm032.pub2.

International Commission on Large Dams (ICOLD). (2004). *Working Group on Uplift Pressures Under Concrete Dams*. ICOLD European Club.

Irwin, G. R. (1957). Analysis of Stresses and Strains Near the End of a Crack Traversing a Plate. *J. Appl. Mech.* doi: citeulike-article-id:810675.

Jäger, P., Steinmann, P. & Kuhl, E. (2008). Modeling Three-Dimensional Crack Propagation - A Comparison of Crack Path Tracking Strategies. *International Journal for Numerical Methods in Engineering*, 76(9), 1328-1352. doi: 10.1002/nme.2353.

Jefferson, A. D., Barr, B., Bennett, T. & Hee, S. (2004). Three Dimensional Finite Element Simulations of Fracture Tests Using the Craft Concrete Model. *Computers and Concrete*, 1(3), 261–284.

Jirasek, M. (2000). Comparative Study on Finite Elements with Embedded Discontinuities. *Computer Methods in Applied Mechanics and Engineering*, 188(1-3), 307–30.

Jirásek, M. (2011). Damage and Smeared Crack Models. Dans Hofstetter, G. & Meschke, G. (Éds.), *Numerical Modeling of Concrete Cracking* (vol. 532, ch. 1, pp. 1-49). Springer Vienna. doi: 10.1007/978-3-7091-0897-0_1.

Jirásek, M. & Grassl, P. (2008). Evaluation of Directional Mesh Bias in Concrete Fracture Simulations Using Continuum Damage Models. *Engineering Fracture Mechanics*, 75(8), 1921–1943. doi: 10.1016/j.engfracmech.2007.11.010.

Jirásek, M. & Zimmermann, T. (1998). Analysis of Rotating Crack Model. *Journal of Engineering Mechanics (ASCE)*, 124(8), 842–851.

Jirásek, M. & Zimmermann, T. (2001). Embedded Crack Model. Part II: Combination with Smeared Cracks. *International Journal for Numerical Methods in Engineering*, 50(6), 1291-1305. doi: 10.1002/1097-0207(20010228)50:6<1291::AID-NME12>3.0.CO;2-Q.

Jox, S., Dumstorff, P. & Meschke, G. (2006). Aspects of Crack Propagation and Hygro-Mechanical Coupling Using X-FEM. *Lisbon, Portugal*, (3rd European Conf. on Computational Mechanics (ECCM)). doi: 10.1007/1-4020-5370-3.

Jox, S., Becker, C. & Meschke, G. (2007). Hygro-Mechanical Modeling of Cracked Concrete in the Framework of the X-FEM. *Catania, Italy*, (VI International Conference on Fracture Mechanics of Concrete and Concrete Structures), 517-524.

Kachanov, L. M. (1999). Rupture Time Under Creep Conditions. *International Journal of Fracture*, 97(1-4), 11–18. doi: 10.1023/A:1018671022008.

Kaczmarczyk, L., Ullah, Z. & Pearce, C. J. (2017). Energy Consistent Framework for Continuously Evolving 3D Crack Propagation. *Computer Methods in Applied Mechanics and Engineering*, 324, 54 - 73. doi: 10.1016/j.cma.2017.06.001.

Léger, P., Tinawi, R., Bhattacharjee, S. & Leclerc, M. (1997). Failure Mechanisms of Gravity Dams Subjected to Hydrostatic Overload: Influence of Weak Lift Joints. *Italy*, (Proceedings 19th International Congress on Large Dams).

Linder, C. & Zhang, X. (2013). A Marching Cubes Based Failure Surface Propagation Concept for Three-Dimensional Finite Elements with Non-Planar Embedded Strong Discontinuities of Higher-Order Kinematics. *International Journal for Numerical Methods in Engineering*, 96(6), 339-372. doi: 10.1002/nme.4546.

LNEC. (1999). *Estudo Experimental Da Barragem Do Alqueva*. Report 222/99.

Lorensen, W. E. & Cline, H. E. (1987). Marching Cubes: A High Resolution 3D Surface Construction Algorithm. *Proceedings of the 14th Annual Conference on Computer Graphics and Interactive Techniques*, (SIGGRAPH '87), 163–169. doi: 10.1145/37401.37422.

Louis, C. (1969). *A Study of Groundwater Flow in Jointed Rock and Its Influence on the Stability of Rock Masses* (Rapport n°10). Imp. Coll. London.

Lu, Y., Belytschko, T. & Gu, L. (1994). A New Implementation of the Element Free Galerkin Method. *Computer Methods in Applied Mechanics and Engineering*, 113(3-4), 397-414. doi: 10.1016/0045-7825(94)90056-6.

Mainguy, M., Coussy, O. & Eymard, R. (1999). *Modélisation Des Transferts Hydriques Isothermes En Milieu Poreux : Application Au Séchage Des Matériaux À Base De Ciment* (Rapport n°32). Laboratoire central des ponts et chaussées. Paris, France.

Mainguy, M., Coussy, O. & Baroghel-Bouny, V. (2001). Role of Air Pressure in Drying of Weakly Permeable Materials. *Journal of Engineering Mechanics (ASCE)*, 127(6), 582-592. doi: 10.1061/(ASCE)0733-9399(2001)127:6(582).

Mazars, J. (1984). *Application De La Mécanique De L'endommagement Au Comportement Non Linéaire Et À La Rupture Du Béton De Structure*. (Thèse de doctorat, Université Paris VI, France).

Melenk, J. & Babuška, I. (1996). The Partition of Unity Finite Element Method: Basic Theory and Applications. *Computer Methods in Applied Mechanics and Engineering*, 139(1), 289 - 314. doi: 10.1016/S0045-7825(96)01087-0.

Melenk., M. (1995). *On Generalized Finite Element Method*. (Thèse de doctorat, University of Maryland).

Mensi, R., Acker, P. V. & Attolou, A. (1988). Séchage Du Béton: Analyse Et Modélisation. *Materials and Structures*, 21, 3-12.

Meschke, G. & Leonhart, D. (2015). A Generalized Finite Element Method for Hydro-Mechanically Coupled Analysis of Hydraulic Fracturing Problems Using Space-Time Variant Enrichment Functions. *Computer Methods in Applied Mechanics and Engineering*, 290, 438 - 465. doi: 10.1016/j.cma.2015.03.005.

Meschke, G. & Dumstorff, P. (2007). Energy-Based Modeling of Cohesive and Cohesionless Cracks Via X-FEM. *Computer Methods in Applied Mechanics and Engineering*, 196(21-24), 2338–2357.

Miehe, C., Welschinger, F. & Hofacker, M. (2010). Thermodynamically Consistent Phase-Field Models of Fracture: Variational Principles and Multi-Field FE Implementations. *International Journal for Numerical Methods in Engineering*, 83(10), 1273-1311. doi: 10.1002/nme.2861.

Miehe, C., Aldakheel, F. & Raina, A. (2016). Phase Field Modeling of Ductile Fracture at Finite Strains: A Variational Gradient-Extended Plasticity-Damage Theory. *International Journal of Plasticity*, 84, 1 - 32. doi: 10.1016/j.ijplas.2016.04.011.

Millington, R. J. (1959). Gas Diffusion in Porous Media. *Science*, 130(3367), 100–102. doi: 10.1126/science.130.3367.100-a.

Moës, N., Dolbow, J. & Belytschko, T. (1999). A Finite Element Method for Crack Growth Without Remeshing. *International Journal for Numerical Methods in Engineering*, 46(1), 131–150.

Mohammadnejad, T. & Khoei, A. R. (2013). Hydro-Mechanical Modeling of Cohesive Crack Propagation in Multiphase Porous Media Using the Extended Finite Element Method. *International Journal for Numerical and Analytical Methods in Geomechanics*, 37(10), 1247-1279. doi: 10.1002/nag.2079.

Morales, R., Brady, B. & Ingraffea, A. (1993). Three-Dimensional Analysis and Visualization of the Wellbore and the Fracturing Process in Inclined Wells. *Denver, Colorado*, (Low Permeability Reservoirs Symposium). doi: 10.2118/25889-MS.

Morenon, P. (2017). *Modélisation Des Réactions De Gonflement Interne Des Bétons Avec Prise En Compte Des Couplages Poro-Mécaniques Et Chimiques*. (Thèse de doctorat, Université Toulouse 3 Paul Sabatier).

Newman, T. S. & Yi, H. (2006). A Survey of the Marching Cubes Algorithm. *Computers & Graphics*, 30(5), 854 - 879. doi: 10.1016/j.cag.2006.07.021.

Ngo, D. & Scordelis, A. C. (1967). Finite Element Analysis of Reinforced Concrete Beams. *American Concrete Institute – Journal*, 64(3), 152–163.

Nilson, A. H. (1967). *Finite Element Analysis of Reinforced Concrete*. (Thèse de doctorat, Dept. of Civil Engineering, University of California, Berkeley, CA).

Nishioka, T. & Atluri, S. (1983). Analytical Solution for Embedded Elliptical Cracks, and Finite Element Alternating Method for Elliptical Surface Cracks, Subjected to Arbitrary Loadings. *Engineering Fracture Mechanics*, 17(3), 247-268. doi: 10.1016/0013-7944(83)90032-2.

Nooru-Mohamed, M. B. (1992). *Mixed-Mode Fracture of Concrete: an Experimental Approach*. (Thèse de doctorat, Technische Universiteit Delft).

Oliver, J. (1989). A Consistent Characteristic Length for Smeared Cracking Models. *International Journal for Numerical Methods in Engineering*, 28(2), 461-474. doi: 10.1002/nme.1620280214.

Oliver, J. (1996). Modelling Strong Discontinuities in Solid Mechanics Via Strain Softening Constitutive Equations. Part 1: Fundamentals. *International Journal for*

Numerical Methods in Engineering, 39(21), 3575-3600. doi: 10.1002/(SICI)1097-0207(19961115)39:21<3575::AID-NME65>3.0.CO;2-E.

Oliver, J., Huespe, A. E., Samaniego, E. & Chaves, E. W. V. (2002). On Strategies for Tracking Strong Discontinuities in Computational Failure Mechanics. *Vienna University of Technology*, (Proc.World Congress on Computational Mechanics).

Oliver, J., Huespe, A. E., Samaniego, E. & Chaves, E. W. V. (2004). Continuum Approach to the Numerical Simulation of Material Failure in Concrete. *International Journal for Numerical and Analytical Methods in Geomechanics*, 28(7-8), 609–632. doi: 10.1002/nag.365.

Oreskes, N., Shrader-Frechette, K. & Belitz, K. (1994). Verification, Validation, and Confirmation of Numerical Models in the Earth Sciences. *Science*, 263(5147), 641–646. doi: 10.1126/science.263.5147.641.

Osher, S. & Sethian, J. A. (1988). Fronts Propagating with Curvature-Dependent Speed: Algorithms Based on Hamilton-Jacobi Formulations. *Journal of Computational Physics*, 79(1), 12–49.

Oshita, H. & aki Tanabe, T. (2000). Water Migration Phenomenon Model in Cracked Concrete. II: Calibration. *Journal of Engineering Mechanics (ASCE)*, 126(5), 544-549. doi: 10.1061/(ASCE)0733-9399(2000)126:5(544).

Paas, M., Schreurs, P. & Brekelmans, W. (1993). A Continuum Approach to Brittle and Fatigue Damage: Theory and Numerical Procedures. *International Journal of Solids and Structures*, 30(4), 579 - 599. doi: 10.1016/0020-7683(93)90189-E.

Patil, R., Mishra, B. & Singh, I. (2018). A Local Moving Extended Phase Field Method (LMXPFM) for Failure Analysis of Brittle Materials. *Computer Methods in Applied Mechanics and Engineering*, 342, 674 - 709. doi: 10.1016/j.cma.2018.08.018.

Pellegrini, R. (1996). *Tecniche Di Modellazione Ed Applicazione Delle Sottopressioni* (Rapport n°RAT-STR-2832). ISMES.

Picandet, V., Khelidj, A. & Bastian, G. (2001). Effect of Axial Compressive Damage on Gas Permeability of Ordinary and High-Performance Concrete. *Cement and Concrete Research*, 31(11), 1525-1532. doi: 10.1016/S0008-8846(01)00546-4.

Picandet, V., Khelidj, A. & Bellegou, H. (2009). Crack Effects on Gas and Water Permeability of Concretes. *Cement and Concrete Research*, 39(6), 537 - 547. doi: 10.1016/j.cemconres.2009.03.009.

Pijaudier-Cabot, G., Dufour, F. & Choinska, M. (2009). Permeability Due to the Increase of Damage in Concrete: From Diffuse to Localized Damage Distributions. *Journal of Engineering Mechanics (ASCE)*, 135(9), 1022-1028. doi: 10.1061/(ASCE)EM.1943-7889.0000016.

Rabczuk, T., Bordas, S. & Zi, G. (2007). A Three-Dimensional Meshfree Method for Continuous Multiple-Crack Initiation, Propagation and Junction in Statics and Dynamics. *Computational Mechanics*, 40(3), 473–495. doi: 10.1007/s00466-006-0122-1.

Rashid, Y. R. (1968). Ultimate Strength Analysis of Prestressed Concrete Pressure Vessels. *Nuclear Engineering and Design*, 7(4), 334–344.

Reinhardt, H. W. & Xu, S. (2000). A Practical Testing Approach to Determine Mode II Fracture Energy $G_I IF$ for Concrete. *International Journal of Fracture*, 105(2), 107–125. doi: 10.1023/A:1007649004465.

Réthoré, J., de Borst, R. d. & Abellan, M.-A. (2007). A Two-Scale Approach for Fluid Flow in Fractured Porous Media. *International Journal for Numerical Methods in Engineering*, 71(7), 780-800. doi: 10.1002/nme.1962.

Riccardi, F., Kishta, E. & Richard, B. (2017). A Step-By-Step Global Crack-Tracking Approach in E-FEM Simulations of Quasi-Brittle Materials. *Engineering Fracture Mechanics*, 170, 44 - 58. doi: 10.1016/j.engfracmech.2016.11.032.

Rice, J. R. (1968). A Path Independent Integral and the Approximate Analysis of Strain Concentration by Notches and Cracks. *Journal of Applied Mechanics*, 35(2), 379-386. doi: 10.1115/1.3601206.

Rice, J. R. & Cleary, M. P. (1976). Some Basic Stress Diffusion Solutions for Fluid-Saturated Elastic Porous Media with Compressible Constituents. *Reviews of Geophysics*, 14(2), 227-241. doi: 10.1029/RG014i002p00227.

Richards, L. A. (1931). Capillary Conduction of Liquids Through Porous Mediums. *Physics*, 1(5), 318-333. doi: 10.1063/1.1745010.

Roth, S. & Léger, P. (2019). Computation of Safety Margins of a Cracked Dam Considering Drainage Efficiency in a Coupled Hydro-Mechanical Model. *Ottawa, ON, Canada*, (Publications du symposium CIGB).

Roth, S.-N., Léger, P. & Soulaïmani, A. (2013). XFEM Using a Non Linear Fracture Mechanics Approach for Concrete Crack Propagation in Dam Safety Assessment. *Toledo, Spain*, (VIII International Conference on Fracture Mechanics of Concrete and Concrete Structures).

Roth, S.-N., Lacombe, A., Léger, P. & Soulaïmani, A. (2015a). Coupled Hydro-Mechanical Cracking of Concrete Arch Dams Considering Drainage Efficiency. *Lisbon, Portugal*, (Second International DAM WORLD Conference).

Roth, S.-N., Lacombe, A., Léger, P. & Soulaïmani, A. (2015b). Coupled Hydro-Mechanical Cracking of Concrete Arch Dams Considering Drainage Efficiency. *Dam Engineering*, 25(4).

Roth, S.-N., Léger, P. & Soulaïmani, A. (2015c). A Combined XFEM--Damage Mechanics Approach for Concrete Crack Propagation. *Computer Methods in Applied Mechanics and Engineering*, 283, 923–955.

Roth, S.-N., Soulaïmani, A. & Léger, P. (2015d). Combined XFEM-Continuous Damage Mechanics Approach for Three Dimensional Concrete Crack Propagation. *Cachan, Paris, France*, (Fourth International Conference on Computational Modeling of Fracture and Failure of Materials and Structures).

Roth, S.-N., Léger, P. & Soulaïmani, A. (2016). Coupled Hydro-Mechanical Cracking of Concrete Using XFEM in 3D. *Berkeley, California, USA*, (IX International Conference on Fracture Mechanics of Concrete and Concrete Structures).

Roth, S.-N., Soulaïmani, A. & Léger, P. (2017a). Combined Segregated-Fully Coupled Hydro-Mechanical Cracking of Concrete Using XFEM in 3D. *Montreal, QC, Canada*, (U.S. National Congress on Computational Mechanics). doi: 10.21012/FC9.263.

Roth, S.-N., Soulaïmani, A. & Léger, P. (2017b). Combined Segregated-Fully Coupled Hydro-Mechanical Cracking of Concrete Using XFEM in 3D. *Umeå, Sweden*, (eXtended Discretization MethodS).

Roth, S.-N., Léger, P. & Soulaïmani, A. (2020). Strongly Coupled XFEM Formulation for Non-Planar Three-Dimensional Simulation of Hydraulic Fracturing with Emphasis on Concrete Dams. *Computer Methods in Applied Mechanics and Engineering*, 363, 112899. doi: 10.1016/j.cma.2020.112899.

Rots, J. G. (1988). *Computational Modeling of Concrete Fracture*. (Thèse de doctorat, Delft University of Technology, Delft, The Netherlands).

Rungamornrat, J., Wheeler, M. & Mear, M. (2005, 12). A Numerical Technique for Simulating Nonplanar Evolution of Hydraulic Fractures. *Dallas, Texas, USA*, (SPE Annual Technical Conference and Exhibition, ATCE 2005), 3813-3821.

Saloustros, S., Cervera, M. & Pelà, L. (2018). Challenges, Tools and Applications of Tracking Algorithms in the Numerical Modelling of Cracks in Concrete and Masonry Structures. *Archives of Computational Methods in Engineering*. doi: 10.1007/s11831-018-9274-3.

Sanjay, G., Gregory, J. K. & Juan, C. S. (1995). Anisotropic Modelling and Numerical Simulation of Brittle Damage in Concrete. *International Journal for Numerical Methods in Engineering*, 38(21), 3611-3633. doi: 10.1002/nme.1620382105.

Saouma, V. E. (2007). *Lecture Notes in Fracture Mechanics*. Dept. of Civil Environmental and Architectural Engineering. University of Colorado, Boulder, CO 80309-0428.

Schrefler, B. A. (1995). F.E. in Environmental Engineering: Coupled Thermo-Hydro-Mechanical Processes in Porous Media Including Pollutant Transport. *Archives of Computational Methods in Engineering*, 2(3), 1–54. doi: 10.1007/BF02736173.

Sethian, J. (1999). *Level Set Methods and Fast Marching Methods: Evolving Interfaces in Computational Geometry, Fluid Mechanics, Computer Vision, and Materials Science*. Cambridge University Press.

Sidoroff, F. & Cordebois, C. (1979). Endommagement Anisotrope En Élasticité Et Plasticité. *Journal de Mécanique appliquée*, 25, 45–60.

Simo, J. C. & Oliver, J. (1994). A New Approach to the Analysis and Simulation of Strain Softening in Solids (éd. Z.P. Bažant et al, pp. 25-39). London: E. and F.N. Spon.

Simo, J. C., Oliver, J. & Armero, F. (1993a). An Analysis of Strong Discontinuities Induced by Strain-Softening in Rate-Independent Inelastic Solids. *Computational Mechanics*, 12(5), 277-296.

Simo, J., Armero, F. & Taylor, R. (1993b). Improved Versions of Assumed Enhanced Strain Tri-Linear Elements for 3D Finite Deformation Problems. *Computer Methods in Applied Mechanics and Engineering*, 110(3), 359 - 386. doi: 10.1016/0045-7825(93)90215-J.

Simone, A., Wells, G. N. & Sluys, L. J. (2003). From Continuous to Discontinuous Failure in a Gradient-Enhanced Continuum Damage Model. *Computer Methods in Applied Mechanics and Engineering*, 192(192), 4581–4607. doi: 10.1016/S0045-7825(03)00428-6.

Slobbe, A., Hendriks, M. & Rots, J. (2013). Systematic Assessment of Directional Mesh Bias with Periodic Boundary Conditions: Applied to the Crack Band Model. *Engineering Fracture Mechanics*, 109, 186 - 208. doi: 10.1016/j.engfracmech.2013.06.005.

Stolarska, M., Chopp, D. L., Moës, N. & Belytschko, T. (2001). Modelling Crack Growth by Level Sets in the Extended Finite Element Method. *International Journal for Numerical Methods in Engineering*, 51(8), 943-960. doi: 10.1002/nme.201.

Strouboulis, T., Babuška, I. & Copps, K. (2000a). The Design and Analysis of the Generalized Finite Element Method. *Computer Methods in Applied Mechanics and Engineering*, 181(1), 43 - 69. doi: 10.1016/S0045-7825(99)00072-9.

Strouboulis, T., Copps, K. & Babuška, I. (2000b). The Generalized Finite Element Method: an Example of Its Implementation and Illustration of Its Performance. *International Journal for Numerical Methods in Engineering*, 47(8), 1401-1417. doi: 10.1002/(SICI)1097-0207(20000320)47:8<1401::AID-NME835>3.0.CO;2-8.

Sukumar, N., Chopp, D. & Moran, B. (2003). Extended Finite Element Method and Fast Marching Method for Three-Dimensional Fatigue Crack Propagation. *Engineering Fracture Mechanics*, 70(1), 29 - 48. doi: 10.1016/S0013-7944(02)00032-2.

Sukumar, N., Chopp, D. L., Béchet, E. & Moës, N. (2008). Three-Dimensional Non-Planar Crack Growth by a Coupled Extended Finite Element and Fast Marching Method. *International Journal for Numerical Methods in Engineering*, 76(5), 727-748. doi: 10.1002/nme.2344.

Taylor, R. L., Beresford, P. J. & Wilson, E. L. (1976). A Non-Conforming Element for Stress Analysis. *International Journal for Numerical Methods in Engineering*, 10(6), 1211–1219. doi: 10.1002/nme.1620100602.

Terzaghi, K. (1923). Die Berechnung Der Durchlassigkeitsziffer Des Tones Aus Dem Verlauf Der Hidrodynamichen Span-Nungserscheinungen. *Mathematish-Naturwissen-Schaftiliche Klasse*, 132, 125-138.

The CGAL Project. (2019). *CGAL User and Reference Manual* (éd. 5.0). CGAL Editorial Board. Repéré à https://doc.cgal.org/5.0/Manual/packages.html.

Turner, M. J., Clough, R. W., Martin, H. C. & Topp, L. J. (1956). Stiffness and Deflection Analysis of Complex Structures. *J. of Aero. Sci.*, 23(9).

Tvergaard, V. (2003). Cohesive Zone Representations of Failure Between Elastic or Rigid Solids and Ductile Solids. *Engineering Fracture Mechanics*, 70(14), 1859 - 1868. doi: 10.1016/S0013-7944(03)00128-0.

Unger, J. F., Eckardt, S. & Knke, C. (2007). Modelling of Cohesive Crack Growth in Concrete Structures with the Extended Finite Element Method. *Computer Methods in Applied Mechanics and Engineering*, 196(41), 4087 - 4100. doi: 10.1016/j.cma.2007.03.023.

U.S. Army Corps of Engineers (USACE). (2000). *Evaluation and Comparison of Stability Analysis and Uplift Criteria for Concrete Gravity Dams by Three Federal Agencies* (Rapport n°ERDC/ITL TR-00-1). U.S. Army Corps of Engineers. Information Technology Laboratory.

van Genuchten, M. T. (1980). A Closed Form Equation for Predicting the Hydraulic Conductivity of Unsaturated Soils. *Soil Sci. Soc. Am. J.*, 44(5), 892-898.

van Mier, J. (2017). *Fracture Processes of Concrete*. CRC Press.

Verruijt, A. (1969). Elastic Storage of Aquifers. *Flow Through Porous Media*, 331-376.

Watanabe, N., Wang, W., Taron, J., Grke, U. J. & Kolditz, O. (2012). Lower-Dimensional Interface Elements with Local Enrichment: Application to Coupled Hydro-Mechanical Problems in Discretely Fractured Porous Media. *International Journal for Numerical Methods in Engineering*, 90(8), 1010-1034. doi: 10.1002/nme.3353.

Wawrzynek, P. & Ingraffea, A. (1987). Interactive Finite Element Analysis of Fracture Processes: An Integrated Approach. *Theoretical and Applied Fracture Mechanics*, 8(2), 137-150. doi: 10.1016/0167-8442(87)90007-3.

Wheeler, M., Wick, T. & Wollner, W. (2014). An Augmented-Lagrangian Method for the Phase-Field Approach for Pressurized Fractures. *Computer Methods in Applied Mechanics and Engineering*, 271, 69 - 85. doi: 10.1016/j.cma.2013.12.005.

Whitaker, S. (1977). Simultaneous Heat, Mass, and Momentum Transfer in Porous Media: A Theory of Drying (vol. 13, pp. 119 - 203). Elsevier. doi: 10.1016/S0065-2717(08)70223-5.

Wilhelms, J. & Van Gelder, A. (1990). Topological Considerations in Isosurface Generation Extended Abstract. *Proceedings of the 1990 Workshop on Volume Visualization*, (VVS '90), 79–86. doi: 10.1145/99307.99325.

Willam, K., Pramono, E. & Sture, S. (1986). Stability and Uniqueness of Strain-Softening Computations. *Proc. Europe-US Symp. on Finite Element Methods for Nonlinear Problems*.

Wilson, Z. A. & Landis, C. M. (2016). Phase-Field Modeling of Hydraulic Fracture. *Journal of the Mechanics and Physics of Solids*, 96, 264 - 290. doi: 10.1016/j.jmps.2016.07.019.

Wittmann, F. H. (1973). Interaction of Hardened Cement Paste and Water. *Journal of the American Ceramic Society*, 56(8), 409-415. doi: 10.1111/j.1151-2916.1973.tb12711.x.

Xu, X. P. & Needleman, A. (1994). Numerical Simulations of Fast Crack Growth in Brittle Solids. *Journal of The Mechanics and Physics of Solids*, 42(9), 1397-1434. doi: 10.1016/0022-5096(94)90003-5.

Yoshioka, K. & Bourdin, B. (2016). A Variational Hydraulic Fracturing Model Coupled to a Reservoir Simulator. *International Journal of Rock Mechanics and Mining Sciences*, 88, 137 - 150. doi: 10.1016/j.ijrmms.2016.07.020.

Zhan, Y. & Meschke, G. (2016). Multilevel Computational Model for Failure Analysis of Steel-Fiber-Reinforced Concrete Structures. *Journal of Engineering Mechanics (ASCE)*, 142(11), 04016090. doi: 10.1061/(ASCE)EM.1943-7889.0001154.

Zienkiewicz, O. C. & Zhu, J. Z. (1992). The Superconvergent Patch Recovery and a Posteriori Error Estimates. Part 1: The Recovery Technique. *International Journal for Numerical Methods in Engineering*, 33(7), 1331-1364. doi: 10.1002/nme.1620330702.